Université de Liège

Faculté des Sciences Appliquées

Année Académique 2008-2009

Development of solid-shell elements for large deformation simulation and springback prediction

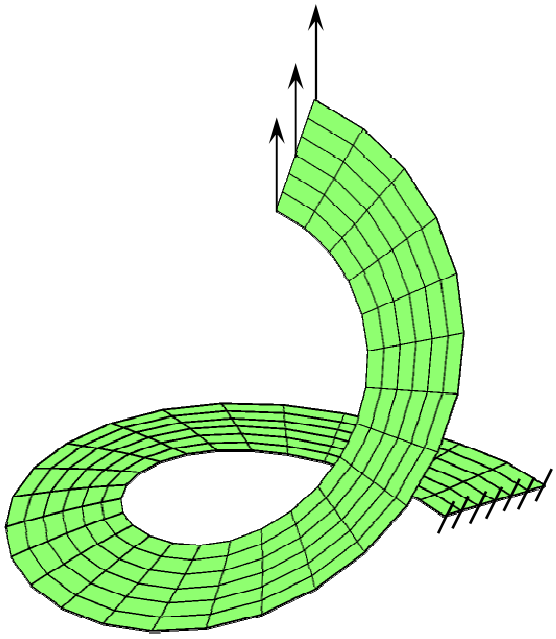

Travail présenté par

Nhu Huynh NGUYEN
Ingénieur mécanicien

pour l'obtention du grade de
Docteur en Sciences de l'Ingénieur

Septembre 2009

To my mother for her sacrifices to sons

To my wife for her understanding and encouragement

To my sincere friends for their precious helps

Acknowledgements

All acknowledgements to the help I have received while completing this thesis are worthless. First of all I would like to thank the financial support from 322 Scholarship Foundation of Vietnamese Government; without that financial support for 1 year in Vietnam and 2.5 years in Belgium I would not have a chance of doing this thesis.

I would like to express my deep emotion to my family in Vietnam and to my Vietnamese friends in Belgium. Thanks to their cares I always felt the familial air nearby. Special thanks are devoted to Dr. Quoc Viet BUI.

I deeply thank Prof. M. HOGGE and Prof. J.P. PONTHOT for their precious supports and their patience. I also thank all the members of the Research Team in MC&T Department – University of Liège for their direct or indirect supports.

Finally, I would like to thank the jury members of my thesis for their participation in reading the thesis.

NOTATIONS AND SYMBOLS

Operator	Meaning
$\boldsymbol{D}$	Differential operator
X	Scalar
$\vec{x}$	Vector with components x_i
$[X]$	Matrix
$\{X\}$	Column vector
$\dot{X}$	Time derivative of X (dX/dt)
$\boldsymbol{X}^{\boldsymbol{T}}$	Transpose of $\boldsymbol{X}$
$Sgn(x)$	+ or – sign of scalar x
$\langle x \rangle$	$\langle x \rangle = x$ if $x > 0$; $\langle x \rangle = 0$ if $x < 0$
$\boldsymbol{X} : \boldsymbol{Y}$	Double contracted product of $\boldsymbol{X}$ with $\boldsymbol{Y}$
X_I	First invariant of $\boldsymbol{X}$: $X_I = Tr(\boldsymbol{X})$
X_{II}	Second invariant of $\boldsymbol{X}$: $X_{II} = \frac{1}{2}[Tr(\boldsymbol{X})^2 - Tr(\boldsymbol{X}^2)]$
X_{III}	Third invariant of $\boldsymbol{X}$: $X_{III} = \det(\boldsymbol{X})$
$\boldsymbol{X'}$	Deviator of $\boldsymbol{X}$: $\boldsymbol{X'} = \boldsymbol{X} - \frac{1}{3} X_I \boldsymbol{I}$
δ	Kronecker delta $\delta_{ij} = 1$ if i=j, $\delta_{ij} = 0$ if i≠j
$\tilde{\boldsymbol{X}}$	A quantity with tilt bar is assumed in natural (isoparametric) coordinate system or physical coordinate system

Scalar	Meaning
A_u	Boundary along which displacements are specified
A_σ	Boundary along which surface tractions are specified
L	Contour line
π	Functional
μ, λ	Lamé coefficients
ρ	Mass density
ν	Poisson ratio
G	Shear modulus
γ_{ij}	Shear strain
A	Surface of a body
t	Time
V	Volume of a body
W	Work
$W_{\boldsymbol{S}(\boldsymbol{E})}$	Stored energy function of a hyperelastic material

1st order Tensor	Meaning
$\boldsymbol{e}_i$	Basic unit vector
$\boldsymbol{b}$	Body force per unit mass
$\boldsymbol{u}$	Current displacement vector
$\boldsymbol{F}_{ext}$	External force vector
$\boldsymbol{F}_{\text{int}}$	Internal force vector
$\boldsymbol{X}(X_1, X_2, X_3)$	Material coordinate vector
$\boldsymbol{\xi}(\xi^1, \xi^2, \xi^3)$	Natural (isoparametric) coordinate vector
$\boldsymbol{U}^h$	Nodal displacement vector, $\boldsymbol{U}^h = [u_1, v_1, w_1, ...u_n, v_n, w_n]$
$\boldsymbol{n}$	Outward normal vector to the surface A
$\boldsymbol{x}(x_1, x_2, x_3)$	Spatial coordinate vector
$\boldsymbol{t}^*$	Specific tractions along A_σ
$\boldsymbol{u}^*$	Specific displacements along A_u
$\boldsymbol{t}$	Traction vector, stress vector

2nd and higher order Tensor	Meaning
$\boldsymbol{\varepsilon}$	Cauchy's strain tensor
$\boldsymbol{\sigma}$	Cauchy's stress tensor
$\boldsymbol{F}$	Deformation gradient tensor
Grad$\boldsymbol{U}$	Material displacement gradient tensor, $Grad\boldsymbol{U} = \nabla_0 \boldsymbol{U}$
grad$\boldsymbol{u}$	Spatial displacement gradient tensor, $grad\boldsymbol{u} = \nabla \boldsymbol{u}$
$\boldsymbol{P}$	First Piola-Kirchhoff stress tensor
$\underline{\boldsymbol{E}}$	Green-Lagrange tensor
$\boldsymbol{E}$	Green-Lagrange vector (Voigt notation): $\boldsymbol{E} = [E_{11}\ \ E_{22}\ \ E_{33}\ \ 2E_{12}\ \ 2E_{23}\ \ 2E_{31}]^T$
$\boldsymbol{J}$	Jacobian matrix
$\boldsymbol{b}$	Left Cauchy-Green tensor (Finger deformation tensor), $\boldsymbol{b} = \boldsymbol{F}\boldsymbol{F}^T$
$\boldsymbol{v}$	Left stretch deformation tensor, $\boldsymbol{v} = \boldsymbol{F}\boldsymbol{R}^{-1}$
${}^4\underline{\boldsymbol{C}}$	Constitutive moduli tensor
${}^4\boldsymbol{C}$	Constitutive moduli matrix, dimension (6x6)
$\boldsymbol{C}$	Right Cauchy-Green tensor, $\boldsymbol{C} = \boldsymbol{F}^T\boldsymbol{F}$
$\boldsymbol{U}$	Right stretch tensor, $\boldsymbol{U} = \boldsymbol{R}^{-1}\boldsymbol{F}$
$\boldsymbol{R}$	Rotation tensor, $\boldsymbol{R} = \boldsymbol{F}\boldsymbol{U}^{-1}$
$\underline{\boldsymbol{S}}$	Second Piola-Kirchhoff stress (PK2) tensor
$\boldsymbol{S}$	Second Piola-Kirchhoff stress vector (Voigt notation): $\boldsymbol{S} = [S_{11}\ \ S_{22}\ \ S_{33}\ \ S_{12}\ \ S_{23}\ \ S_{31}]^T$
$\boldsymbol{K}$	Tangent stiffness matrix
$\boldsymbol{I}$	Unity second order tensor

FIGURE LIST

TABLE LIST

Chapter 1. INTRODUCTION

INTRODUCTION

Since the sixties of the 20th century, the development of numerical methods has been the base for developing various advanced engineering simulation tools. Still nowadays, at the beginning of the 21st century, applications of numerical methods in simulation and prediction of industrial problems and/or technological processes become more and more important The most popular numerical methods is the finite element method with applications for simulation of biomechanic problems [HOL96], elastoplasticity problems [SIM88a], thermalmechanic problems [HOG76] and contact problems [PON99], etc.

Thin shell structures, whose numerical analysis is the target of this thesis, appear in many products, such as the outer-body of a car, the fuselage and wings of an airplane, etc. Modeling these parts with standard solid elements would require a huge number of elements and leads to prohibitive computational costs. For instance, to prevent locking effects, i.e. artificial stiffness in the model, modeling a beam with hexahedral solid elements requires a minimum of about 3 - 5 elements through the thickness. In such cases, a low-order shell element can replace 3 - 5 or more solid elements, which improves computational efficiency immensely. Furthermore, modeling thin structures with standard solid elements often leads to elements with high aspect ratios, which degrades the conditioning of the equations and the accuracy of the solution. However, for certain problems in structural analysis displacement degrees of freedom (DOF) at the nodes of the element are more advantageous for analysis than displacement and rotational DOF's. For example, consider complex structures which consist of both thin and thick walls. For the sake of effectiveness, shell elements should be used for thin-walled parts and solid elements should be used for thick-walled parts. If both solid and shell elements have the same DOF's (e.g. only displacements at nodes), the analysis process exhibits one type of DOF only, no requirement on transition elements exhibiting displacement and rotational DOF, e.g. Figure 1.0.1.

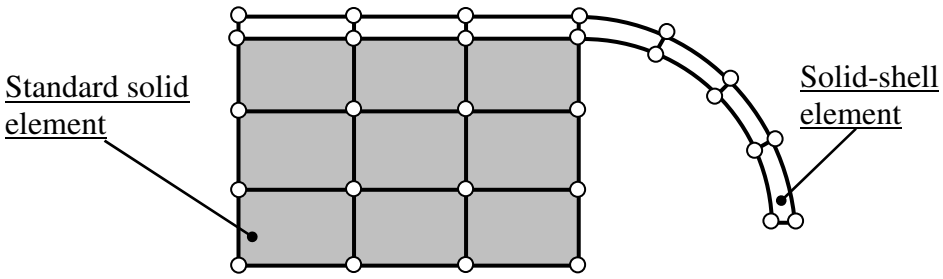

Figure 1.0.1: Connection of solid-shell element (white color) with standard solid element (grey color)

The deformation processes also with contact and friction of shell elements, such as happening in metal forming, are easier to consider if shell elements have those configuration displacement DOF. Motivated by these arguments, the thesis concentrates on developing an element that has simple kinematics (only displacement DOF's at nodes) as solid elements but is as effective in computation as shell elements. A class of those finite elements called solid-shell has been recently investigated by many researchers ([HAU98], [HAU00], [QUO03a,b], [TAN05], [JET08]) because that element is not only capable of modeling complicated structures but it can also be used to simulate metal forming problems. Literature shows indeed that solid-shell element is the most suitable choice for the above mentioned tasks.

1.1 OBJECTIVES OF THE THESIS

The use of low-order elements in finite element computations remains a popular feature in solid mechanics because of the following reasons. First, they require a simpler manipulation for meshing, especially, for a distorted configuration. Second, these elements facilitate more convenient manipulations in the adaptive *h*-type of mesh refinement. Finally, using low-order elements will remarkably save computation time, especially, for simulation with large number of DOF's such as in nonlinear problems. In this thesis, high-order elements are therefore not considered. They would, in addition, exhibit more difficulties to deal with at contact surface interfaces. From now on, for the sake of briefness, let's call the low-order standard solid element in three-dimension (3D) is the eight-node hexahedral element and the low-order standard solid element in two-dimension (2D) is the four-node quadrilateral element.

Although the structure of the low-order standard displacement elements is straightforward, they should not be used directly in the following situations:

- The elements tend to be too stiff in bending, e.g. for slender beams or thin plates under bending.
- The elements are too stiff in nearly incompressible or incompressible behavior.

In other words, four-node quadrilateral elements and eight-node hexahedral element in two and three dimensions, respectively, have a major drawback since they lead to locking in the incompressible limit. It means they do not possess the property of being uniformly convergent. In addition, even in compressible problems the use of these standard elements leads to poor accuracy particularly in bending-dominated problems, when coarse meshes are used.

The linear and nonlinear finite element analysis of plates and shells has attracted much attention in recent decades. It is necessary to capture the bending-stretching coupling of thin shell behavior. Hence, one of the motivations for designing new elements is their potential ability to capture the membrane-bending coupling correctly. So far, there are two ways in which this could be done. One is to use elements based on specific shell theories (e.g. the Vlasov [VLA49], Flugge [FLU73] theories, etc.). There are considerable controversies regarding the relative merits and drawbacks of these theories. Each theory has been obtained by carrying out approximations to different degrees when the 3D field equations are reduced to the particular class of shell equations.

The second approach is called degenerated shell approach – 3D solid elements can be reduced (degenerated) into shell elements having only mid-surface nodal variables - these are no longer dependent on the various forms of shell theories proposed and should be simple to use. They are in fact equivalent to a Mindlin type curved shell element (equivalent to a shear deformable theory), see [PRA01], [STO95]. With the standard procedure, a plate or shell theory is used as a basis for the finite element formulation. It begins with the field equations of the 3D theory and makes various assumptions, which lead to the plate or shell theory. Meanwhile, in the reduction from the three to two dimensions, an analytical integration over the thickness was included. The mid-surface geometry (in the case of shells) and the field variables are approximated using discretized nodal values and suitable interpolation functions. Integration of various element stiffness and force terms is carried out over the reference surface. Examples of such an approach include the simple facet element and many elements derived from the classical thin plate theory: the Mindlin-Reissner plate theory, shallow shell theory or even high-order shell theories. Currently, we can introduce the solid-shell theory as the third approach for capturing the bending-stretching coupling of thin shell behavior. The low-order solid-shell element has two nodes along vertical sides. Naturally, the low-order solid-shell element obeys the straight normal assumption of Mindlin-Reissner theories. Without any assumptions because of possessing solid configuration, integration of the solid-shell element stiffness is carried out over the element's physical volume.

The solid-shell elements are combinations of solid elements with shell elements. The elements are generally used for nonlinear problems (finite strain, contact, etc.) so they have to satisfy some requirements, e.g. free from all locking types, simple kinematics, etc. The following features of the solid elements and shell elements are found in the solid-shell elements:

Features from the solid elements:

- Same DOF's as solid;
- Integrating directly 3D material model (versus plane stress assumption);
- In contrast to the degenerated shell concept the complete 3D strain tensor and stress tensor are used (strains and stresses in thickness direction are also included).

Features from the shell elements:

- Use of a shell element method to remove transverse shear locking. The solid-shell elements, hence, are applicable to thin-walled structures.
- The normal to the mid-surface remains straight.

Through investigating the literatures, there are two assumed strain methods that have been exploited so far to develop solid-shell elements. They are the Assumed Natural Strain (ANS) of Dvorkin and Bathe [DVO84] and the Enhanced Assumed Strain (EAS) proposed by Simo and Rifai [SIM90]. The strain field of the EAS element is additionally modified to be a complete polynomial field. The strain field of the ANS element is replaced by an incompatible strain field that satisfies the pure bending requirement. Otherwise, there is a sound variational method: Mixed Enhanced Strain (MES) method proposed by Kasper and Taylor [KAS00b] where stresses are independent from the strain field. The MES method requires more variables (apart from the displacement field and strain field as required by the EAS and ANS methods, the MES further considers the stress field as variables) than the EAS and the ANS, thus is not an attractive approach.

Objective of the thesis is to develop a finite element that is effective for simulation of thin-walled behavior in metal forming processes. It means the element gives precise results while proposing a low computational cost. Application of that element is mainly exploited in springback simulation. Springback relates to the change in shape between the fully loaded and subsequent unloaded configurations. The springback effect is encountered during a stamping operation. This can result in the formed component being out of tolerance and thus creates major problems in assembly or installation. Accurate description of the contact is one of the main factors which renders metal forming simulation predictive or not. Let's consider the solid-shell element. Contact algorithms are more easily applied for solid like elements, thanks to the geometrical description of the lower and upper surfaces than for shell elements where nodes lie in the mid-plane. However, due to limitation of a thesis, only performance of the solid-shell for springback simulation is mainly exploited in this thesis.

Table 1.1.1: Features of low-order solid elements

Element	Features	Application domain
Standard	The standard element exhibits deficiencies as: • Volumetric locking; • Shear locking; • Poisson locking.	• Being applicable to all of problems but require very fine mesh to converge
EAS	The standard element, which is enhanced by EAS parameters, is: • locking free; • high in computational cost.	• Metal forming • Incompressible material, etc
ANS	The standard element, which adopts the ANS method, is: • only shear locking free; • cheap in computational cost.	• Thin-walled structures • Collapse of shells, etc
Solid-shell	The standard element, which adopts both the ANS and the EAS methods, is: • locking free; • cheaper in computational cost than the EAS element.	• Thin-walled structures • Metal forming • Incompressible material, etc.

1.2 APPLICATION DOMAIN

Nowadays, aims of the new 3D solid elements are:

1. No locking for incompressible materials;
2. Good bending behavior;
3. No locking in the limit of very thin elements;

4. Distortion insensitivity;
5. Good coarse mesh accuracy;
6. Simple implementation of nonlinear constitutive laws.

The first two aims are essential requirements of solid structured analyses. The third aim is usually required for structural elements, such as plate, shell and beam elements. The fourth aim is important because in discretizing an arbitrary geometry the existence of distorted elements is inevitable. In addition, elements can get highly distorted during nonlinear simulations including finite deformations. The fifth aim results from the fact that many engineering problems have to be modeled as 3D problems. Due to computer limitations, quite coarse meshes have to be used often to solve these problems. Thus, an element which provides good coarse mesh accuracy is valuable in these situations. The sixth aim is associated with the fact that more and more nonlinear computations involving nonlinear constitutive models have to be performed to design engineering structures. Thus, an element formulation which allows a straightforward implementation of such constitutive equations is desirable.

The third aim becomes increasingly important since it enables the solid elements to simulate shell problems. This makes the simulation work become more effective, especially, for simulation of complicated structures. This spares the need for introducing finite rotations as variables in thin shell elements, results in simpler contact detection on upper and lower surfaces and provides the possibility to apply 3D constitutive equations straight away.

The EAS elements can satisfy all requirements, except the third one. The solid-shell elements are the ones who could satisfy all of that 6 six requirements. Due to their dominant performance, the solid-shell elements are applicable to various applications in structural analyses. The solid-shell elements could be applied for both solid and structural engineering problems and in both linear and nonlinear applications (finite strain, contact, etc.). Concretely, the solid-shell elements are suitable choice for metal forming simulations, civil-engineering structures, impact/crash analysis, etc.

SUMMARY OF THE THESIS

Nowadays, in computational mechanics, there is a trend to treat plates and shells as a 3D continuum, using solid finite elements or 3D-like plate and shell elements, taking into account thickness changes throughout deformation and using 3D material laws. The EAS elements are very suitable to that trend; they are applicable to almost any engineering problems. However, the EAS elements are sensitive to distorted mesh (e.g. bending patch test), and they exhibit poor performances in bending for very thin-walled structures. Most important is the fact that the EAS elements are very time consuming for calculation. In contrary, Reduced Integration (RI) elements are computational time saving elements. They could be free from volumetric locking and shear locking. However, in some situations they are not stable (due to hourglass modes), see [HAN98].

The solid-shell elements are attractive ones. Currently, they attract much consideration of researchers. They possess performance of the EAS elements while they are insensitive to distorted mesh. Furthermore, they are stable and time saving elements.

Obviously, because of having the solid's configuration, the solid-shell elements are suitable for handling contact in metal forming simulation, particularly for simulation of sheet metal products whose ratio between length and thickness is large. They have only translational DOF's of solid elements so they can be easily combined with the standard solid elements in problems dealing with complex structures meanwhile they can also work as shell elements. For transverse shear locking removal, the elements employ the ANS techniques because the ANS method is cheaper (higher performance but cheaper computational cost) than the EAS method in removing transverse shear locking. To get rid of volumetric locking and membrane locking, the elements adopt techniques of the EAS method. Due to the use of ANS techniques, that were originally applied for plate and shell elements, the solid-shell elements are able to simulate thin and moderately thick-walled structures.

The thesis includes six chapters and is structured as follows. The first chapter presents the objects for the research. The second chapter introduces background methods which will be incorporated in the solid-shell elements. The third chapter develops an alternative ANS technique and applies it to the solid-shell elements. As a result, in that chapter a new solid-shell element based on the alternative ANS technique is proposed. Elastic applications of the just developed solid-shell element are illustrated in Chapter 4. In Chapter 5, plasticity theory and numerical problems in plasticity deformation are presented. The thesis specially concentrates on treating a current industrial problem: spring back prediction. Results in Chapter 4 and Chapter 5 demonstrate the capabilities of the proposed solid-shell element. Chapter 6 withdraws conclusions and then makes some remarkable future developments.

Chapter 2. BACKGROUND ON THE DEVELOPMENT OF SOLID-SHELL ELEMENTS

INTRODUCTION

The solid-shell is a solid element that has incorporated shell features, e.g. ANS technique for shear locking and curvature thickness locking removals, and EAS or RI techniques for other locking effects. In order to better understand the solid-shell concept, let's start considering some features of the low-order standard solid element and the obstacles that the solid element is facing. The difficulties when using the well-known degenerated shell elements are also investigated. Later in the chapter, all the methods that concern the solid-shell elements: the EAS (formulated in Green-Lagrange strain) [KLI97] and the classical ANS methods [DVO84] (applied for finite deformation solid elements) are introduced. These methods have been implemented in a MATLAB code. In this chapter separated performances of the ANS and EAS elements are presented. Details for their combination and co-operated performances are presented later in Chapter 3, where we also present how the solid-shell element remedies all the obstacles that the low-order standard solid elements have to overcome.

2.1 THREE DIMENSIONAL STANDARD ELEMENT

In this section we investigate the low-order standard solid element. Let's consider the following trilinear displacement field, which is conventionally employed for the eight-node standard element, Figure 2.1.1. To facilitate understanding, the analysis is restricted to a rectangular prismatic geometry element so that the physical system (X,Y,Z) and the isoparametric (natural) system (ξ^1,ξ^2,ξ^3) can be used interchangeably. The displacement fields u, v and w are linearly interpolated with the help of coefficients a_i, b_i and c_i (i = 0, ..., 7) stemming from a trilinear assumption:

$$\begin{aligned} u &= a_0 + a_1 X + a_2 Y + a_3 Z + a_4 XY + a_5 YZ + a_6 XZ + a_7 XYZ \\ \mathrm{v} &= b_0 + b_1 X + b_2 Y + b_3 Z + b_4 XY + b_5 YZ + b_6 XZ + b_7 XYZ \\ w &= c_0 + c_1 X + c_2 Y + c_3 Z + c_4 XY + c_5 YZ + c_6 XZ + c_7 XYZ \end{aligned} \tag{2.1.1a}$$

or under the form:

$$\begin{aligned} u &= (\alpha_1 + \alpha_2 X)(\beta_1 + \beta_2 Y)(\gamma_1 + \gamma_2 Z) \\ \mathrm{v} &= (\alpha_1^* + \alpha_2^* X)(\beta_1^* + \beta_2^* Y)(\gamma_1^* + \gamma_2^* Z) \\ w &= (\alpha_1^{**} + \alpha_2^{**} X)(\beta_1^{**} + \beta_2^{**} Y)(\gamma_1^{**} + \gamma_2^{**} Z) \end{aligned} \tag{2.1.1b}$$

where $\alpha_1, \alpha_2, \ldots \gamma_2^{**}$ are constants.

The Green-Lagrange strain components used in large deformation theories are given by:

$$\boldsymbol{E}_{(u)}^{com}=\begin{Bmatrix}E_{XX}\\E_{YY}\\E_{ZZ}\\2E_{XY}\\2E_{ZX}\\2E_{YZ}\end{Bmatrix}=\underbrace{\begin{Bmatrix}u_{,X}\\v_{,Y}\\w_{,Z}\\u_{,Y}+v_{,X}\\u_{,Z}+w_{,X}\\v_{,Z}+w_{,Y}\end{Bmatrix}}_{\boldsymbol{\varepsilon}_{(u)}^{com}}+\underbrace{\begin{Bmatrix}0.5(u_{,X}u_{,X}+v_{,X}v_{,X}+w_{,X}w_{,X})\\0.5(u_{,Y}u_{,Y}+v_{,Y}v_{,Y}+w_{,Y}w_{,Y})\\0.5(u_{,Z}u_{,Z}+v_{,Z}v_{,Z}+w_{,Z}w_{,Z})\\(u_{,X}u_{,Y}+v_{,X}v_{,Y}+w_{,X}w_{,Y})\\(u_{,X}u_{,Z}+v_{,X}v_{,Z}+w_{,X}w_{,Z})\\(u_{,Y}u_{,Z}+v_{,Y}v_{,Z}+w_{,Y}w_{,Z})\end{Bmatrix}}_{nonlinear\ terms} \tag{2.1.2}$$

where:

- The superscript "*com*" and the subscript "(*u*)" mean that the strain field is compatible with the displacement field.
- $u_{i,A}\equiv\dfrac{\partial u}{\partial A}\quad;\quad u_i=u,v,w\quad;\quad A=X,Y,Z\ ;$
- The infinitesimal strains are $\boldsymbol{\varepsilon}_{(u)}^{com}=\{\varepsilon_X,\varepsilon_Y,\varepsilon_Z,\gamma_{XY},\gamma_{XZ},\gamma_{YZ}\}^T$.

For the sake of simplicity, locking effects are simply considered with infinitesimal strains. It means we consider infinitesimal strains $\boldsymbol{\varepsilon}$ instead of Green-Lagrange strain $\boldsymbol{E}$. All types of locking and their remedies for low-order solid elements will be mentioned in details in the following section.

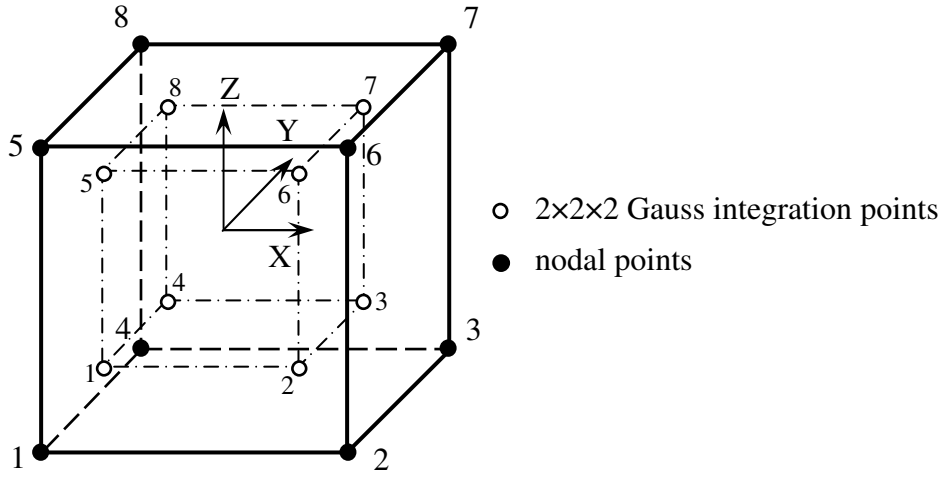

Figure 2.1.1: Hexahedral solid element

2.1.1 Difficulties with low-order standard elements

Low-order elements are preferred in nonlinear structural mechanics because of their low computational cost and simplicity in dealing with the geometry. However, in many cases, especially in pure bending problems, the low-order solid element exhibits a low-precision result due to stiffening effects known as locking.

Locking terminology

A number of different concepts to define, explain and quantify the locking effects have been discussed in the past. In the sequel it is tried to classify some of them in two different groups.

Mathematical point of view:

In the mathematical literature, the term "locking" is not as popular as in engineering literature. From a mathematical point of view, it is rather an *ill-conditioning* of the underlying mechanical problem, or the system of partial differential equations, to be more precise. The crucial property is the presence of a certain "small scale parameter" within the equations. This parameter leads to a high ratio of the coefficients in the discretized system of equations (e.g. the stiffness). Thus, the parasitic terms, evolving from unbalanced shape functions, are overly enlarged. The element "locks" if there is no uniform convergence with respect to this parameter (i.e. the rate of convergence in the range of coarse meshes depends on this parameter). According to Wilson et al. [WIL73], effect of the ill-conditioning will be minimized by the use of a computer with high (double, for example) precision or by restricting the application of the element to thick-walled structures.

Mechanical point of view:

The simplest way to explain locking is to associate the effect with the presence of "parasitic" (or spurious) strains or stresses. With parasitic we mean such strains (stresses) that do not show up in the exact solution of a certain problem. These are, for instance, transverse shear strains in the case of pure bending of a plate element (transverse shear locking) or membrane strains in the case of inextensional bending of shells (membrane locking) or volumetric strain in the case of incompressible behavior (volumetric locking). In fact, the well-known locking phenomenon of displacement based finite elements for thin-walled beams, plates, shells and solids is caused by an unbalance of the trial functions.

It should also be mentioned, that a natural strategy to remedy locking effects is the design of higher order finite elements. However, they are not attractive for nonlinear structural analysis because of expensive computation and complicated configuration. Locking of certain low-order standard displacement based finite elements comes along in different ways, namely as volumetric locking if incompressible or nearly incompressible materials are used or as membrane, shear and curvature thickness locking if the stress and strain space is not compatible due to the spatial discretization. The phenomena presented hereafter are the severe locking effects that happen with the low-order standard solid element. Other severe locking effects which happen to the solid-shell elements are mentioned in the next chapter.

2.1.1.1 Volumetric locking

If nearly-incompressible or incompressible material behavior is concerned, the low-order standard solid elements suffer from volumetric locking. In dealing with this locking, the following condition on the volumetric strain ε_v is required during the deformation process:

$$\varepsilon_v = tr(\boldsymbol{\varepsilon}) = \frac{\partial u}{\partial X} + \frac{\partial v}{\partial Y} + \frac{\partial w}{\partial Z} \equiv 0 \tag{2.1.3}$$

With the above tri-linear displacement field (2.1.1), the volumetric strain ε_v^{com} is correspondingly calculated as:

$$\varepsilon_v^{com} = (a_1 + b_2 + c_3) + (b_4 + c_6)X + (a_4 + c_5)Y + (a_6 + b_5)Z + (c_7 XY + a_7 YZ + b_7 ZX) \quad (2.1.4)$$

The volumetric strain (2.1.4) can be constrained to be zero by imposing that the coefficients of each term in (2.1.4) vanish as:

$$a_1 + b_2 + c_3 = 0 \quad (2.1.5a)$$

$$b_4 + c_6 = 0 \quad (2.1.5b)$$

$$a_4 + c_5 = 0 \quad (2.1.5c)$$

$$a_6 + b_5 = 0 \quad (2.1.5d)$$

$$a_7 = 0 \;\; ; \;\; b_7 = 0 \;\; ; \;\; c_7 = 0 \quad (2.1.5e)$$

But the volumetric strain ε_v^{com} is generally non-zero, since the presence of the terms a_7, b_7 and c_7 in the sense that they come from isolated terms of *u* or *v* or *w*, see (2.1.1). These isolated terms are different from zero in order to assure the completeness of interpolation functions. In other words, the terms a_7, b_7 and c_7 make ε_v^{com} usually different from zero. Forcing the incompressibility condition (e.g. for ν = 0.5 in elasticity or for incompressible plasticity such as J2 von Mises plasticity) will impose $a_7 = b_7 = c_7 = 0$ and thus an excessive stiffness is generated by this condition hence the name locking.

Consequently, the constraint of an incompressible material, (2.1.3), cannot generally be fulfilled by the normal strains of the pure displacement element. The effect of this deficiency on the deformation behavior of an element can be explained by using the internal energy. The internal energy π_{int} of an element consists of a deviatoric term π_d and a volumetric term π_v. It is defined by $\pi_{int} = \frac{1}{2}(\boldsymbol{u}^e)^T \boldsymbol{K}^e \boldsymbol{u}^e$ and the relative contribution of deviatoric and volumetric deformation to the element stiffness can be shown to be:

$$\pi_{int} = \pi_d + \pi_v = 2G\int_{V_e} \boldsymbol{\varepsilon}_d : \boldsymbol{\varepsilon}_d dV_e + 3\kappa\int_{V_e} \boldsymbol{\varepsilon}_v : \boldsymbol{\varepsilon}_v dV_e = 2G\int_{V_e} \boldsymbol{\varepsilon}_d : \boldsymbol{\varepsilon}_d dV_e + \kappa\int_{V_e} tr(\boldsymbol{\varepsilon})^2 dV_e \quad (2.1.6)$$

with: - bulk modulus $\kappa = \frac{2}{3}\frac{(1+\nu)}{(1-2\nu)}G$;

- volumetric strains $\boldsymbol{\varepsilon}_v = \frac{1}{3}\varepsilon_{ii}\boldsymbol{I} = tr(\boldsymbol{\varepsilon}) \;\; ; \;\; i = 1,2,3$;

- deviatoric strains $\boldsymbol{\varepsilon}_d = \boldsymbol{\varepsilon} - \boldsymbol{\varepsilon}_v$.

In contrast to all other known locking effects, which are primarily kinematic or geometric effects, volumetric locking depends on a material parameter, Poisson's ratio ν. Therefore, also the term Poisson locking is sometimes used in the literature. It is straightforward to consider the bulk modulus as the critical parameter. For ν = 0 there is no spurious volumetric locking at all; the effect becomes more and more pronounced as ν → 0.5 because $\lim\kappa_{(\nu \to 0.5)} = \infty$. In solid mechanics this effect can occur, e.g. for rubber materials, but also for metals in the range of plastic deformations (yielding).

The bulk modulus κ becomes very large for $\nu \to 1/2$. If $tr(\boldsymbol{\varepsilon})$ is not vanishing, the stiffness of one element or a group of elements will thus be much larger than the stiffness of the real incompressible continuum, for which the term π_v is vanishing. For the standard solid element, since the incompressible condition (2.1.3) cannot be accomplished, consequently, an undesirable stiffness is added to the rigidity of the

element and it makes the element stiffer than the real continuum. In other words, the non-zero volumetric strain ε_v^{com} leads to volumetric locking.

2.1.1.2 Shear locking

Transverse shear locking can occur in shear deformable beam, plate and shell elements. In principle, it is also present in solid elements if these are applied to the analysis of thin-walled structures. However, with solid elements, it is simply called "shear locking", because there is no distinct "transverse" direction in a solid element. On the contrary, the solid-shell elements take the shell behavior in thickness direction hence the transverse direction is distinct. Shear locking in the solid elements is one of the most severe locking effects because it does not only slows down the convergence but also can essentially preclude an analysis with a reasonable amount of numerical effort in practical applications.

From the classical theory of elasticity when the element is subjected to a pure bending situation, such as bending in 0X direction around 0Z axis (Figure 2.1.1), the shear strain, γ_{XY} in this case, must vanish. However, with the above trilinear field (2.1.1), the shear strain γ_{XY}^{com} in (2.1.2) is calculated as:

$$\gamma_{XY}^{com} = \frac{\partial u}{\partial Y} + \frac{\partial v}{\partial X} = (a_2 + b_1) + (a_5 + b_6)Z + a_4 X + b_4 Y + a_7 XZ + b_7 YZ \,. \tag{2.1.7}$$

That shear strain is generally non-zero. It is equal to zero only when the coefficients of each term vanish as:

$$a_2 + b_1 = 0; \quad a_5 + b_6 = 0; \tag{2.1.8a}$$

$$a_4 = 0; \quad b_4 = 0; \quad a_7 = 0; \quad b_7 = 0; \tag{2.1.8b}$$

Equations (2.1.8a) contain coefficients from both the contributing interpolation functions (u and v) which are relevant to the description of the shear strain field γ_{XY}^{com}. Hence, these coefficients can correctly represent a true zero condition on shear strain γ_{XY}^{com} when $a_2 = -b_1$ and $a_5 = -b_6$. Each equation (2.1.8b) contains only an isolated term from u or v, (a_4 or a_7) and (b_4 or b_7). In general, these isolated terms are different from zero in order to assure the completeness of interpolation functions, see (2.1.1). As a consequence, these coefficients make γ_{XY}^{com} also different from zero. In other words, the presence of coefficients a_4, b_4, a_7 and b_7 in γ_{XY}^{com} cause shear locking, hence, they are called inconsistent terms [CHA89].

The same arguments are applied for the other shear strain components γ_{YZ}^{com}, γ_{XZ}^{com}:

$$\gamma_{YZ}^{com} = \frac{\partial w}{\partial y} + \frac{\partial v}{\partial z} = (b_3 + c_2) + (b_6 + c_4)X + b_5 Y + c_5 Z + b_7 XY + c_7 XZ \tag{2.1.9a}$$

$$\gamma_{XZ}^{com} = \frac{\partial u}{\partial Z} + \frac{\partial w}{\partial X} = (a_3 + c_1) + (a_5 + c_4)Y + a_6 X + c_6 Z + a_7 XY + c_7 YZ \tag{2.1.9b}$$

The shear strain γ_{YZ}^{com} is equal to zero only when the coefficients of each terms in (2.1.9a) vanish as:

$$b_3 + c_2 = 0; \quad b_6 + c_4 = 0; \tag{2.1.10a}$$

$$b_5 = 0; \quad c_5 = 0; \quad b_7 = 0; \quad c_7 = 0; \tag{2.1.10b}$$

Similarly, the shear strain γ_{XZ}^{com} is equal to zero only when the coefficients of each terms in (2.1.9b) vanish as:

$$a_3 + c_1 = 0; \quad a_5 + c_4 = 0; \tag{2.1.11a}$$

$$a_6 = 0; \quad c_6 = 0; \quad a_7 = 0; \quad c_7 = 0; \tag{2.1.11b}$$

Consequently, non-physical effects with compatible shear strains cause the so-called shear locking for the standard elements by introducing artificial flexural stiffness. This phenomenon is essential with the vanishing of the thickness of standard elements in the modeling of bending dominated problems.

Table 2.1.1: Deformation modes of bilinear element (2D.Q1)

Mode ⟹	c_1	c_2	c_3	c_4	c_5	c_6	c_7	c_8
u w	1 0	0 1	X 0	0 X	Z 0	0 Z	XZ 0	0 XZ
ε_X	0	0	c_3	0	0	0	c_7Y	0
ε_Z	0	0	0	0	0	c_6	0	c_8X
γ_{XZ}	0	0	0	c_4	c_5	0	c_7X	c_8Z

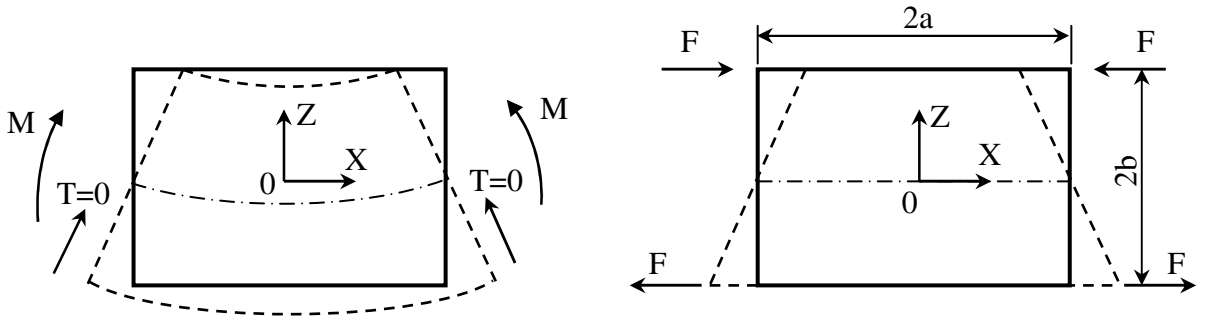

a) Continuum mechanics
$\gamma_{XZ} = 0$

b) FEM representative
$\gamma_{XZ} \neq 0$ in general

Figure 2.1.2: Pure bending of a rectangle

For the sake of more clarity, let's investigate deformation modes of a beam in bending, Figure 2.1.2. Deformation of the beam is assumed to be independent of Y – the width direction. In that case, the displacement field (2.1.1) becomes:

$$\begin{aligned} u_{(X,Z)} &= c_1 + c_3 X + c_5 Z + c_7 XZ \\ w_{(X,Z)} &= c_2 + c_4 X + c_6 Z + c_8 XZ \end{aligned} \tag{2.1.12}$$

It means the trilinear eight-node hexahedral element reduces to the bilinear four-node quadrilateral element. Let's consider deformation modes of the displacement field (2.1.12). All of those deformation modes are tabulated in Table 2.1.1.

In Table 2.1.1, c_1 and c_2 are rigid body modes. c_3 to c_6 are constant strain modes and c_7 and c_8 are linear strain modes. When an in-plane bending deformation happens, it means bending in X-direction around Z-axis, the mode No. 7 is active – only the coefficient c_7 is non-zero, thus leading to a parasitic linear shear strain γ_{XZ} in X-direction (see Table 2.1.1). In other words, it is impossible to find a linear combination of modes that leads to a linear variation of ε_X in Z-direction without being accompanied by shear

strain γ_{XZ}. This phenomenon is the manifestation of (transverse) shear locking. The same is, in turn, true for the bending in Z-direction (see Table 2.1.1 - mode 8).

Let's investigate analytical solution of a beam of rectangular cross section which is bent by two equal and opposite couples M (Figure 2.1.2). Stress components of the beam are:

$$\begin{aligned} \sigma_Z &= \frac{MZ}{I} \\ \sigma_X &= \tau_{XZ} = 0 \end{aligned} \tag{2.1.13}$$

where I is the area moment of inertia of the beam cross section.

From (2.1.13) and stress-strain relations we attain displacement components by integrating strain-displacement relations, see [DUR58]. Finally, the analytical formulations for displacements are:

$$\begin{aligned} u^{CM}_{(X,Z)} &= \frac{M}{EI} XZ + C_1 Z + C_2 \\ w^{CM}_{(X,Z)} &= -\frac{M}{2EI}(X^2 + \nu Z^2) - C_1 X + C_3 \end{aligned} \tag{2.1.14}$$

where C_1, C_2 and C_3 are constants of integration. The superscript "*CM*" means that the displacement field is calculated by the continuum mechanics.

If we impose the boundary conditions as: symmetric plane of the beam is the plane which goes through X=0; vertical displacement at the 4 corners is equal to zero. Then, the analytical solution of the problem in Figure 2.1.2 is:

$$\begin{aligned} u^{CM}_{(X,Z)} &= \frac{M}{EI} XZ = \alpha_1 XZ \\ w^{CM}_{(X,Z)} &= \frac{M}{2EI}(a^2 - X^2) - \frac{M}{2EI}\nu(b^2 - Z^2) = \frac{1}{2}\alpha_1(a^2 - X^2) - \alpha_2(b^2 - Z^2) \end{aligned} \tag{2.1.15}$$

where $\alpha_1 = {}^{M}\!/_{EI}$ and $\alpha_2 = {}^{M\nu}\!/_{2EI}$ are constants. The constant α_2 is a function depends on material properties, for Poisson's ratio equal to zero that constant is $\alpha_2 = 0$.

The analytical strains calculated from (2.1.15) are:

$$\begin{aligned} \varepsilon^{CM}_X &= \alpha_1 Z \\ \varepsilon^{CM}_Z &= \begin{cases} 0 & \text{if} \quad \nu = 0 \\ -2\alpha_2 Z & \text{if} \quad \nu \neq 0 \end{cases} \\ \gamma^{CM}_{XZ} &= \frac{\partial u}{\partial Z} + \frac{\partial w}{\partial X} = 0 \end{aligned} \tag{2.1.16}$$

Obviously, the solution (2.1.15) satisfies the pure bending condition – zero shear strain constraint.

For finite element solution, when pure bending occurs, only the mode 7 (Table 2.1.1) is active, it means:

$$\begin{aligned} u_{(X,Z)} &= c_7 XZ \\ w_{(X,Z)} &= 0 \end{aligned} \tag{2.1.17}$$

Hence, compare with the analytical solution, the form of error in the numerical solution is:

$$Error(w_{(X,Z)}) = \beta_1(a^2 - X^2) + \beta_2(b^2 - Z^2) \tag{2.1.18}$$

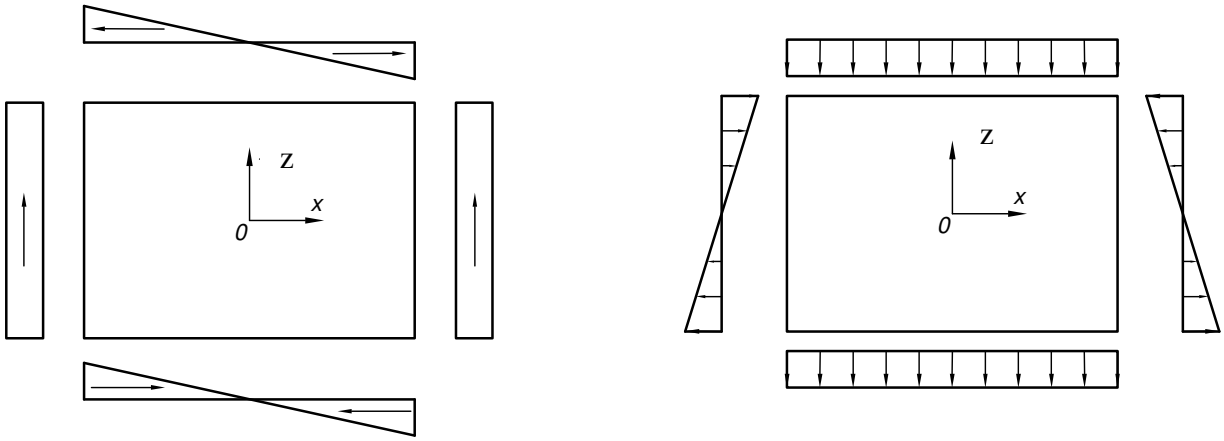

a) σ_{XZ} b) $\sigma_Z (\upsilon \neq 0)$

Figure 2.1.3: Errors in stresses – in pure bending

Therefore, the errors in strains are followed by the errors in displacement as:

$$Error(\varepsilon_Z) = \begin{cases} 0 & \text{if} \quad \nu = 0 \\ -2\beta_2 Z & \text{if} \quad \nu \neq 0 \end{cases} \tag{2.1.19}$$
$$Error(\gamma_{XZ}) = c_7 X$$

These errors cause parasitic stresses as shown in Figure 2.1.3. In fact, the *Error(γ_{XZ})* causes shear locking, the *Error(ε_Z)* causes Poisson thickness locking (will be discussed in the next section).

In conclusion, shear locking happens because normal strains of linear elements are coupled by shear strains. Elements do not have pure bending modes to behave correctly for pure bending load cases. The consequence is there are parasitic shear strains appear simultaneously with normal strains, which are physical in pure bending cases. These shear strains are important compared to the normal strains.

Consider the pure bending problem under the point of view of the continuum mechanics theory. In pure bending, the applied moment is constant and then shear stress must vanish since the shear stress is the derivative of the bending moment with respect to the axial coordinate. When solving the pure bending problem by the finite element method, since the shear stiffness is often significantly greater than the bending stiffness, the spurious shear absorbs a large part of the energy induced by the external forces and the predicted deflections and strains are much too small. In other words, the additional shear stress in the element (which does not occur in the actual beam) causes the element to reach equilibrium with smaller displacements, i.e., it makes the element appear to be stiffer than it actually is and gives bending displacements smaller than they should be. Long, slender structures in bending have greater curvature than do short, deep ones, and when modeled with low-order elements, will be affected more by shear locking. Increasing the number of elements will allow a more accurate modeling of the curvature, and reduce the effects of shear locking. Shear locking is prevented through the use of high order elements.

2.1.1.3 Poisson thickness locking

Also in bending problems, e.g. bending in 0X direction around 0Z axis (Figure 2.1.2), a linear distribution of strain ε_Z^{CM} over the thickness in the 0Z direction, see (2.1.16b) $\varepsilon_Z^{CM} = -2\alpha_2 Z$, is theoretically expected. However, the standard element (2.1.12) gives only a constant strain (with respect to Z) as:

$$\varepsilon_Z^{com} = \frac{\partial w}{\partial z} = c_6 + c_8 X \tag{2.1.20}$$

This constant (with respect to Z) approximation of the strain ε_Z^{com} in the thickness direction is contrary to the linear variation along 0Z of ε_Z^{CM}. In the real structure, due to Poisson effect the normal strain ($\varepsilon_X^{CM} = \frac{MZ}{EI}$), which linearly vary in the 0Z direction, would cause a transverse normal strain also linearly varies along 0Z ($\varepsilon_Z^{CM} = -\nu\varepsilon_X^{CM}$). However, it is not the case with ε_Z^{com} calculated by the low-order interpolation function, see (2.1.20). Consequently, the transverse normal stress in 0Z direction, which is calculated as

$$\sigma_Z^{com} = \frac{E}{(1+\nu)(1-2\nu)}[(1-\nu)\varepsilon_Z^{com} + \nu\varepsilon_X^{com}] \tag{2.1.21}$$

is not equal to the analytical solution along the thickness when bending occurs. It leads to an undesired locking, which is known as Poisson thickness locking phenomenon.

In general, Poisson thickness locking is due to the resulting incorrect-linear distribution of the normal stress in thickness direction. That locking effect does not diminish with mesh refinement in all directions except the thickness direction (layers).

2.1.2 Solution for a locking free element

As discussed above, the low-order standard solid element suffers from locking effects. It has been pointed out that the stiffening in the case of incompressibility is caused by redundant terms in the normal strains. Using the SRI method, will be discussed at the end of this chapter, is one of the best way for eliminating volumetric locking. Restriction of the SRI method is that the applied material laws must allow a decoupling stress and also strain into volumetric parts and deviatoric parts. Volumetric locking could also be vanished by inserting suitable enhancing components in order that the incompressible condition (2.1.3) be satisfied. The use of the EAS method with nine volumetric modes (see Section 2.4), as proposed by Andelfinger and Ramm [AND93], assures that all three normal strains ε_{ii} consist of the same polynomial fields, then no spurious constraint is produced. Disadvantage of this way is highly computational cost for each element because the enhancing strains making the element system of equations larger. In the thesis, only three EAS internal parameters are used to remove volumetric locking for solid-shell element, see Chapter 3.

Shear locking for solid elements can be removed by the ANS method. Detailed discussions are presented in Section 3.3.

To overcome Poisson thickness locking additional terms with linear distribution in thickness direction must be introduced for the transverse normal strains. This also assures

the stress field σ_z correctly varies linearly along the thickness in bending situations. Using the EAS method, the terms (ξ^3, $\xi^1\xi^3$, $\xi^2\xi^3$) of EAS7 element (see Section 3.4 below) can be used to circumvent Poisson thickness locking. In fact, the constant normal strain in thickness direction is enhanced with a linear extension over the thickness and linear in in-plane direction according to the EAS method.

In general, it is quite possible to use standard solid elements for the analysis of shell-type structures if one can overcome the following problems as pointed out by Wilson et al. [WIL73]:

1. Most solid elements have not had ability to represent accurately bending moments.
2. Due to the full integration, i.e. 2×2×2 Gauss integration (see Figure 2.1.1), the element will behave badly for isochoric material behavior, i.e. for high values of Poisson's ratio or plastic behavior (due to volumetric locking, see SRI method at the end of this chapter for a reference solution).
3. Errors in the transverse shear cause the element to be very stiff (transverse shear locking).
4. For simulation of thin shells, because the thickness of the element is relatively small compared to the in-plane dimensions there are relatively large stiffness coefficients in the thickness direction of numerical problems that are introduced. This effect makes the simulation problem ill-conditioned.

The design of the solid-shell elements aims to overcome these disadvantages of the standard solid element. Indeed, the first two problems can be solved by the use of the EAS method. The third and fourth problems can be minimized by applying the ANS method originally developed for thin shell elements. Practically, the solid-shell elements adopt the EAS technique for the in-plane shear strains and in-plane normal strains, and adopt the ANS technique for the transverse shear strains and transverse normal strain. As a result, the solid-shell elements may overcome all of the above difficulties. Thanks to intrinsic performance of the ANS method, the solid-shell element can be applied not only for thin but also for moderately thick shell structures.

2.2 INTRODUCTION TO CONVENTIONAL SHELLS

In this section the conventional shell elements are briefly introduced. Some basic concepts mentioned here are useful for building the solid-shell elements. We will briefly discuss about disadvantages of the conventional shell elements compared with the solid-shell elements, such as modified material models, variation of thickness strains, contradictions of assumptions for shell elements, etc.

Basically, the conventional shell finite elements are developed from one of the two following approaches:

1. Develop the formulation for shell elements by using classical strain, displacement and momentum (or equilibrium) equations for shells to develop a weak form of the momentum (or equilibrium) equations.

2. Develop the element directly from a continuum element by imposing the structural assumptions on the weak form or on the discrete equations; this is called the *continuum based approach*. For example, the kinematic assumptions will be imposed on the discrete equations, i.e. the continuum finite element will be modified so that it behaves like a shell [AHM70], [DVO84].

The first approach, also called classical shell theories, is difficult, particularly for nonlinear shells, since the governing equations for nonlinear shells are very complex and awkward to deal with. They are usually formulated in terms of curvilinear components of tensors, and features such as variations in thickness, junctions and stiffeners are generally difficult to incorporate. There is still a disagreement as to what are the best nonlinear classical shell equations [STO95].

The continuum-based approach, on the other hand, is straight forward, yields excellent results, is applicable to arbitrarily large deformations and is widely used in commercial softwares and researches. The popular continuum-based method used in structural analysis is called the degenerated continuum approach, see e.g. Ahmad et al. [AHM70].

2.2.1 Classical shell theories

Earlier, a shell was considered as a curved form of a plate and its structural action is a combination of stretching and bending [ZIE00b]. It is possible to perform a finite element analysis of a shell by using what is called a facet representation - i.e. the shell surface is replaced by a flat triangular and/or quadrilateral plate elements in which a membrane stiffness (membrane element) is superposed on a bending stiffness (plate bending element). Such a model is understandably inaccurate in the sense that with very coarse meshes, they do not capture the bending-stretching coupling of thin shell behavior. Hence, the motivation for designing elements is twofold: mid-surface curvature has to be taken into account and the element has to capture the membrane-bending coupling correctly. There are two types of kinematic assumptions, those that admit transverse shear strains and those that don't. The theory which admit transverse shear strains are called Mindlin-Reissner theories, whereas the theory which does not admit transverse shear strains is called Kirchhoff-Love theory. The essential kinematic assumptions in these shell theories are:

1. The normal to the mid-surface remains straight and normal (Kirchhoff-Love theory).
2. The normal to the mid-surface remains straight (Mindlin-Reissner theory).

Shell theories, see [ZIE00b], proved that the Kirchhoff-Love assumptions are the most accurate in predicting the behavior of thin shells. For thick shells, the Mindlin-Reissner assumptions are more accurate because transverse shear effects become important. Transverse shear effects are particularly important in composites. Mindlin-Reissner theory can also be used for thin shells. In that case the normal will remain approximately normal and the transverse shear strains will almost vanish.

The assumptions for Kirchhoff-Love shell theory are:

1) The shell is thin compared to the radius of curvature, i.e. $t/R << 1$.
2) The linear and angular deformations of the shell are small.

3) The transverse normal stress is negligible: $\sigma_{ZZ} = 0$.
4) The normals to the reference plane before deformation remain normal, straight and inextensible after deformation.

The first assumption is the most basic since it implies the other three. It means the assumption 1) cannot be violated without violating assumptions 2-4. Assumption 2) in effect means that the state of the deformed shell can be related directly to the state of the non-deformed shell. Assumption 3) is reasonable for thin shells (except for plasticity) and has no further implications besides simplifying the derivation of the governing equations. Assumption 4) has two implications; first, the inextensibility assumption implies zero normal strain ($\varepsilon_{ZZ} = 0$); second, the normal remains normal, this assumption eliminates the possibility of transverse angular distortions and consequently, lead to neglect the transverse shearing ($\gamma_{XZ} = \gamma_{YZ} = 0$, see the coordinate system in Figure 2.1.1).

Mindlin-Reissner theory is applied for thin to thick shells. The kinematic assumptions are:

1. The normal to the mid-surface remains straight throughout deformation.
2. The length of the normal remains unchanged throughout deformation.
3. Transverse normal stresses are negligible $\sigma_{ZZ} = 0$.

When Poisson's ratio is not equal to zero the latter two assumptions are contradictory because the normal must stretch when $\sigma_{ZZ} = 0$. Reissner's and Mindlin's theories differ from each other in the way they solve this problem. While Reissner assumes a cubic variation in thickness direction of the transverse normal stresses, Mindlin manipulates the material law in order to comply with his assumptions. Although conceptually different, both theories practically lead to the same results for transverse displacements, shear forces and bending moments in actual structural analysis. The method of Mindlin is simpler so it is popularly applied for numerical plate and shell models. In order to construct the finite element formulas, the Mindlin method requires the variational principle with only a displacement field but the Reissner method needs two fields (displacement and stress) variational principle.

Although these elements have the advantage of being able to account for the transverse shear that occurs for thick shell, low-order forms of these elements are subject to shear locking.

Employing the first and second assumptions makes the transverse shear strains are constant over thickness direction. Meanwhile, employing the third assumption requires modifications of the 3D-material law. This work is not simple in such an approach, especially for complicated material laws which are described only for 3D-continuum.

In order to use 3D-material laws directly, the normal stress in the thickness direction must be taken into account. This leads to an interpolation of the extensible director vector (defined in Figure 2.2.1), see [BET96], [BIS97].

2.2.2 Degenerated shell elements

There were various shell elements whose formulations are derived from the degeneration concept introduced by Ahmad et al. [AHM70]. The core of this concept is

the discretization of a 3D mathematical model with 3D elements and their subsequent reduction into 2D elements. As classified above, the degenerated shell elements are built from a so-called continuum based approach (CM). In comparison the CM to shell theory, it is not necessary to develop the complete formulation, i.e. developing a weak form, discretizing the problem by using finite element interpolations, etc. The degeneration of this 3D shell element is done by eliminating the nodes with the same (ξ^1, ξ^2) coordinates into a single node located at the mid-surface of the element, as shown in Figure 2.2.1.

The procedure when creating a shell element using the degenerated solid approach is to eliminate nodes by enforcing different constraints on the behavior of the element. First, nodes on the mid-surface are removed (nodes 17 to 20, Figure 2.2.1), corresponding to assuming constant transverse strains. Then, opposite nodes (1&9, 3&11, 5&13, 7&15; 2&10, 4&12, 6&14, 8&16) are linked by assuming equal displacements (u, v and w) and assigning two rotational DOF's (θ_x and θ_y) to each pair of nodes. Finally, the motion of each straight line is described by five DOF's in one node, lying on the reference surface, Figure 2.2.1b.

Assumptions: For the shear deformable shells, the following assumptions are made:

1. The fibers (line connects bottom node with top node) remain straight. The unit vector along each fiber is called a director vector;
2. The element is in a plane stress state, so $\sigma_{ZZ} = 0$;
3. The elongation of the fibers is governed by conservation of mass and/or the constitutive equation.

The first assumption will be called the *modified Mindlin-Reissner assumption*. It differs from what we call the classical Mindlin-Reissner assumption, which requires the normal to remain straight; the fibers are not initially normal to the midline. For the CM shell element to satisfy the classical Mindlin-Reissner assumptions, it is necessary for the fibers to be aligned as closely as possible with the normal to the midline. This can be accomplished by placing the slave nodes (nodes of the original solid element) so that the fibers are as close to normal to the midline as possible in the initial configuration. Otherwise the behavior of the degenerated shell element may deviate substantially from classical Mindlin-Reissner theory and may not agree with the physical behavior. Obviously, it is impossible to align the fibers with the normal exactly along the entire length of the element when the motion of the continuum element is C^0. Contrarily, if the fibers are inclined too much with respect to the normal while the transverse normal strain is taken into account, there is an effect call curvature thickness locking occurs, see Chapter 3 for more details.

Instead of the third assumption, many authors assume that the fibers are inextensible. Inextensibility contradicts the plane stress assumption: the fibers are usually close to the z direction and so if $\sigma_{ZZ} = 0$, the strain in the z direction generally cannot vanish. The assumption of constant fiber length is inconsistent with the conservation of mass: if the shell element is horizontally stretched, it must become thinner to conserve mass. Therefore, if the thickness strain is calculated through the constitutive equation via the plane stress requirement, conservation of mass is enforced. The important feature of the third assumption is that the extension of the fibers is not governed by the equations of motion or equilibrium. From the third assumption, it follows automatically that the

equations of motion or equilibrium associated with the thickness modes are eliminated from the system.

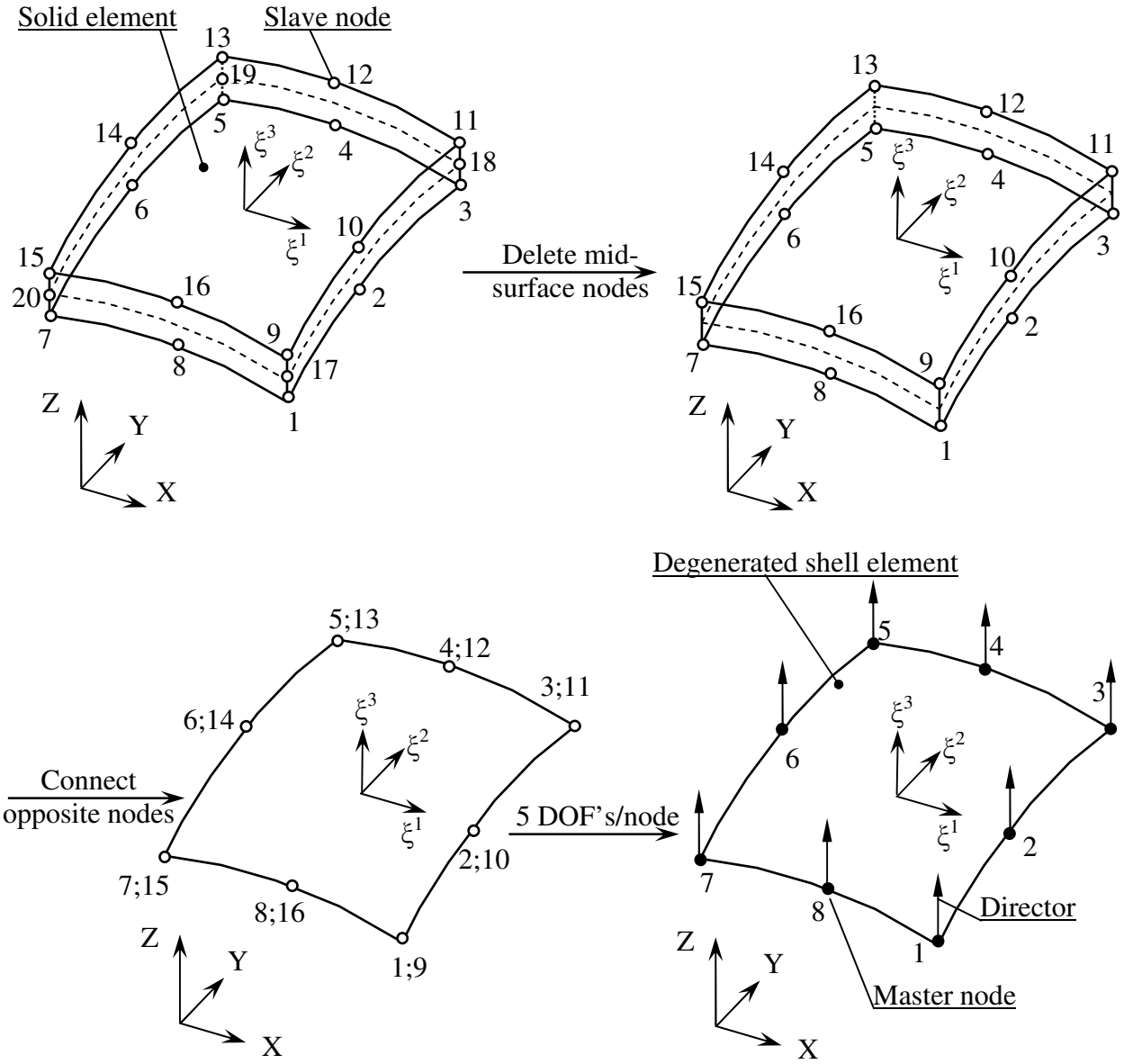

Figure 2.2.1: Degeneration of a 3D solid element into a degenerated shell element

The third assumption can be replaced by an inextensibility assumption if the change in thickness is small. In that case, effect of the thickness strain on the position of the slave nodes is neglected, so that the nodal internal forces do not reflect changes in the thickness. The theory is then applicable only to problems with moderate strains (on the order of 0.01, for instance).

The degenerated shell elements are in general cheap in computational cost due to the reduced number of DOF and using coarse mesh. The major shortcoming of the elements is the problems of locking for thin shells. However, the degenerated shell elements are attractive since they propose a simple method without discretization of the governing shell equation as in the case of the direct formulations - the classical shell theories. We have presented above a brief discussion about shell elements. In the next

chapter we will discover performances of the one called solid-shell in comparison with the degenerated and classical shell elements in simulating thin-walled structures.

2.3 INCOMPATIBLE DISPLACEMENT ELEMENT

Incompatible method, also called assumed displacement method, is derived from the potential energy variational principle. In the thesis the incompatible method is presented as a reference to motivate for the EAS method. Hence, the incompatible method is briefly introduced and only considered in linear elastic theory.

The standard solid elements pose the following difficulties: locking phenomena for bending and incompressible problems. By adding incompatible displacements to 3-D isoparametric nodes, the mentioned difficulties are canceled.

2.3.1 Finite element formulation

Consider a continuum body occupying a volume V in a space of boundary surface A. Assume that the body force and the tension force are conservative and the object is in static state. Under the theory of linear elasticity, the principle of minimum potential energy can be stated as:

$$\boldsymbol{\pi}_{(\boldsymbol{u})} = \int_V \frac{1}{2} (\boldsymbol{\varepsilon}_{(\boldsymbol{u})}^{com})^T \, {}^4\boldsymbol{C} \, \boldsymbol{\varepsilon}_{(\boldsymbol{u})}^{com} dV - \int_{A_\sigma} \boldsymbol{u} \cdot \boldsymbol{t}^* dA - \int_V \boldsymbol{u} \cdot \boldsymbol{b}^* \rho dV \tag{2.3.1}$$

When the solid continuum is discretized into a finite number of elements, the above variational is rewritten in the form as:

$$\boldsymbol{\pi}_{(\boldsymbol{u})} = \sum_{e=1}^{Nele} \left\{ \left[\int_{V^e} \frac{1}{2} (\boldsymbol{D}\boldsymbol{u}^e)^T \, {}^4\boldsymbol{C} \, (\boldsymbol{D}\boldsymbol{u}^e) \; - \; \boldsymbol{u}^e \cdot \boldsymbol{b}^{*e} \right] dV - \int_{A_\sigma^e} \boldsymbol{u}^e \cdot \boldsymbol{t}^{*e} \, dA \right\} \tag{2.3.2}$$

where $Nele$: number of elements.

In the finite element formulation the element displacements $\boldsymbol{u}^e$ are interpolated in terms of nodal displacements that may be at both boundary nodes (Serendipity elements) and internal nodes (Lagrange elements). Elements can also be formulated by adding to the original element displacements $\boldsymbol{u}^e$, which are in terms of nodal displacements $\boldsymbol{U}^e$, higher-order displacements $\boldsymbol{\lambda}$, which are not expressed in terms of nodal displacements of the boundary nodes. For example, the displacements u and v for the standard four-node quadrilateral element are based on bilinear interpolation functions. They are incomplete in quadratic terms, see (2.1.12). Improvement of the performance of a four-node element can be made by adding terms such that the displacements are complete in quadratic terms. Wilson et al. [WIL73] suggested the addition of incompatible displacements that vanish at all corner nodes. In these cases the element strain $\boldsymbol{\varepsilon} = \boldsymbol{D}\boldsymbol{u}^e$ can be expressed as

$$\boldsymbol{Du}^e = [\boldsymbol{B}_u \quad \boldsymbol{B}_\lambda]\begin{Bmatrix}\boldsymbol{U}^e \\ \boldsymbol{\Lambda}^e\end{Bmatrix} \tag{2.3.3}$$

where

$\boldsymbol{B}_u$, $\boldsymbol{B}_\lambda$ are compatible strain matrix and incompatible strain matrix, respectively.

$\boldsymbol{U}^e$ is nodal displacement vector and $\boldsymbol{\Lambda}^e$ is incompatible mode vector of element:

$$\begin{aligned}\boldsymbol{U}^e &= [U_1 \;\; V_1 \;\; W_1 \;\; U_2 \;\; V_2 \;\; W_2 \ldots \;\; U_{Nnode} \;\; V_{Nnode} \;\; W_{Nnode}] \\ \boldsymbol{\Lambda}^e &= [\Lambda_1 \; \Lambda_2 \; \ldots \; \Lambda_{inMod}]\end{aligned} \tag{2.3.4}$$

with *Nnode* is the number of nodes per element; *inMod* is the number of incompatible modes per element.

Introducing (2.3.3) into (2.3.2) we have:

$$\begin{aligned}\boldsymbol{\pi}_{(u)} = \sum_{e=1}^{Nele}\Big[\frac{1}{2}(\boldsymbol{U}^e)^T \cdot \boldsymbol{k}^e_{uu} \cdot \boldsymbol{U}^e + \boldsymbol{\Lambda}^e \cdot \boldsymbol{k}^e_{\lambda u} \cdot \boldsymbol{U}^e + \frac{1}{2}(\boldsymbol{\Lambda}^e)^T \cdot \boldsymbol{k}^e_{\lambda\lambda} \cdot \boldsymbol{\Lambda}^e \\ - (\boldsymbol{U}^e)^T \cdot \boldsymbol{f}^e_{ext} - (\boldsymbol{\Lambda}^e)^T \cdot \boldsymbol{f}^e_{\lambda}\Big]\end{aligned} \tag{2.3.5}$$

where:

- The standard stiffness matrix of the element is:

$$\boldsymbol{k}^e_{uu} = \int_{V_0^e} (\boldsymbol{B}_u)^T \, {}^4\boldsymbol{C} \;\; \boldsymbol{B}_u dV \tag{2.3.6}$$

- The incompatible-standard stiffness matrix of the element is defined as:

$$\boldsymbol{k}^e_{\lambda u} = \int_{V_0^e} (\boldsymbol{B}_\lambda)^T \, {}^4\boldsymbol{C} \;\; \boldsymbol{B}_u dV \tag{2.3.7}$$

- The incompatible stiffness matrix of the element is defined as:

$$\boldsymbol{k}^e_{\lambda\lambda} = \int_{V_0^e} (\boldsymbol{B}_\lambda)^T \, {}^4\boldsymbol{C} \;\; \boldsymbol{B}_\lambda dV \tag{2.3.8}$$

- The standard nodal force vector is:

$$\boldsymbol{f}^e_{ext} = \int_{V^e} (\boldsymbol{N}_u)^T \boldsymbol{b}^{*e} \, dV + \int_{A^e_\sigma} (\boldsymbol{N}_u)^T \boldsymbol{t}^{*e} \, dA \tag{2.3.9}$$

- The incompatible nodal force vector is defined as:

$$\boldsymbol{f}^e_{\lambda} = \int_{V^e} (\boldsymbol{N}_\lambda)^T \boldsymbol{b}^{*e} \, dV + \int_{A^e_\sigma} (\boldsymbol{N}_\lambda)^T \boldsymbol{t}^{*e} \, dA \tag{2.3.10}$$

with $\boldsymbol{N}_\lambda$ are the incompatible shape functions.

The incompatible vector $\boldsymbol{\Lambda}^e$ consists of internal variables hence it can be condensed out of the variational formulation by setting $\partial\boldsymbol{\pi}/\partial\boldsymbol{\Lambda} = 0$ in order to get $\boldsymbol{\Lambda}^e$ in function of $\boldsymbol{U}^e$ as:

$$\boldsymbol{\Lambda}^e = -[\boldsymbol{k}^e_{\lambda\lambda}]^{-1}(\boldsymbol{k}^e_{\lambda u}\ \boldsymbol{U}^e - \boldsymbol{f}_\lambda) \tag{2.3.11}$$

Then, the total potential energy $\boldsymbol{\pi}_{(u)}$ is rewritten:

$$\boldsymbol{\pi}_{(u)} = \sum_{e=1}^{Nele}\left[\frac{1}{2}(\boldsymbol{U}^e)^T \cdot \boldsymbol{k}^e \cdot \boldsymbol{U}^e - (\boldsymbol{U}^e)^T \cdot \boldsymbol{f}^e\right] \tag{2.3.12}$$

where the equivalent element stiffness matrix is

$$\boldsymbol{k}^e = \boldsymbol{k}^e_{uu} - (\boldsymbol{k}^e_{\lambda u})^T(\boldsymbol{k}^e_{\lambda\lambda})^{-1}\boldsymbol{k}^e_{\lambda u} \tag{2.3.13}$$

and the equivalent nodal force vector is

$$\boldsymbol{f}^e = \boldsymbol{f}^e_{ext} - (\boldsymbol{k}^e_{\lambda u})^T(\boldsymbol{k}^e_{\lambda\lambda})^{-1}\boldsymbol{f}^e_\lambda \tag{2.3.14}$$

Assembling $\boldsymbol{k}^e$ into the global stiffness matrix $\boldsymbol{K}$ and $\boldsymbol{f}^e$ into global nodal vector $\boldsymbol{F}$, finally, the total potential energy $\boldsymbol{\pi}_{(u)}$ is:

$$\boldsymbol{\pi}_{(u)} = \frac{1}{2}(\boldsymbol{U})^T \cdot \boldsymbol{K} \cdot \boldsymbol{U} - (\boldsymbol{U})^T \cdot \boldsymbol{F} \tag{2.3.15}$$

where:

- $\boldsymbol{U}$ is the global nodal displacement vector;
- $\boldsymbol{K} = \sum_{e=1}^{Nele} \boldsymbol{k}^e$;
- $\boldsymbol{F} = \sum_{e=1}^{Nele} \boldsymbol{f}^e$.

Let's take the first variation of $\boldsymbol{\pi}_{(u)}$ with respect to global displacement vector $\boldsymbol{U}$ and impose it equal to zero, $\partial\boldsymbol{\pi}_{(u)}/\partial\boldsymbol{U} = 0$, the equation for displacement solution is

$$\boldsymbol{K} \cdot \boldsymbol{U} = \boldsymbol{F} \tag{2.3.16}$$

After the solution process, solving system (2.3.16), all the nodal displacements are known. Other variables, strains and stresses, are obtained as in the standard manner.

In the next section, the EAS method, based on the three field Hu-Washizu variational principle, is presented. The EAS method is considered as a generalized approach of the incompatible method as pointed by Simo and Rifai [SIM90].

2.4 EAS ELEMENT

Due to their efficiency and simple geometry, low-order solid elements are often preferred in structural mechanics. As mentioned above, the low-order standard displacement elements exhibit, in many cases, severe stiffening effects known as locking. Shear locking occurs when simulating thin-walled structures by the low-order standard displacement elements, where pure bending modes are spoiled by parasitic shear strains. Membrane locking is encountered in high aspect ratio elements when bending modes

cannot be separated from membrane strains and, thus, not allowing the verification of pure inextensional modes. For incompressible or nearly incompressible conditions, volumetric locking may also occur; in this case, deviatoric modes always come along undesirably with volumetric strains. The class of EAS elements presented below allows the systematic development of low-order elements with enhanced accuracy for coarse meshes.

The EAS elements have been applied to simulate geometrically and materially nonlinear problems due to the fact that they perform well in severe situations as the nearly incompressible limit and pure bending situations. Compared with almost all finite elements, the EAS elements show very good coarse mesh accuracy. In general, a low-order free-locking element can be developed based on EAS technique.

2.4.1 Variational formulation

Initially proposed by Simo and Rifai [SIM90] for small strains, the EAS method, which involves the three field variational principle of Hu-Washizu, was lately extended to the finite strain theory by Simo and Armero [SIM92] and open to the thermomechanically coupled behavior [ADA05]. When incorporated with the ANS technique, that assumes directly on strain components, a formulation in terms of the Green-Lagrange strains is however more favourable than the one based on the displacement gradient. In the light of this consideration, the following form of the Hu-Washizu principle is taken as the variational principle for a hyperelastic material:

$$\begin{aligned}\pi_{(\boldsymbol{u},\boldsymbol{E},\boldsymbol{S})} = \pi_{\text{int}} + \pi_{ext} \quad &= \int_{V_0} W_{\boldsymbol{S}(\boldsymbol{E})} dV + \int_{V_0} \underline{\boldsymbol{S}} : [\underline{\boldsymbol{E}}^{com}_{(\boldsymbol{u})} - \underline{\boldsymbol{E}}] dV + \\ &+ \int_{A_u} (\boldsymbol{u}^* - \boldsymbol{u}) \cdot \boldsymbol{t} dA - \int_{A_\sigma} \boldsymbol{u} \cdot \boldsymbol{t}^* dA - \int_{V_0} \boldsymbol{u} \cdot \boldsymbol{b}^* \rho dV\end{aligned} \tag{2.4.1}$$

where:

- π_{int} and π_{ext} : internal and external energies, respectively;
- The script "*" denotes prescribed values;
- $\boldsymbol{u}$: admissible displacement field;
- $\underline{\boldsymbol{S}}$: admissible second Piola-Kirchhoff stress field;
- $\boldsymbol{b}, \boldsymbol{t}$: body force and surface traction vectors, respectively;
- $W_{\boldsymbol{S}(\boldsymbol{E})}$: stored energy function;
- $\underline{\boldsymbol{E}}^{com}_{(\boldsymbol{u})}$: admissible Green-Lagrange strain field. In the thesis, the letter "*com*" in upper position designates for compatible quantities.

In (2.4.1), the body under consideration occupy a volume V_0 and has the boundary $A = A_\sigma \cup A_u$ where A_σ denotes the prescribed traction ($\boldsymbol{t}^*$) parts while A_u denotes the prescribed displacement ($\boldsymbol{u}^*$) ones. As the thesis concentrates on quasi-static problems, hence, the inertial force in (2.4.1) is not considered. Furthermore, the body force and surface traction are assumed to be conservative.

In (2.4.1), three independent fields are the strain field $\underline{\boldsymbol{E}}$, the stress field $\underline{\boldsymbol{S}}$ and the displacement field $\boldsymbol{u}$. According to the EAS method the independent strain field is proposed as:

$$\underline{\boldsymbol{E}} \equiv \underline{\boldsymbol{E}}^{mod} = \underline{\boldsymbol{E}}^{com}_{(\boldsymbol{u})} + \underline{\boldsymbol{E}}^{enh} \tag{2.4.2}$$

The strain tensor $\underline{\boldsymbol{E}}^{enh}$ in (2.4.2) is named the enhanced assumed strain field. The strain tensor $\underline{\boldsymbol{E}}^{mod}$ is named the modified strain field. Introducing the modified strain field $\underline{\boldsymbol{E}}^{mod}$ into (2.4.1) we have the Hu-Washizu principle as the variational basis for the EAS method:

$$\begin{aligned}\pi_{(\boldsymbol{u},\boldsymbol{E}^{mod},\boldsymbol{S})} = \pi_{int} + \pi_{ext} \quad &= \int_{V_0} W_{\boldsymbol{S}(\boldsymbol{E}^{mod})} dV + \int_{V_0} \underline{\boldsymbol{S}} : [\underline{\boldsymbol{E}}^{com}_{(\boldsymbol{u})} - \underline{\boldsymbol{E}}^{mod}] dV + \\ &+ \int_{A_u} (\boldsymbol{u}^* - \boldsymbol{u}) \cdot \boldsymbol{t} dA - \int_{A_\sigma} \boldsymbol{u} \cdot \boldsymbol{t}^* dA - \int_{V_0} \boldsymbol{u} \cdot \boldsymbol{b}^* \rho dV\end{aligned} \tag{2.4.3}$$

Once the modified strain tensor $\underline{\boldsymbol{E}}^{mod}$ is obtained, the gradient deformation tensor $\boldsymbol{F}^{mod}$ can be consistently derived through the use of a polar decomposition, see Section 3.5.1. In (2.4.3), three fields $\boldsymbol{u}$, $\underline{\boldsymbol{E}}^{mod}$ and $\underline{\boldsymbol{S}}$ are independent, while the two fields $\boldsymbol{t}$ and $\underline{\boldsymbol{S}}$ relate together through the Cauchy's stress theorem.

In order to pass the patch test, see details in Section 2.4.4, the approximation of $\underline{\boldsymbol{E}}^{enh}$ and $\underline{\boldsymbol{S}}$ are chosen to satisfy the following orthogonality condition as proposed in [SIM90]:

$$\int_{V_0} \underline{\boldsymbol{S}} : \underline{\boldsymbol{E}}^{enh} dV = 0 \tag{2.4.4}$$

Applying (2.4.4) in combination with (2.4.2) the three field variational (2.4.3) reduces to a two field variational principle as below:

$$\pi_{(\boldsymbol{u},\boldsymbol{E}^{enh})} = \int_{V_0} W_{\boldsymbol{S}(\boldsymbol{E}^{com}+\boldsymbol{E}^{enh})} dV + \int_{A_u} (\boldsymbol{u}^* - \boldsymbol{u}) \cdot \boldsymbol{t}_{(\boldsymbol{S})} dA - \int_{A_\sigma} \boldsymbol{u} \cdot \boldsymbol{t}^* dA - \int_{V_0} \boldsymbol{u} \cdot \boldsymbol{b}^* \rho dV \tag{2.4.5}$$

The first variation $\delta\pi_{(\boldsymbol{u},\boldsymbol{E}^{enh})}$ immediately follows:

$$\delta\pi_{(\boldsymbol{u},\boldsymbol{E}^{enh})} = \delta\pi_{int} + \delta\pi_{ext} \tag{2.4.6}$$

where:

- $\delta\pi_{\text{int}}$: the variation of the internal term

$$\delta\pi_{\text{int}} = \int_{V_0} (\delta\underline{\boldsymbol{E}}^{com} + \delta\underline{\boldsymbol{E}}^{enh}) : \underline{\boldsymbol{S}}^{mod} dV \tag{2.4.7}$$

and the second Piola-Kirchhoff stress $\underline{\boldsymbol{S}}^{mod}$ is given by

$$\underline{\boldsymbol{S}}^{mod} = \frac{\partial W_S}{\partial \underline{\boldsymbol{E}}^{mod}} \tag{2.4.8}$$

- $\delta\pi_{ext}$: the variation of the external term

$$\delta\pi_{ext} = -\int_{A_\sigma} \delta\boldsymbol{u} \cdot \boldsymbol{t}^* dA - \int_{V_0} \delta\boldsymbol{u} \cdot \boldsymbol{b}^* \rho dV \tag{2.4.9}$$

The orthogonality (consistency) condition (2.4.4) can be interpreted such that the variationally consistent stress field of an EAS element is complementary to the enhanced strain interpolation.

Following the finite element method, the approximation of the current geometry vector $\boldsymbol{x}$ and displacement vector $\boldsymbol{u}$ at the element level are read as:

$$\boldsymbol{x}^{e}_{(\xi)} = \boldsymbol{N}_{(\xi)}\boldsymbol{x}^{h}_{(\xi^1,\xi^2,\xi^3)} \quad \text{and} \quad \boldsymbol{u}^{e}_{(\xi)} = \boldsymbol{N}_{(\xi)}\boldsymbol{U}^{h} \tag{2.4.10}$$

where:

- superior index "*e*" refers to quantities at the element level;
- for eight-node hexahedral element $\boldsymbol{N}_{(\xi)} = [\boldsymbol{N}_1, \boldsymbol{N}_2, \boldsymbol{N}_3, ..., \boldsymbol{N}_8]$ is matrix of shape functions (2.4.11)

in which:

$$\boldsymbol{N}_I = \begin{bmatrix} N_I & 0 & 0 \\ 0 & N_I & 0 \\ 0 & 0 & N_I \end{bmatrix} \tag{2.4.12}$$

with the standard trilinear shape functions as

$$N_{I(\xi)} = \frac{1}{8}\left(1 + \xi^1\xi^1_I\right)\left(1 + \xi^2\xi^2_I\right)\left(1 + \xi^3\xi^3_I\right); \text{ I=1-8 is nodal number.} \tag{2.4.13}$$

- $\boldsymbol{x}^{h}_{(\xi^1,\xi^2,\xi^3)}$ and $\boldsymbol{U}^{h}$ are the vectors of nodal coordinates and nodal displacements, respectively. They are defined as follows

$$\begin{aligned} \boldsymbol{x}^{h} &= [x_1 \;\; y_1 \;\; z_1 \;\; x_2 \;\; y_2 \;\; z_2 ... \;\; x_8 \;\; y_8 \;\; z_8] \\ \boldsymbol{U}^{h} &= [U_1 \;\; V_1 \;\; W_1 \;\; U_2 \;\; V_2 \;\; W_2 ... \;\; U_8 \;\; V_8 \;\; W_8] \end{aligned} \tag{2.4.14}$$

- The superscript "*h*" refers to nodal values.

The displacement variation and increment are required by the linearization of the variational. The displacement variation $\delta\boldsymbol{u}^{e}_{(\xi)}$ are interpolated as:

$$\delta\boldsymbol{u}^{e}_{(\xi)} = \boldsymbol{N}_{(\xi)}\delta\boldsymbol{U}^{h}_{(\xi^1,\xi^2,\xi^3)} \tag{2.4.15}$$

The displacement increment $\Delta\boldsymbol{u}^{e}_{(\xi)}$ are interpolated in the same manner:

$$\Delta\boldsymbol{u}^{e}_{(\xi)} = \boldsymbol{N}_{(\xi)}\Delta\boldsymbol{U}^{h}_{(\xi^1,\xi^2,\xi^3)} \tag{2.4.16}$$

In the following sections, the superscript "*e*" in $\boldsymbol{u}^{e}$ will be omitted.

The variation $\delta\boldsymbol{E}$ and increment $\Delta\boldsymbol{E}$ of Green-Lagrange strain at the element level are interpolated as:

$$\delta\boldsymbol{E}^{com} = \boldsymbol{B}_{(\boldsymbol{U}^h)}\delta\boldsymbol{U}^{h}_{(\xi^1,\xi^2,\xi^3)} \quad \text{and} \quad \Delta\boldsymbol{E}^{com} = \boldsymbol{B}_{(\boldsymbol{U}^h)}\Delta\boldsymbol{U}^{h}_{(\xi^1,\xi^2,\xi^3)} \tag{2.4.17}$$

where the compatible strain-displacement matrix $\boldsymbol{B}$ is a function of displacements $\boldsymbol{u}$, see [ZIE00b], such as:

$$\boldsymbol{B}^{com} = [\boldsymbol{B}^{com}_1 \quad \boldsymbol{B}^{com}_2 ... \quad \boldsymbol{B}^{com}_8] \tag{2.4.18}$$

with

$$\boldsymbol{B}_i^{com} = \begin{bmatrix} u_{,X} & 0 & 0 \\ 0 & v_{,Y} & 0 \\ 0 & 0 & w_{,Z} \\ v_{,Y} & u_{,X} & 0 \\ w_{,Z} & 0 & u_{,X} \\ 0 & w_{,Z} & v_{,Y} \end{bmatrix} + \begin{bmatrix} u_{,X}\, N_{i},_X & v_{,X}\, N_{i},_X & w_{,X}\, N_{i},_X \\ u_{,Y}\, N_{i},_Y & v_{,Y}\, N_{i},_Y & w_{,Y}\, N_{i},_Y \\ u_{,Z}\, N_{i},_Z & v_{,Z}\, N_{i},_Z & w_{,Z}\, N_{i},_Z \\ u_{,X}\, N_{i},_Y + u_{,Y}\, N_{i},_X & v_{,X}\, N_{i},_Y + v_{,Y}\, N_{i},_X & w_{,X}\, N_{i},_Y + w_{,Y}\, N_{i},_X \\ u_{,Z}\, N_{i},_X + u_{,X}\, N_{i},_Z & v_{,Z}\, N_{i},_X + v_{,X}\, N_{i},_Z & w_{,Z}\, N_{i},_X + w_{,X}\, N_{i},_Z \\ u_{,Y}\, N_{i},_Z + u_{,Z}\, N_{i},_Y & v_{,Y}\, N_{i},_Z + v_{,Z}\, N_{i},_Y & w_{,Y}\, N_{i},_Z + w_{,Z}\, N_{i},_Y \end{bmatrix} \tag{2.4.19}$$

In order to simplify the notation we are going to introduce Voigt notation. Thus, components of Green-Lagrange strain vector $\boldsymbol{E}^{com}$ and PK2 vector $\boldsymbol{S}$ are transformed from the corresponding matrices with indices as listed in the table below.

Table 2.4.1: Index transformation

Matrix index	11	22	33	12 (21)	13 (31)	23 (32)
Vector index	1	2	3	4	5	6

The enhanced strains $\boldsymbol{E}^{enh}$, which will be presented in details below as functions of enhanced strain interpolation matrix $\boldsymbol{\Gamma}$, see (2.4.45), and internal strain parameters $\boldsymbol{\alpha}$, variation $\delta\boldsymbol{E}^{enh}$ and increment $\Delta\boldsymbol{E}^{enh}$ of the enhanced strains are:

$$\boldsymbol{E}^{enh} = \boldsymbol{\Gamma}\,\boldsymbol{\alpha}\ ; \qquad \delta\boldsymbol{E}^{enh} = \boldsymbol{\Gamma}\,\delta\boldsymbol{\alpha}\ ; \qquad \Delta\boldsymbol{E}^{enh} = \boldsymbol{\Gamma}\,\Delta\boldsymbol{\alpha} \tag{2.4.20}$$

This variation and increment are required by the linearization of the weak form, see (2.4.23).

2.4.2 Linearization of discrete weak form

Employing the Voigt notation (Table 2.4.1), we rewrite the internal term (2.4.7) at the element level:

$$\delta\pi^e_{int(\boldsymbol{u},\boldsymbol{E}^{enh})} = \int_{V_0^e} \delta(\boldsymbol{E}^{com})^T_{1\times 6}\, \boldsymbol{S}^{mod}{}_{6\times 1} dV + \int_{V_0^e} \delta(\boldsymbol{E}^{enh})^T_{1\times 6}\, \boldsymbol{S}^{mod}{}_{6\times 1} dV \tag{2.4.21}$$

The first variation of the external term (2.4.9) is

$$\delta\pi^e_{ext} = -\int_{V^e} \delta\boldsymbol{u}\cdot\boldsymbol{b}^*\rho dV - \int_{A^e_\sigma} \delta\boldsymbol{u}\cdot\boldsymbol{t}^* dA\,. \tag{2.4.22}$$

We use $\delta\pi^e_{int}$ and $\delta\pi^e_{ext}$ to formulate the linearization of the weak form $\delta\pi^e_{(\boldsymbol{u},\boldsymbol{E}^{enh})}$ by employing the truncated Taylor series about the k^{th} iteration:

$$\begin{aligned} \delta\pi^e_{(\boldsymbol{u}_{k+1},\boldsymbol{E}^{enh}_{k+1})} = \left(\delta\pi^e_{int} + \delta\pi^e_{ext}\right)_{k+1} &= \delta\pi^e_{(\boldsymbol{u}_k,\boldsymbol{E}^{enh}_k)} + \frac{\partial\left(\delta\pi^e\right)}{\partial\left(\boldsymbol{u},\boldsymbol{E}^{enh}\right)}\Big|_{(\boldsymbol{u}_k,\boldsymbol{E}^{enh}_k)} \cdot \left(\Delta\boldsymbol{u},\Delta\boldsymbol{E}^{enh}\right) \\ &= \delta\pi^e_{(\boldsymbol{u}_k,\boldsymbol{E}^{enh}_k)} + D\left(\delta\pi\right)\Big|_{(\boldsymbol{u}_k,\boldsymbol{E}^{enh}_k)} \cdot \left(\Delta\boldsymbol{u},\Delta\boldsymbol{E}^{enh}\right) \end{aligned} \tag{2.4.23}$$

where $D(\ )$ is the Gateaux derivative operator, see Simo and Hughes [SIM98].

To alleviate the notation, the right subscript "*k*" designating the iterative index is omitted. In order to calculate ($\Delta\boldsymbol{u}$, $\Delta\boldsymbol{E}^{enh}$) we let the right hand side of (2.4.23) equal to zero, the result is:

$$\begin{aligned} -\left(\delta\pi^e_{int}+\delta\pi^e_{ext}\right) &= D\left(\delta\pi^e\right)|_{(\boldsymbol{u},\boldsymbol{E}^{enh})}\cdot\left(\Delta\boldsymbol{u},\Delta\boldsymbol{E}^{enh}\right) \\ &= \frac{\partial\left(\delta\pi^e_{int}+\delta\pi^e_{ext}\right)}{\partial\left(\boldsymbol{U}^h,\boldsymbol{\alpha}^e\right)}\cdot\left(\Delta\boldsymbol{U}^h,\Delta\boldsymbol{\alpha}^e\right)= \frac{\partial\left(\delta\pi^e_{int}\right)}{\partial\left(\boldsymbol{U}^h,\boldsymbol{\alpha}^e\right)}\cdot\left(\Delta\boldsymbol{U}^h,\Delta\boldsymbol{\alpha}^e\right) \end{aligned} \tag{2.4.24}$$

Introducing (2.4.15), (2.4.17) and (2.4.20) into (2.4.21), we get the internal virtual work as:

$$\begin{aligned} \delta\pi^e_{int(\boldsymbol{U}^h,\boldsymbol{\alpha}^e)} &= \int_{V_0^e}(\boldsymbol{B}\delta\boldsymbol{U}^h)^T\boldsymbol{S}^{mod}dV+\int_{V_0^e}(\boldsymbol{\Gamma}\delta\boldsymbol{\alpha})^T\boldsymbol{S}^{mod}dV \\ &= \delta\boldsymbol{U}^{(h)T}\boldsymbol{f}^e_{int}+\delta\boldsymbol{\alpha}^{(e)T}\boldsymbol{f}^e_{enh} \end{aligned} \tag{2.4.25}$$

with:

$$\boldsymbol{f}^e_{int}=\int_{V_0^e}\boldsymbol{B}^T\boldsymbol{S}^{mod}dV \quad ; \qquad \boldsymbol{f}^e_{enh}=\int_{V_0^e}\boldsymbol{\Gamma}^T\boldsymbol{S}^{mod}dV \tag{2.4.26}$$

Introducing (2.4.15) into (2.4.22) of the external virtual work we get:

$$\delta\pi^e_{ext}=-\delta\boldsymbol{U}^{(h)T}\boldsymbol{f}^e_{ext} \tag{2.4.27}$$

where:

$$\boldsymbol{f}^e_{ext}=\int_{V_0^e}\boldsymbol{N}^T\boldsymbol{b}^*\rho dV+\int_{A^e_\sigma}\boldsymbol{N}^T\boldsymbol{t}^*\rho dA \tag{2.4.28}$$

Observe that the element external force vector $\boldsymbol{f}^e_{ext}$ (2.4.28) has the usual expression of the standard displacement element.

Substituting (2.4.25) and (2.4.27) into (2.4.24) we have:

$$\begin{aligned} D\left(\delta\pi^e_{int}\right)\cdot\left(\Delta\boldsymbol{u},\Delta\boldsymbol{E}^{enh}\right) &= \frac{\partial\left(\delta\pi^e_{int}\right)}{\partial\boldsymbol{U}^h}\cdot\left(\Delta\boldsymbol{U}^h\right)+\frac{\partial\left(\delta\pi^e_{int}\right)}{\partial\boldsymbol{\alpha}^e}\cdot\left(\Delta\boldsymbol{\alpha}^e\right) \\ &= \delta\boldsymbol{U}^{(h)T}\frac{\partial\left(\boldsymbol{f}^e_{int}\right)}{\partial\boldsymbol{U}^h}\cdot\left(\Delta\boldsymbol{U}^h\right)+\delta\boldsymbol{\alpha}^{(e)T}\frac{\partial\left(\boldsymbol{f}^e_{enh}\right)}{\partial\boldsymbol{U}^h}\cdot\left(\Delta\boldsymbol{U}^h\right)+ \\ &\quad +\delta\boldsymbol{U}^{(h)T}\frac{\partial\left(\boldsymbol{f}^e_{int}\right)}{\partial\boldsymbol{\alpha}^e}\cdot\left(\Delta\boldsymbol{\alpha}^e\right)+\delta\boldsymbol{\alpha}^{(e)T}\frac{\partial\left(\boldsymbol{f}^e_{enh}\right)}{\partial\boldsymbol{\alpha}^e}\cdot\left(\Delta\boldsymbol{\alpha}^e\right) \\ &= \left[\delta\boldsymbol{U}^{(h)T}\boldsymbol{k}^e_{uu}+\delta\boldsymbol{\alpha}^{(e)T}\boldsymbol{k}^e_{\alpha u}\right]\cdot\Delta\boldsymbol{U}^h+\left[\delta\boldsymbol{U}^{(h)T}\boldsymbol{k}^e_{u\alpha}+\delta\boldsymbol{\alpha}^{(e)T}\boldsymbol{k}^e_{\alpha\alpha}\right]\cdot\Delta\boldsymbol{\alpha}^e \end{aligned} \tag{2.4.29}$$

The constitutive tensor in the physical space is expressed through the following stress-strain relationship:

$${}^4\boldsymbol{C}=\left[C^{ijkl}\right]=\left[\frac{\partial\boldsymbol{S}^{(ij)mod}}{\partial\boldsymbol{E}^{mod}_{kl}}\right]_{6\times6} \tag{2.4.30}$$

In (2.4.29) the stiffness matrices are established and listed hereafter.

The standard stiffness matrix of the element includes the material part $\boldsymbol{k}^e_{mat}$ and geometrical part $\boldsymbol{k}^e_{geo}$ that is

$$\boldsymbol{k}^e_{uu} = \frac{\partial \boldsymbol{f}^e_{int}}{\partial \boldsymbol{U}^h} = \boldsymbol{k}^e_{mat} + \boldsymbol{k}^e_{geo} = \int_{V_0^e} (\boldsymbol{B}\ )^T\ {}^4\boldsymbol{C}\ \boldsymbol{B}\ dV + \int_{V_0^e} \boldsymbol{B}_{,\boldsymbol{U}^h} \boldsymbol{S}^{\mathrm{mod}} dV \tag{2.4.31}$$

where, for a geometrical nonlinear theory the strain-displacement matrix $\boldsymbol{B}$, see (2.4.19), is a function of the displacements $\boldsymbol{u}$. Furthermore, the strain-displacement matrix contains the derivatives of the shape functions with respect to the global co-ordinates $\boldsymbol{X}$ in the reference configuration. Components of the geometrical part $\boldsymbol{k}^e_{geo}$ is defined as, see (10.69) of [ZIE00b]:

$$\boldsymbol{k}^e_{geo_{(24\times24)}} = \begin{bmatrix} \boldsymbol{G}_{11} & \boldsymbol{G}_{12} & \cdots & \boldsymbol{G}_{18} \\ \boldsymbol{G}_{21} & \boldsymbol{G}_{22} & \cdots & \boldsymbol{G}_{28} \\ \vdots & \vdots & \ddots & \vdots \\ \boldsymbol{G}_{81} & \boldsymbol{G}_{82} & \cdots & \boldsymbol{G}_{88} \end{bmatrix} \tag{2.4.32}$$

where $\boldsymbol{G}_{IJ}$ (I, J = 1-8) is defined for a node combination I and J as $\boldsymbol{G}_{IJ} = G_{IJ}\boldsymbol{I}_3$; with $\boldsymbol{I}_3$ is the unit matrix of dimension (3×3) and:

$$G_{IJ} = \int_{V_0^e} N_{I,K}\, S_{KL} N_{J,L} dV \ ; \ \ K,L\ =\ 1\text{-}3\,. \tag{2.4.33}$$

Enhanced-compatible stiffness matrix of the element is

$$\boldsymbol{k}^e_{\alpha u} = (\boldsymbol{k}^e_{u\alpha})^T = \left(\frac{\partial \boldsymbol{f}^e_{int}}{\partial \boldsymbol{\alpha}^e} \right)^T = \int_{V_0^e} \boldsymbol{\Gamma}^T\ {}^4\boldsymbol{C}\ \boldsymbol{B}\ dV \tag{2.4.34}$$

where $\boldsymbol{\Gamma}$ is defined in the next section, expression (2.4.45).

Enhanced stiffness matrix of the element is

$$\boldsymbol{k}^e_{\alpha\alpha} = \frac{\partial \boldsymbol{f}^e_{enh}}{\partial \boldsymbol{\alpha}^e} = \frac{\partial \boldsymbol{f}^e_{enh}}{\partial \boldsymbol{E}^{mod}} \frac{\partial \boldsymbol{E}^{mod}}{\partial \boldsymbol{\alpha}^e} = \int_{V_0^e} \boldsymbol{\Gamma}^T\ {}^4\boldsymbol{C}\ \boldsymbol{\Gamma} dV \tag{2.4.35}$$

Combination of (2.4.23), (2.4.25), (2.4.27), (2.4.29) with (2.4.31) and (2.4.34) and (2.4.35) we get the discrete linearized system of equations to solve for the increment $\Delta\boldsymbol{U}^h$ and $\Delta\boldsymbol{\alpha}^e$, for more details see Klinkel and Wagner [KLI97]:

$$\begin{bmatrix} \boldsymbol{k}^e_{uu} & \boldsymbol{k}^e_{u\alpha} \\ \boldsymbol{k}^e_{\alpha u} & \boldsymbol{k}^e_{\alpha\alpha} \end{bmatrix} \begin{Bmatrix} \Delta\boldsymbol{U}^h \\ \Delta\boldsymbol{\alpha}^e \end{Bmatrix} = \begin{Bmatrix} \boldsymbol{f}_{ext} - \boldsymbol{f}_{\mathrm{int}} \\ -\boldsymbol{f}_{enh} \end{Bmatrix} \tag{2.4.36}$$

The algorithm for solving the system (2.4.36) is listed in Chapter3 - Figure 3.4.1.

Since $\boldsymbol{E}^{enh}$ is not required to enhance inter-element continuity, we could eliminate $\Delta\boldsymbol{\alpha}^e$ at the element level before assembling the element matrices to the global matrices. From (2.4.36), we withdraw the formula for $\Delta\boldsymbol{\alpha}^e$:

$$\Delta\boldsymbol{\alpha}^e = -\left[\boldsymbol{k}^e_{\alpha\alpha}\right]^{-1} \left(\boldsymbol{f}^e_{enh} + \boldsymbol{k}^e_{\alpha u} \Delta\boldsymbol{U}^h \right) \tag{2.4.37}$$

Introducing (2.4.37) into (2.4.36) we finally get the condensed element stiffness matrix $\boldsymbol{k}_T^{(e)}$ and element residual force vector $\boldsymbol{r}^e$:

$$\boldsymbol{k}_T^e = \boldsymbol{k}_{uu}^e - \left[\boldsymbol{k}_{\alpha u}^e\right]^T \left[\boldsymbol{k}_{\alpha\alpha}^e\right]^{-1} \boldsymbol{k}_{\alpha u}^e \tag{2.4.38}$$

$$\boldsymbol{r}^e = \boldsymbol{f}_{ext}^e - \boldsymbol{f}_{int}^e + \left[\boldsymbol{k}_{\alpha u}^e\right]^T \left[\boldsymbol{k}_{\alpha\alpha}^e\right]^{-1} \boldsymbol{f}_{enh}^e \tag{2.4.39}$$

Assembling element matrices, the global system has the form:

$$\boldsymbol{K}_T \Delta \boldsymbol{U}^h = \boldsymbol{R} \tag{2.4.40}$$

After condensing, the global system (2.4.40) has the similar form as the global system of the standard displacement FEM.

2.4.3 EAS parameters

In this section we investigate the modified strain $\boldsymbol{E}^{mod} = \boldsymbol{E}_{(\boldsymbol{u})}^{com} + \boldsymbol{E}^{enh}$ under the framework of the EAS approach. The enhancing strain field for an element in the Cartesian coordinate system $\boldsymbol{E}^{enh}$ is usually assumed, see [KLI97], by

$$\boldsymbol{E}^{enh} = \frac{|\boldsymbol{J}_0|}{|\boldsymbol{J}|} \boldsymbol{T}_0^{-T} \boldsymbol{E}_{\xi}^{enh} \tag{2.4.41}$$

where:

- $\boldsymbol{J}$ is the Jacobian matrix,

$$\boldsymbol{J} = \begin{bmatrix} X,_{\xi^1} & Y,_{\xi^1} & Z,_{\xi^1} \\ X,_{\xi^2} & Y,_{\xi^2} & Z,_{\xi^2} \\ X,_{\xi^3} & Y,_{\xi^3} & Z,_{\xi^3} \end{bmatrix} \tag{2.4.42}$$

- $\boldsymbol{J}_0$ is the Jacobian matrix at the center of the element $(\boldsymbol{\xi} = \boldsymbol{0})$;
- $\boldsymbol{T}$ is the transformation matrix that maps quantities in the physical space to the natural space:

$$\boldsymbol{T} = \begin{bmatrix} J_{11}^2 & J_{21}^2 & J_{31}^2 & 2J_{11}J_{21} & 2J_{11}J_{31} & 2J_{21}J_{31} \\ J_{12}^2 & J_{22}^2 & J_{32}^2 & 2J_{12}J_{22} & 2J_{12}J_{32} & 2J_{22}J_{32} \\ J_{13}^2 & J_{23}^2 & J_{33}^2 & 2J_{13}J_{23} & 2J_{13}J_{33} & 2J_{23}J_{33} \\ J_{11}J_{12} & J_{21}J_{22} & J_{31}J_{32} & (J_{11}J_{22}+J_{12}J_{21}) & (J_{11}J_{32}+J_{12}J_{31}) & (J_{21}J_{32}+J_{22}J_{31}) \\ J_{11}J_{13} & J_{21}J_{23} & J_{31}J_{33} & (J_{11}J_{23}+J_{13}J_{21}) & (J_{11}J_{33}+J_{13}J_{31}) & (J_{21}J_{33}+J_{23}J_{31}) \\ J_{12}J_{13} & J_{22}J_{23} & J_{32}J_{33} & (J_{12}J_{23}+J_{13}J_{22}) & (J_{12}J_{33}+J_{13}J_{32}) & (J_{22}J_{33}+J_{23}J_{32}) \end{bmatrix} \tag{2.4.43}$$

with $J_{ij} \equiv J(i, j)$.

- $\boldsymbol{T}_0$ is natural-physical transformation matrix at the element center $(\boldsymbol{\xi} = \boldsymbol{0})$.

For enhancing strain interpolation in the natural coordinate system, the following formulation is used:

$$\boldsymbol{E}_{\xi}^{enh} = \boldsymbol{M}_{(\xi)} \boldsymbol{\alpha} \tag{2.4.44}$$

where $\boldsymbol{\alpha}$ is the vector of internal parameters. The dimension of $\boldsymbol{\alpha}$ is various, it depends on the type of the free-locking EAS elements in volumetric, membrane and shear responses. It is equal to the number of the additionally enhanced modes defined in Table 2.4.2 below. The natural - physical mapping is realized at element's center to obtain unique values for the parameters α_i. Otherwise, values of the α_i parameters will vary according to integration points. These internal strains fill in the available compatible strain field to alleviate parasitic terms.

The additional factor $|\boldsymbol{J}_0|/|\mathbf{J}|$ in (2.4.41) is introduced to be able to enforce the orthogonality condition (2.4.4). The justification of its use, as suggested by Taylor et al. [TAY76], is based on the same considerations which led to the approximation of the local-global transformation at the element center ($\boldsymbol{\xi} = \mathbf{0}$), i.e. using $\boldsymbol{T}_0$ rather than the transformation $\boldsymbol{T}$. In fact, the factor $|\boldsymbol{J}_0|/|\mathbf{J}|$ relates the transformation of an infinitesimal volume element to the element center as well, thus facilitating the enforcement of the orthogonality condition for the constant stress and strain states, i.e. the patch test, see the next section for a more detailed analyses.

After combination of (2.4.41) and (2.4.44), the enhancing strain field $\boldsymbol{E}^{enh}$ in the physical coordinate system is written as:

$$\boldsymbol{E}^{enh} = \frac{|\boldsymbol{J}_0|}{|\boldsymbol{J}|}\boldsymbol{T}_0^{-T}\boldsymbol{M}_{(\xi)}\boldsymbol{\alpha} = \boldsymbol{\Gamma}\,\boldsymbol{\alpha} \quad \text{with} \quad \boldsymbol{\Gamma} = \frac{|\boldsymbol{J}_0|}{|\boldsymbol{J}|}\boldsymbol{T}_0^{-T}\boldsymbol{M}_{(\xi)} \tag{2.4.45}$$

The enhancing matrix $\boldsymbol{M}$, according to Andelfinger and Ramm [AND93], is defined:

$$\boldsymbol{M} = \left[\begin{array}{ccc|ccccc|ccccccc|cccccc|ccccccc|cccccc}
\xi & 0 & 0 & 0 & 0 & 0 & 0 & 0 & 0 & 0 & 0 & 0 & 0 & 0 & \xi\eta & \xi\varsigma & 0 & 0 & 0 & 0 & 0 & 0 & 0 & \xi\eta\varsigma & 0 & 0 & 0 & 0 & 0 \\
0 & \eta & 0 & 0 & 0 & 0 & 0 & 0 & 0 & 0 & 0 & 0 & 0 & 0 & 0 & 0 & \xi\eta & \eta\varsigma & 0 & 0 & 0 & 0 & 0 & 0 & \xi\eta\varsigma & 0 & 0 & 0 & 0 \\
0 & 0 & \varsigma & 0 & 0 & 0 & 0 & 0 & 0 & 0 & 0 & 0 & 0 & 0 & 0 & 0 & 0 & 0 & \xi\varsigma & \eta\varsigma & 0 & 0 & 0 & 0 & 0 & \xi\eta\varsigma & 0 & 0 & 0 \\
0 & 0 & 0 & \xi & \eta & 0 & 0 & 0 & \xi\varsigma & \eta\varsigma & 0 & 0 & 0 & 0 & 0 & 0 & 0 & 0 & 0 & 0 & \xi\eta & 0 & 0 & 0 & 0 & 0 & \xi\eta\varsigma & 0 & 0 \\
0 & 0 & 0 & 0 & \xi & \varsigma & 0 & 0 & 0 & \xi\eta & \eta\varsigma & 0 & 0 & 0 & 0 & 0 & 0 & 0 & 0 & \xi\varsigma & 0 & 0 & 0 & 0 & 0 & 0 & \xi\eta\varsigma & 0 \\
0 & 0 & 0 & 0 & 0 & 0 & \eta & \varsigma & 0 & 0 & 0 & \xi\eta & \xi\varsigma & 0 & 0 & 0 & 0 & 0 & 0 & 0 & 0 & \eta\varsigma & 0 & 0 & 0 & 0 & 0 & 0 & \xi\eta\varsigma
\end{array}\right] \tag{2.4.46}$$

25 30 35 40 45 50 54

where $\xi \equiv \xi^1; \eta \equiv \xi^2$ and $\varsigma \equiv \xi^3$.

In (2.4.46), non-zero terms in the three upper-rows are applied for enhancing the additional modes of the normal strains; non-zero terms in the three lower-rows are applied for enhancing the additional modes of the shear strains. For the sake of comprehension, let's consider the compatible strain $\varepsilon_{11(\boldsymbol{\xi})}$ in the natural space for the eight-node solid element:

$$\begin{aligned} u_{(\boldsymbol{\xi})} &= a_0 + a_1\xi^1 + a_2\xi^2 + a_3\xi^3 + a_4\xi^1\xi^2 + a_5\xi^2\xi^3 + a_6\xi^1\xi^3 + a_7\xi^1\xi^2\xi^3 \\ \varepsilon^{com}_{11(\boldsymbol{\xi})} &= \frac{\partial u_{(\xi)}}{\partial \xi^1} = a_1 + a_4\xi^2 + a_6\xi^3 + a_7\xi^2\xi^3 \end{aligned} \tag{2.4.47}$$

When additionally enhanced by the non-zero terms in the first row of matrix $\boldsymbol{M}$ in (2.4.46) the expression $\varepsilon_{11(\boldsymbol{\xi})}$ will becomes a complete tri-linear polynomial as:

$$\begin{aligned} E^{mod}_{11(\boldsymbol{\xi})} &= \varepsilon^{com}_{11(\boldsymbol{\xi})} + E^{enh}_{11(\boldsymbol{\xi})} \\ &= (a_1 + a_4\xi^2 + a_6\xi^3 + a_7\xi^2\xi^3) + (d_1\xi^1 + d_2\xi^1\xi^2 + d_3\xi^1\xi^3 + d_4\xi^1\xi^2\xi^3) \end{aligned} \tag{2.4.48}$$

where $d_i (i = 1-4)$ are components of vector $\boldsymbol{\alpha}$. The modified strains as (2.4.48) will help the EAS element to satisfy the incompressible condition and pure bending condition because there is no inconsistent term (see Section 2.1.1) in the enhanced strains.

Table 2.4.2: EAS elements

EAS element	Additional modes *Detailed modes*	Capability
EAS3v	3v + 0s *(only modes 25÷27 in (2.4.46) are adopted to enhanced normal strains)*	Free volumetric locking
EAS6s	0v + 6s *(modes 28÷33 in (2.4.46) are adopted to enhanced shear strains)*	Free shear locking
EAS9	3v + 6s *(25÷27) + (28÷33)*	Free volumetric & shear locking
EAS12	6v + 6s *(25÷27;40,43,44) + (28÷33)*	Improved incompressibility behavior with respect to EAS9
EAS15	3v + 12s *(25÷27) + (28÷39)*	Improved bending behavior with respect to EAS9
EAS21	9v + 12s *(25÷27;40÷45) + (28÷39)*	Totally free volumetric locking & free shear locking
EAS24	9v + 15s *(25÷27;40÷45) + (28÷39;46÷48)*	Totally free shear & volumetric locking
EAS30	12v + 18s *(25÷27;40÷45;49÷51) + (28÷39;46÷48;52÷54)*	Totally free shear & volumetric locking, applied for distorted mesh

The enhancing matrix $\boldsymbol{M}$ in (2.4.46), when introduced in the expression (2.4.45) to calculate $\boldsymbol{E}^{enh}$, will make $\boldsymbol{E}^{enh}$ satisfy the orthogonality condition (2.4.4). In other words, this matrix $\boldsymbol{M}$ is designed in such a way that the EAS elements are locking free while pass the patch test, see the next section for a detailed expression.

Consequently, as chosen in (2.4.46) the matrix $\boldsymbol{M}$ expands the compatible strain field up to the complete tri-linear field (EAS30). It means the enhanced element has 30 additional modes and 54 modes in total (24 compatible modes and 30 enhanced modes). However, the number of additional modes should be suitable to each problem so as to limit the calculation time. The list in Table 2.4.2 gives some suggestions for reducing additional mode elements.

Above, a formulation of the EAS elements in the Green-Lagrange strains has been presented. This formulation was implemented in a MATLAB code. The numerical results at the end of this chapter show performances of the EAS elements and also assure quality of the implementation.

2.4.4 Patch test

The arguments in this section are valid for both the incompatible method (Section 2.3) and the EAS method. For C^0 elements, such as the eight-node hexahedral, the

method for deriving the incompatible shape functions $\boldsymbol{N}_\lambda$ (Section 2.3) for the incompatible elements (or enhancing matrix $\boldsymbol{M}$ (2.4.46) for the EAS elements) is so detail. Not only filling higher order terms in the standard displacement field but the incompatible shape functions also have to satisfy the patch test requirement. That is the necessary condition for an element to converge to the correct solution.

Designate the space of the enhanced strain field as $\widehat{\boldsymbol{\varepsilon}}^{enh}$ and the space of admissible strain field defined in the standard fashion as $\widehat{\boldsymbol{\varepsilon}}^{com}$. The enhanced strain interpolation and the compatible strain interpolation are independent in a sense as:

$$\widehat{\boldsymbol{\varepsilon}}^{enh} \cap \widehat{\boldsymbol{\varepsilon}}^{com} = \{0\} \tag{2.4.49}$$

Consider the enhanced stiffness matrix (2.4.35) and use $\boldsymbol{\Gamma}$ in (2.4.45), we have:

$$\boldsymbol{k}^e_{\alpha\alpha} = \int_{V_0^e} \boldsymbol{\Gamma}^T \, {}^4\boldsymbol{C} \, \boldsymbol{\Gamma} dV = \int_{V_0^e} \frac{|\boldsymbol{J}_0|^2}{|\boldsymbol{J}|^2} (\boldsymbol{M}_{(\xi)} \boldsymbol{T}_0^{-1}) \, {}^4\boldsymbol{C} \, (\boldsymbol{T}_0^{-T} \boldsymbol{M}_{(\xi)}) dV \tag{2.4.50}$$

In order to consider positive definite of $\boldsymbol{k}^e_{\alpha\alpha}$, the constant values ($|\boldsymbol{J}_0|^2, \boldsymbol{T}_0^{-1}$) and positive values ($|\boldsymbol{J}|^2$) can be eliminated from the expression. In addition, rows of $\boldsymbol{M}$, see (2.4.46), have been assumed to be linearly independent. Since the constitutive matrix ${}^4\boldsymbol{C}$ is positive definite, the assumption of linearly independent rows of $\boldsymbol{M}$ assure the enhanced stiffness matrix $\boldsymbol{k}^e_{\alpha\alpha} = \int_{V_0^e} \boldsymbol{\Gamma}^T \, {}^4\boldsymbol{C} \, \boldsymbol{\Gamma} dV$ (in fact, the integral $\int_{V_0^e} \boldsymbol{M}_{(\xi)} \, {}^4\boldsymbol{C} \, \boldsymbol{M}_{(\xi)} dV$) also positive definite.

Let's consider rigid body motions or constant strain conditions. In nonlinear problems, we consider the increment quantities. Hence, the constant strain condition is $\Delta \boldsymbol{E} = const$. Denote $\Delta \boldsymbol{U}^h_{\boldsymbol{0}}$ as the set of nodal displacements, which corresponds to one of the rigid body cases or a constant strain state. Then we also have $\Delta \boldsymbol{E} = \boldsymbol{B} \Delta \boldsymbol{U}^h_{\boldsymbol{0}} = const$. Denote $\Delta \boldsymbol{\alpha}^e_{\boldsymbol{0}}$ as the values of internal variables in the case of the motion $\Delta \boldsymbol{U}^h_{\boldsymbol{0}}$. In order to pass the patch test, the EAS element requires $\Delta \boldsymbol{\alpha}^e$ to be zero whenever $\Delta \boldsymbol{U}^h$ corresponds to rigid body motions or constant strain conditions. Since the matrix $\boldsymbol{k}^e_{\alpha\alpha}$ is always positive definite, the condition for $\Delta \boldsymbol{\alpha}^e = \boldsymbol{0}$ from the second set of equations in (2.4.36) reduces to:

$$\begin{aligned} & [\boldsymbol{k}^e_{\alpha u}] \Delta \boldsymbol{U}^h_0 + \boldsymbol{f}^e_{enh,0} = \boldsymbol{0} \\ \Leftrightarrow \quad & \int_{V_0^e} \boldsymbol{\Gamma}^T \, {}^4\boldsymbol{C} \, \boldsymbol{B} \, \Delta \boldsymbol{U}^h_0 dV + \int_{V_0^e} \boldsymbol{\Gamma}^T \boldsymbol{S}^{\text{mod}}_0 dV = \boldsymbol{0} \end{aligned} \tag{2.4.51}$$

Pay attention that the term (${}^4\boldsymbol{C} \, \boldsymbol{B} \, \Delta \boldsymbol{U}^h_0$) is in fact some constant stress state $\boldsymbol{S}^{\text{mod}}_0$ that is correspond to rigid body motions or constant strain conditions. Consequently, the requirement for the patch test to be satisfied reduces to:

$$\int_{V_0^e} \boldsymbol{\Gamma} dV = \boldsymbol{0} \tag{2.4.52}$$

Calculation of the left hand side expression will be performed in the natural space (ξ^1, ξ^2, ξ^3) where the presence of the Jacobian (2.4.42) is evident as:

$$\int_{V_0^e} \boldsymbol{\Gamma} dV = \int_{-1}^{1} \int_{-1}^{1} \int_{-1}^{1} \boldsymbol{\Gamma} |\boldsymbol{J}| d\xi^1 d\xi^2 d\xi^3 \tag{2.4.53}$$

This will generally lead to non-zero value of $\int_{V_0^e} \boldsymbol{\Gamma} dV$ and hence the element will not pass the patch test except when the element is a parallelepiped. In this latter case, the Jacobian will consist of constants and $\int_{V_0^e} \boldsymbol{\Gamma} dV$ will be equal to zero and the patch test will be passed. As a remedy, it was proposed (Taylor et al., [TAY76]) to replace $\boldsymbol{J}$ by the constant values computed at the origin ($\boldsymbol{\xi} = \boldsymbol{0}$) of natural coordinates as:

$$\begin{aligned}\int_{V_0^e} \boldsymbol{\Gamma} dV &= \int_{-1}^{1}\int_{-1}^{1}\int_{-1}^{1} \boldsymbol{\Gamma} |\boldsymbol{J}| d\xi^1 d\xi^2 d\xi^3 = \int_{-1}^{1}\int_{-1}^{1}\int_{-1}^{1} \frac{|\boldsymbol{J}_0|}{|\boldsymbol{J}|} \boldsymbol{T}_0^{-T} \boldsymbol{M}_{(\xi)} |\boldsymbol{J}| d\xi^1 d\xi^2 d\xi^3 \\ &= \int_{-1}^{1}\int_{-1}^{1}\int_{-1}^{1} |\boldsymbol{J}_0| \boldsymbol{T}_0^{-T} \boldsymbol{M}_{(\xi)} d\xi^1 d\xi^2 d\xi^3 = |\boldsymbol{J}_0| \boldsymbol{T}_0^{-T} \int_{-1}^{1}\int_{-1}^{1}\int_{-1}^{1} \boldsymbol{M}_{(\xi)} d\xi^1 d\xi^2 d\xi^3 = 0\end{aligned} \tag{2.4.54}$$

In fact, the orthogonality condition (2.4.4) did imply expression (2.4.52) because:

$$\int_{V_0} \underline{\boldsymbol{E}}^{enh} : \underline{\boldsymbol{S}}\, dV = \int_{V_0} \boldsymbol{\alpha} \cdot (\boldsymbol{\Gamma} \boldsymbol{S}) dV = 0 \tag{2.4.55}$$

We see that expression (2.4.55) is the strong form of the patch test condition. The condition in (2.4.55) is valid for an arbitrary stress field while the patch test condition is only valid for a constant stress field $\boldsymbol{S}_0^{\text{mod}}$.

The use of $\mathbf{J}_0$ to approximate $\boldsymbol{J}$ is equivalent to the introduction of a geometric approximation by replacing the original hexahedral (for 2D: quadrilateral) element into a parallelepiped of the same volume (for 2D: parallelogram of the same area).

2.4.5 Equivalence between EAS and Hellinger-Reissner elements

A so-called hybrid stress method can be derived from the Hellinger-Reissner (HR) principle which consists of the stress field and the displacement field. Before comparing with the EAS elements the formulation of HR element is briefly introduced. From the Hu-Washizu principle in (2.4.1) one obtains the conventional stress-displacement HR functional by eliminating $\boldsymbol{E} = \boldsymbol{E}^S = ({}^4\boldsymbol{C})^{-1}\boldsymbol{S}$. The result is:

$$\begin{aligned}\boldsymbol{\pi}_{(\boldsymbol{u},\boldsymbol{S})} = \boldsymbol{\pi}_{\text{int}} + \boldsymbol{\pi}_{ext} \quad &= \int_{V_0} [-\frac{1}{2}\boldsymbol{S}({}^4\boldsymbol{C})^{-1}\boldsymbol{S} + \boldsymbol{S}\boldsymbol{E}_{(\boldsymbol{u})}^{com}] dV + \\ &\int_{A_u} (\boldsymbol{u}^* - \boldsymbol{u}) \cdot \boldsymbol{t} dA - \int_{A_\sigma} \boldsymbol{u} \cdot \boldsymbol{t}^* dA - \int_{V_0} \boldsymbol{u} \cdot \boldsymbol{b}^* \rho dV\end{aligned} \tag{2.4.56}$$

The HR elements with compatible displacement and assumed stress fields that are built as follow:

$$\boldsymbol{u}_{(\xi)}^e = \boldsymbol{N}_{(\xi)} \cdot \boldsymbol{U}^h \tag{2.4.57}$$

$$\boldsymbol{S}_H^e = \boldsymbol{T}_0 \cdot \boldsymbol{P}_{(\xi)} \cdot \boldsymbol{\beta}^h = \boldsymbol{P} \cdot \boldsymbol{\beta}^h \tag{2.4.58}$$

where:

- $\boldsymbol{S}_H^e$ is assumed stress at element level;

- $\boldsymbol{P}_{(\xi)}$ is the matrix that enhances the stress field;
- $\boldsymbol{P} = \boldsymbol{T}_0 \cdot \boldsymbol{P}_{(\xi)}$ with $\boldsymbol{T}_0$ is defined in (2.4.43);
- $\boldsymbol{\beta}^h$ is vector of internal stress variables.

The displacement trial functions $\boldsymbol{N}_{(\xi)}$ should be compatible (C^0 continuous) across inter-element boundaries because there are first derivatives of the displacement field in the HR-functional. But stress trial functions $\boldsymbol{P}$ are not subject to derivation so could be chosen to be incompatible (C^{-1} continuous). This help for eliminating the internal stress variables $\boldsymbol{\beta}^h$ at the element level more easily.

For the sake of simplicity, the following abbreviations are defined:

$$\boldsymbol{H} = \int_{V_0^e} (\boldsymbol{P})^T \cdot ({}^4\boldsymbol{C})^{-1} \cdot \boldsymbol{P}\, dV \tag{2.4.59}$$

$$\boldsymbol{G} = \int_{V_0^e} (\boldsymbol{P})^T \cdot \boldsymbol{B}\, dV \tag{2.4.60}$$

The element stiffness matrix of the HR elements is derived from HR principle has the form as:

$$\boldsymbol{k}^e = (\boldsymbol{G})^T \cdot (\boldsymbol{H})^{-1} \cdot \boldsymbol{G} \tag{2.4.61}$$

The (2.4.61) is achieved after eliminating stress parameters $\boldsymbol{\beta}^h$ from the system of equations. Then, the element stiffness matrix (2.4.61) can be used for the standard displacement formulation.

After the solution process, the stresses can be obtained at the element level as:

$$\boldsymbol{S}_H^e = \boldsymbol{P} \cdot (\boldsymbol{H})^{-1} \cdot \boldsymbol{G} \cdot \boldsymbol{d} \tag{2.4.62}$$

Simo and Rifai [SIM90] generalized the incompatible displacement method to the EAS method. Both of these methods are the dual ones of the hybrid stress method. Hence, the EAS and the incompatible displacement methods with respect to the hybrid stress method are correspondent in some special cases. In this section some relationships between these methods are introduced. These relationships provide a helpful theoretical basis for development and exploitation of the incompatible and EAS methods and also the hybrid method.

It was proven by inspection [AND93] that the stiffness matrix of the EAS elements is equivalent to the stiffness matrix of HR elements if the polynomials in $\boldsymbol{M}_{(\xi)}$ (2.4.46) and $\boldsymbol{P}_{(\xi)}$ (2.4.58) are complementary. It means a polynomial term used for a strain component in $\boldsymbol{M}_{(\xi)}$ is not considered for the corresponding stress component in $\boldsymbol{P}_{(\xi)}$. Consequently, the hybrid stress and enhanced assumed strain fields are orthogonal to each other as:

$$\int_{-1}^{1}\int_{-1}^{1}\int_{-1}^{1} (\boldsymbol{P}_{(\xi)})^T \boldsymbol{M}_{(\xi)} d\xi^1 d\xi^2 d\xi^3 = 0$$

or $$\int_{V_0^e} (\boldsymbol{S}_H^e)^T \boldsymbol{E}^{enh} dV = 0 \tag{2.4.63}$$

In Table 2.4.3, a rectangle low-order element with 2×2 integration will provide an equivalent stiffness matrix whether assumed by a strain field (EAS method) or by a stress field (hybrid stress method).

Table 2.4.3: Equivalent bilinear EAS - HR elements

EAS element	HR element
EAS7 : $\boldsymbol{M}_{(\xi)}=\begin{bmatrix}\xi^1 & 0 & 0 & 0 & \xi^1\xi^2 & 0 & 0\\ 0 & \xi^2 & 0 & 0 & 0 & \xi^1\xi^2 & 0\\ 0 & 0 & \xi^1 & \xi^2 & 0 & 0 & \xi^1\xi^2\end{bmatrix}$	PS : $\boldsymbol{P}_{(\xi)}=\begin{bmatrix}1 & 0 & 0 & \xi^2 & 0\\ 0 & 1 & 0 & 0 & \xi^1\\ 0 & 0 & 1 & 0 & 0\end{bmatrix}$
EAS4: $\boldsymbol{M}_{(\xi)}=\begin{bmatrix}\xi^1 & 0 & 0 & 0\\ 0 & \xi^2 & 0 & 0\\ 0 & 0 & \xi^1 & \xi^2\end{bmatrix}$	HR8: $\boldsymbol{P}_{(\xi)}=\begin{bmatrix}1 & 0 & 0 & \xi^2 & 0 & \xi^1\xi^2 & 0 & 0\\ 0 & 1 & 0 & 0 & \xi^1 & 0 & \xi^1\xi^2 & 0\\ 0 & 0 & 1 & 0 & 0 & 0 & 0 & \xi^1\xi^2\end{bmatrix}$
EAS0: $\boldsymbol{M}_{(\xi)}=[0]$	HR12: $\boldsymbol{P}_{(\xi)}=\begin{bmatrix}1 & 0 & 0 & \xi^2 & 0 & \xi^1\xi^2 & 0 & 0 & 0 & 0 & 0 & 0\\ 0 & 1 & 0 & 0 & \xi^1 & 0 & \xi^1\xi^2 & 0 & \xi^1\xi^2 & 0 & 0 & 0\\ 0 & 0 & 1 & 0 & 0 & 0 & 0 & \xi^1\xi^2 & 0 & \xi^1 & \xi^2 & \xi^1\xi^2\end{bmatrix}$

2.5 ANS ELEMENT

Application of the EAS method that is described in the preceding sections to shear deformable elements does not work satisfactorily in all situations. Particularly in the case of severely distorted meshes or too thin structures these elements do not perform well. The method that is most widely used in these situations is the ANS method. In this context, we focus on the problem of transverse shear locking in solid elements, although the same have been done in a similar way for shell elements. There are also a number of publications on application of the ANS concept to overcome volumetric locking, shear locking and membrane locking. However, the ANS method is only effective in transverse shear locking removal [BIS97].

The ANS abbreviation means Assumed Natural Strain. Here, strain components are assumed in the natural (isoparametric) space. The principal idea of the ANS method is to choose a certain interpolation for the transverse shear strains instead of deriving the strains directly from the interpolation of the displacements. Hence, the method also named “mixed interpolation”, it means both the interpolation for displacement field and interpolation for strain field are required by the method. The bilinear ANS plate element is the most widely used element in both scientific and commercial finite element packages (e.g. ADINA, ANSYS). It is also known as MITC4 element (MITC = Mixed Interpolation of Tensorial Components) or “Dvorkin- Bathe” element [BAT96].

The natural strains at an interior point of the MITC4 element are obtained by linear interpolations of the strains on boundary lines. Finally, the physical strains, which are required at numerical integration points for evaluating the element stiffness and internal force arrays are obtained by tensorial transformation of the natural strain components instead of the standard isoparametric derivative transformations. The procedure of the natural strains and transforming tensorially to physical coordinates has been found to play a key role in improving element performance when the mesh is distorted or curved.

The ANS method can also be combined with the EAS method to improve the in-plane bending behavior. For an explicit definition of an ANS element one has to specify two things, namely:

- The number of nodes and the corresponding shape functions for the displacements (which are the standard shape functions of a displacement element) and
- The number and location of the sampling points and the corresponding shape functions.

The ANS elements do not contain any spurious zero energy mode and show good convergence behavior [PAR86]. All the ANS elements can be used in linear analysis, and in large displacement and large strain analyses, e.g. in the simulations of structural problems and collapse of shells.

The ANS was conceived as one of several competing methods with which to solve shear locking problems. Its most noteworthy feature is that, unlike many forms of reduced integration elements, it produces no rank deficiency. Furthermore, it is easily extendible to geometrically nonlinear problems.

2.5.1 Kinematics in natural coordinate system

The ANS method requires the interpolation of all assumed strains in natural coordinate system. Therefore, it is necessary to define a convected description, which naturally preserves the objectivity (in the convected description, the material base vectors reflect the geometrical and kinematic aspects, hence, the corresponding components are indifferent with respect to their material base vectors). To this end, let's denote the position vectors of the reference configuration Ω_0 and the current configuration Ω_t in the local coordinate system by $\boldsymbol{X}_{(\xi)}$ and $\boldsymbol{x}_{(\xi)}$, respectively. The convected basis vector $\boldsymbol{G}_i$ and its components G_{ij} in the initial basis system are defined by:

$$\boldsymbol{G}_i = \partial \boldsymbol{X} / \partial \xi^i \quad ; \quad \boldsymbol{G}_i \cdot \boldsymbol{G}_j = G_{ij} \quad ; \quad i = 1-3 \tag{2.5.1}$$

while the contravariant vector $\boldsymbol{G}^j$ and its components G^{ji} are defined following:

$$\boldsymbol{G}_i \cdot \boldsymbol{G}^j = \delta_i^j \quad ; \boldsymbol{G}^j = G^{ji}\boldsymbol{G}_i = G_{ji}^{-1}\boldsymbol{G}_i \quad ; \; i,j = 1-3 \tag{2.5.2}$$

Similarly, the convected basis vector $\boldsymbol{g}_i$ and its components g_{ij} in the current basis system are defined:

$$\boldsymbol{g}_i = \partial \boldsymbol{x} / \partial \xi^i = \boldsymbol{G}_i + \partial \boldsymbol{u} / \partial \xi^i \quad ; \quad \boldsymbol{g}_i \cdot \boldsymbol{g}_j = g_{ij} \quad ; \quad i = 1-3 \tag{2.5.3}$$

and its contravariant vector $\boldsymbol{g}^j$ and its components g^{ij} are defined through the following expressions:

$$\boldsymbol{g}_i \cdot \boldsymbol{g}^j = \delta_i^j \quad ; \quad \boldsymbol{g}^i = g^{ij}\boldsymbol{g}_j = g_{ij}^{-1}\boldsymbol{g}_j \quad ; \quad i,j = 1-3 \tag{2.5.4}$$

The deformation gradient in the form of the convected vectors is calculated as:

$$\boldsymbol{F}_{(\xi)} = \frac{\partial \boldsymbol{x}_{(\xi)}}{\partial \boldsymbol{X}_{(\xi)}} = \boldsymbol{g}_i \otimes \boldsymbol{G}^i \tag{2.5.5}$$

while the Green-Lagrange strain tensor takes the following form

$$\underline{\boldsymbol{E}}_{(\xi)} = \frac{1}{2}(\boldsymbol{F}_{(\xi)}^T \boldsymbol{F}_{(\xi)} - \boldsymbol{I}) = \frac{1}{2}(g_{ij} - G_{ij})\boldsymbol{G}^i \otimes \boldsymbol{G}^j = \frac{1}{2}E_{ij}\boldsymbol{G}^i \otimes \boldsymbol{G}^j \tag{2.5.6}$$

or alternatively:

$$\underline{\boldsymbol{E}}_{(\xi)} = \frac{1}{2}\left(\boldsymbol{G}_i \cdot \frac{\partial \boldsymbol{u}}{\partial \xi^j} + \frac{\partial \boldsymbol{u}}{\partial \xi^i} \cdot \boldsymbol{G}_j + \frac{\partial \boldsymbol{u}}{\partial \xi^i} \cdot \frac{\partial \boldsymbol{u}}{\partial \xi^j}\right)\boldsymbol{G}^i \otimes \boldsymbol{G}^j \qquad i,j = 1-3 \tag{2.5.7}$$

In the context of large deformation, the ANS method modifies shear components of Green-Lagrange strain tensor $\underline{\boldsymbol{E}}$. Hence, the variational equation should be written in material configuration (or total Lagrange formulation) in terms of the Green-Lagrange strain tensor $\underline{\boldsymbol{E}}$ and its energy conjugated quantity $\underline{\boldsymbol{S}}$, the second Piola-Kirchhoff stress tensor.

2.5.2 Classical ANS formulation

In this section we present the classical ANS technique for the removal of transverse shear locking in an eight-node hexahedral element. For the sake of simplicity, let's consider the case with a rectangular prismatic geometric configuration. It means the physical space (X,Y,Z) is chosen to be identical to the natural space (ξ^1, ξ^2, ξ^3), see (Figure 2.5.1).

Instead of the standard computation, which leads to shear locking, the transverse shear strains E_{13} and E_{23} are assumed, according to Dvorkin and Bathe [DVO84], to be interpolated through the use of certain sampling points as follows

$$\begin{aligned} \tilde{E}_{XZ} \equiv \tilde{E}_{13} &= \frac{1}{2}(1-\xi^2)E_{13(A)} + \frac{1}{2}(1+\xi^2)E_{13(C)} \\ \tilde{E}_{YZ} \equiv \tilde{E}_{23} &= \frac{1}{2}(1-\xi^1)E_{23(D)} + \frac{1}{2}(1+\xi^1)E_{23(B)} \end{aligned} \tag{2.5.8}$$

where $E_{13(A)}, E_{13(C)}, E_{23(B)}$ and $E_{23(D)}$ are the natural shear strains at points A, C, B and D situated on the mid-surface of the solid element (Figure 2.5.1), respectively. Values of these sampling strains can be directly derived through the use of the covariant components in the contravariant base vectors as by E_{ij} in (2.5.6):

$$\boldsymbol{E} = \begin{Bmatrix} E_{11} \\ E_{22} \\ E_{33} \\ 2E_{12} \\ 2E_{13} \\ 2E_{23} \end{Bmatrix} = \begin{Bmatrix} 0.5(g_{11}^e - G_{11}^e) \\ 0.5(g_{22}^e - G_{22}^e) \\ 0.5(g_{33}^e - G_{33}^e) \\ (g_{12}^e - G_{12}^e) \\ (g_{13}^e - G_{13}^e) \\ (g_{23}^e - G_{23}^e) \end{Bmatrix} \tag{2.5.9}$$

Once the transverse shear strains are assumed, all assumed strain-displacement matrices can be immediately formulated as:

$$\tilde{\boldsymbol{B}} = [\tilde{\boldsymbol{B}}_1, \tilde{\boldsymbol{B}}_2, \tilde{\boldsymbol{B}}_3, \tilde{\boldsymbol{B}}_4, \tilde{\boldsymbol{B}}_5, \tilde{\boldsymbol{B}}_6, \tilde{\boldsymbol{B}}_7, \tilde{\boldsymbol{B}}_8]$$

$$\tilde{\boldsymbol{B}}_I = \begin{bmatrix} N_{I,1}\boldsymbol{g}_1^T \\ N_{I,2}\boldsymbol{g}_2^T \\ N_{I,3}\boldsymbol{g}_3^T \\ N_{I,1}\boldsymbol{g}_2^T + N_{I,2}\boldsymbol{g}_1^T \\ \frac{1}{2}(1-\xi^2)(N_{I,1}\boldsymbol{g}_3^T + N_{I,3}\boldsymbol{g}_1^T)_{(A)} + \frac{1}{2}(1+\xi^2)(N_{I,1}\boldsymbol{g}_3^T + N_{I,3}\boldsymbol{g}_1^T)_{(C)} \\ \frac{1}{2}(1-\xi^1)(N_{I,2}\boldsymbol{g}_3^T + N_{I,3}\boldsymbol{g}_2^T)_{(D)} + \frac{1}{2}(1+\xi^1)(N_{I,2}\boldsymbol{g}_3^T + N_{I,3}\boldsymbol{g}_2^T)_{(B)} \end{bmatrix}; \text{I=1-8} \tag{2.5.10}$$

Then the stiffness matrix is formulated as in the standard manner. Expressions (2.5.8-10) are only valid when the physical space is identical to the natural space, i.e., $(X,Y,Z) \equiv (\xi^1, \xi^2, \xi^3)$.

For the general case, where the mid-surface quadrilateral is not a rectangle and the X-Y frame is not aligned to the $\xi^1 - \xi^2$ frame, the natural shear strain components must be firstly interpolated in the covariant space, as defined in (2.5.11). This allows taking into account the element distortion.

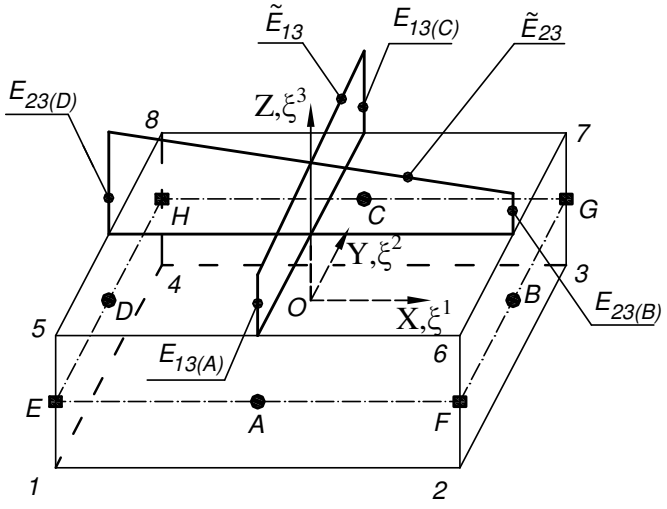

Figure 2.5.1: ANS method illustration, special case: X-Y aligns ξ^1- ξ^2

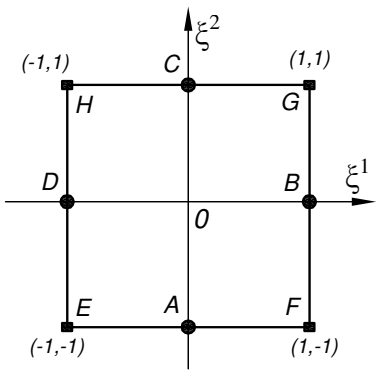

Figure 2.5.2: Mid-surface of element in isoparametric coordinates

From (2.5.8) and (2.5.9), the assumed shear strains in the general case can be computed by:

$$\tilde{\boldsymbol{E}}_s = \begin{Bmatrix} 2\tilde{E}_{13} \\ 2\tilde{E}_{23} \end{Bmatrix} = \begin{Bmatrix} (1-\xi^2)E_{13(A)} + (1+\xi^2)E_{13(C)} \\ (1-\xi^1)E_{23(D)} + (1+\xi^1)E_{23(B)} \end{Bmatrix}$$
$$= \begin{Bmatrix} (1-\xi^2)(g^e_{13} - G^e_{13})_{(A)} + (1+\xi^2)(g^e_{13} - G^e_{13})_{(C)} \\ (1-\xi^1)(g^e_{23} - G^e_{23})_{(D)} + (1+\xi^1)(g^e_{23} - G^e_{23})_{(B)} \end{Bmatrix} \tag{2.5.11}$$

where $E_{13(A)}, E_{13(C)}, E_{23(D)}$ and $E_{23(B)}$ are natural shear strains, evaluated by displacement interpolations, at points A, C, D and B respectively, see Figure 2.5.1.

Clearly, $\tilde{E}_{13}$ is constant with respect to ξ^1 and discontinuous at $\xi^1 = \pm 1$ (between elements), while $\tilde{E}_{23}$ is constant with ξ^2 and discontinuous at $\xi^2 = \pm 1$.

The strain tensor can be equivalently expressed in both the natural space and the physical (Cartesian) space. The transformation of the strain components between the natural space and the physical space is done by using the transforming matrix $\boldsymbol{T}_{(\boldsymbol{\xi}\neq\boldsymbol{0})}$ as defined in (2.4.43). In order to alleviate the shear locking, the natural shear strains E_{13} and E_{23} are replaced by the assumed natural shear strains $\tilde{E}_{13}$ and $\tilde{E}_{23}$ before doing the transformation from the natural space to the physical space. Finally, the physical assumed strain vector is:

$$\tilde{\boldsymbol{E}}^{ANS} = \begin{Bmatrix} E_{XX} \\ E_{YY} \\ E_{ZZ} \\ 2E_{XY} \\ 2\tilde{E}_{XZ} \\ 2\tilde{E}_{YZ} \end{Bmatrix} = \boldsymbol{T}^{-T} \begin{Bmatrix} E_{11} \\ E_{22} \\ E_{33} \\ 2E_{12} \\ 2\tilde{E}_{13} \\ 2\tilde{E}_{23} \end{Bmatrix} = \boldsymbol{T}^{-T} \begin{Bmatrix} 0.5(g^e_{11} - G^e_{11}) \\ 0.5(g^e_{22} - G^e_{22}) \\ 0.5(g^e_{33} - G^e_{33}) \\ (g^e_{12} - G^e_{12}) \\ (1-\xi^2)(g^e_{13} - G^e_{13})_{(A)} + (1+\xi^2)(g^e_{13} - G^e_{13})_{(C)} \\ (1-\xi^1)(g^e_{23} - G^e_{23})_{(D)} + (1+\xi^1)(g^e_{23} - G^e_{23})_{(B)} \end{Bmatrix} \tag{2.5.12}$$

These assumed strains can be implemented in the standard solid element in a straightforward manner. These assumptions allow the element to represent pure bending modes without any spurious shear effect.

The modified shear strains lead to the new operator matrix $\tilde{\boldsymbol{B}}$ (2.5.10) in the natural space. However, the formulation can be slightly modified so that no explicit strain evaluation at the sampling points is necessary in the numerical calculation. The physical assumed strain-displacement matrix at node I of the eight-node solid element is:

$$\tilde{\boldsymbol{B}}_I^{ANS} = \boldsymbol{T}^{-T}\begin{bmatrix} N_{I,1}\boldsymbol{g}_1^T \\ N_{I,2}\boldsymbol{g}_2^T \\ N_{I,3}\boldsymbol{g}_3^T \\ N_{I,1}\boldsymbol{g}_2^T + N_{I,2}\boldsymbol{g}_1^T \\ \frac{1}{2}(1-\xi^2)(N_{I,1}\boldsymbol{g}_3^T + N_{I,3}\boldsymbol{g}_1^T)_{(A)} + \frac{1}{2}(1+\xi^2)(N_{I,1}\boldsymbol{g}_3^T + N_{I,3}\boldsymbol{g}_1^T)_{(C)} \\ \frac{1}{2}(1-\xi^1)(N_{I,2}\boldsymbol{g}_3^T + N_{I,3}\boldsymbol{g}_2^T)_{(D)} + \frac{1}{2}(1+\xi^1)(N_{I,2}\boldsymbol{g}_3^T + N_{I,3}\boldsymbol{g}_2^T)_{(B)} \end{bmatrix} \tag{2.5.13}$$

2.5.3 Some variational basis for the ANS method

The ANS element is locking-free, rank sufficient and distortion insensitive even with coarse meshes as it has been pointed out by Park and Stanley [PAR86]. The ANS method has originally been derived from engineering intuition without a convincing variational background. Firstly, a restricted form of the method was proposed in 1969 for four-node plane stress element by assuming a constant shear strain that is independent to the direct strains [MIL90a]. In 1981 Hughes and Tezduyar [HUG81] used the method to avoid shear locking for plates; later in 1984 it was applied successfully by Dvorkin and Bathe to four-node shell element for geometric and material nonlinear analysis [DVO84]. In fact, the mathematical justifications, based on the Hu-Washizu and mixed functionals, have been provided a couple of years later in separate publications, e.g. Militello and Felippa [MIL90a,b].

In ANS method, there are two strain fields: the derived-displacement strain field and the assumed natural strain field. If we consider these fields as independent fields, the ANS formulation can be interpreted by a Reissner type functional: the functional that uses the strains and displacements as independent fields. Departure from the three fields general Hu-Washizu functional (2.4.1) the displacements $\boldsymbol{u}$, stresses $\boldsymbol{S}$ and strains $\boldsymbol{E}$ are independently varied, let's re-write the functional (2.4.1):

$$\begin{aligned} \pi_{(\boldsymbol{u},\boldsymbol{E},\boldsymbol{S})} = \pi_{\text{int}} + \pi_{ext} &= \int_{V_0} W_{\boldsymbol{S}(\boldsymbol{E})} dV + \int_{V_0} \boldsymbol{S}\cdot[\boldsymbol{E}_{(\boldsymbol{u})}^{com} - \boldsymbol{E}]dV + \\ &+ \int_{A_u} (\boldsymbol{u}^* - \boldsymbol{u})\cdot \boldsymbol{t} dA - \int_{A_\sigma} \boldsymbol{u}\cdot \boldsymbol{t}^* dA - \int_{V_0} \boldsymbol{u}\cdot \boldsymbol{b}^* \rho dV \end{aligned} \tag{2.5.14}$$

From $\pi_{(\boldsymbol{u},\boldsymbol{E},\boldsymbol{S})}$ one obtains the conventional stress-displacement Heillinger-Reissner functional by eliminating $\boldsymbol{E}$ by:

$$\boldsymbol{E} = \boldsymbol{E}^S = ({}^4\boldsymbol{C})^{-1}\boldsymbol{S} \tag{2.5.15}$$

Another Reissner type, strain-displacement functional is obtained by eliminating $\boldsymbol{S}$ through:

$$\boldsymbol{S} = \boldsymbol{S}^E = {}^4\boldsymbol{C}\boldsymbol{E} \tag{2.5.16}$$

which yields:

$$\pi_{(u,E)} = \int_{V_0} [-\frac{1}{2} \boldsymbol{E}^T \, {}^4\boldsymbol{C}\boldsymbol{E} + \boldsymbol{E}^T \, {}^4\boldsymbol{C}\boldsymbol{E}^{com}_{(u)}] dV + \int_{A_u} (\boldsymbol{u}^* - \boldsymbol{u}) \cdot \boldsymbol{t} dA - \int_{A_\sigma} \boldsymbol{u} \cdot \boldsymbol{t}^* \, dA - \int_{V_0} \boldsymbol{u} \cdot \boldsymbol{b}^* \rho dV \tag{2.5.17}$$

Setting $\boldsymbol{E} = \boldsymbol{E}^{com}_{(u)}$ and $\boldsymbol{u} = \boldsymbol{u}^*$ on A_u reduces $\pi_{(u,E)}$ to the potential energy functional

$$\pi_{(u)} = \pi_{\text{int}} + \pi_{ext} == \int_{V_0} \frac{1}{2} (\boldsymbol{E}^{com}_{(u)})^T \, {}^4\boldsymbol{C}\boldsymbol{E}^{com}_{(u)} dV - \int_{A_\sigma} \boldsymbol{u} \cdot \boldsymbol{t}^* \, dA - \int_{V_0} \boldsymbol{u} \cdot \boldsymbol{b}^* \rho dV \tag{2.5.18}$$

Partial Strain Assumption

It is common practice to assume only a part of the strains to be independent fields. For instance, with MITC4 element independent assumptions are only made for the transverse shear strains [BAT96], whereas the bending strains are entirely derived from displacements:

$$\boldsymbol{E} = [\boldsymbol{E}_a \quad \boldsymbol{E}_b]^T \tag{2.5.19}$$

where $\boldsymbol{E}_a$ stands for the assumed strain field and $\boldsymbol{E}_b = \boldsymbol{E}^{com}_b$ stands for the derived-displacement (bending) strain field.

The $\pi_{(u,E)}$ functional (2.5.17) requires obvious modification in the volume term:

$$\begin{aligned} \pi_{(u,E_a)} = \int_{V_0} [\boldsymbol{E}_a^T \quad \boldsymbol{E}_b^T] \begin{bmatrix} {}^4\boldsymbol{C}_{aa} & {}^4\boldsymbol{C}_{ab} \\ {}^4\boldsymbol{C}_{ba} & {}^4\boldsymbol{C}_{bb} \end{bmatrix} \begin{bmatrix} \boldsymbol{E}^{com}_a - 0.5\boldsymbol{E}_a \\ 0.5\boldsymbol{E}_b \end{bmatrix} dV + \\ + \int_{A_u} (\boldsymbol{u}^* - \boldsymbol{u}) \cdot \boldsymbol{t} dA - \int_{A_\sigma} \boldsymbol{u} \cdot \boldsymbol{t}^* \, dA - \int_{V_0} \boldsymbol{u} \cdot \boldsymbol{b}^* \rho dV \end{aligned} \tag{2.5.20}$$

The resulting principles take a particularly simple form if the constitutive coupling terms $\boldsymbol{C}_{ab}$ and $\boldsymbol{C}_{ba}$ vanish, in that case:

$$\pi_{(u,E_a)} = \pi_{a(u,E_a)} + \pi_{b(u)} + \pi_{ext} \tag{2.5.21}$$

where $\pi_{a(u,E_a)}$ is a mixed strain-displacement energy involving $\boldsymbol{E}_a$; $\pi_{b(u)}$ is a potential energy involving the $\boldsymbol{E}^{com}_b$; π_{ext} is the external energy.

Up to now a compatible displacement field and a discontinuous strain field are involved. Hence use $\pi_{(u,E_a)}$ is a suitable functional for the ANS method.

The element displacement field is interpolated as:

$$\boldsymbol{u}^e = \boldsymbol{N}_c \boldsymbol{U}^h_c \tag{2.5.22}$$

where $\boldsymbol{N}_c$ is the compatible shape functions as defined in (2.4.11), $\boldsymbol{U}^h_c$ is the nodal displacement vector as defined in (2.4.14).

The strain fields derived from the displacements are:

- bending strains:

$$\boldsymbol{E}^{com}_b = \boldsymbol{B}^c_b \boldsymbol{U}^h_c \tag{2.5.23}$$

- shear strains:

$$\boldsymbol{E}^{com}_s = \boldsymbol{B}^c_s \boldsymbol{U}^h_c \tag{2.5.24}$$

where $\boldsymbol{B}_b^c$ and $\boldsymbol{B}_s^c$ are parts of strain-displacement matrix that relate to bending strains and shear strains, respectively (the letter "c" stands for compatible values).

The independent strains in $\pi_{(\boldsymbol{u},\boldsymbol{E}_a)}$ are:

- bending strains as the derived-displacement bending strains (2.5.23);
- shear strains (the superscript "a" stands for ANS values):

$$\boldsymbol{E}_a = \boldsymbol{B}_s^a \boldsymbol{a} \tag{2.5.25}$$

with $\boldsymbol{B}_s^a$ is natural assumed strain-displacement matrix and $\boldsymbol{a}$ is strain coefficient vector.

Introduce (2.5.23) - (2.5.25) into (2.5.21) and carrying out the interpolations at the element level we will have:

$$\pi_{(\boldsymbol{U}_c^h,\boldsymbol{a})} = \frac{1}{2}\left(\boldsymbol{U}_c^h\right)^T \boldsymbol{K}^{cc}\boldsymbol{U}_c^h - \frac{1}{2}\boldsymbol{a}^T\boldsymbol{K}^{aa}\boldsymbol{a} + \left(\boldsymbol{U}\boldsymbol{h}\right)^T \boldsymbol{K}^{ca}\boldsymbol{a} - \left(\boldsymbol{U}_c^h\right)^T \boldsymbol{f}^c \tag{2.5.26}$$

where

$$\begin{aligned} \boldsymbol{K}^{cc} &= \int_{V^e} \left(\boldsymbol{B}_b^c\right)^T \boldsymbol{C}_b \, \boldsymbol{B}_b^c dV \quad ; \; \boldsymbol{K}^{aa} = \int_{V^e} \left(\boldsymbol{B}_s^a\right)^T \boldsymbol{C}_s \, \boldsymbol{B}_s^a dV \\ \boldsymbol{K}^{ca} &= \int_{V^e} \left(\boldsymbol{B}_s^c\right)^T \boldsymbol{C}_s \, \boldsymbol{B}_s^a dV \quad ; \; \boldsymbol{f}^c = \int_{V^e} \left(\boldsymbol{N}_c\right)^T \boldsymbol{b}^* dV + \int_{A_\sigma^e} \left(\boldsymbol{N}_c\right)^T \boldsymbol{t}^* dA \end{aligned} \tag{2.5.27}$$

On performing the variations we obtain the matrix equation:

$$\begin{bmatrix} \boldsymbol{K}_b^{cc} & \boldsymbol{K}^{ca} \\ (\boldsymbol{K}^{ca})^T & -\boldsymbol{K}^{aa} \end{bmatrix} \begin{Bmatrix} \boldsymbol{U}_c^h \\ \boldsymbol{a} \end{Bmatrix} = \begin{Bmatrix} \boldsymbol{f}^c \\ \boldsymbol{0} \end{Bmatrix} \tag{2.5.28}$$

From the second equation of (2.5.28) we obtained the shear strain coefficients:

$$\boldsymbol{a} = (\boldsymbol{K}^{aa})^{-1}(\boldsymbol{K}^{ca})^T \boldsymbol{U}_c^h = \boldsymbol{Q}_c \boldsymbol{U}_c^h \tag{2.5.29}$$

Introduce (2.5.29) into (2.5.28) gives the statically condensed system:

$$(\boldsymbol{K}_b^{cc} + \boldsymbol{Q}_c^T \boldsymbol{K}^{aa} \boldsymbol{Q}_c)\boldsymbol{U}_c^h = \boldsymbol{f}^c \tag{2.5.30}$$

In (2.5.30) $\boldsymbol{K}_b^{cc}$ is the bending stiffness matrix, which is also obtainable from the potential energy principle. While $\boldsymbol{Q}_c^T \boldsymbol{K}^{aa} \boldsymbol{Q}_c$ stands for the new shear stiffness matrix. The system of equations (2.5.30) now contains only nodal displacement vector $\boldsymbol{U}_c^h$ as in the standard displacement method.

A variational justification of the ANS formulation as presented above has been done by Militello and Felippa [MIL90a,b]. This study is based on two hybrid extensions of Reissner-type functional that uses strains and displacements as independent fields. However, the work of Militello and Felippa is not applicable to all types of material models. The material is firstly required to be decoupled as in (2.5.20). Furthermore, the proposal of Militello and Felippa, currently, is only valid to transverse shear locking removal. Meanwhile the ANS method could apply for another locking effect, such as curvature thickness locking (Chapter 3). By these arguments, we see that variational base of the ANS method is still an open problem. However, as it has been pointed out [BAT96] that a variational basis of an element might not exist, but whether the element is

useful and effective can of course be determined only by a deeper analysis of the formulation.

Advantages of the ANS method are simplicity while remaining effective. The ANS elements could be applied for both structural (plate, shell) and continuum (solid) elements. Numerical results in literature show that ANS elements are locking-free, rank sufficient and distortion insensitive even with coarse meshes. Furthermore, the method is easy to be implemented in any code. Because of its attractions, the ANS method has been being developed by many authors as Dvorkin and Bathe [DVO84], Park and Stanley [PAR86], Betsch and Stein [BET95], Bathe et al. [BAT00], etc.

2.6 NUMERICAL RESULTS

This section investigates performances of the EAS and ANS elements. In the following tests, the low-order standard solid element is designated as Q1. While the standard solid element Q1, which employs the classical ANS technique [DVO84] for alleviating transverse shear locking and curvature locking, is designated as ANS. The EAS elements are designated as EASx, where 'x' is the number of internal parameters. The additional letter "2D." stands for elements in 2D, without this additional letter means elements are in 3D. The ANS, EAS elements used in the following tests are implemented in a MATLAB code, according to the theories presented in this chapter.

2.6.1 Membrane patch test

Let's consider a patch test as suggested by McNeal and Harder [MAC85] and originally aimed to check the membrane behavior of plate and shell elements. In order to adapt to 3D elements, the number of nodes has been doubled (Figure 2.6.1) as Vu-Quoc and Tan [QUO03a]. An imposed displacement field at the boundary nodes is chosen to cause a constant stress field in the plate. ,

Table 2.6.1: Interior nodal coordinates

	5	6	7	8	13	14	15	16
X	0.04	0.18	0.16	0.08	0.04	0.18	0.16	0.08
Y	0.02	0.03	0.08	0.08	0.02	0.03	0.08	0.08
Z	-h/2	-h/2	-h/2	-h/2	h/2	h/2	h/2	h/2

Practically, consider a rectangle plate of dimensions L×W×h = 0.24×0.12×0.001. The material parameters are taken as E = 10^6 and ν = 0.25. In the original problem designed for plane stress problems, McNeal and Harder [MAC85] employed the following boundary conditions:

$$u = (X + Y/2)10^{-3}; \quad v = (X/2 + Y)10^{-3} \tag{2.6.1}$$

which lead to the corresponding reference solutions of constant strains and stresses:

$$\varepsilon_X = \varepsilon_Y = \gamma_{XY} = 10^{-3};$$
$$\sigma_X = \sigma_Y = 1333; \quad \tau_{XY} = 400. \tag{2.6.2}$$

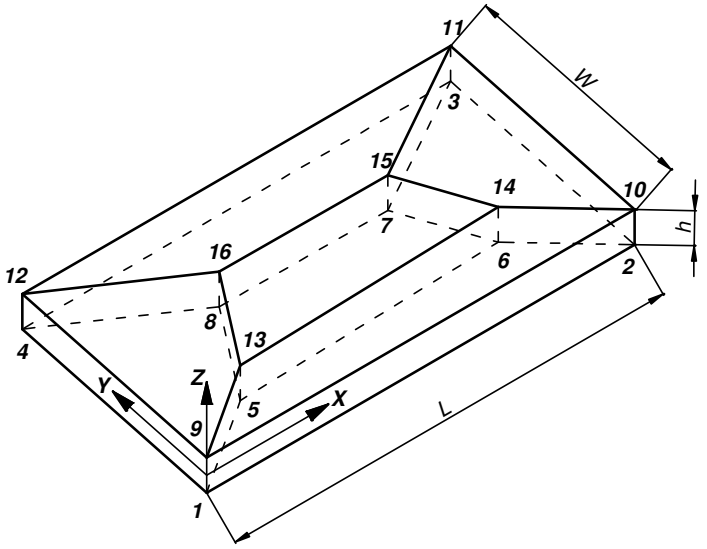

Figure 2.6.1: Membrane patch test

Motivated by this result, the above boundary conditions (2.6.1) are also adopted for the modified doubled-surface membrane patch test. Additionally, the condition w = 0 has also be imposed to a bottom node, e.g. node 1, to prevent rigid body motions. Because the plate is too thin, L/h=240, it is possible to assure a constant stress state in the plate when apply these conditions.

Numerical results show that the ANS element passes the modified patch test; i.e. the computed stresses are constant all over the plate and consistent with (2.6.2). The computed displacements of interior nodes also fully agree with (2.6.1). We also note that the EAS elements also pass this patch test as previously reported in [KLI06], [QUO03a].

2.6.2 Out-of-plane bending patch test

Let's re-consider the above plate, Figure 2.6.1, but in bending situation. Again, a patch test for 2D elements (plates and shells) is extended for 3D elements. In order to create a constant stress state, the original boundary conditions, see [MAC85], for the displacement (w_0) and rotations (θ_x, θ_y) at the reference surface of the plate are:

$$w_0 = 10^{-3}(X^2 + XY + Y^2)/2;$$
$$\theta_X = \frac{\partial w}{\partial Y} = 10^{-3}(Y + X/2); \quad \theta_Y = \frac{\partial w}{\partial X} = -10^{-3}(X + Y/2). \tag{2.6.3}$$

The boundary conditions (2.6.3) are not directly applicable to the solid elements because they contain the rotations. If the cross sections of the plate are assumed plane (it is plausible because the plate is thin) the boundary conditions can be modified, as in [QUO03a], in such a way that:

$$w = w_0 = 10^{-3}(X^2 + XY + Y^2)/2; \tag{2.6.4}$$

$$u = \pm\frac{h}{2}\theta_Y = \mp\frac{h}{2}(X + Y/2)10^{-3};\ \text{v} = \mp\frac{h}{2}\theta_X = \mp\frac{h}{2}(Y + X/2)10^{-3};$$

i.e. different displacements are imposed to the exterior nodes on the top (upper sign) and bottom (lower sign) surfaces of the plate, respectively. The theoretical stresses, see [MAC85], at the top and bottom surfaces of the plate are:

$$\sigma_X = \sigma_Y = \pm 0.667;\ \tau_{XY} = \pm 0.200 \qquad (2.6.5)$$

Table 2.6.2: Displacements of the interior nodes

Node	u	v	w
5	2.500×10^{-8}	2.000×10^{-8}	1.400×10^{-6}
6	9.750×10^{-8}	6.000×10^{-8}	1.935×10^{-5}
7	1.000×10^{-7}	8.000×10^{-8}	2.240×10^{-5}
8	6.000×10^{-8}	6.000×10^{-8}	9.600×10^{-6}

Table 2.6.3: Normalized displacements at interior nodes

Node	Displacement	ANS	EAS3v6s	EAS12v18s
5	u	1.0000	2.6009	4.6332
	v	1.0000	-2.5450	1.1749
	w	0.9999	3.0543	3.8885
6	u	1.0000	0.6086	0.1436
	v	1.0000	-0.1536	1.4310
	w	0.9999	1.1603	1.3021
7	u	1.0000	0.6719	0.1815
	v	1.0000	1.9783	0.7567
	w	1.0000	1.1643	1.2923
8	u	1.0000	1.5000	0.2291
	v	1.0000	1.8627	0.7849
	w	1.0000	1.4216	1.7288

As also already reported by Vu-Quoc and Tan [QUO03a], all EAS elements are unable to converge to the analytic solution listed in Table 2.6.2. The displacements of the EAS12v18s in Table 2.6.3 are identical to those reported by Vu-Quoc and Tan [QUO03a]. This helps to evaluate the quality of our EAS implementation in the MATLAB code.

In contrast, the classical ANS enables the exact solution. This presents the superior performance of the ANS techniques over the EAS ones in the removal of shear locking and in working with distorted mesh, see Table 2.6.3.

2.6.3 Eigenvalues analyses of a rectangle

This is one of the basic tests. The eigenvalues of stiffness matrices of regular meshes are calculated. We examine a single element of rectangle shape with length is equal to unit, material properties are Young's modulus E = 1000 and Poisson's ratio ν = 0.

In order to check whether the element is free from shear locking, eigenvalues of pure bending mode of the stiffness matrix are analysed. As references, let's take free-

shear locking elements as 2D.EAS4 (see Table 2.4.3), based on the EAS method, proposed by Simo and Rifai [SIM90] and DSG element proposed by Bischoff et al. [BIS03] to compare with the 2D.ANS element.

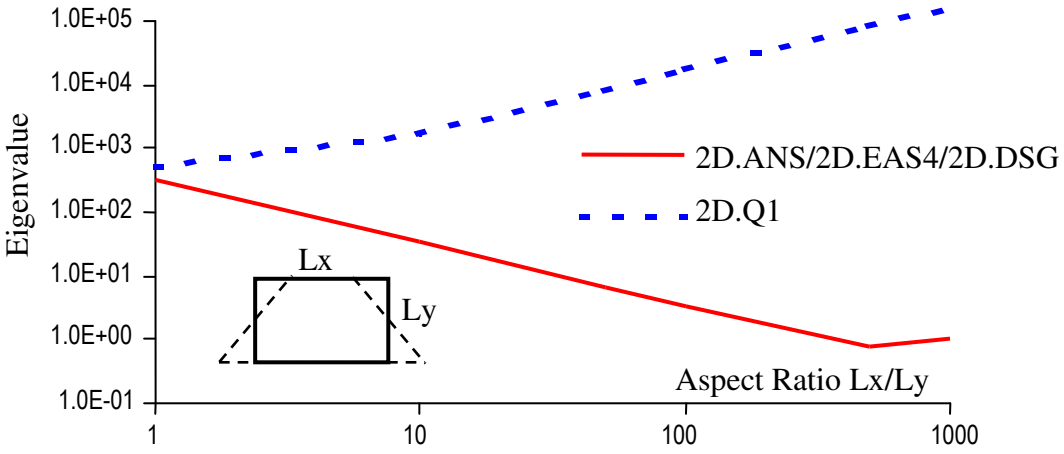

Figure 2.6.2: Eigenvalue analyses of element stiffness matrices, in-plane bending mode

The Poisson's ratio is set to zero, $\nu = 0$, in order to preventing the element from volumetric locking and Poisson thickness locking. The results show that with various aspect ratios (length is fixed, thickness is changed) the 2D.ANS element displayed 3 rigid body modes and no spurious zero energy modes. Figure 2.6.2 shows that behavior of the present 2D.ANS solid is completely coincident with results given by 2D.EAS4 and DSG. It means all of them are free from shear locking at high aspect ratio. Meanwhile the standard element 2D.Q1 shows stiffer (locking) behavior when aspect ratio increasing.

2.6.4 Circular cantilever beam at large displacements

The following example shows the applicability for thin 3D-beams. Let's consider a circular cantilever of dimension R = 100, $\alpha = 45°$ and cross section 1×1, see Figure 2.6.3. Material parameters are elastic modulus $E = 10^7$ and Poisson ratio $\nu = 0$. The cantilever is clamped at one end and loaded by a force P at the other extremity.

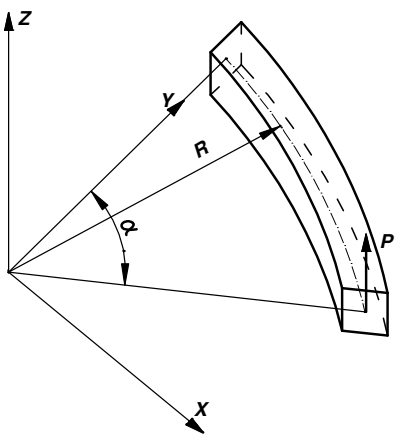

Figure 2.6.3: Circular cantilever

The problem has been modeled by Slavkovic et al. [SLA94], who used 18 internal strain parameters to enhance the solid element. The problem has also been modeled by Klinkel et al. [KLI97], who also used EAS solid element. Both the enhanced elements of authors in [SLA94] and [KLI97] are EAS elements but enhanced by different modes. However, these elements are shear and volumetric locking free. The large deformation response will be calculated for different vertical tip loads. In this test, behavior of the classical ANS method is very attractive. Figure 2.6.4 shows that displacements of the cantilever discretized by only 10 ANS elements are quite comparable to the results of Slavkovic and Klinkel with 16 elements. The ANS element is softer in displacement u (curve 5) but stiffer in displacement v (curve 6) while give a well approximated displacement w (curve 7) to the references, [SLA94] and [KLI97]. This is the result of shear locking removal in thickness direction (z).

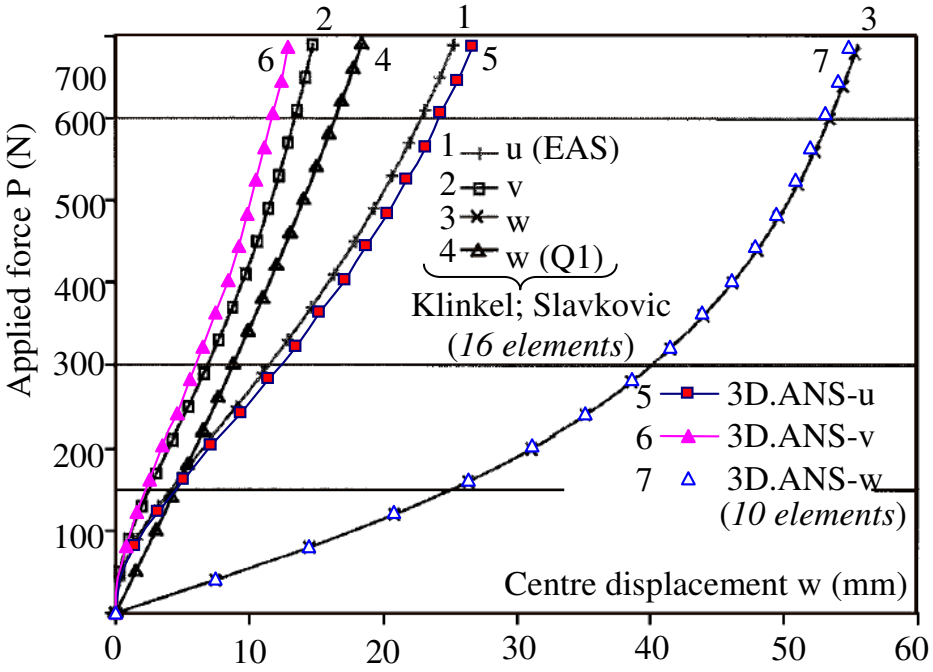

Figure 2.6.4: Curved cantilever beam: displacements

2.6.5 Scordelis-Lo roof with rigid end diaphragms

Consider a shell of radius R = 25, thickness t = 0.25, length L = 50 and open angle $\alpha = 40°$ under a gravity load p = 90 (per unit area) distributed on the shell surface (Figure 2.6.5). Both ends of the shell are constrained with only a free movement in the axial direction. The material parameters are: $E = 4.32\times10^8$ and $\nu = 0.0$. The vertical deflection of the mid-side free edge v = 0.3024 is taken as the reference solution (McNeal and Harder [MAC85]).

Due to the symmetry of the structure, only a single quarter of the shell is modeled. Different types of discretization are considered together with various elements (Figure 2.6.6). The ANS element delivers a good solution with a rather coarse mesh (4×4). In contrast, the EAS9 element, which has 9 incompatible modes, requires a finer mesh (16×16) to reach the correct solution.

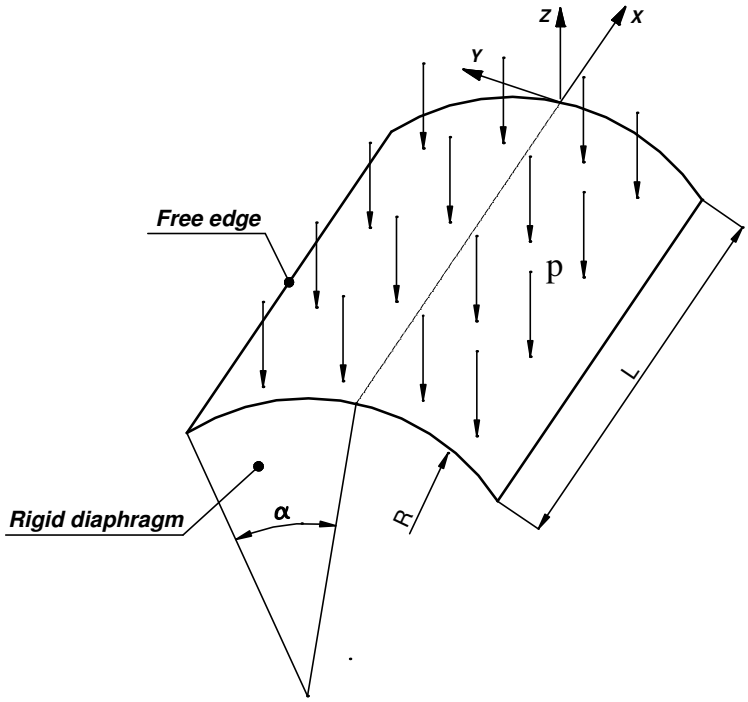

Figure 2.6.5: Scordelis-Lo roof

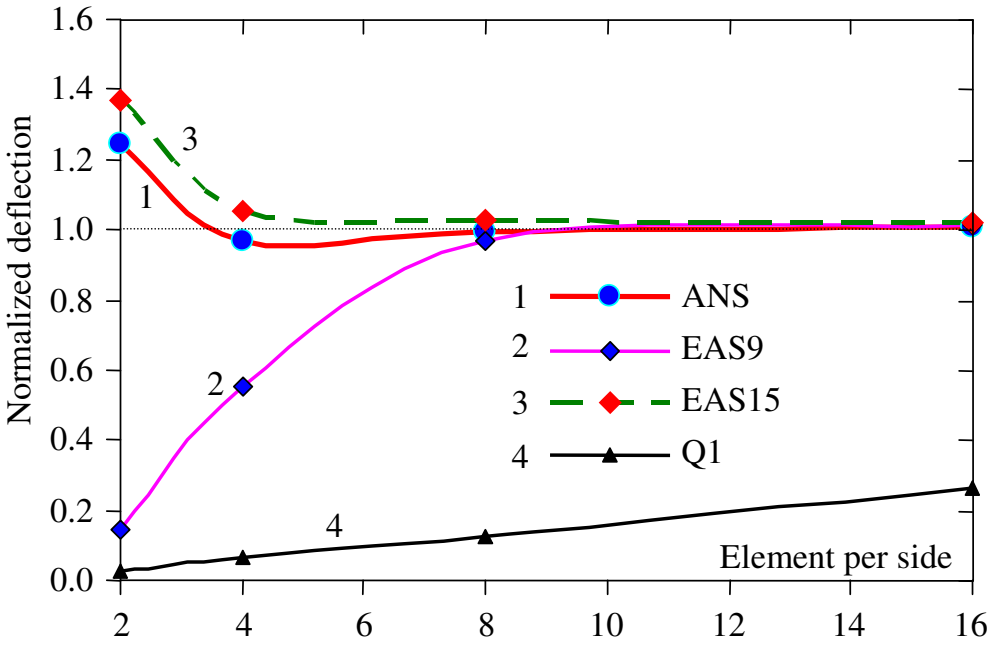

Figure 2.6.6: Scordelis-Lo roof: convergence of finite element solution

With an increase of enhanced modes, the EAS15 element appears to give a better result more theoretically expected than the EAS9 element. However, instead of starting from a low value of displacement at coarse meshes and then progressively increasing this value with the refinement of mesh as seen for the EAS9 element, the EAS15 element gives first a higher value of deflection at coarse meshes and then lower values due to a mesh refinement. This can be explained by the effects of the high-order incompatible modes (modes 34-39, see (2.4.46)), they make the EAS15 soft by fairly alleviating the shear locking. As regards the Q1 standard element, a rather slow convergence is found. Obviously, the shear locking contributes to this behavior.

2.6.6 Regular block with nearly incompressible material

In order to investigate the performance of the ANS and EAS elements in volumetric locking conditions, a regular block of dimensions 100×100×50 clamped at bottom and loaded by a uniform pressure of q = 250/unit area, acting on a top area of 20×20 at the center is considered [AND93], see Figure 2.6.7. The material has an elastic modulus $E = 2.1\times10^5$ and Poisson ratio ν = 0.4999, i.e. nearly incompressible material. Due to symmetry, only a quadrant of the block is modeled by a mesh of 5×5×5 elements.

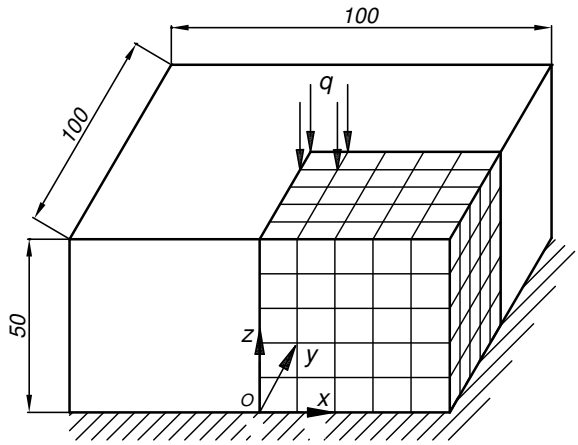

Figure 2.6.7: Regular block

In Table 2.6.4 the vertical displacement simulated by different elements is listed. Take the result of the free-volumetric locking SRI element as the reference. Obviously, the volumetric locking response is observed with the standard element. Since volumetric locking cannot be removed by the ANS techniques, the ANS element is nearly as stiff as the standard element Q1 in this problem.

Table 2.6.4: Vertical displacement at the block's center

Element	Q1	ANS	EAS3v6s	EAS9v	EAS21	EAS30	SRI
w	0.00160	0.00161	0.01136	0.01844	0.01907	0.01907	0.01966
w/w_{SRI}	0.08140	0.08190	0.57780	0.93790	0.97000	0.97000	1.00000

Compare to the EAS30, we see that EAS3v6s with 3 volumetric modes is rather stiff. The EAS21 element with 9 volumetric modes gives as good result as the EAS30. Note that the shear modes can assist the volumetric modes in volumetric locking removal. It explains why the locking response can be more removed with the additional introduction of shear enhanced modes. For example, the EAS21 with 12 shear modes besides 9 volumetric modes gives a quite better result than the EAS9v with unique 9 volumetric modes. The SRI technique shows a better performance in removing the incompressible locking in comparison with the EAS technique.

CONCLUSION

Through the numerical tests we see that the transverse shear locking treatment is ideally suited by the ANS method. In the case the Poisson's ratio is different from zero, the ANS method gives less accuracy but always remains too much better than the standard displacement-based method (see Section 2.6.5, for example). The EAS method is also useful to shear locking removal but computational cost of the EAS method is more expensive than the ANS because the EAS method requires calculation of internal variables. The volumetric locking is effectively removed by the EAS method. The SRI is completely suitable for volumetric locking removal but this method cannot pass the patch test (see Appendix in the next page) so it is not taken into consider in the thesis. However the SRI elements are still used by many authors because of its simplicity.

There was a combination between methods of ANS with EAS proposed by Andelfinger and Ramm [AND93] for four-node degenerated-shell elements. In order to improve the element performance, Andelfinger and Ramm use the EAS method for the membrane and bending components, while the transverse shear component is formulated according to the ANS method. To alleviate the shear locking, the shear strains are referred to natural coordinates. Next, the combination of Andelfinger and Ramm was continually extended to geometrically nonlinear Reissner-Mindlin shell by Bischoff and Ramm [BIS97]. Authors in [BIS97] did apply the ANS method for avoiding curvature thickness locking by use of interpolation functions for transverse normal strains at nodal points instead of an evaluation at the integration quadrature points. Other example of EAS-ANS combination results in a simple shell model, built directly from basis of ANS shell model of Dvorkin and Bathe, where the EAS techniques are integrated for membrane locking, was introduced by Slavkovic et al. [SLA94], etc.

Other successful combination of the EAS concepts and ANS method is the generating of the solid-shell elements. The solid-shell concept was built on modifying assumptions of the standard shell theory (Reissner-Mindlin shell model). In fact, the solid-shell elements form a class of finite element models which are intermediate between thin shell and conventional solid elements. Detail for the solid-shell elements are presented in the chapter following.

APPENDIX of Chapter 2

Free-volumetric locking element - SRI element

If nearly incompressible material behavior is use, the elements suffer from volumetric locking. Using the SRI method is one of the best ways for eliminating volumetric locking [PON95]. By the way, use the SRI method with reduced integration for volumetric part and full integration for deviatoric part assures that all three normal strains satisfy the volumetric constraint $\varepsilon_{ii} = 0$.

Consider the SRI method, starting from the potential energy functional (2.5.18):

$$\pi_{(u)} = \int_{V_0} W_{S(E^{com})} dV + \pi_{ext} \tag{A.1}$$

The first variation of the functional is:

$$\int_{V_0} \delta \boldsymbol{E} : \boldsymbol{S} dV + \delta \pi_{ext} = 0 \tag{A.2}$$

We split the strain $\boldsymbol{E}$ and stress $\boldsymbol{S}$ of (A.2) additively into volumetric (dilatational) parts and deviatoric parts. The volumetric parts are:

$$\boldsymbol{E}_v = \frac{1}{3} E_{ii} \boldsymbol{I} \qquad i = 1\text{-}3 \tag{A.3}$$

$$\boldsymbol{S}_v = \frac{1}{3} S_{ii} \boldsymbol{I} \qquad i = 1\text{-}3 \tag{A.4}$$

And the deviatoric parts are:

$$\boldsymbol{E}_d = \boldsymbol{E} - \boldsymbol{E}_v \tag{A.5}$$

$$\boldsymbol{S}_d = \boldsymbol{S} - \boldsymbol{S}_v \tag{A.6}$$

Rewriting the expression (A.2) with tensors decoupled into volumetric and deviatoric parts, we have:

$$\int_{V_0} \delta \boldsymbol{E}_d : \boldsymbol{S}_d dV + \int_{V_0} \delta \boldsymbol{E}_v : \boldsymbol{S}_v dV + \int_{V_0} \delta \boldsymbol{E}_d : \boldsymbol{S}_v dV + \int_{V_0} \delta \boldsymbol{E}_v : \boldsymbol{S}_d dV + \delta \pi_{ext} = 0 \tag{A.7}$$

Assume that:

$$\int_{V_0} \delta \boldsymbol{E}_d : \boldsymbol{S}_v dV = \int_{V_0} \delta \boldsymbol{E}_v : \boldsymbol{S}_d dV = 0 \tag{A.8}$$

So the weak form (A.7) becomes:

$$\int_{V_0} \delta \boldsymbol{E}_d : \boldsymbol{S}_d dV + \int_{V_0} \delta \boldsymbol{E}_v : \boldsymbol{S}_v dV + \delta \pi_{ext} = 0 \tag{A.9}$$

The second integrand of the expression (A.9) is calculated by the reduced integration, but this is only applied for in-plane components, 1×1 integration instead of 2×2 while the integration in thickness direction remains unchanged. Restriction of the SRI method is that the applied material laws must allow a decoupling stress field and strain field into volumetric parts and deviatoric parts. It means the tangent moduli tensor ${}^4\boldsymbol{C}$ could be also split into a volumetric part and a deviatoric part as:

$$^4\boldsymbol{C} = {}^4\boldsymbol{C}_d + {}^4\boldsymbol{C}_v \tag{A.10}$$

As mentioned above, the SRI is the best method to remove volumetric locking. Its severe problem is cannot pass the patch test. In order to understand the problem, let's consider a cubic patch test.

The patch test for convergence is a fascinating area in the development of nonconforming finite element methods. It has been intuitionally proposed by Irons since the mid-1960s. By the early 1970s the test had became a powerful and practical tool for evaluating and checking nonconforming elements. We consider the following example: a unit cube modeled by seven elements - distorted mesh [MAC85]. Material parameters are: elastic modulus $E = 10^6$ and Poisson ratio $\nu = 0.25$.

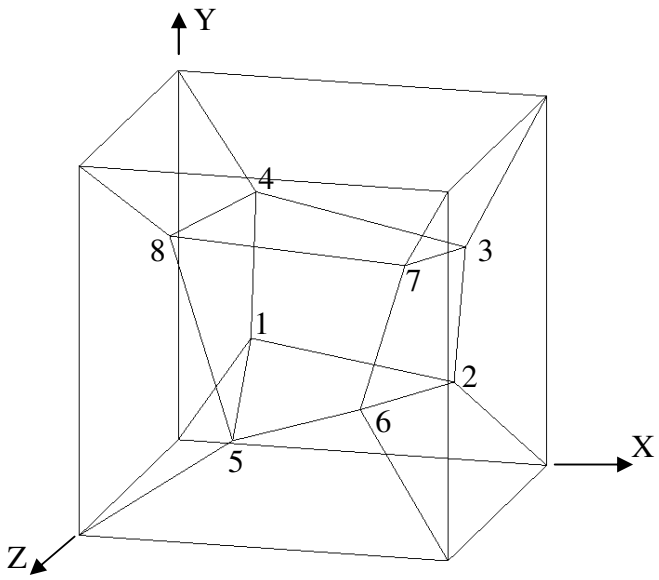

Figure A1. Cubic patch test

Table A1: Location of inner nodes

Nodes	Coordinates		
	X	Y	Z
1	0.249	0.342	0.192
2	0.826	0.288	0.288
3	0.850	0.649	0.263
4	0.273	0.750	0.230
5	0.320	0.186	0.643
6	0.677	0.305	0.683
7	0.788	0.693	0.644
8	0.165	0.745	0.702

The outer nodes subject to following conditions:

$$u = 10^{-3}(2X+Y+Z)/2$$
$$v = 10^{-3}(X+2Y+Z)/2 \tag{A.11}$$
$$w = 10^{-3}(X+Y+2Z)/2$$

These conditions assure a uniform strain in the cubic. Reference solution of the problem is analytically derived as:

$$\varepsilon_X = \varepsilon_Y = \varepsilon_Z = \gamma_{XY} = \gamma_{YZ} = \gamma_{ZX} = 10^{-3}$$

$$\sigma_X = \sigma_Y = \sigma_Z = 2000 \qquad \text{(A.12)}$$

$$\tau_{XY} = \tau_{YZ} = \tau_{ZX} = 400$$

The 3D element patch test is used to verify whether volume elements can exactly reproduce a constant strain state for any configuration. If this is the case, then the element will converge to the analytically exact solution (assuming that the materials are elastic and deformations are small), as the mesh is refined. Depending on the element type and problem, however, convergence may be too slow for practical purposes. The values of stress at the Gauss points obtained with the EAS9 are presented in Table A2.

Table A2: Results of EAS9

Element	$\sigma_X = \sigma_{X\ vol.} + \sigma_{X\ dev.}$		τ_{XY}	τ_{XZ}
	$\sigma_{X\ vol.}$	$\sigma_{X\ dev.}$		
1	1998.5	0.95E-5	399.5	399.5
2	1998.5	0.25E-5	399.5	399.5
3	1998.5	0.35E-4	399.5	399.5
4	1998.5	-0.11E-4	399.5	399.5
5	1998.5	-0.35E-4	399.5	399.5
6	1998.5	-0.68E-4	399.5	399.5
7	1998.5	0.23E-5	399.5	399.5
Ref.	2000		400	400

A quite similar trend is observed with different schemes of enhanced modes (EAS15, EAS21, etc). In contrast with the SRI elements where the hydrostatic stress $\sigma_{vol.}$ is spurious and hence these elements fail to pass the patch test, the EAS elements really pass the patch test, see Figure A2.

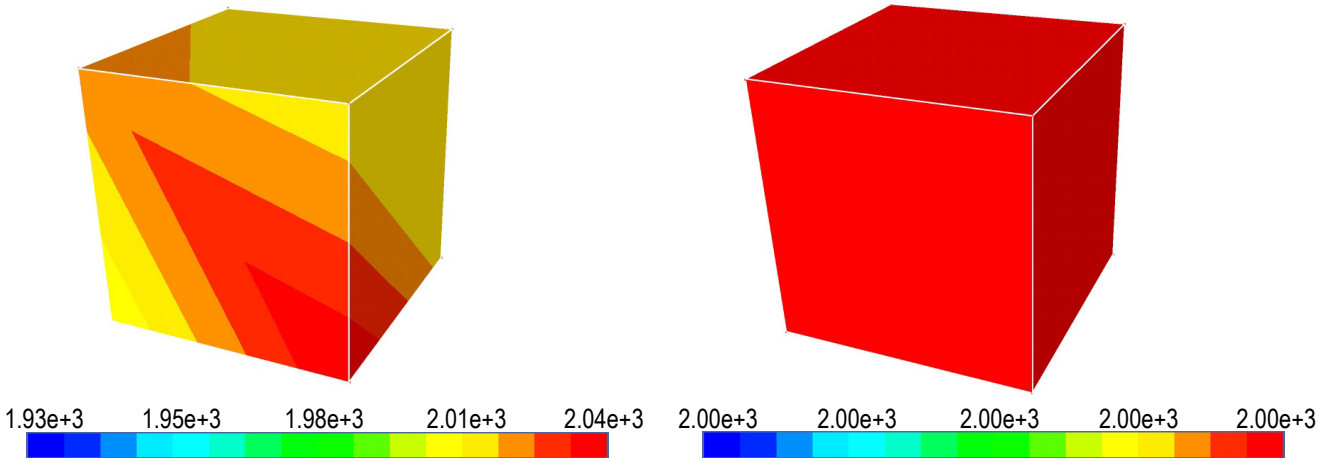

σ_z is spurious with SRI σ_z is smooth with EAS

Figure A2. Stress in patch elements (METAFOR [MET08])

As stated by McNeal and Harder [MAC85], if an element produces correct results for the patch test, the results of any problem solved with that element will converge

toward the correct solution as the elements are subdivided. Many authors supposed that an element that does not pass the patch test should not be trusted. On the other hand, passing the patch test does not guarantee satisfaction since the rate of convergence may be too slow for practical use. However, in the thesis the SRI element is not furthermore considered because employment of the SRI technique may be the cause makes the solid-shell elements cannot pass the bending patch test, see [CAR07] and [REE07].

Chapter 3. SOLID-SHELL ELEMENTS FOR FINITE DEFORMATION

INTRODUCTION

For the analysis of nonlinear mechanical behavior of structures, low-order elements are widely applied because of their efficiency and simple geometry. However, the standard pure displacement elements usually exhibit severe stiffening effects known as locking. Concretely, in thin-walled structures pure bending modes are spoiled by the parasitic shear strains, shear locking occurs. For nearly incompressible materials and incompressible conditions, volumetric locking occurs, when deviatoric modes come along undesirably with volumetric strains. In this work, we attempt to develop a low-order solid-shell element, which is free from all kinds of locking effects. Indeed, transverse shear locking and curvature thickness locking can be circumvented by using the ANS method, while membrane locking and volumetric locking can be removed by the EAS method.

The solid-shell elements are well applicable for geometrically nonlinear problems ([HAU98], [QUO03a,b]) or for both geometrically and materially (elastoplastic) nonlinear problems ([HAU00], [TAN05], [JET08]). In comparison with other shell elements, the solid-shell elements enable an easy connection with other continuum elements due to their solid topology, (Figure 1.0.1).

The solid-shell elements here refer to the finite element models which are applicable to shell analyses and possess no rotational DOF's. They are different from the degenerated shell elements in the sense that the latter elements are equipped with both translational and rotational DOF's. The solid-shell elements have the characteristics of solid elements where strains can be extended up to complete trilinear fields by internal parameters [AND93] or can be naturally assumed. There are several advantages of the solid-shell elements compared to the degenerated shell elements. First, the solid-shell elements are simpler in their kinematic and geometric descriptions. Second, no special effort is required for matching the translational and rotational DOF's when a structure consists of both solid and thin-walled regions. The laborious task of defining algebraic constraints or introducing solid-to-shell transition elements can be exempted. Third, the complication on handling finite rotational increments can be avoided. Nevertheless, formulating the robust solid-shell elements is indeed more demanding than formulating the degenerated shell elements. However, the latter elements are only plagued by shear and membrane locking effects while the former elements are also bothered by Poisson thickness and trapezoidal (curvature) locking effects, see Section 3.1.

Starting from the principle of shear locking removal by the available ANS method [DVO84] an ANS technique with an alternative scheme of sampling points, which can be employed for the solid-shell elements, is investigated. In fact, several ways can be employed for the interpolation of natural strains such as linear interpolations [DVO84], quadratic interpolations [HAU01], [PAR86]. In Section 3.3 an alternative bilinear interpolation is introduced.

Table 3.0.1: Dominant features of degenerated shell and solid-shell

Degenerated shell	Solid-shell
▪ The kinematic DOF are the components of the displacement vector and of the extensible director vector of the reference surface.	▪ The kinematic degrees of freedom are the components of the displacement vector.
▪ Locking effects (Poisson thickness locking), which occur if a 3D material law is used along with constant normal thickness strains, can be avoided.	▪ The stresses are evaluated from a 3D material law. This feature is especially useful for complicated nonlinear constitutive equations.

3.1 LOCKING PHENOMENA WITH SOLID-SHELL

The well-known locking phenomenon of displacement based finite elements for thin-walled beams, plates and shells is caused by unbalances of the trial functions. This unbalance, described in innumerable papers, can be cured by either reduction or enhancement of the DOF to strengthen the interpolations of variable fields.

With solid elements, there are essential locking effects as:

- Shear locking;
- Poisson thickness locking;
- Curvature thickness locking (Section 3.1.1);
- Volumetric locking.

Meanwhile, for shell elements, there are also some shell-typical locking phenomena to face with:

- Transverse shear locking;
- Membrane locking.

The solid-shell elements are solid elements where the shell like-behaviors are integrated so the elements can be coped with thin-walled problems. With the assumption of straight normal to the element mid-surface, the solid-shell formulation can take into account transverse shear effects.

If the solid-shell elements are applied for simulation of thick structures, the locking effects they meet are similar to locking effects happen with solid elements. On the contrary, being applied for thin and curve structure the solid-shell elements behave similarly to shell elements, so the anti-locking techniques for shell elements would be useful.

In general, methods to remedy locking effects may be classified as follows:

- Incompatible displacement models by Wilson et al. [WIL73] and Taylor et al. [TAY76], designed by the extension of the trial functions through additional incompatible modes.
- ANS elements by Hughes & Tezduyar [HUG81], Dvorkin and Bathe [DVO84].

- Assumed stress elements by Pian [PIA86], based on the Hellinger-Reissner functional to enrich the stress space.
- Reduced or selected reduced integration techniques, e.g. [DOL00], to clear the parasitic stresses by a modified numerical integration.
- EAS elements by Simo and Rifai [SIM90], Simo and Armero [SIM92] based on the Hu-Washizu functional and the extension of the strain tensor or the material deformation gradient by additional terms.

The solid-shell element would suffer transverse shear locking and membrane locking as the degenerated shell if we do not apply any one of the remedial methods as: ANS, EAS, RI or assumed stress method. On the other hand, the solid-shell elements would show volumetric locking as solid element if plasticity in either small or large displacement occurs. To overcome those, the solid-shell formulation has to adopt the above methods. In order to improve the element performance, it means remove locking effects, the EAS method could be used for the membrane and bending strains, while the transverse shear strain components are formulated according to the ANS method.

In Chapter 2 we did discuss about severe locking effects (volumetric locking, Poisson thickness locking and shear locking) that happen to the low-order solid and, of course, also happen to the solid-shell elements. Hereafter, under mechanical point of view (Section 2.1.1), other locking phenomena happen to the solid-shell elements are continuous discussed.

3.1.1 Curvature (trapezoidal) locking

A further locking effect observed for solid elements is the phenomenon of a so called curvature locking or sometimes "trapezoidal locking". The phenomenon is only found in structures where the out-of-plane element edges are not perpendicular to the mid-layer, which is the case for originally curved as well as for heavily deformed structures. However, curvature locking only occurs when the elements include thickness strains. It means continuum elements and some extensible-director degenerated shell elements suffer this locking. Other degenerated shell elements, whose thickness strains are equal to zero, do not suffer this locking. In brief, curvature locking happens when the two following factors are present in the same time:

1) When element models include normal strains in thickness direction and
2) The out-of-plane element edges are not perpendicular to the mid-layer, it will activate incompatible normal strains in thickness direction.

Trapezoidal locking is the least envisioned deficiency in the solid-shell element development. This ignorance is probably due to the fact that curvature locking does not occur in degenerated shell elements and flat plate geometry. Curvature locking was first put forward by McNeal [MAC87]. Let's consider a simple case of four node element, trapezoidal shape as Figure 3.1.1.

In the Cartesian coordinates, the element has the height H = 2; the average width W = H×Λ, where Λ is the element aspect ratio. The trapezoidal element relates to the isoparametric space by:

$$X = \Lambda\xi^1(1 - \alpha\xi^3) \;;\quad Z = \xi^3 \;;\quad \Lambda\alpha = tan(\delta) \tag{3.1.1}$$

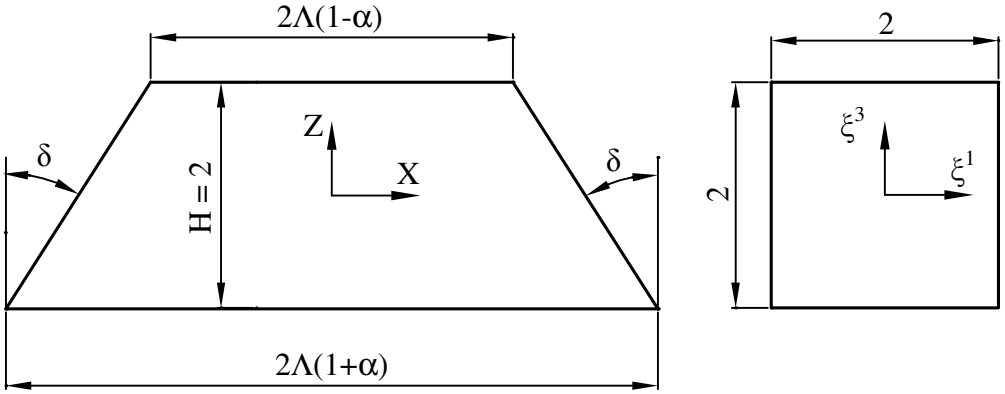

a) In Cartesian space b) In isoparametric space

Figure 3.1.1: Four node element

Consider the analytical displacements for in-plane bending, see (2.1.15). For the sake of simplicity we assume M/EI = 1; ν = 0 and we do not consider the constant term in vertical displacement. Finally, the solutions are:

$$u^{CM} = XZ$$
$$w^{CM} = -X^2/2 \qquad (3.1.2)$$

or in the form of isoparametric coordinates

$$u^{CM} = \Lambda[\xi^1\xi^3 - \alpha\xi^1(\xi^3)^2]$$
$$w^{CM} = -\Lambda^2[(\xi^1)^2 - 2\alpha(\xi^1)^2\xi^3 + (\alpha\xi^1\xi^3)^2]/2 \qquad (3.1.3)$$

The displacement within the element is calculated, see [MAC94], as:

$$u^a = \Lambda(\xi^1\xi^3 - \alpha\xi^1)$$
$$w^a = -\Lambda^2(1 - 2\alpha\xi^3 + \alpha^2)/2 \qquad (3.1.4)$$

The compatible strains in the element are:

$$\varepsilon_X^a = \frac{(\xi^3 - \alpha)}{(1 - \alpha\xi^3)}$$
$$\varepsilon_Z^a = \Lambda^2\alpha \qquad (3.1.5)$$
$$2\gamma_{XZ}^a = \Lambda\xi^1\left[1 + \frac{\alpha(\xi^3 - \alpha)}{(1 - \alpha\xi^3)}\right]$$

While the analytical strains are:

$$\varepsilon_X^{CM} = \xi^3$$
$$\varepsilon_Z^{CM} = 0 \qquad (3.1.6)$$
$$2\gamma_{XZ}^{CM} = 0$$

In the case of rectangular, $\alpha = 0$, the strain components ε_X and ε_Z are correct. In case $\alpha \neq 0$, the error in ε_X is small for α small. The error in shear term γ_{XZ} (causes transverse shear locking) can be eliminated by the ANS method when shear strain is interpolated by strains at sampling points in order to assure shear strains are equal to zero in pure bending, see Chapter 2. Here we can see that apart from the inconsistent terms (see Section 2.1.1.2) that cause transverse shear locking, the distorted mesh also causes a similar effect. This locking effect becomes severe, due to parasitic strain ε_Z^a, when the curvature of the structure is high with respect to the thickness, i.e. when $\tan(\delta) = \Lambda\alpha >>$

1. Curvature locking is a consequence of geometric irregular (distortion) on analysis accuracy.

Curvature locking shows up if 2D or 3D solid elements are used to model curved, thin-walled structures (the name “trapezoidal locking” reflects the fact that in these cases the individual elements have a trapezoidal shape). When shell elements are built on extensible director kinematics and are incorporated unmodified 3D constitutive models these elements will also show severe locking behavior in the case of curved-thin shell structures. We make conclusions that when multiple trapezoidal elements are used to model bending problems, the transverse bending stress/strain mode, which should physically vanish, is most detrimental to the element accuracy and leads to a deficiency. In other words, the element accuracy drops substantially if trapezoidal meshes are used. The oblique edges activate parasitic normal strains in thickness direction and may lead to locking. The effect happens only for curved structures, and is severe for thin solid and solid-shell elements. One method to resolve this problem is using a naturally assumed strain interpolation of the normal strain in thickness direction as proposed by Bischoff and Ramm [BIS97], Betsch and Stein [BET95]. The detail formulation is presented in Section 3.4 below.

3.1.2 Membrane locking

In order to understand membrane locking, it is necessary to distinguish “extensional bending” and “inextensional bending”. The term "inextensional bending" refers to a class of plate and shell problems in which the potential energy is dominated by flexural strains as opposed to extensional strains. It means the in-plane strains (ε_X, ε_Y and γ_{XY}) become vanishingly small when compared to the bending strains (ε_Z). In contrast, the term “extensional bending” is referred if the mid-surface experiences significant stretching or contraction; also called *combined bending-stretching* or *coupled membrane-bending*.

Membrane locking, also known as inextensional locking, does only occur in curved beam and shell elements when the curvature is large. It is sometimes confused with shear locking and volumetric locking because these affect the *membrane* part of shell elements. However, they are completely different phenomena.

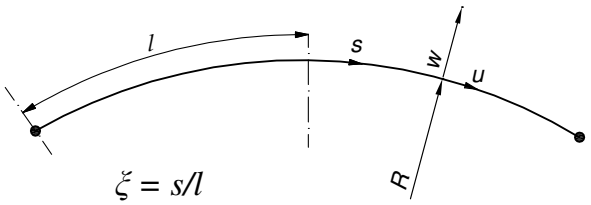

Figure 3.1.2: Curved beam element

For the sake of simplicity, in order to understand membrane locking easily, let’s consider a curved beam element of length *2l* and radius of curvature *R* based on classical thin beam theory, see Figure 3.1.2. The displacement degrees of freedom required are the circumferential displacement *u* and the radial displacement *w*. The coordinate *s* follows

the middle line of the curved beam. The membrane strain ε and the bending strain χ are described by the strain-displacement relations [PRA01]:

$$\varepsilon = u_{,s} + w/R$$
$$\chi = u_{,s}/R - w_{,ss} \tag{3.1.7}$$

Base on derivatives of (3.1.7), obviously, a C^0 description for u and a C^2 description for w are required. Kinematically admissible displacement interpolations for u and w are:

$$u = a_0 + a_1\xi$$
$$w = b_0 + b_1\xi + b_2\xi^2 + b_3\xi^3 \tag{3.1.8}$$

where a_0 to b_3 coefficients are the generalized DOF's which can be related to the nodal degrees of freedom U, W and $W_{,s}$ at the two nodes.

The strain field interpolations can be derived as

$$\varepsilon = (a_1/l + b_0/R) + (b_1/R)\xi + (b_2/R)\xi^2 - (b_3/R)\,\xi^3$$
$$\chi = (a_1/Rl - 2b_2/l^2) - (6b_3/l^2)\xi \tag{3.1.9}$$

When the above curved element is applied for simulating an inextensional bending problem the physical response requires that the membrane strain (ε) tends to vanish. It means:

$$a_1/l + b_0/R = 0 \tag{3.1.10a}$$
$$b_1/R = 0 \tag{3.1.10b}$$
$$b_2/R = 0 \tag{3.1.10c}$$
$$b_3/R = 0 \tag{3.1.10d}$$

We can observe that constraint (3.1.10a) has terms participating from both the u and w fields. It can therefore represent the condition ($\varepsilon \rightarrow 0$) in a physical way. However, the three remaining constraint (3.1.10b) to (3.1.10d) have no participation from the u field. Let's examine what these three constraints imply for the physical problem. From the three constraints we have the conditions ($b_1 \rightarrow 0$), ($b_2 \rightarrow 0$), ($b_3 \rightarrow 0$). Each of these the conditions in turn implies following conditions ($w_{,s} \rightarrow 0$), ($w_{,ss} \rightarrow 0$) and ($w_{,sss} \rightarrow 0$). These are the *spurious constraints* due to b_1, b_2 and b_3 must be different from zero, see (3.1.8). Consequently, the exist of b_1, b_2 and b_3 causes membrane locking. Apart from the EAS method, there are two ways are popularly applied for membrane locking removal. Use high-order approximations for in-plane displacements or use RI technique for in-plane strains [STO82]. The first method requires a dramatical reduction of time step for explicit time integration while the second method may cause spurious modes.

Membrane locking does not occur in flat elements, e.g. the four-node quadrilateral shell only manifests membrane locking in *wrapped configurations*. With the solid-shell elements, due to the coupling of the transverse normal strains with in-plane strains, when the mesh is distorted, membrane locking may occur. Particularly, it is severe with large aspect ratios of the elements. For the solid-shell element, this locking is overcomed effectively by using the EAS method, see [HAU01], with an enhancing matrix $\boldsymbol{M}$ as:

$$\boldsymbol{M}=\begin{bmatrix} \xi^1 & 0 & 0 & 0 \\ 0 & \xi^2 & 0 & 0 \\ 0 & 0 & 0 & 0 \\ 0 & 0 & \xi^1 & \xi^2 \\ 0 & 0 & 0 & 0 \\ 0 & 0 & 0 & 0 \end{bmatrix} \tag{3.1.11}$$

where only in-plane strains, which are equivalent to rows 1, 2 and 4 of the enhancing matrix $\boldsymbol{M}$ in (2.4.46), are enhanced.

In conclusion, membrane locking occurs if exist two conditions. First, the transverse strains and the in-plane strains interlock. Second, the interpolations are unable to model the inextensional behavior in inextensional bending problems. Consequently, a stiffening effect occurs when pure bending deformations are accompanied by parasitic membrane stresses.

In the following sections we will formulate a solid-shell element which incorporates an alternative ANS technique that is different from the classical ANS technique presented in Section 2.5. This element is free from all locking effects that have been mentioned.

3.2 KINEMATICS OF SOLID-SHELL

For the use of the ANS and the EAS methods to design the free-locking solid-shell elements the weak form is written in a local coordinate system, where the two axes X and Y are aligned with the element mid-surface and the third axis Z is aligned with the thickness direction. To ease for presentation, some kinematic definitions in Section 2.5.1 will be repeated in this section.

For the development of the low-order solid-shell element, we naturally adopt the assumption of Naghdi for shells: "*the normal to the element mid-surface remains straight but not necessarily normal during the deformation*". Also adopted by Timoshenko beam theory and the Mindlin-Reissner plate theory, this assumption is fulfilled by a linear approximation of the in-plane displacements over the shell thickness [HAU98]. In this context, the interpolation formulations for geometrical vectors can be read as

$$\boldsymbol{X}_{(\xi)}=\frac{1}{2}[(1+\xi^3)\boldsymbol{X}^h_{u(\xi^1,\xi^2)}-(1-\xi^3)\boldsymbol{X}^h_{l(\xi^1,\xi^2)}] \tag{3.2.1}$$

$$\boldsymbol{x}_{(\xi)}=\frac{1}{2}[(1+\xi^3)\boldsymbol{x}^h_{u(\xi^1,\xi^2)}-(1-\xi^3)\boldsymbol{x}^h_{l(\xi^1,\xi^2)}] \tag{3.2.2}$$

where: $\xi=\{\xi^1,\xi^2,\xi^3\}^T\in\square=[-1,1]\times[-1,1]\times[-1,1]$, tri-unit cube in R^3.

In the above formulas, $\boldsymbol{X}_{(\xi)}$ and $\boldsymbol{x}_{(\xi)}$ are the geometrical descriptions of the solid-shell element in the initial and current coordinate systems, respectively. The vectors $\boldsymbol{X}^h_{u(\xi^1,\xi^2)}$ and $\boldsymbol{X}^h_{l(\xi^1,\xi^2)}$ are the position vectors of nodes in upper and lower surfaces, respectively, of the element in the initial coordinate system. Similarly, the position

vectors of nodes in the current coordinate system are denoted by $\boldsymbol{x}^h_{u(\xi^1,\xi^2)}$ and $\boldsymbol{x}^h_{l(\xi^1,\xi^2)}$. Here the subscript "*l*" is the index for terms in lower surface and the subscript "*u*" is the index for terms in upper surface.

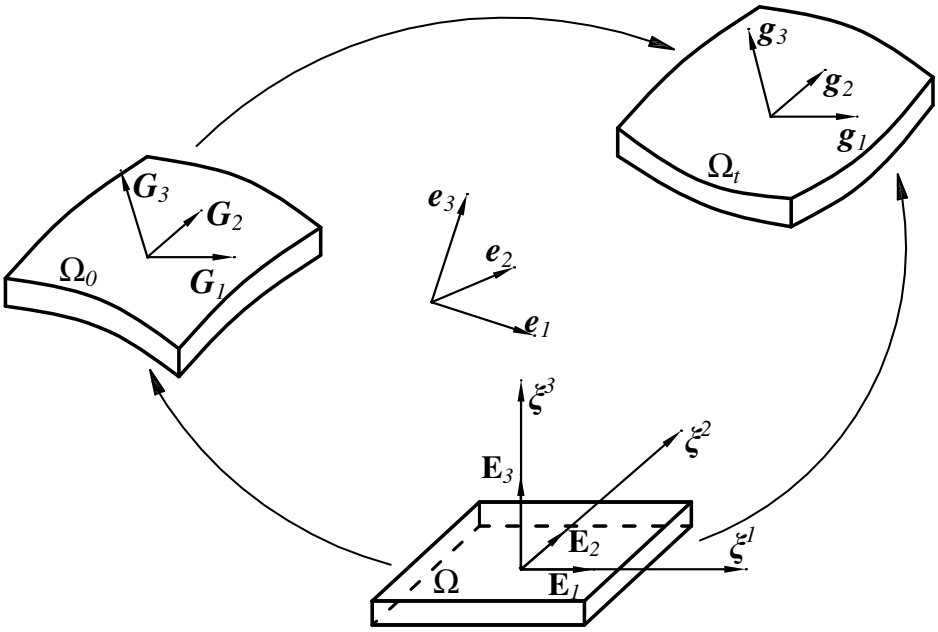

- $(\mathbf{E}_1,\mathbf{E}_2,\mathbf{E}_3)$: unit vectors of isoparametric system
- $(\boldsymbol{e}_1,\boldsymbol{e}_2,\boldsymbol{e}_3)$: unit vectors of global (physical) system

Figure 3.2.1: Initial configuration Ω_0, current configuration Ω_t and isoparametric configuration Ω

The displacement vector $\boldsymbol{u}$ is calculated as

$$\boldsymbol{u}_{(\xi)} = \boldsymbol{x}_{(\xi)} - \boldsymbol{X}_{(\xi)} \tag{3.2.3}$$

and the deformation gradient tensor $\boldsymbol{F}$ is defined by

$$\boldsymbol{F}_{(\xi)} = \frac{\partial \boldsymbol{x}_{(\xi)}}{\partial \boldsymbol{X}_{(\xi)}} \tag{3.2.4}$$

The Green-Lagrange strain tensor is defined as below

$$\underline{\boldsymbol{E}}_{(\xi)} = \frac{1}{2}(\boldsymbol{F}^T_{(\xi)}\boldsymbol{F}_{(\xi)} - \boldsymbol{I}) = \frac{1}{2}[(\frac{\partial \boldsymbol{x}_{(\xi)}}{\partial \boldsymbol{X}_{(\xi)}})^T \frac{\partial \boldsymbol{x}_{(\xi)}}{\partial \boldsymbol{X}_{(\xi)}} - \boldsymbol{I}] \tag{3.2.5}$$

Originally proposed by Dvorkin and Bathe for small strains [DVO84], the ANS method requires a modification of the shear components of the Green-Lagrange strain tensor $\underline{\boldsymbol{E}}$ when dealing with large deformation. Consequently, it is necessary to write the variational equation in the material configuration (or the total Lagrange formulation) in terms of the Green-Lagrange strain tensor $\underline{\boldsymbol{E}}$ and its conjugated second Piola-Kirchhoff stress tensor $\underline{\boldsymbol{S}}$.

Moreover, the ANS method requires the interpolation of all assumed terms in natural coordinate system. Therefore, it is necessary to define a convected description. Let's consider the position vectors $\boldsymbol{X}_{(\xi)}$ of the reference configuration Ω_0 and the

position vectors $\boldsymbol{x}_{(\xi)}$ of the current configuration Ω_t in the local coordinate system. As illustrated in Figure 3.2.1, the convected basis vector $\boldsymbol{G}_i$ and its components in the initial basis system are defined by:

$$\boldsymbol{G}_i = \partial \boldsymbol{X} / \partial \xi^i \quad ; \quad G_{ij} = \boldsymbol{G}_i \cdot \boldsymbol{G}_j \quad ; \quad i = 1-3 \tag{3.2.6}$$

while the contravariant vector $\boldsymbol{G}^j$ and its components G^{ji} are defined following:

$$\boldsymbol{G}_i \cdot \boldsymbol{G}^j = \delta_i^j \quad ; \; \boldsymbol{G}^j = G^{ji}\boldsymbol{G}_i = G_{ji}^{-1}\boldsymbol{G}_i \quad ; \; i,j = 1-3 \tag{3.2.7}$$

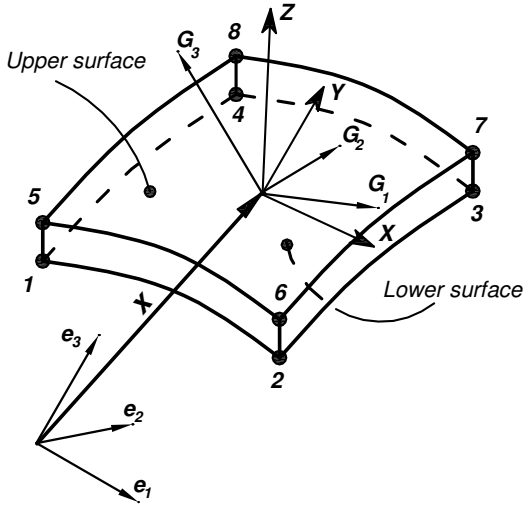

Figure 3.2.2: Configuration of low-order solid-shell element

Similarly, the convected basis vector $\boldsymbol{g}_i$ in the current basis system and its components g_{ij} are defined as:

$$\begin{aligned} &\boldsymbol{g}_i = \partial \boldsymbol{x} / \partial \xi^i = \boldsymbol{G}_i + \partial \boldsymbol{u} / \partial \xi^i \quad ; \qquad i = 1-3 \\ &g_{ij} = \boldsymbol{g}_i \cdot \boldsymbol{g}_j \end{aligned} \tag{3.2.8}$$

and its contravariant vector $\boldsymbol{g}^j$ and its components g^{ij} are defined through the following expressions

$$\boldsymbol{g}_i \cdot \boldsymbol{g}^j = \delta_i^j \quad ; \quad \boldsymbol{g}^i = g^{ij}\boldsymbol{g}_j = g_{ij}^{-1}\boldsymbol{g}_j \quad ; \quad i,j = 1-3 \tag{3.2.9}$$

Anticipating the transition to a shell element, one of the solid-element dimension is identified as the shell thickness direction. We call the element face (1,2,3,4) as the lower face, the element face (5,6,7,8) as the upper face, see Figure 3.2.2. All the edges 1-5, 2-6, 3-7 and 4-8, the ones that connect the lower node with the upper nodes, are thickness edges.

The deformation gradient in the form of the convected vectors becomes

$$\boldsymbol{F}_{(\xi)} = \frac{\partial \boldsymbol{x}_{(\xi)}}{\partial \boldsymbol{X}_{(\xi)}} = \boldsymbol{g}_i \otimes \boldsymbol{G}^i \tag{3.2.10}$$

while the Green-Lagrange strain tensor takes the following form

$$\underline{\boldsymbol{E}}_{(\xi)} = \frac{1}{2}(\boldsymbol{F}_{(\xi)}^{T}\boldsymbol{F}_{(\xi)} - \boldsymbol{I}) = \frac{1}{2}(g_{ij} - G_{ij})\boldsymbol{G}^{i} \otimes \boldsymbol{G}^{j} = \frac{1}{2}E_{ij}\boldsymbol{G}^{i} \otimes \boldsymbol{G}^{j} \tag{3.2.11}$$

or alternatively:

$$\underline{\boldsymbol{E}}_{(\xi)} = \frac{1}{2}\left(\boldsymbol{G}_{i} \cdot \frac{\partial \boldsymbol{u}}{\partial \xi^{j}} + \frac{\partial \boldsymbol{u}}{\partial \xi^{i}} \cdot \boldsymbol{G}_{j} + \frac{\partial \boldsymbol{u}}{\partial \xi^{i}} \cdot \frac{\partial \boldsymbol{u}}{\partial \xi^{j}}\right)\boldsymbol{G}^{i} \otimes \boldsymbol{G}^{j} \qquad i,j = 1-3 \tag{3.2.12}$$

3.3 AN ALTERNATIVE ANS TECHNIQUE FOR TRANSVERSE SHEAR LOCKING REMOVAL

The classical ANS technique presented in Chapter 2 has been widely adopted and thus applied for shell [DVO84] and solid-shell elements ([HAU98], [HAU00], [HAU01], [QUO03a]), i.e. 3D modeling. Its 2D counterpart can be obtained through a degeneration of the 3D version, and is applicable to a 2D solid-shell element (Figure 3.3.1). The 2D.ANS element has only a single sampling point (A ≡ C) for the assumed shear strain $\tilde{E}_{XZ}$ (2D case). Such a configuration can be also obtained through the application of a selective-reduced integration to the shear part of the element. Consequently, the assumed shear strain $\tilde{E}_{XZ}$ becomes, in the 2D version, constant over the element, while it is not the case for the 3D version.

We alternatively investigate another ANS technique, where the 3D and 2D versions always feature a linearly assumed shear strain (along the thickness direction). To this end, let's first start from the standard solid element to develop a new 3D ANS-solid element (designated by ANSn). Its 2D counterpart (designated by 2D.ANSn) can be immediately followed through a simple degeneration, see [NGU08].

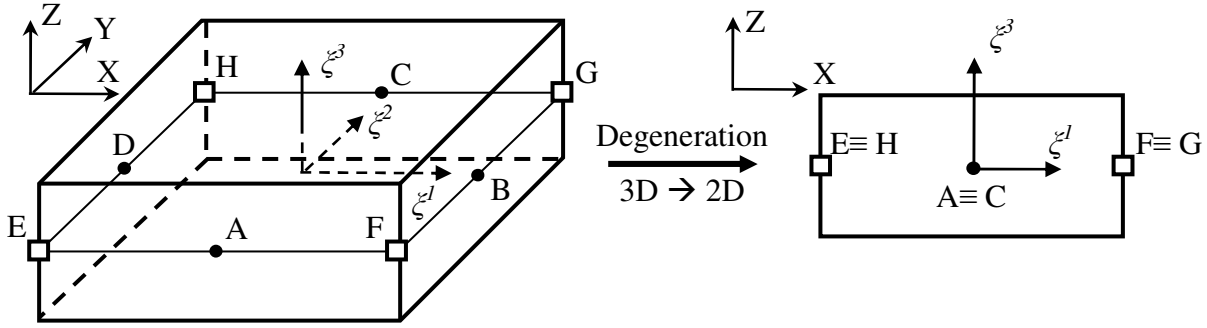

Figure 3.3.1: Degeneration from 3D to 2D of ANS-solid element

3.3.1 Cubic hexahedral ANS element (ANSn)

Consider a single solid element of tri-unit geometry (size 2×2×2), see Figure 3.3.2. For the sake of simplicity, the isoparametric space (ξ^1, ξ^2, ξ^3) and the physical space (X,Y,Z) are taken identical. Hence, it is possible to investigate the problem directly in the physical space. Recall the Green-Lagrange strain components in (2.1.2):

$$\boldsymbol{E}_{(u)}^{com}=\begin{Bmatrix}E_{XX}\\E_{YY}\\E_{ZZ}\\2E_{XY}\\2E_{ZX}\\2E_{YZ}\end{Bmatrix}=\begin{Bmatrix}u_{,X}\\v_{,Y}\\w_{,Z}\\u_{,Y}+v_{,X}\\u_{,Z}+w_{,X}\\v_{,Z}+w_{,Y}\end{Bmatrix}+\begin{Bmatrix}0.5(u_{,X}u_{,X}+v_{,X}v_{,X}+w_{,X}w_{,X})\\0.5(u_{,Y}u_{,Y}+v_{,Y}v_{,Y}+w_{,Y}w_{,Y})\\0.5(u_{,Z}u_{,Z}+v_{,Z}v_{,Z}+w_{,Z}w_{,Z})\\(u_{,X}u_{,Y}+v_{,X}v_{,Y}+w_{,X}w_{,Y})\\(u_{,X}u_{,Z}+v_{,X}v_{,Z}+w_{,X}w_{,Z})\\(u_{,Y}u_{,Z}+v_{,Y}v_{,Z}+w_{,Y}w_{,Z})\end{Bmatrix} \tag{3.3.1}$$

The displacement derivatives of displacement in 0X direction are defined as follows

$$\begin{Bmatrix}u_{,X}\\u_{,Y}\\u_{,Z}\end{Bmatrix}=\begin{Bmatrix}\sum_{I=1}^{8}\frac{\partial N_I}{\partial X}U_I\\\sum_{I=1}^{8}\frac{\partial N_I}{\partial Y}U_I\\\sum_{I=1}^{8}\frac{\partial N_I}{\partial Z}U_I\end{Bmatrix}=\begin{Bmatrix}\sum_{I=1}^{8}\frac{\partial N_I}{\partial \xi^1}U_I\\\sum_{I=1}^{8}\frac{\partial N_I}{\partial \xi^2}U_I\\\sum_{I=1}^{8}\frac{\partial N_I}{\partial \xi^3}U_I\end{Bmatrix} \tag{3.3.2}$$

If the element is subjected to a pure bending in 0X direction, Figure 3.3.3, and assuming that the Poisson ratio is equal to zero, the following relations are hold:

$$\left.\begin{aligned}&\Delta U=-U_1=U_2=\ U_3=-U_4\\&\Delta U=\ U_5=-U_6=-U_7=\ U_8\\&V_I=W_I=0;\quad \mathrm{I}=1-8\end{aligned}\right\} \tag{3.3.3}$$

and then

$$\left.\begin{aligned}&v_{,X}=v_{,Y}=v_{,Z}=0\\&w_{,X}=w_{,Y}=w_{,Z}=0\end{aligned}\right\} \tag{3.3.4}$$

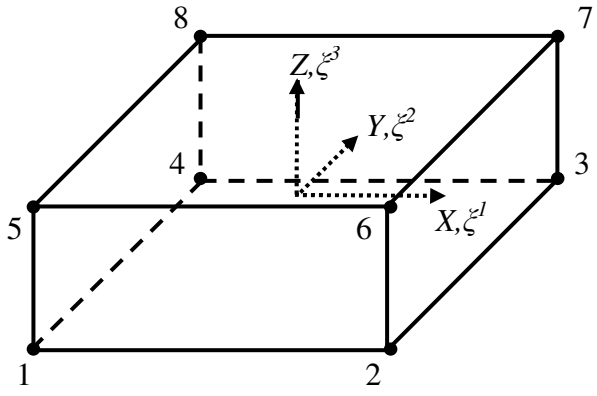

Nodal coordinates:

1(-1,-1,-1)	*5(-1,-1,1)*
2(1,-1,-1)	*6(1,-1,1)*
3(1,1,-1)	*7(1,1,1)*
4(-1,1,-1)	*8(-1,1,1)*

Figure 3.3.2: Solid element, special case (X,Y,Z) ≡ (ξ^1, ξ^2, ξ^3)

Let's investigate the compatible shear strain E_{XZ}, which can be directly derived from (3.3.1) - (3.3.4):

$$2E_{XZ}=u_{,Z}+u_{,X}\,u_{,Z}=(1+u_{,X})u_{,Z} \tag{3.3.5}$$

where the second term represents the nonlinear geometrical quantities. Notice that:

$$u_{,Z} = \sum_{I=1}^{8} \frac{\partial N_I}{\partial Z} U_I = \sum_{I=1}^{8} \frac{\partial N_I}{\partial \xi^3} U_I = -\frac{1}{2}\left(U_2 + U_5\right)\xi^1 \tag{3.3.6}$$

$$u_{,X} = \frac{1}{2}[U_2 + U_6 - (U_2 - U_6)\,\xi^3] \tag{3.3.7}$$

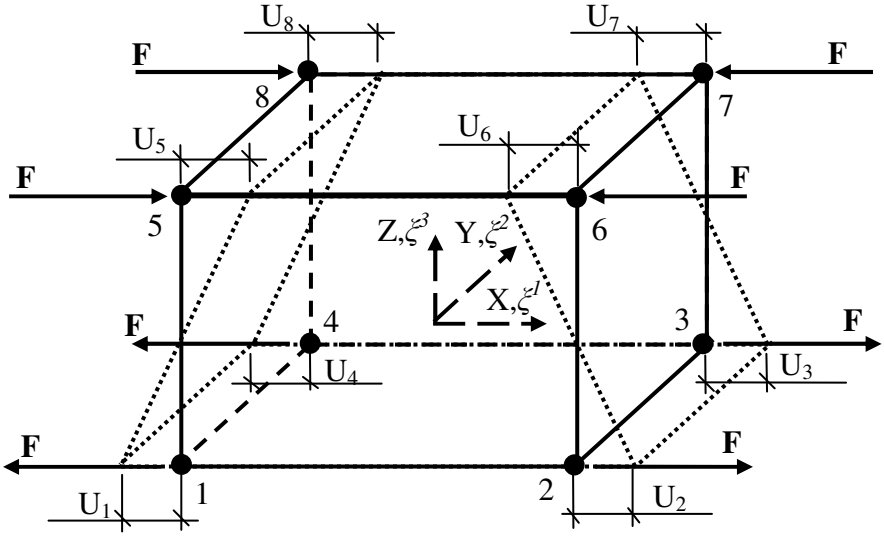

Figure 3.3.3: Pure bending in 0X direction

Thus, the standard element clearly presents a strain E_{XZ}, which is a bilinear function in both ξ^1 and ξ^3, while this strain component must be physically zero in the pure bending case. In other words, E_{XZ} contributes to the so-called parasitic transverse shear strain in pure bending problems. In order to remove this shear locking, we observe that this parasitic shear strain is only equal to zero at $\xi^1 = 0$, see (3.3.5) and (3.3.6) or line ∂u/∂Z in Figure 3.3.4. This motivates the use of sampling points, which are employed later for the interpolation of assumed strains, on the vertical plane including the point $\xi^1 = 0$ and the axis $O\xi^2$. Indeed, the shear strain E_{XZ} is equal to zero at the points A_l, A_u, C_l and C_u (Figure 3.3.4) under the pure bending condition. As a result, the physical strain $\tilde{E}_{XZ}$ is assumed to take the following form:

$$\tilde{E}_{XZ} = \frac{1}{2}(1-\xi^2)\tilde{E}_{XZ}^{A} + \frac{1}{2}(1+\xi^2)\tilde{E}_{XZ}^{C} \tag{3.3.8}$$

where $\tilde{E}_{XZ}^{A}$ and $\tilde{E}_{XZ}^{C}$ are derived through the strains at sampling points on the face (A_l, A_u, C_u, C_l) on Figure 3.3.4:

$$\begin{aligned} \tilde{E}_{XZ}^{A} &= \frac{1}{2}(1-\xi^3)E_{XZ}^{A_l} + \frac{1}{2}(1+\xi^3)E_{XZ}^{A_u} \\ \tilde{E}_{XZ}^{C} &= \frac{1}{2}(1-\xi^3)E_{XZ}^{C_l} + \frac{1}{2}(1+\xi^3)E_{XZ}^{C_u} \end{aligned} \tag{3.3.9}$$

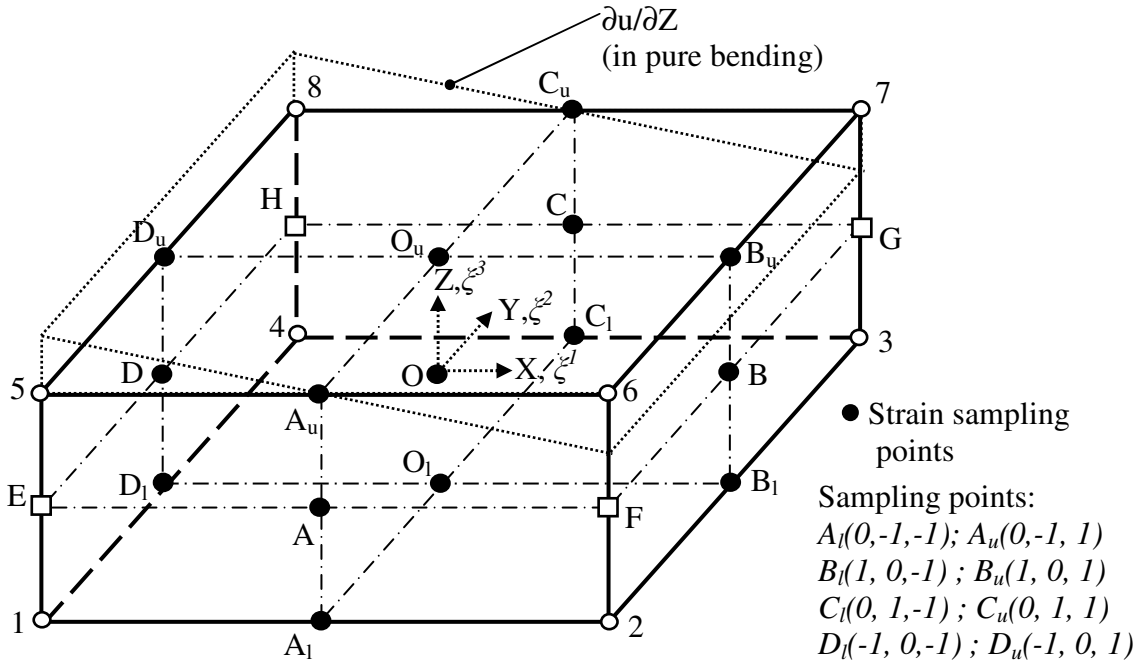

Figure 3.3.4: Sampling points for ANSn element

Similarly, the assumed shear strain $\tilde{E}_{YZ}$ is interpolated as

$$\tilde{E}_{YZ} = \frac{1}{2}(1-\xi^1)\tilde{E}^D_{YZ} + \frac{1}{2}(1+\xi^1)\tilde{E}^B_{YZ} \tag{3.3.10}$$

where $\tilde{E}^D_{YZ}$ and $\tilde{E}^B_{YZ}$ are assumed by using sampling points on the face (D_l, D_u, B_u, B_l), Figure 3.3.4, as

$$\begin{aligned}\tilde{E}^D_{YZ} &= \frac{1}{2}(1-\xi^3)E^{D_l}_{YZ} + \frac{1}{2}(1+\xi^3)E^{D_u}_{YZ}\\ \tilde{E}^B_{YZ} &= \frac{1}{2}(1-\xi^3)E^{B_l}_{YZ} + \frac{1}{2}(1+\xi^3)E^{B_u}_{YZ}\end{aligned} \tag{3.3.11}$$

Interpolation of the transverse shear strains as (3.3.8) and (3.3.10) make sure of preserving the bilinear variation of the assumed strains as the derived-displacement shear strains.

The 2D version (Figure 3.3.5) of the ANSn element can be deduced in a straightforward manner. Indeed, under pure bending in 0X direction, the bending mode is activated so that ∂w/∂X = ∂w/∂Z = 0. Hence, the compatible transverse shear strain becomes:

$$2E_{12} = 2E_{XZ} = \frac{\partial u}{\partial Z} + \frac{\partial u}{\partial Z}\frac{\partial u}{\partial X} = -\frac{1}{2}(U_2+U_4)\xi^1[1+\frac{1}{2}(U_2-U_3)(1+\xi^3)] \tag{3.3.12}$$

Since this shear strain is equal to zero at $\xi^1 = 0$, we can employ sampling points on the vertical line through the point $\xi^1 = 0$. For example, with the use of two sampling points $\mathrm{A}(\xi^1 = 0, \xi^3 = -1)$ and $\mathrm{B}(\xi^1 = 0, \xi^3 = 1)$, and the corresponding assumed shape functions are:

$$N_A^{\xi} = \frac{1}{2}(1-\xi^3); \quad N_B^{\xi} = \frac{1}{2}(1+\xi^3) \tag{3.3.13}$$

The assumed shear strain $\tilde{E}_{xz}$ can be linearly interpolated through two points A and B:

$$\tilde{E}_{XZ} = N_A^{\xi} E_{XZ}^A + N_B^{\xi} E_{XZ}^B \tag{3.3.14}$$

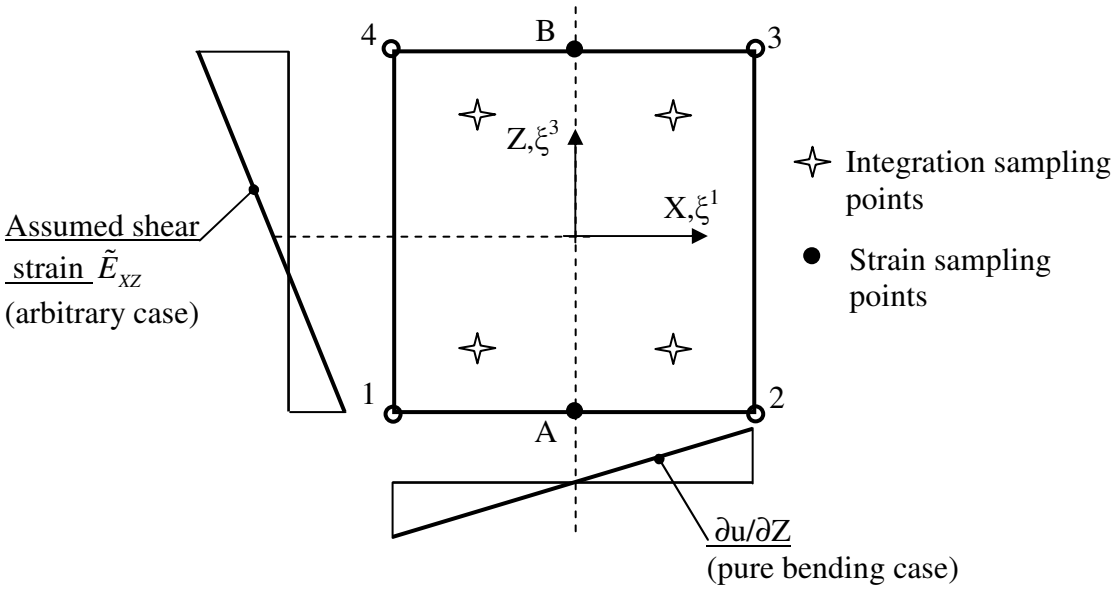

Figure 3.3.5: Sampling points for 2D.ANSn element

In the case of 3D elements, being applied for the pure bending in 0X direction, the above ANS technique for the shear locking removal can be also employed for the pure bending in 0Z direction. We however note that the bending in 0Z direction is not considered in the conventional shell elements.

In the general case, where the element geometry is not regular, the shear term needs to be evaluated in the natural space. The assumed strains are then transformed to the physical space for the computation of the stiffness matrices. All of these problems are addressed below.

3.3.2 Distorted hexahedral ANSn element

As a requirement, the order of the assumed strain field should be equal to the one of the derivation of the displacement field so that the assumed strains may consistently capture the strain field resulting from the derivation of the displacement in non-pure bending modes. Notice that only the transverse shear strains (E_{13} and E_{23}) are considered for shear locking removal by the ANS technique.

Consider the Green-Lagrange strain values, which can be derived from (3.2.11) and (3.2.12) as:

$$E_{ij} = g_{ij} - G_{ij} = \boldsymbol{G}_i \cdot \frac{\partial \boldsymbol{u}}{\partial \xi^j} + \frac{\partial \boldsymbol{u}}{\partial \xi^i} \cdot \boldsymbol{G}_j + \frac{\partial \boldsymbol{u}}{\partial \xi^i} \cdot \frac{\partial \boldsymbol{u}}{\partial \xi^j} \tag{3.3.15}$$

In order to determine the order of the function E_{ij} with respect to the natural variables ξ^i, we investigate the constituents of the strains in (3.3.15). The vector $\boldsymbol{G}_i$ is a bilinear function of the natural coordinates as follows:

$$\boldsymbol{G}_i = \left\{ \frac{\partial X}{\partial \xi^i} \quad \frac{\partial Y}{\partial \xi^i} \quad \frac{\partial Z}{\partial \xi^i} \right\}^T = \sum_{k=1}^{8} \frac{\partial N_K}{\partial \xi^i} \{ X_k \quad Y_k \quad Z_k \}^T \tag{3.3.16}$$

where $\{X_k, Y_k, Z_k\}^{\mathrm{T}}$ are reference nodal coordinate vector. The derivatives of the displacement vector with respect to the natural coordinate ξ^i is

$$\frac{\partial \boldsymbol{u}}{\partial \xi^i} = \left\{ \frac{\partial u}{\partial \xi^i} \quad \frac{\partial v}{\partial \xi^i} \quad \frac{\partial w}{\partial \xi^i} \right\}^T = \sum_{k=1}^{8} \frac{\partial N_k}{\partial \xi^i} \{ U_k \quad V_k \quad W_k \}^T \tag{3.3.17}$$

Based on (3.3.15) - (3.3.17) we can examine the order of the natural constituents in the shear strain function E_{13} as

$$E_{13} = \boldsymbol{G}_1 \cdot \frac{\partial \boldsymbol{u}}{\partial \xi^3} + \frac{\partial \boldsymbol{u}}{\partial \xi^1} \cdot \boldsymbol{G}_3 + \frac{\partial \boldsymbol{u}}{\partial \xi^1} \cdot \frac{\partial \boldsymbol{u}}{\partial \xi^3} \tag{3.3.18}$$

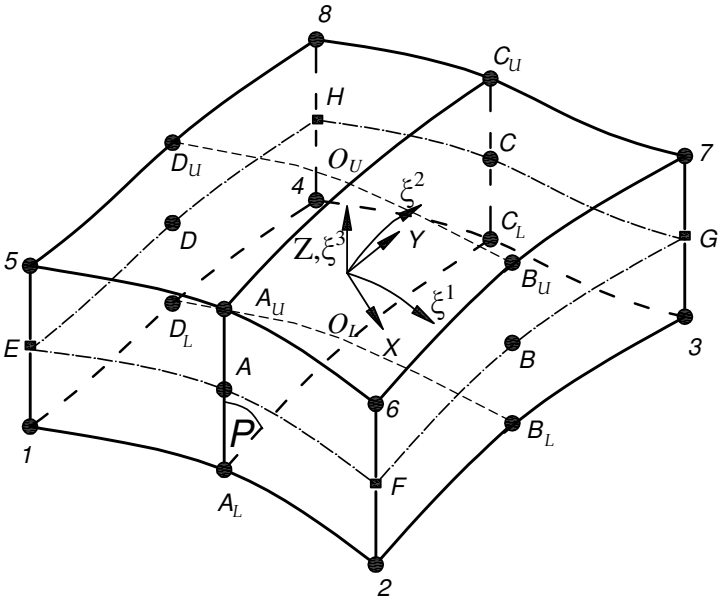

Figure 3.3.6: Distorted element - sampling points for strains

Vectors $\boldsymbol{G}_1$ and $\partial \boldsymbol{u}/\partial \xi^1$ are derivatives of the shape functions with respect to ξ^1, hence, $\boldsymbol{G}_1$ and $\partial \boldsymbol{u}/\partial \xi^1$ are functions of $(\xi^2, \xi^3, \xi^2\xi^3)$; similarly, vectors $\boldsymbol{G}_3$ and $\partial \boldsymbol{u}/\partial \xi^3$ are functions of $(\xi^1, \xi^2, \xi^1\xi^2)$. Consequently, E_{13} is a function of the natural coordinates of the type:

$$E_{13} = f[\xi^1, \xi^2, \xi^3, \xi^1\xi^2, (\xi^2)^2, \xi^1\xi^3, \xi^2\xi^3, \xi^1\xi^2\xi^3, (\xi^2)^2\xi^3, \xi^1(\xi^2)^2, \xi^1(\xi^2)^2\xi^3] \tag{3.3.19}$$

Clearly, (3.3.19) shows that E_{13} is a linear function of ξ^1. In order to remove shear locking the naturally transverse assumed shear strain E_{13} is interpolated on the face that goes through $\xi^1 = 0$ and contains the axis $\mathrm{O}\xi^2$, see plane (P) in Figure 3.3.6. On that natural face the shear strain is quadratic with respect to ξ^2 but linear with respect to ξ^3

as $E_{13} = f[\xi^2, \xi^3, (\xi^2)^2, \xi^2\xi^3, (\xi^2)^2\xi^3]$. Hence, the naturally assumed shear strain $\tilde{E}_{13}$ can be assumed to be a function whose order of natural variables is equal to or lower than the order of natural variables in the derived-displacement strain (3.3.19). It can be:

- Constant in thickness direction $O\xi^3$ and linear in horizontal direction $O\xi^2$. This is the classical ANS method [DVO84]. Hauptmann and Schweizerhof [HAU98], Klinkel et al. [KLI06], Vu-Quoc and Tan [QUO03a] use this interpolation in their solid-shell elements. This interpolation requires only two sampling points A and C, see (2.5.8) and Figure 3.3.6.
- Linear in both thickness direction $O\xi^3$ and horizontal direction $O\xi^2$. This interpolation requires two sampling points along both $O\xi^3$ and $O\xi^2$ (A_l, A_u and C_l, C_u), Figure 3.3.6. Similarly to (3.3.8), the natural assumed strain $\tilde{E}_{13}$ is interpolated as

$$\tilde{E}_{13} = \frac{1}{2}(1-\xi^2)\tilde{E}_{13}^A + \frac{1}{2}(1+\xi^2)\tilde{E}_{13}^C \tag{3.3.20}$$

  where $\tilde{E}_{13}^A$ and $\tilde{E}_{13}^C$ are evaluated by using sampling points on the face that goes through (A_l, A_u, C_l, C_u):

$$\begin{aligned} \tilde{E}_{13}^A &= \frac{1}{2}(1-\xi^3)E_{13}^{A_l} + \frac{1}{2}(1+\xi^3)E_{13}^{A_u} \\ \tilde{E}_{13}^C &= \frac{1}{2}(1-\xi^3)E_{13}^{C_l} + \frac{1}{2}(1+\xi^3)E_{13}^{C_u} \end{aligned} \tag{3.3.21}$$

- Linear in thickness direction $O\xi^3$ and quadratic in $O\xi^2$ direction. This interpolation requires two sampling points along $O\xi^3$ (A_l, A_u and C_l, C_u) and three sampling points along $O\xi^2$ (A_l, O_l, C_l and A_u, O_u, C_u), Figure 3.3.6. This assumed interpolation is the closest to the consistent displacement-derived strain E_{13}. Our numerical tests show that this quadratic interpolation for assumed strains in $O\xi^2$ axis significantly increases computational time with respect to the corresponding linear interpolation while the improvement is not remarkable.

In the thesis, the second option is chosen to be investigated. Similar to E_{13} (3.3.19), the shear strain E_{23} is a function of the natural coordinates as shown below

$$E_{23} = f[\xi^1, \xi^2, \xi^3, (\xi^1)^2, \xi^1\xi^2, \xi^1\xi^3, \xi^2\xi^3, (\xi^1)^2\xi^2, (\xi^1)^2\xi^3, \xi^1\xi^2\xi^3, (\xi^1)^2\xi^2\xi^3] \tag{3.3.22}$$

In order to overcome that shear locking occurs with the pure bending in 0Y direction, we consider E_{23} at $\xi^2 = 0$. At that coordinate the shear strain E_{23} is quadratic with respect to ξ^1 as $E_{23} = f[\xi^1, \xi^3, (\xi^1)^2, \xi^1\xi^3, (\xi^1)^2\xi^3]$ but E_{23} is linear with respect to ξ^3. Similar to (3.3.20), the natural assumed strain $\tilde{E}_{23}$, if linearly interpolated in both thickness direction $O\xi^3$ and horizontal direction $O\xi^1$, is expressed as

$$\tilde{E}_{23} = \frac{1}{2}(1-\xi^1)\tilde{E}_{23}^D + \frac{1}{2}(1+\xi^1)\tilde{E}_{23}^B \tag{3.3.23}$$

where $\tilde{E}_{23}^{D}$ and $\tilde{E}_{23}^{B}$ are linear functions of ξ^3 with sampling points on faces parallel axis $O\xi^2$ and go through a pair of points (D_l, D_u) and (B_l, B_u), respectively:

$$\tilde{E}_{23}^{D} = \frac{1}{2}(1-\xi^3)E_{23}^{D_l} + \frac{1}{2}(1+\xi^3)E_{23}^{D_u}$$
$$\tilde{E}_{23}^{B} = \frac{1}{2}(1-\xi^3)E_{23}^{B_l} + \frac{1}{2}(1+\xi^3)E_{23}^{B_u} \tag{3.3.24}$$

In order to alleviate shear locking, the natural shear strains E_{13} and E_{23} are replaced by the assumed natural shear strains $\tilde{E}_{13}$ and $\tilde{E}_{23}$ before doing the transformation from the natural space to the physical space. Finally, the physical assumed strain vector by the alternative ANS technique is:

$$\tilde{\boldsymbol{E}}^{ANS} = \boldsymbol{T}^{-T}\begin{Bmatrix} E_{11} \\ E_{22} \\ E_{33} \\ 2E_{12} \\ 2\tilde{E}_{13} \\ 2\tilde{E}_{23} \end{Bmatrix} = \boldsymbol{T}^{-T}\begin{Bmatrix} 0.5(g_{11}^e - G_{11}^e) \\ 0.5(g_{22}^e - G_{22}^e) \\ 0.5(g_{33}^e - G_{33}^e) \\ (g_{12}^e - G_{12}^e) \\ \frac{1}{2}\{(1-\xi^2)[(1-\xi^3)(g_{13}^e - G_{13}^e)_{(A_L)} + (1+\xi^3)(g_{13}^e - G_{13}^e)_{(A_U)}] + \\ \quad (1+\xi^2)[(1-\xi^3)(g_{13}^e - G_{13}^e)_{(C_L)} + (1+\xi^3)(g_{13}^e - G_{13}^e)_{(C_U)}]\} \\ \frac{1}{2}\{(1-\xi^1)[(1-\xi^3)(g_{23}^e - G_{23}^e)_{(D_L)} + (1+\xi^3)(g_{23}^e - G_{23}^e)_{(D_U)}] + \\ \quad (1+\xi^1)[(1-\xi^3)(g_{23}^e - G_{23}^e)_{(B_L)} + (1+\xi^3)(g_{23}^e - G_{23}^e)_{(B_U)}]\} \end{Bmatrix} \tag{3.3.25}$$

These assumed strains can be implemented in the standard solid element in a straightforward manner. The physical assumed strain-displacement matrix at node I (I = 1-8) of the solid-shell element is similarly assumed:

$$\tilde{\boldsymbol{B}}_I^{ANS} = \boldsymbol{T}^{-T}\begin{bmatrix} N_{I,1}\boldsymbol{g}_1^T \\ N_{I,2}\boldsymbol{g}_2^T \\ N_{I,3}\boldsymbol{g}_3^T \\ N_{I,1}\boldsymbol{g}_2^T + N_{I,2}\boldsymbol{g}_1^T \\ \frac{1}{2}\{(1-\xi^2)[(1-\xi^3)(N_{I,1}\boldsymbol{g}_3^T + N_{I,3}\boldsymbol{g}_1^T)_{(A_L)} + (1+\xi^3)(N_{I,1}\boldsymbol{g}_3^T + N_{I,3}\boldsymbol{g}_1^T)_{(A_U)}] + \\ + (1+\xi^2)[(1-\xi^3)(N_{I,1}\boldsymbol{g}_3^T + N_{I,3}\boldsymbol{g}_1^T)_{(C_L)} + (1+\xi^3)(N_{I,1}\boldsymbol{g}_3^T + N_{I,3}\boldsymbol{g}_1^T)_{(C_U)}]\} \\ \frac{1}{2}\{(1-\xi^1)[(1-\xi^3)(N_{I,2}\boldsymbol{g}_3^T + N_{I,3}\boldsymbol{g}_2^T)_{(D_L)} + (1+\xi^3)(N_{I,2}\boldsymbol{g}_3^T + N_{I,3}\boldsymbol{g}_2^T)_{(D_U)}] + \\ (1+\xi^1)[(1-\xi^3)(N_{I,2}\boldsymbol{g}_3^T + N_{I,3}\boldsymbol{g}_2^T)_{(B_L)} + (1+\xi^3)(N_{I,2}\boldsymbol{g}_3^T + N_{I,3}\boldsymbol{g}_2^T)_{(B_U)}]\} \end{bmatrix} \tag{3.3.26}$$

We can see that the ANS technique with alternative sampling points (the bilinear assumed strains (3.3.25) and the classical ANS technique (2.5.12) have some common and uncommon features:

- For both techniques, the strain sampling points are taken at coordinate $\xi^1 = 0$ for E_{13} and $\xi^2 = 0$ for E_{23}.
- For the alternative ANS technique the assumed strains are linear in the thickness direction. Meanwhile for the classical ANS technique the assumed strains are constant in the thickness direction. When strain is not too large, the two techniques are similar because the strain at the mid-surface (the classical ANS) will be the average value of the strains at the lower and the upper surfaces (the alternative ANS presented here).
- As being employed in the degenerated shell elements [AHM70], the classical ANS technique uses sampling points on the mid-surface, which is usually considered to be the reference plane. Contrarily, the alternative ANS technique employs sampling points located on the physical, upper and lower surfaces, but not on the reference plane of the solid element.

For distorted 2D.ANSn element, the shear strain is similarly assumed as (3.3.14), Figure 3.3.5,

$$\tilde{E}_{12} = \frac{1}{2}(1-\xi^2)E_{12}^A + \frac{1}{2}(1+\xi^2)E_{12}^B \tag{3.3.27}$$

These assumed strains are then transformed to the physical space by the transform matrix $\boldsymbol{T}$ in (2.4.43).

The 3D eight-node solid element which directly employs assumed strains as (3.3.25) is hereinafter referred as ANSn. The element can be applied for distorted mesh model. It is a 3D solid element which is free from shear locking for thin and moderate thick-wall structures, see Section 3.6 below for numerical illustration.

3.4 COMBINED ANS-EAS SOLID-SHELL ELEMENT

The solid-shell element presented in this chapter possesses the performances of the ANS elements in alleviating transversal shear locking and curvature locking. Further more, to be free from volumetric locking, Poisson thickness locking (see [HAU98], [HAU00]) and membrane locking the EAS method needs to be adopted. The solid-shell elements which only employ the ANS techniques [FEL03] should not be applied for incompressible deformation problems because they exhibit poor performance for volumetric locking removal, see [BIS97].

In the above paragraphs, curvature locking was mentioned. In order to circumvent curvature locking several authors, e.g. Bischoff and Ramm [BIS97] and Betsch and Stein [BET95], suggested employing an assumed strain approximation for the strain component E_{33}. Corner nodes on the mid-surface play the role of the sampling points (points E, F, G and H, Figure 3.3.6). The C^0-continuous strain field is thus given by:

$$\tilde{E}_{33} = \sum_I N_{I(\xi^1,\xi^2)} E_{33(\xi_I)} \qquad ;\ \mathrm{I} = \mathrm{E, F, G, H} \tag{3.4.1}$$

where $N_{I(\xi^1,\xi^2)}$ are the shape functions in mid-surface, $\xi^3 = 0$, as:

$$N_{I(\xi^1,\xi^2)} = \frac{1}{4}\left(1+\xi_I^1\xi^1\right)\left(1+\xi_I^2\xi^2\right) \tag{3.4.2}$$

Hauptmann et al. [HAU00] did show that, this kind of locking is minor compared to other types, a bilinear interpolation of the transverse normal strain as (3.4.1) is enough for subduing this locking. One simple way to overcome curvature locking is using fine mesh on thickness direction.

Introducing the assumed natural strain $\tilde{E}_{33}$ (3.4.1) into the assumed strain vector $\tilde{\boldsymbol{E}}^{ANS}$ (2.5.12) or (3.3.25) we receive the strain field of an element that is free from both transversal shear locking and curvature locking. The classical ANS element that is free from transverse shear locking and curvature locking is given by:

$$\tilde{\boldsymbol{E}}^{ANS} = \boldsymbol{T}^{-T}\begin{Bmatrix} E_{11} \\ E_{22} \\ \tilde{E}_{33} \\ 2E_{12} \\ 2\tilde{E}_{13} \\ 2\tilde{E}_{23} \end{Bmatrix} = \boldsymbol{T}^{-T}\begin{Bmatrix} 0.5(g_{11}^e - G_{11}^e) \\ 0.5(g_{22}^e - G_{22}^e) \\ \sum_I^4 N_{I(\xi^1,\xi^2)}\, 0.5(g_{33}^e - G_{33}^e)_{(\xi_I)} \\ (g_{12}^e - G_{12}^e) \\ (1-\xi^2)(g_{13}^e - G_{13}^e)_{(A)} + (1+\xi^2)(g_{13}^e - G_{13}^e)_{(C)} \\ (1-\xi^1)(g_{23}^e - G_{23}^e)_{(D)} + (1+\xi^1)(g_{23}^e - G_{23}^e)_{(B)} \end{Bmatrix} \tag{3.4.3}$$

where the transverse normal strain (3.4.1), which is assumed in order to alleviate curvature thickness locking [BIS97], were rewritten as

$$\tilde{E}_{33} = \sum_I^4 N_{I(\xi^1,\xi^2)}\, 0.5(g_{33}^e - G_{33}^e)_{(\xi_I)} \tag{3.4.4}$$

Once the transverse shear strains are assumed, all strain-displacement matrices can be similarly formulated. The classical ANS strain-displacement matrices are given by:

$$\tilde{\boldsymbol{B}}_I^{ANS} = \boldsymbol{T}^{-T}\begin{bmatrix} N_{I,1}\boldsymbol{g}_1^T \\ N_{I,2}\boldsymbol{g}_2^T \\ \sum_J^4 N_{J(\xi^1,\xi^2)}(N_{I,3}\boldsymbol{g}_3^T)_J \\ N_{I,1}\boldsymbol{g}_2^T + N_{I,2}\boldsymbol{g}_1^T \\ \frac{1}{2}(1-\xi^2)(N_{I,1}\boldsymbol{g}_3^T + N_{I,3}\boldsymbol{g}_1^T)_{(A)} + \frac{1}{2}(1+\xi^2)(N_{I,1}\boldsymbol{g}_3^T + N_{I,3}\boldsymbol{g}_1^T)_{(C)} \\ \frac{1}{2}(1-\xi^1)(N_{I,2}\boldsymbol{g}_3^T + N_{I,3}\boldsymbol{g}_2^T)_{(D)} + \frac{1}{2}(1+\xi^1)(N_{I,2}\boldsymbol{g}_3^T + N_{I,3}\boldsymbol{g}_2^T)_{(B)} \end{bmatrix} \tag{3.4.5}$$

with I = 1-8 (node number) and J = E, F, G, H.

The alternative assumed natural strains and the associate strain-displacement matrices with curvature locking removal are formulated similarly to the classical ANS ones (3.4.3) and (3.4.5).

An EAS element that is free from volumetric locking and membrane locking [HAU01] has an enhancing matrix $\boldsymbol{M}$ such as

$$\boldsymbol{M} = \begin{bmatrix} \xi^1 & 0 & 0 & 0 & 0 \\ 0 & \xi^2 & 0 & 0 & 0 \\ 0 & 0 & \xi^3 & 0 & 0 \\ 0 & 0 & 0 & \xi^1 & \xi^2 \\ 0 & 0 & 0 & 0 & 0 \\ 0 & 0 & 0 & 0 & 0 \end{bmatrix} \begin{matrix} \\ \\ \\ \\ \\ \\ 25 \ 26 \ 27 \ 29 \ 30 \end{matrix} \tag{3.4.6}$$

An EAS element that is free from volumetric locking, membrane locking and Poisson thickness locking [QUO03a] has an enhancing matrix $\boldsymbol{M}$ such as

$$\boldsymbol{M} = \begin{bmatrix} \xi^1 & 0 & 0 & 0 & 0 & 0 & 0 \\ 0 & \xi^2 & 0 & 0 & 0 & 0 & 0 \\ 0 & 0 & \xi^3 & 0 & 0 & \xi^1\xi^3 & \xi^2\xi^3 \\ 0 & 0 & 0 & \xi^1 & \xi^2 & 0 & 0 \\ 0 & 0 & 0 & 0 & 0 & 0 & 0 \\ 0 & 0 & 0 & 0 & 0 & 0 & 0 \end{bmatrix} \begin{matrix} \\ \\ \\ \\ \\ \\ 25 \ 26 \ 27 \ 29 \ 30 \ 44 \ 45 \end{matrix} \tag{3.4.7}$$

The EAS element, which is interpolated by a matrix $\boldsymbol{M}$ such as (3.4.7), is enhanced by seven internal parameters hence it is named EAS7. Recall that the enhancing matrix (3.4.7) is extracted from matrix (2.4.46). Therefore, the EAS7 always satisfies the patch test. The trilinear terms in modes 49, 50 and 51 of (2.4.46) are not taken into account because they only improve element performance a little while making the computational cost increase significantly.

Eventually, a completely original element that combines both the advantages of the EAS and ANS formulations can be designed, simply by combining the ANS strain field (3.3.25) and (3.4.1) with the 7 EAS modes (3.4.7) thus resulting in the so-called SS7n. It means the solid-shell element with 7 EAS modes and the alternative ANS technique. In this element, the resulting strain field is

$$\boldsymbol{E}^{mod} = \tilde{\boldsymbol{E}}^{ANS}_{(\boldsymbol{u})} + \boldsymbol{E}^{enh}_{(\boldsymbol{\alpha})} \tag{3.4.8}$$

Similarly, a solid-shell element with 7 EAS modes (3.4.7) and the classical ANS technique (3.4.3) results in the so-called SS7. This element has already been presented in [QUO03a]. In the thesis, the EAS internal parameters are used to remove volumetric locking for solid-shell element. Instead of 9 modes (25-27 and 40-45) as proposed in [AND93], only three modes 25 - 27 of (2.4.46) are adopted for the solid-shell element to limit computational cost.

Detail of the solid-shell implementation is given in Figure 3.4.1. In general, the implementation is valid for the EAS element. If the compatible strains are assumed as in (3.4.3) or (3.3.25) and then introduced in step 3 of the algorithm (Figure 3.4.1) we then have the solid-shell element formulation.

ALGORITHM FOR SOLID-SHELL IMPLEMENTATION

1. *Step 1:* Initial values

   $k=0$; $\Delta \boldsymbol{U}_{(k)} = \boldsymbol{0}$; $\boldsymbol{\alpha}_{(k)} = \boldsymbol{0}$; $\boldsymbol{U}_{(k)}$ from the last time step; tolerance *Tol*

2. *Step 2:* Update at element level for iteration $(k+1)$:

   - Nodal displacement: $\boldsymbol{U}^h_{(k+1)} = \boldsymbol{U}^h_{(k)} + \Delta \boldsymbol{U}^h_{(k)}$
   - EAS parameters:

     $$\boldsymbol{\alpha}^e_{(k+1)} = \boldsymbol{\alpha}^e_{(k)} - [\boldsymbol{k}^e_{\alpha\alpha(k)}]^{-1}(\boldsymbol{k}^e_{\alpha u(k)} \Delta \boldsymbol{U}^h_{(k)} + \boldsymbol{f}^e_{enh(k)})$$

3. *Step 3:* at each Gauss point for each element,

   a. calculate:

   - Compatible strains: $\boldsymbol{E}^{com}_{(k+1)}$ as in (3.3.1)
   - Enhanced strains (2.4.45):

     $$\boldsymbol{E}^{enh}_{(k+1)} = \boldsymbol{\Gamma}^e_{(k+1)} \boldsymbol{\alpha}^e_{(k+1)} \quad \text{where } \boldsymbol{\Gamma}^e = \boldsymbol{T}_0^{-T} \boldsymbol{M} \, |J_0| / |J|$$

   - ANS strains, e.g. (3.4.3) for the classical ANS method,:

     if (solid-shell element)

     $$\boldsymbol{E}^{mod}_{(k+1)} = \tilde{\boldsymbol{E}}^{ANS}_{(k+1)} + \boldsymbol{E}^{enh}_{(k+1)} \; ; \; \boldsymbol{B}_{(k+1)} = \tilde{\boldsymbol{B}}^{ANS}_{(k+1)} \; ; \; \boldsymbol{S}^{mod}_{(k+1)} = \frac{\partial W_S}{\partial \boldsymbol{E}^{mod}_{(k+1)}}$$

     else (EAS element)

     $$\boldsymbol{E}^{mod}_{(k+1)} = \boldsymbol{E}^{com}_{(k+1)} + \boldsymbol{E}^{enh}_{(k+1)} \; ; \; \boldsymbol{S}^{mod}_{(k+1)} = \frac{\partial W_S}{\partial \boldsymbol{E}^{mod}_{(k+1)}}$$

     end if

   b. calculate tangent matrices and internal forces, Section 2.4.2

   - $\boldsymbol{k}^e_{uu(k+1)} = \boldsymbol{k}^e_{mat(k+1)} + \boldsymbol{k}^e_{geo(k+1)} = \int_{V_0^e} (\boldsymbol{B}^T \, {}^4\boldsymbol{C}\boldsymbol{B})_{(k+1)} dV + \int_{V_0^e} (\boldsymbol{B}_{,\boldsymbol{U}^h}^{\boldsymbol{T}} \boldsymbol{S}^{mod})_{(k+1)} dV$
   - $\boldsymbol{k}^e_{\alpha u(k+1)} = \int_{V_0^e} (\boldsymbol{\Gamma}^T \, {}^4\boldsymbol{C} \, \boldsymbol{B})_{(k+1)} dV \; ; \; \boldsymbol{k}^e_{\alpha\alpha(k+1)} = \int_{V_0^e} (\boldsymbol{\Gamma}^T \, {}^4\boldsymbol{C} \, \boldsymbol{\Gamma})_{(k+1)} dV$
   - $\boldsymbol{f}^e_{\text{int}(k+1)} = \int_{V_0^e} (\boldsymbol{B}^T \boldsymbol{S}^{mod})_{(k+1)} dV \; ; \; \boldsymbol{f}^e_{enh(k+1)} = \int_{V_0^e} (\boldsymbol{\Gamma}^T \boldsymbol{S}^{mod})_{(k+1)} \, dV$

     $$\boldsymbol{f}^e_{ext(k+1)} = \int_{V_0^e} (\boldsymbol{N}_{\boldsymbol{c}})^T_{(k+1)} \boldsymbol{b}^* dV + \int_{A^e_\sigma} (\boldsymbol{N}_{\boldsymbol{c}})^T_{(k+1)} \boldsymbol{t}^* dA$$

   - Update at element level $\boldsymbol{k}^e_{T(k+1)} = \boldsymbol{k}^e_{uu(k+1)} - \left[\boldsymbol{k}^e_{\alpha u(k+1)}\right]^T \left[\boldsymbol{k}^e_{\alpha\alpha(k+1)}\right]^{-1} \boldsymbol{k}^e_{\alpha u(k+1)}$

     $$\boldsymbol{r}^e_{(k+1)} = \boldsymbol{f}^e_{ext(k+1)} - \boldsymbol{f}^e_{int(k+1)} + \left[\boldsymbol{k}^e_{\alpha u(k+1)}\right]^T \left[\boldsymbol{k}^e_{\alpha\alpha(k+1)}\right]^{-1} \boldsymbol{f}^e_{enh(k+1)}$$

   - Save EAS arrays: $\left[\boldsymbol{k}^e_{\alpha u(k+1)}\right]^T, \left[\boldsymbol{k}^e_{\alpha\alpha(k+1)}\right]^{-1}, \boldsymbol{f}^e_{enh(k+1)}, \boldsymbol{\alpha}^e_{(k+1)}$

4. *Step 4:* Assemble global matrices $\boldsymbol{K}_{(k+1)}, \boldsymbol{R}_{(k+1)}$.

5. *Step 5:* Solve the incremental displacement and check for global convergence

   $$\Delta \boldsymbol{U}_{(k+1)} = \boldsymbol{K}^{-1}_{(k+1)} \boldsymbol{R}_{(k+1)}$$

   if $\left|\boldsymbol{R}_{(k+1)}\right| < Tol$ *or* $\left|\Delta \boldsymbol{U}_{(k+1)} \cdot \boldsymbol{R}_{(k+1)}\right| < Tol$

   goto next time step

   else

   k=k+1; return Step 2

   end if

Figure 3.4.1: Solid-shell algorithm

3.5 ENHANCED QUANTITIES

3.5.1 Consistent deformation gradient

The solid-shell element presented in this chapter has been built on the modified strain $\boldsymbol{E}^{mod}$ (3.4.8). The associated modified deformation gradient $\boldsymbol{F}^{mod}$ is required if the element is implemented in a source code base on the updated Lagrange formulation or when a material algorithm for large elastoplastic strains is needed.

The deformation gradient can be split into right-stretch tensor $\boldsymbol{U}$ and rotation tensor $\boldsymbol{R}$ as:

$$\boldsymbol{F} = \boldsymbol{R}\boldsymbol{U} \tag{3.5.1}$$

Introduce $\boldsymbol{U}$ and $\boldsymbol{R}$ into the formulation for calculating Green-Lagrange strain tensor (3.2.5) we have:

$$\underline{\boldsymbol{E}} = \frac{1}{2}(\boldsymbol{F}^T\boldsymbol{F} - \boldsymbol{I}) = \frac{1}{2}[\boldsymbol{U}^T(\boldsymbol{R}^T\boldsymbol{R})\boldsymbol{U} - \boldsymbol{I}] = \frac{1}{2}(\boldsymbol{U}^2 - \boldsymbol{I}) \tag{3.5.2}$$

Clearly, Green-Lagrange strain tensor depends only on the right-stretch tensor $\boldsymbol{U}$. Thus, from the modified strain $\underline{\boldsymbol{E}}^{mod}$ we can derive the associated modified right-stretch tensor $\boldsymbol{U}^{mod}$. According to Hauptmann et al. [HAU00], the modified deformation gradient $\boldsymbol{F}^{mod}$ is calculated as

$$\boldsymbol{F}^{mod} = \boldsymbol{R}\boldsymbol{U}^{mod} \tag{3.5.3}$$

We see that calculation of $\boldsymbol{F}^{mod}$ requires twice of polar decomposition. The first time is calculation of rotation tensor $\boldsymbol{R}$ in (3.5.1). The second time is calculation of modified right-stretch tensor $\boldsymbol{U}^{mod}$ from $\underline{\boldsymbol{E}}^{mod}$. These calculations will increase computational cost of the algorithm when the deformation gradient $\boldsymbol{F}^{mod}$ is required.

3.5.2 Local static condensation

The internal parameters of the EAS element are condensed out at the element level, see (2.4.37), before assembling. As shown in the solid-shell algorithm (Figure 3.4.1), the internal parameters at iteration (k+1) is calculated by:

$$\boldsymbol{\alpha}^e_{(k+1)} = \boldsymbol{\alpha}^e_{(k)} - [\boldsymbol{k}^e_{\alpha\alpha(k)}]^{-1}(\boldsymbol{k}^e_{\alpha u(k)}\Delta\boldsymbol{U}^h_{(k)} + \boldsymbol{f}^e_{enh(k)}) \tag{3.5.4}$$

This procedure requires, for each element, that apart from the internal parameters at iteration (k) - $\boldsymbol{\alpha}^e_{(k)}$ must be stored for the calculation of $\boldsymbol{\alpha}^e_{(k+1)}$, other quantities as $\boldsymbol{k}^e_{\alpha\alpha(k)}$, $\boldsymbol{k}^e_{\alpha u(k)}$ and $\boldsymbol{f}^e_{enh(k)}$ also need to be kept. When solving a problem with a huge number of DOF's, a large memory space must be reserved for storing these items. Simo et al. [SIM93] did propose a "local static condensation algorithm". According to this local algorithm, the internal parameters $\boldsymbol{\alpha}^e_{(k+1)}$ are not calculated at Step 2. Instead, they are calculated at the end of Step 3b (Figure 3.4.1) from $\boldsymbol{k}^e_{\alpha\alpha(k+1)}$, $\boldsymbol{k}^e_{\alpha u(k+1)}$ and $\boldsymbol{f}^e_{enh(k+1)}$. Consequently, it is not necessary to save EAS arrays that usually demand a significant memory allocation. Details of the local static condensation algorithm are presented in Figure 3.5.1.

LOCAL STATIC CONDENSATION ALGORITHM

Let $\{\boldsymbol{U}_n^h, \Delta\boldsymbol{U}_n^h\}$ be the correct solutions at time t_n and $\{\boldsymbol{U}_{n+1(k)}^h, \Delta\boldsymbol{U}_{n+1(k)}^h\}$ be solutions at a given iteration (k) within the interval $[t_n, t_{n+1}]$. Fix this iteration and compute $\boldsymbol{\alpha}_{n+1(k)}^e$ for each element by means of the following sub-iteration (at the element level):

2. *Step 1:* Initial values

   $k = 1$; $\boldsymbol{\alpha}_{n+1(1)}^e = \boldsymbol{\alpha}_n^e$; tolerance *tol* ; Calculate $\boldsymbol{E}_{(k+1)}^{com}$

3. *Step 2:* Update at element level for iteration $(k+1)$:
   - Compute: $\boldsymbol{E}_{(k+1)}^{enh}$; $\boldsymbol{E}_{(k+1)}^{mod} = \boldsymbol{E}_{(k+1)}^{com} + \boldsymbol{E}_{(k+1)}^{enh}$
   - Use constitutive equations to compute: $\boldsymbol{S}_{(k+1)}^{mod} = \dfrac{\partial W_S}{\partial \boldsymbol{E}_{(k+1)}^{mod}}$

4. *Step 3:*
   - Compute increment: $\Delta\boldsymbol{\alpha}_{(k+1)}^e = [\boldsymbol{k}_{\alpha\alpha(k+1)}^e]^{-1} \boldsymbol{f}_{enh(k+1)}^e$
   - Test for convergence:

     if $(\left|\Delta\boldsymbol{\alpha}_{(k+1)}^e \cdot \boldsymbol{f}_{enh(k+1)}^e\right| < tol)$ or $(k \le 3)$

     stop

     else

     update $\boldsymbol{\alpha}_{(k+1)}^e = \boldsymbol{\alpha}_{(k)}^e - \Delta\boldsymbol{\alpha}$

     k=k+1; return Step 2

     end if

Figure 3.5.1: Static condensation algorithm [SIM93]

In the algorithm of Simo et al. [SIM93], Figure 3.5.1, the internal parameters are calculated by an approximation formulation:

$$\boldsymbol{\alpha}_{(k+1)}^e = \boldsymbol{\alpha}_{(k)}^e - [\boldsymbol{k}_{\alpha\alpha(k)}^e]^{-1}(\boldsymbol{f}_{enh(k)}^e) \tag{3.5.5}$$

Hence, a limited number of iterations (≤ 3) have to be realized to get a correct solution.

3.6 NUMERICAL RESULTS AND DISCUSSION

In the thesis, the solid-shell, which adopts 7 EAS parameters (3.4.7) and the classical ANS techniques (3.4.3), is designated by SS7. While the solid-shell element with the alternative ANS technique that is presented in the above section, expression (3.3.25), is designated by SS7n. The additional letter "n" stands for the elements that employ the new alternative ANS technique.

3.6.1 Patch tests

The patch test has been originally proposed in the mid-sixties as a simple means to proof convergence of an element. Beside a numerical verification there is also the possibility of a theoretical analysis. The patch test checks, whether a constant distribution of any state variable within an arbitrary element patch (i.e. a distorted mesh) can be represented exactly. It is especially useful for finite element formulations which violate the compatibility condition (and thus cannot be proven to be consistent), such as the ANS, EAS, etc. Nature of the patch test is to verify an element's ability to represent a constant strain/stress field, and thus ensure completeness and an ability to converge in the limit as the element size decreases.

The membrane patch test (for membrane constant stress state) and the bending patch test (for bending constant stress state) presented in Chapter 2 – Section 2.6 are satisfied by the classical ANS, SS7 elements and the proposed ANSn, SS7n elements.

3.6.2 Eigenvalue analysis of an incompressible cube

In order to estimate the behavior of the ANSn and SS7n elements at the nearly incompressible limit an eigenvalue analysis of a unit cube is performed as in [AND93]. The material parameters are elastic modulus E = 1.0 and Poisson ratio ν = 0.4999. The cube is considered in regular configuration, and furthermore, in distorted configuration to check the sensitivity to distorted mesh of elements, see Figure 3.6.1.

Table 3.6.1 shows the eigenvalues of 18 deformable modes of the regular cube (Figure 3.6.1a), the six zero eigenvalues for the six rigid body modes are not shown.

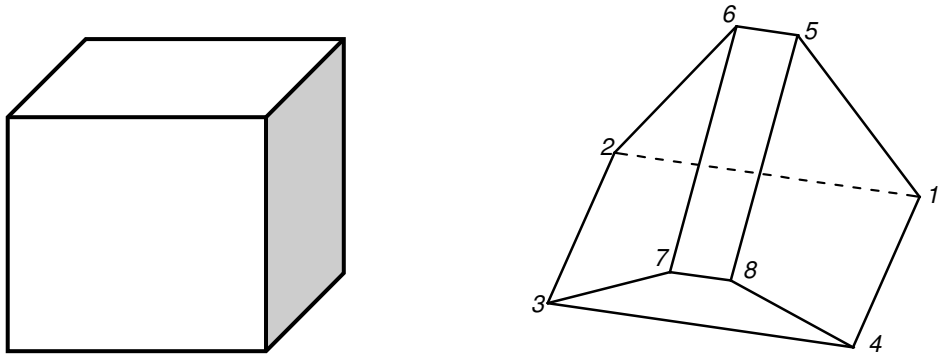

a) Regular shape b) Distorted shape

Figure 3.6.1: Regular and distorted cubes

The six eigenvalues of the constant strain-states, which are identical for all elements, are printed in italic letters. Their corresponding eigenmodes can be identified as three shear modes, two tension modes and one dilatation (or incompressible) mode (Figure 3.6.2). The eigenvalues of the EAS3v, EAS6v and EAS9v, in Table 3.6.1 are totally identical to those values of METAFOR [BUI02]. This assures the quality of our EAS implementation in the MATLAB code.

Table 3.6.1: Eigenvalues of regular cube

Mode	Q1	EAS3v	EAS6v	EAS9v	SS7	SS7n	ANS	ANSn
1	0.056	0.056	0.056	0.056	0.056	0.056	0.056	0.056
2	0.056	0.056	0.056	0.056	0.056	0.056	0.056	0.056
3	0.167	0.167	0.093	0.093	0.093	0.093	0.111	0.111
4	0.167	0.167	0.111	0.093	0.093	0.093	0.139	0.167
5	0.167	0.167	0.167	0.093	0.111	0.111	0.139	0.167
6	0.222	0,222	0.167	0.167	0.111	0.135	0.222	0.222
7	*0.333*	*0.333*	0.167	0.167	0.111	0.135	*0.333*	*0.333*
8	*0.333*	*0.333*	0.222	0.167	0.222	0.222	*0.333*	*0.333*
9	*0.333*	*0.333*	*0.333*	0.222	0.333	0.333	*0.333*	*0.333*
10	*0.333*	*0.333*	*0.333*	*0.333*	0.333	*0.333*	*0.333*	*0.333*
11	*0.333*	*0.333*	*0.333*	*0.333*	0.333	*0.333*	*0.333*	*0.333*
12	92.654	0.389	*0.333*	*0.333*	*0.333*	*0.333*	92.617	92.654
13	92.654	0.389	*0.333*	*0.333*	*0.333*	*0.333*	92.636	92.636
14	92.654	0.389	0.389	*0.333*	*0.333*	*0.333*	92.636	92.636
15	555.648	92,654	0.388	0.389	*0.333*	0.365	555.593	555.593
16	555.648	92,654	0.389	0.389	*0.333*	0.365	555.620	555.648
17	555.648	92,654	92.654	0.389	92.617	92.654	555.620	555.648
18	*2500.00*	*2500.00*	*2500.00*	*2500.00*	*2500.00*	*2500.00*	*2500.00*	*2500.00*

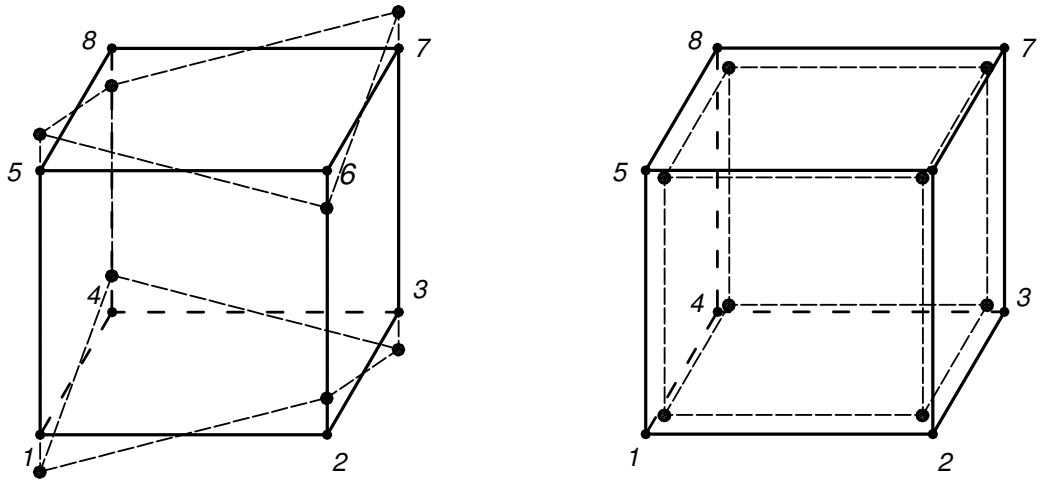

a) warping mode b) dilatation mode

Figure 3.6.2: Two deformation modes

For a volumetric-locking free behavior, the elements should contain only one infinite eigenvalue, it is the eigenvalue of the dilatation mode (mode number 18, eigenvalue = 2500 is considered as infinite). In the case of the standard elements Q1, six deviatoric modes (modes 12-17) are always mixed up by volumetric strains which when $\nu \rightarrow 0.5$ leads to six unrealistic infinite eigenvalues. The same consequences are found with ANS and ANSn, it means Q1 and both ANS and ANSn are not volumetric locking free. With the introduction of 3 enhanced modes, the most important part of volumetric locking is removed in the EAS3v element, which has now a better volumetric locking

response in comparison to the Q1. However, higher order parts in the interpolation functions still exist and this might cause volumetric locking in certain cases. With the additional enhanced modes, the EAS6v becomes nearly free volumetric locking. Introduce more enhanced modes, for example EAS9v we obtains totally free volumetric locking element. As we might observe, after removing volumetric locking, the infinite eigenvalue becomes finite. The solid-shell elements, SS7 and SS7n, are almost free volumetric locking, except a warping mode (Figure 3.6.2) has a moderate eigenvalue of 92.6 (mode 17).

Table 3.6.2: Distorted cube - location of nodes

	1	2	3	4	5	6	7	8
x	-2.5	+2.5	+2.5	-2.5	-0.5	+0.5	+0.5	-0.5
y	-2.5	-2.5	+2.5	+2.5	-2.5	-2.5	+2.5	+2.5
z	-1.5	-1.5	-0.5	-0.5	+1.5	+1.5	+0.5	+0.5

Table 3.6.3: Eigenvalues of distorted cube

Mode	Q1	EAS3v	EAS6v	EAS9v	SS7	SS7n	ANS	ANSn
1	0.056	0.056	0.056	0.056	0.057	0.059	0.059	0.069
2	0.378	0.378	0.391	0.298	0.067	0.070	0.133	0.135
3	0.401	0.391	0.312	0.276	0.171	0.164	0.202	0.217
4	0.493	0.464	0.422	0.412	0.163	0.181	0.372	0.344
5	0.622	0.614	0.464	0.454	0.284	0.414	0.428	0.589
6	0.679	0.674	0.578	0.553	0.442	0.440	0.591	0.633
7	1.109	0.935	0.614	0.578	0.484	0.667	0.606	0.814
8	1.185	1.109	0.935	0.811	0.660	0.675	1.055	1.031
9	1.783	1.457	0.989	0.925	0.919	0.958	1.436	1.730
10	1.722	1.646	1.457	0.988	1.392	1.448	1.704	1.826
11	12.916	1.724	1.477	1.473	1.805	1.677	177.914	9.241
12	202.125	3.129	1.662	1.614	1.789	1.754	652.063	197.282
13	464.475	3.706	1.724	1.686	3.040	3.035	901.394	771.135
14	1171.097	13.803	3.129	2.020	3.580	3.739	953.793	899.555
15	1764.644	204.498	3.689	3.061	6.863	6.906	2712.966	2721.249
16	3443.134	707.527	17.078	3.280	228.098	26.162	3995.422	4400.630
17	4268.216	1197.604	707.527	17.031	735.750	832.995	6639.616	6566.450
18	10673.478	10278.645	10278.645	10167.644	21513.640	21281.558	25092.928	25024.503

For distorted case (Figure 3.6.1b), the general trend is quite similar as in the regular case. Table 3.6.3 shows the eigenvalues of 18 deformable modes of the distorted cube. The ANS and ANSn elements and the Q1 standard element are locked because of the presence of many infinite eigenvalues (modes 12-17). With the introduction of enhanced modes in volume, volumetric locking is removed. However, in this distorted configuration, the EAS elements cannot remove completely the locking effect. For example, it exists two locking eigenmodes (modes 16, 17) in the EAS6v. Fortunately, the eigenvalue is rather moderate and we expect a very mild locking. The solid-shell elements, SS7 an SS7n, also show two locking eigenmodes (modes 16, 17) as the EAS6v. Anyway, the ANSn and SS7n seem to be better than ANS and SS7, respectively, in this distorted configuration, see Table 3.6.3 (by comparing eigenvalues of mode 11 of the

ANS and ANSn; and by comparing eigenvalues of mode 16 of the SS7 and SS7n). In the distorted configuration, the SS7n and ANSn elements have only one more moderate eigenvalue compare to their eigenvalues in the regular configuration, respectively. These arguments improve that the ANSn and SS7n elements are less sensitive to distorted mesh than the ANS and SS7 elements, respectively.

The distorted case of the cube was also analysed by Jetteur [JET08]. In [JET08] the incompatible element, the SRI, EAS24 and EAS9 elements were invoked. Analysed results in [JET08] showed that the incompatible element behaves similarly as the EAS3v element. Volumetric locking was almost removed by the EAS9v element. Hence, in this case the EAS9v and EAS24 give similar results. Only the SRI element is completely volumetric locking free in this case.

3.6.3 Eigenvalues of a square plate

Eigenvalues of a square plate with zero Poisson's ratio is investigated to check performance of elements in bending [HAU00]. Dimensions and material parameters of the plate are given in Figure 3.6.3.

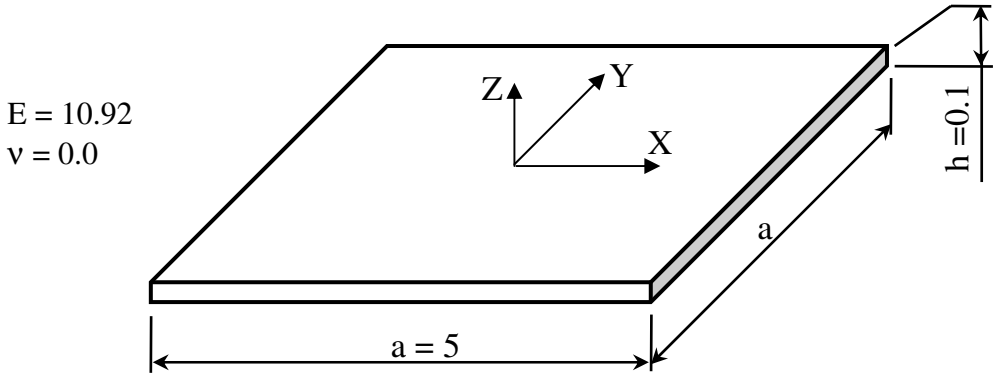

Figure 3.6.3: Square plate

Eigenvalues of elements are shown in Table 3.6.4. Result of EAS3DEAS solid-shell element of Hauptmann et al. [HAU00] is also gathered to compare with the solid-shell elements presented in this thesis. The EAS3DEAS element incorporated the classical ANS technique for removal of transverse shear locking, and incorporated the EAS method for membrane and Poisson thickness locking removals.

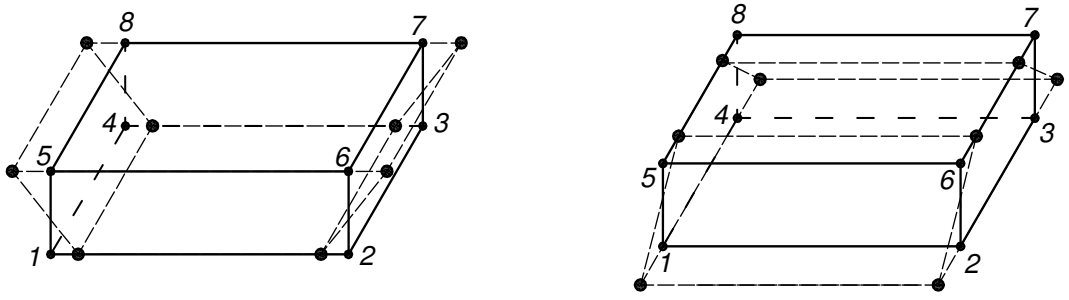

a) Bending in 0X b) Bending in 0Y

Figure 3.6.4: Two bending modes

All of the elements have six rigid body modes. The standard element, Q1, suffers transverse shear locking as we see its eigenvalues for bending modes in 0X and 0Y axes (Figure 3.6.4) are infinite. These eigenvalues of Q1 are equal to 227.7 while the correspondent values of non-locking elements are smaller than 1.0 (Table 3.6.4, modes 11 and 12). Furthermore, the Q1 element and also the EAS3v6s element may suffer a mild locking caused by two warping modes (Figure 3.6.5) because these modes were affected by transverse shear strains. The warping-mode eigenvalues of the Q1 and the EAS3v6s are equal to 75.9 while the equivalent values of other elements in Table 3.6.4 are smaller than 1.0 (modes 9 and 10).

Table 3.6.4: Eigenvalues of the square plate

Eigen mode	Q1	EAS3v6s	ANS-SC	SS7	ANSn	SS7n
1	1365.0	1365.000	1365.000	1365.000	1365.000	1365.000
2	682.8	227.864	227.864	227.864	227.863	227.864
3	682.8	227.500	227.500	227.500	227.500	227.500
4	227.9	682.773	682.773	682.773	682.773	682.773
5	227.5	682.773	682.773	682.773	682.773	682.773
6	151.7	151.727	151.667	151.666	151.727	151.727
7	455.1	455.000	455.000	455.000	455.091	455.091
8	455.1	455.000	455.000	455.000	455.091	455.091
9	75.9	75.924	0.273	0.546	0.273	0.546
10	75.9	75.924	0.273	0.546	0.273	0.546
11	227.7	0.546	0.182	0.546	0.182	0.546
12	227.7	0.546	0.182	0.091	0.182	0.091
13	0.3	0.091	0.091	0.091	0.091	0.546
14	0.3	0.091	0.182	0.091	0.182	0.182
15	0.5	0.546	0.182	0.546	0.182	0.182
16	0.5	0.546	0.182	0.546	0.182	0.182
17	0.5	0.546	0.182	0.546	0.182	0.182
18	1.5E-4	1.454e-4	1.45e-4	1.454e-4	1.45e-4	1.45e-4

Table 3.6.5: Eigenvalues of the square plate - Summary

Element	Rigid body modes	Eigenvalues (of deformable modes)			
		< 0.1	< 1.0	$\approx \infty$	Max.
Q1	1 – 6	7	8 – 12	–	1365
EAS3v6s	1 – 6	7	8 – 14	–	1365
EAS3DEAS (Hauptmann)	1 – 6	7 – 9	10 – 16	–	1365
ANS	1 – 6	7 – 9	10 – 16	–	1365
ANSn	1 – 6	7 – 9	10 – 16	–	1365
SS7	1 – 6	7 – 9	10 – 16	–	1365
SS7n	1 – 6	7 – 9	10 – 16	–	1365

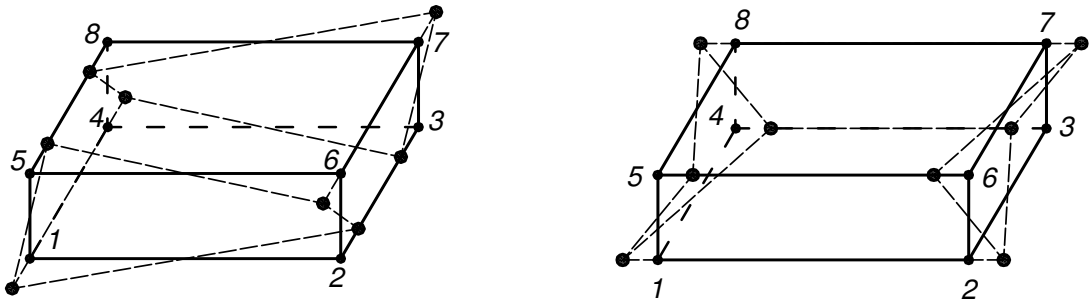

Figure 3.6.5: Two warping modes of EAS3v6s & Q1

3.6.4 Square plate at large displacements and strains

Consider a square plate of dimension a×a×h with a = 100 and h = 1. Young modulus is E = 2×10^5 and Poisson's ratio is ν = 0.3. The plate is considered in two cases: fully clamped and simply supported at all edges. A concentrated force P is applied at the center of the plate.

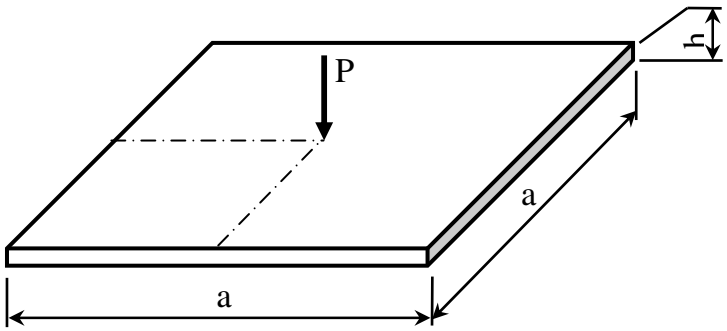

Figure 3.6.6: Square plate geometry

Due to symmetry, only one quarter of the plate is analysed, see Figure 3.6.6. By adopting the assumption on small displacements and strains, analytical results for the displacement at the center of the plate can be obtained thanks to Timoshenko's plate theory. These analytical results are:

for the clamped plate: $w_{\max} = 0.0056Pa^2/D$, (3.6.1a)

for the simply supported plate: $w_{\max} = 0.0116Pa^2/D$, (3.6.1b)

where $D = Eh^3/12(1-\nu^2)$ is the flexural rigidity of the plate cross-section.

The analytical solution with the assumption of small displacements and strains offers a reference to examine the correctness of the numerical results. The problem is modeled by a coarse mesh of 5×5×1 elements. In both clamped and supported cases, the ANS and ANSn give the same results, similarly, the SS7 and SS7n give the same results. Hence, in this example we only expose results of the ANSn and SS7n.

Consider first the case where the plate is clamped, Figure 3.6.7. At a rather moderate loading (P < 100), displacements and strains in the plate remain small. Hence numerical results from large strain version should match the analytical solution. Results are also compared to results from reduced integration (RI) element of Li and Cescotto, [LI97], with automatic hourglass control. Notice that if the RI results match quite well

the EAS15 and SS7n, this is at the expense of 3 layers over the plate thickness for the RI while only one layer is required by other elements. The elements derived from the RI technique undergo Poisson thickness locking. Therefore, for RI elements, more than one layer should be used over thickness in order to obtain a good result of stress distribution along thickness in bending dominated problems.

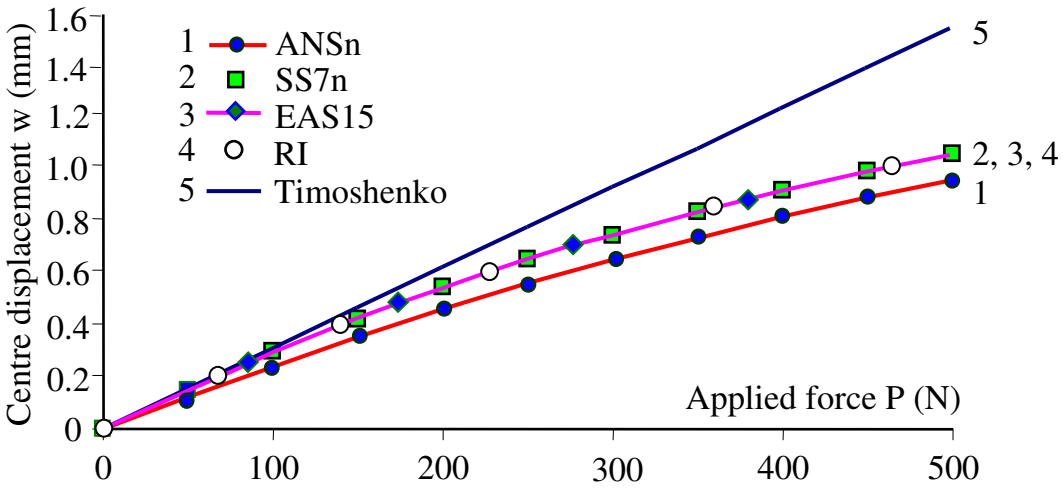

Figure 3.6.7: Displacement versus applied force for fully clamped plate

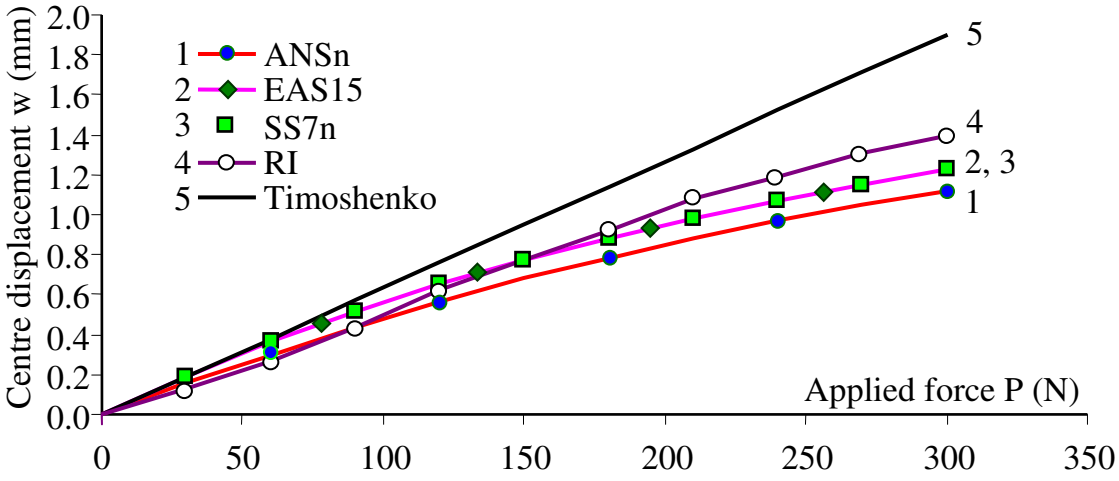

Figure 3.6.8: Displacement versus applied force for simply supported plate

The EAS15, RI and SS7n elements are very satisfactory by approaching the analytical curve up to a loading level about P = 100. With increasing loading, geometrically nonlinear effects become important and this due to membrane effects makes the plate stiffer. It explains why all numerical results are lower than the theoretical ones. Also, large strains might happen and this will have an influence on the behavior of the structure. The accuracy of the alternative ANS technique is confirmed when a very good agreement is found in comparison of the SS7n element with the EAS15 and RI elements being developed in the framework of large displacement and strains.

Consider now the case when the plate is simply supported, Figure 3.6.8. The results of the EAS15, SS7n and the RI are rather close to each other. However, while the EAS15 and SS7n results approach the analytical solution at a moderate loading (P < 100)

as expected, it is not the case of the RI element. The deviation of the RI results from the analytical solution at small strains. When the applied force is over 150N, the EAS15 and SS7n continue giving the same result but they are a little stiffer than the RI element.

The behavior of the EAS15 in both clamped and simply supported cases are totally identical to those values of METAFOR [BUI02]. This assures the quality of our EAS implementation in the MATLAB code.

CONCLUSION

The ANSn and SS7n elements, which base on the alternative ANS technique, satisfy the patch tests. By analysing eigenvalues we see that they are free from volumetric locking and transverse shear locking.

The solid-shell elements are full-integrated scheme hence the stiffness matrix is stable; it means there is not hourglass modes. It should be noted that the derivation of the solid-shell stiffness matrix is carried out on the flattened (unwarped) solid geometry, then globalized to the actual geometry. If the element is too warped or tapered, certain tests are only approximately satisfied. Poor results can be expected if the element is excessively warped. Unlike others plane-stress shell formulations for metal forming simulation, the solid-shell elements provide a natural and efficient way for shell contact problem since double-side surfaces of shell are available and the transverse normal stress is included.

Featuring an appropriate combination of the ANS and the EAS methods dedicated to alleviate locking effects, the solid-shell elements are free from locking due to parasitic shear strains, distorted geometries and incompressible materials. Through an investigation of the ANS method in the removal of shear locking, an alternative scheme of sampling points, which enables a linear distribution instead of a constant value of shear strains, is developed in this chapter. As it was revealed by numerical results, the solid-shell elements with this alternative scheme offer a comparable performance in comparison with that employed the classical ANS scheme.

In the next chapter performances of the ANS and ANSn, the SS7 and SS7n solid-shell elements for elastic applications are continuously investigated with various linear and nonlinear tests.

Chapter 4. ELASTIC APPLICATIONS

INTRODUCTION

In Chapter 3 a solid-shell element, which integrates the alternative ANS technique, has been developed. In this chapter, various numerical tests are presented to demonstrate the capabilities of the proposed solid-shell element. For the sake of clarity, all denotations for elements in Chapter 2 and Chapter 3 are recalled below.

The standard solid element with full integration is designated by Q1, while the solid element, which employs the classical ANS technique [DVO84] for alleviating transverse shear locking and curvature locking, is designated by ANS. The solid-shell element described in Chapter 3, which adopts 7 EAS parameters and the classical ANS techniques (3.4.3), is designated by SS7, while the solid-shell element with the alternative ANS technique presented in Chapter 3 (3.3.25) is designated by SS7n. The additional letter "n" stands for the elements that employ the alternative ANS technique. The EAS elements are designated by EASx, where 'x' is the number of internal parameters. For linear and nonlinear elasticity tests in this chapter, all of these elements are implemented in a MATLAB code.

Table 4.0.1: Summary of employed elements

Name	Type	Description
Q1	Standard solid element	Only compatible strains
ANS	Classical ANS element	Linear transverse shear strains (3.4.3)
ANSn	New ANS element	Bi-linear transverse shear strains (3.3.25)
EASx	Enhanced assumed strain element	"x" enhanced modes (Table 2.4.2)
SS7	Solid-shell element	7 enhanced modes (3.4.7) Linear transverse shear strains (3.4.3)
SS7n	New solid-shell element	7 enhanced modes (3.4.7) Bi-linear transverse shear strains (3.3.25)

4.1 LINEAR APPLICATIONS

In this section we investigate performances of the ANSn and SS7n elements. Various tests, which include shear, membrane and volumetric locking, are taken into considered. All of tests in this section are linear problems. Nonlinear problems are considered later, in section 4.2.

4.1.1 Cantilever beam under pure bending

Consider a cantilever of dimension 10×1×1 clamped at left end and loaded by a constant moment (induced by forces P = 0.5) at right end, Figure 4.1.1. This test presented by Chandra and Prathap [CHA89]. The elastic modulus is $E = 10^6$ and Poisson's ratio is $\nu = 0.0$. From the theory of the strength of materials, the analytical solutions for vertical displacement w and maximum normal stress are:

$$w = \frac{ML^2}{2EI} = 6\times10^{-4} \quad ; \quad \sigma_{max} = \frac{M}{W} = 6 \quad with \;\; W = \frac{bh^2}{6} \tag{4.1.1}$$

A mesh of one element is used. Since the structure undergoes pure bending, an enhancement in volumetric locking is quite useless. Therefore, we will employ here 3 shear-enhanced modes. With this rather moderate enhancement, the EAS3s is already able to attain the expected results both in displacement and normal stress. The stress results in Table 4.1.1 are averages of absolute values at upper and lower surfaces of the cantilever. Except the Q1 standard element is too stiff due to shear locking, all the other elements, ANS, ANSn, SS7 an SS7n, are shear locking free.

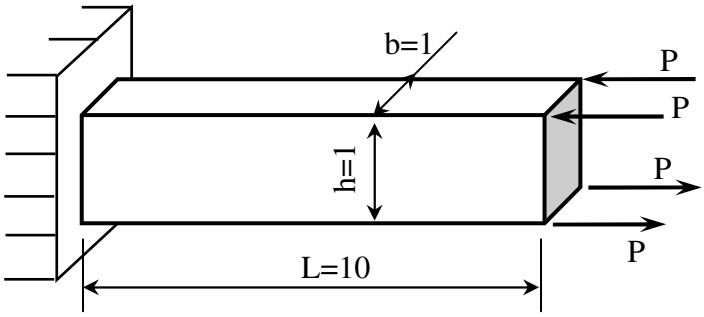

Figure 4.1.1: Cantilever under pure bending

Table 4.1.1. Normalized results

	Q1	EAS3s	ANS	ANSn	SS7	SS7n
w	0.0195	0.9998	0.9998	1.0000	0.9998	0.9998
σ_{max}	0.0195	0.9998	0.9998	0.9998	0.9998	0.9998

4.1.2 Twisted beam with warping effects

In order to test the warping effect on elements McNeal and Harder [MAC85] proposed the twisted cantilever in bending in-plane direction (P_v = 1) and out-of-plane direction (P_h = 1), Figure 4.1.2. The cantilever length is L = 12, the width is w = 1.1 and the thickness is t = 0.32. The cantilever is twisted 90° from root to tip. Young's modulus is E = 29×10^6 and Poisson's ratio is ν = 0.22.

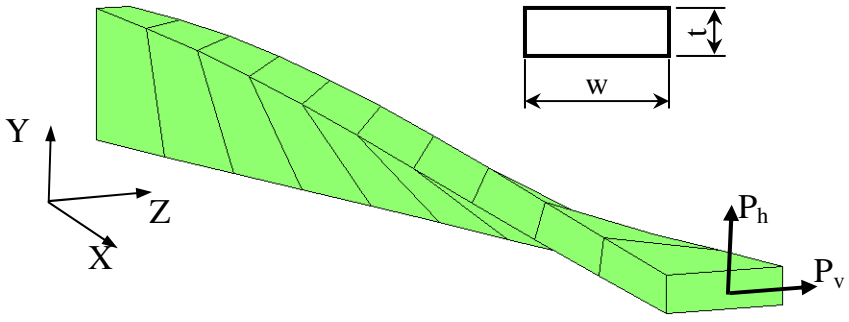

Figure 4.1.2: Twisted beam

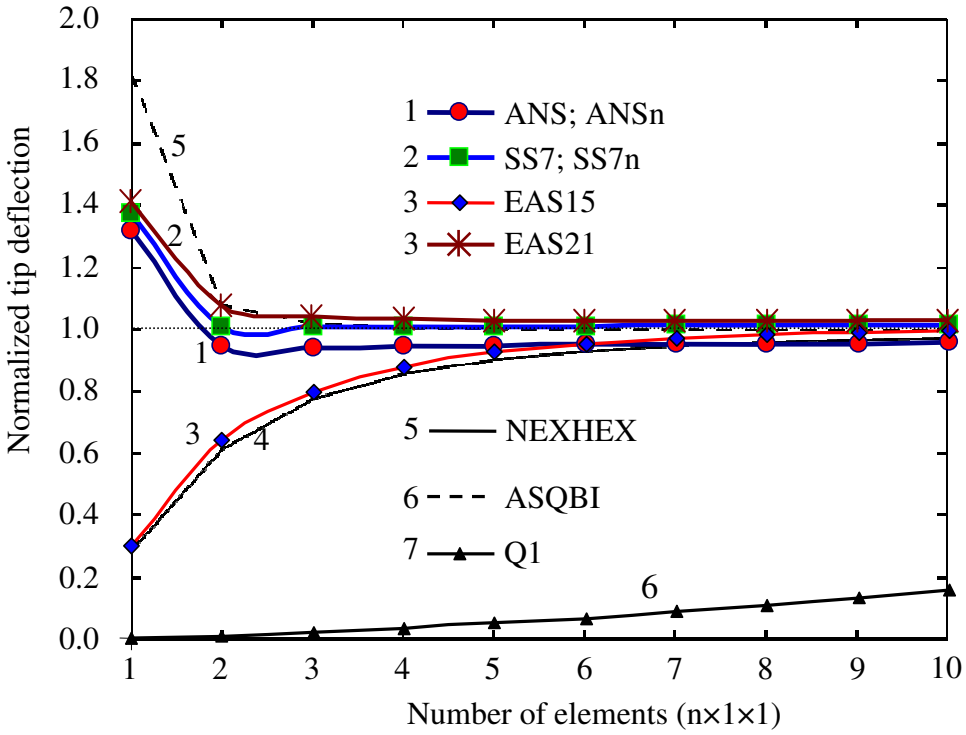

Figure 4.1.3: Twisted beam, case of load along 0Z

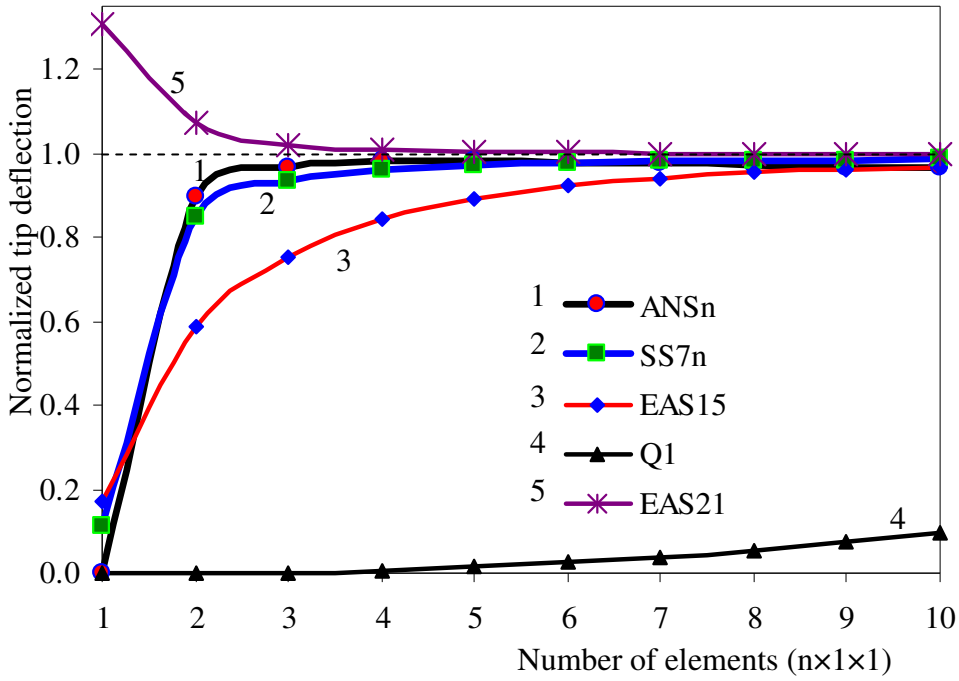

Figure 4.1.4: Twisted beam, case of load along 0Y

The cantilever is fixed at left end and loaded by a unit force at right end. The reference solutions are:

- In-plane direction ($P_v = 1$): $w_{ref} = 5.424\times10^{-3}$;
- Out-of-plane direction ($P_h = 1$): $v_{ref} = 1.754\times10^{-3}$.

The cantilever is modeled with a mesh of n×1×1 elements, where n is number of elements along the cantilever length.

Numerical results for the case of bending in-plane direction are listed in Figure 4.1.3, where results of ASQBI element of Belytschko and Bindeman [BEL93] and NEWHEX element of Fredriksson and Ottosen [FRE07] are also taken into considered. Both ASQBI and NEWHEX elements are assumed strain elements where element underintegration is adopted. The SS7 and SS7n elements converge with very coarse mesh (n = 2) while the convergence with other elements requires finer mesh: n = 3 for ASQBI and EAS21, n = 10 for NEWHEX and n = 9 for the EAS15. The ANS and ANSn elements also converge as quickly as SS7. The Q1 element continues to show poor performance in this bending case as usual.

Numerical results for the case of bending in out-of-plane direction are listed in Figure 4.1.4. In this case, all of the elements (ANSn, SS7n and EAS) only converge with rather fine mesh ($n \geq 5$). However, with coarse meshes, the ANSn and SS7n elements give better results than the EAS15. In contrary, the EAS21 converges as fast as the SS7n. The Q1 element suffer shear locking hence show poor performance in this bending case.

Solid-shell in Samcef is a volumetric, quadrature shell element which can perform the thickness deformation [JET08]. That element adopts the ANS method for shear locking removal. Furthermore, 12 EAS modes are also adopted to remove other locking effects. That solid-shell element passes the bending and membrane patch tests [JET08]. For this twisted beam problem, the solid-shell in Samcef converges with a mesh of 12×2×1 elements (for both bending in-plane direction and bending out-of-plane direction).

4.1.3 Clamped and simply supported plates under uniformed pressure

A square plate of dimension a×a×h with fixed thickness h = 1 and various values of width a = (10, 100, 1000) is modeled. All edges of the plate are clamped or simply supported. A uniform pressure p = 1 loads on the upper face of the plate. This test is presented by Chandra and Prathap [CHA89].

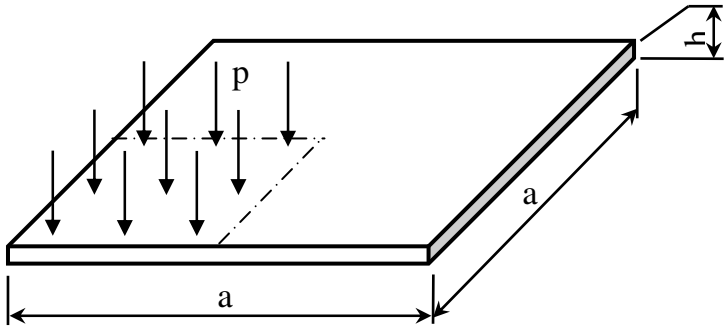

Figure 4.1.5: Square plate under uniformed pressure

The symmetry of the structure allows to simulate a quarter of the plate, see Figure 4.1.5. The material properties are Poisson's ratio $\upsilon = 0.3$ and the elastic modulus E is artificially dependent on the length a, see (4.1.3). The analytical result on the centre deflection can be obtained [TIM59]:

$$w = 0.01\alpha \frac{pa^4}{D} \quad \text{with} \quad D = \frac{Eh^3}{12(1-\nu^2)} \tag{4.1.2}$$

where D is the flexural stiffness of plate and dimensionless deflection α depends on boundary condition, see Table 4.1.2.

In order to respect the condition of small displacements, the centre deflection has to be limited to a small value. Here, a typical value w = h/1000 is respected. Correspondingly, the Young's modulus takes the following value from (4.1.2):

$$E = 12\frac{(1-\nu^2)D}{h^3} = 12\frac{(1-\nu^2)}{h^3}0.01\alpha\frac{pa^4}{w} \tag{4.1.3}$$

Table 4.1.2. Dimensionless deflection α (from [BLE00] and [TIM59])

h/a	0.1	0.01	0.001	0.0001
Plate	thick	thin	very thin	very thin
Clamped				
α	0.15	0.126	0.126	0.126
Simply supported				
α	0.424	0.406	0.406	0.406

For the comparison reason, the numerical dimensionless coefficient α_{num}, which is defined below, derived from (4.1.2), will be employed:

$$\alpha_{num} = 100\frac{w_{num}D}{pa^4} \tag{4.1.4}$$

Consider first the case where all the edges of the plate are clamped, Table 4.1.3. Numerical analysis shows that the EAS15, SS7 and SS7n elements give very satisfactory results for all cases ranging from thick to thin plates. While the Q1 element delivers a poor prediction, especially when shear locking and Poisson thickness locking (due to Poisson ratio is different from zero) becomes important with a decrease of the plate thickness. The EAS9 element only gives good results for thick plate. When the aspect ratio (a/h) is over 100, the EAS9 is too much worse than the ANS and ANSn elements. However, the ANS and ANSn elements exhibit a stable tendency of convergence but cannot reach the desired value because Poisson's ratio is not equal to zero.

Table 4.1.3. Normalization of dimensionless deflection α - Clamped plate (υ = 0.3)

h/a	0.1		0.01		0.001		0.0001	
Mesh	2×2	4×4	2×2	4×4	2×2	4×4	2×2	4×4
Q1	0.38540	0.63140	0.00667	0.02428	0.00007	0.00025	0.007e-4	0.002e-3
EAS9	0.84413	0.95780	0.08126	0.59397	0.00087	0.01452	0.088e-4	0.148e-3
EAS15	0.93347	0.96627	0.96897	0.99579	0.96754	0.99413	0.95682	0.99960
ANS	0.78220	0.81200	0.78881	0.81254	0.78738	0.81095	0.79269	0.83643
ANSn	0.78220	0.81200	0.78881	0.81254	0.78738	0.81095	0.78809	0.81333
SS7	0.92860	0.96507	0.96278	0.99421	0.96103	0.99262	0.95087	1.02436
SS7n	0.92853	0.96507	0.96278	0.99421	0.96103	0.99262	0.96992	0.99897

Let's pass now to the case where the plate is simply supported at all edges, see Table 4.1.4. Locking response occurs in the case of Q1 - standard element. The EAS15 element show again its performance with a quick convergence toward the expected results but the EAS9 element continues to give poor result at high aspect ratio. The SS7n and SS7 solid-shell elements show good performance as the EAS15 at coarse mesh for thick and thin plate. As expected, the ANSn and ANS element behave better than the EAS9, as in the clamped case when the aspect ratio (a/h) is over 100.

Table 4.1.4. Normalization of dimensionless deflection α - Simply supported plate ($\upsilon = 0.3$)

h/a	0.1		0.01		0.001		0.0001	
Mesh	2×2	4×4	2×2	4×4	2×2	4×4	2×2	4×4
Q1	0.45014	0.69738	0.00916	0.03543	0.00009	0.00037	0.009e-4	0.004e-3
EAS9	0.95395	1.03089	0.14190	0.73649	0.00165	0.02737	0.165e-4	0.281e-3
EAS15	1.00977	1.03632	0.98173	0.99728	0.98097	0.99624	1.00235	0.99947
ANS	0.82675	0.84711	0.80011	0.81377	0.79944	0.81294	0.84025	0.78776
ANSn	0.82666	0.84653	0.80011	0.81377	0.79945	0.81294	0.83871	0.83123
SS7	1.00662	1.03589	0.97831	0.99648	0.97753	0.99544	0.99989	0.95143
SS7n	1.00649	1.03486	0.97831	0.99648	0.97754	0.99543	1.06946	1.04330

Table 4.1.5. Normalization of dimensionless deflection α - Clamped plate ($\upsilon = 0.0$)

h/a	0.1		0.01		0.001		0.0001	
Mesh	2×2	4×4	2×2	4×4	2×2	4×4	2×2	4×4
Q1	0.30742	0.60525	0.00469	0.01718	0.00005	0.00017	0.047e-5	0.002e-3
EAS9	0.78011	0.91660	0.05836	0.50669	0.00062	0.01024	0.620e-5	0.103e-3
EAS15	0.90605	0.92896	0.98001	0.99804	0.97902	0.99690	0.97884	1.00560
ANS	0.88575	0.92410	0.95492	0.99190	0.95391	0.99079	0.95011	0.97469
ANSn	0.88571	0.92408	0.95492	0.99192	0.95391	0.99079	0.93525	1.00998
SS7	0.88575	0.92410	0.95492	0.99192	0.95391	0.99079	0.95666	0.96606
SS7n	0.88571	0.92408	0.95492	0.99192	0.95391	0.99079	0.94112	0.97986

Table 4.1.6. Normalization of dimensionless deflection α - Simply supported plate ($\upsilon = 0.0$)

h/a	0.1		0.01		0.001		0.0001	
Mesh	2×2	4×4	2×2	4×4	2×2	4×4	2×2	4×4
Q1	0.39922	0.75090	0.00644	0.02526	0.00006	0.00026	0.006e-4	0.003e-3
EAS9	0.94032	1.04521	0.10388	0.66287	0.00116	0.01932	0.116e-4	0.197e-3
EAS15	1.02024	1.05355	0.98788	0.99888	0.98710	0.99770	1.02352	1.03863
ANS	1.00826	1.05032	0.97435	0.99565	0.97357	0.99446	1.08355	0.99346
ANSn	1.00769	1.04795	0.97435	0.99565	0.97355	0.99447	0.96104	1.01437
SS7	1.00951	1.05249	0.97435	0.99565	0.97358	0.99446	1.01366	0.96576
SS7n	1.00865	1.04932	0.97435	0.99566	0.97356	0.99447	1.00054	0.99384

In order to check performance of elements when there is no Poisson thickness locking, let's impose $\upsilon = 0.0$, see Tables 4.1.5 and 4.1.6. For both clamped and simply supported cases, the EAS9 element continues to give poor results when a/h > 100. Hence we can conclude that due to shear locking the EAS9 element shows bad performance. The ANS and ANSn elements are only shear locking free. When there is no Poisson thickness locking they behave as well as the SS7 and SS7n. Due to free from Poisson thickness locking, performance of the other elements (SS7, SS7n and EAS15) are almost similar to the case where Poisson thickness locking exists.

4.1.4 Square clamped plates with concentrated loads

A square plate of dimension a×a×h = 100×100×1 is clamped at all edges and loaded by a concentrated load P = 16.367 at the center. Material properties are $E = 10^4$ and $\upsilon = 0.3$. Due to symmetry one quadrant of the plate is modeled with one layer of 2×2 and 4×4 elements. The structure has been modeled with EAS elements by Andelfinger and Ramm [AND93].

By adopting the assumption on small displacements, analytical results on the center displacement can obtained thanks to the Kirchhoff's plate theory:

$$w = 0.0056\frac{Pa^2}{D} \quad \text{with} \quad D = \frac{Eh^3}{12(1-\nu^2)} \tag{4.1.5}$$

where D is the flexural stiffness of the plate.

Table 4.1.7. Center deflection

Mesh	2×2	4×4
Q1	0.00683	0.02516
EAS9	0.07342	0.55351
EAS15	0.87357	0.97050
ANS	0.71124	0.79194
ANSn	0.71124	0.79194
SS7	0.86773	0.96848
SS7n	0.86773	0.96848
Theory	1.0	

Applying (4.1.5), the theoretical displacement is imposed w = 1 at the center of the plate. Without the presence of geometrical (nonlinear) stiffness the EAS15, SS7n and SS7 elements give very good approximation, see Table 4.1.7.

This thin plate bending problem is modeled by coarse meshes, hence, the Q1 standard element is too stiff. Better results are given by the EAS9 element but with both very coarse mesh 2×2 and finer mesh 4×4 the EAS9 is always worse than the ANSn and ANS elements. The solid-shell elements who adopt the classical ANS technique (ANS and SS7) or the alternative ANS technique (ANSn and SS7n) behave identically in this test.

4.1.5 Simply supported square plate with various thickness and distorted mesh

This test illustrates the distorted mesh insensitivity of the solid-shell elements and their performance in shear locking and Poisson thickness locking removal at high aspect ratio (a/h ≤ 2000). Consider a plate of dimensions a×a×h (Figure 4.1.6) with a = 20 and different values of the thickness h (Table 4.1.8). The plate is simply supported along the four edges and loaded by a unit concentrated force at the center. Young's modulus is E = 10^7 and the Poisson's ratio is ν = 0.25. The problem is symmetric, hence, only one quarter of the plate is considered in two cases: regular mesh and distorted mesh of 4×4 elements (Figure 4.1.6).

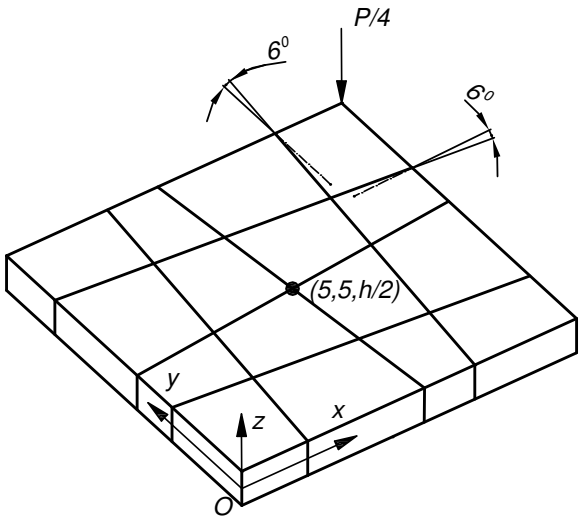

Figure 4.1.6: A quarter of the plate - distorted mesh

Table 4.1.8. Regular mesh - Normalization of displacement

h	Q1	ASQBI	NEW-HEX	EAS9	ANSn, ANS	SS7n, SS7
1.5	0.667	1.089	1.089	1.070	0.965	1.080
1.0	0.454	1.039	1.039	1.014	0.921	1.034
0.5	0.173	1.009	1.009	0.935	0.894	1.005
0.1	0.008	0.999	0.999	0.377	0.885	0.995
0.05	0.002	0.999	0.999	0.133	0.884	0.995
0.01	8.4e-5	0.999	0.999	0.006	0.884	0.995

Table 4.1.9. Irregular mesh - Normalization of displacement

h	Q1	ASQBI	NEW-HEX	EAS9	ANSn, ANS	SS7n, SS7
1.5	0.660	1.090	1.090	1.064	0.964	1.079
1.0	0.449	1.040	1.040	0.994	0.920	1.033
0.5	0.172	0.990	0.990	0.873	0.893	1.003
0.1	0.008	0.680	0.700	0.236	0.883	0.994
0.05	0.002	-	-	0.073	0.883	0.993
0.01	8.5e-5	-	-	0.003	0.883	0.993

The analytical solution of displacement at the center of this problem is given by (3.6.1b). Numerical solutions are listed in Table 4.1.8 for the regular mesh and in Table 4.1.9 for the distorted mesh.

Results from the SS7n and ANSn elements are compared with results of the EAS9, ASQBI of Belytschko and Bindeman [BEL93] and with NEWHEX of Fredriksson and Ottosen [FRE07]. When the aspect ratio is less than 40 (i.e., h > 0.5), all the elements, except Q1, give good results for both regular and distorted meshes. When the aspect ratio is larger than 200 (i.e., h < 0.1) ASQBI and NEWHEX only give good results for regular mesh while results of the EAS9 deteriorate rapidly even for regular mesh. On the contrary, the behavior of ANSn and SS7n is stable with both distortion and high aspect ratio (a/h = 2000). These elements can thus be considered as robust.

4.1.6 Pinched cylinder with rigid end diaphragms

Consider a cylinder of inner radius r = 300, thickness t = 3 and length L = 600, see Figure 4.1.7. Young's modulus is $E = 3\times10^6$ and the Poisson's ratio is $\nu = 0.3$. The concentrated forces F = 1 apply at the mid-length of the cylinder.

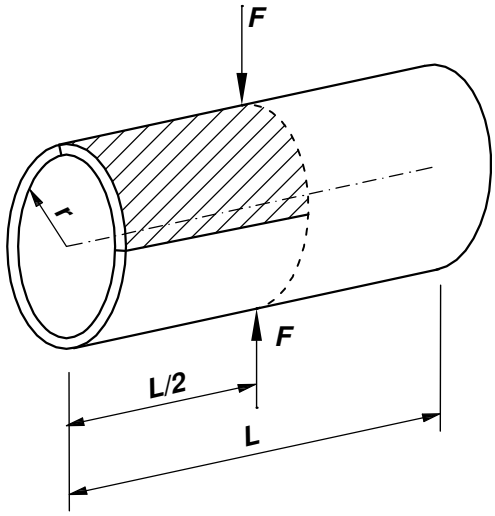

Figure 4.1.7: Pinched cylinder with two rigid end diaphragms

Reference deflection $w = 1.8248\times10^{-5}$ is coincident with the loaded points. Due to symmetry only one-eighth of the cylinder is modeled. The structure is dominated by inextensional bending response hence membrane locking may occur. Furthermore, the thin structure with highly curve geometry also cause curvature thickness locking and shear locking.

In this test a solid-shell element, ANS3DEAS, of Hauptmann and Schweizerhof [HAU98] is used for comparison. The ANS3DEAS adopts the ANS method for transverse shear locking removal and adopts the EAS method to enhance the membrane strains. The ANS3DEAS element is superior in membrane dominated problems as stated in [HAU98]. Mindlin shell and the solid-shell element of Samcef [JET08], see Section 4.1.2, are also taken into comparison.

Figure 4.1.8 shows that the vertical displacements of the alternative ANS method, ANSn element (only with N < 100) and SS7n element, are better than ANS3DEAS and

the EAS elements. The SS7n, EAS15 and ANS3DEAS elements converge with very fine mesh (32×32). The Samcef solid-shell element behaves as well as the SS7n element. The Mindlin (Samcef) element converges at very coarse mesh; but does not provide the correct result when the mesh is finer.

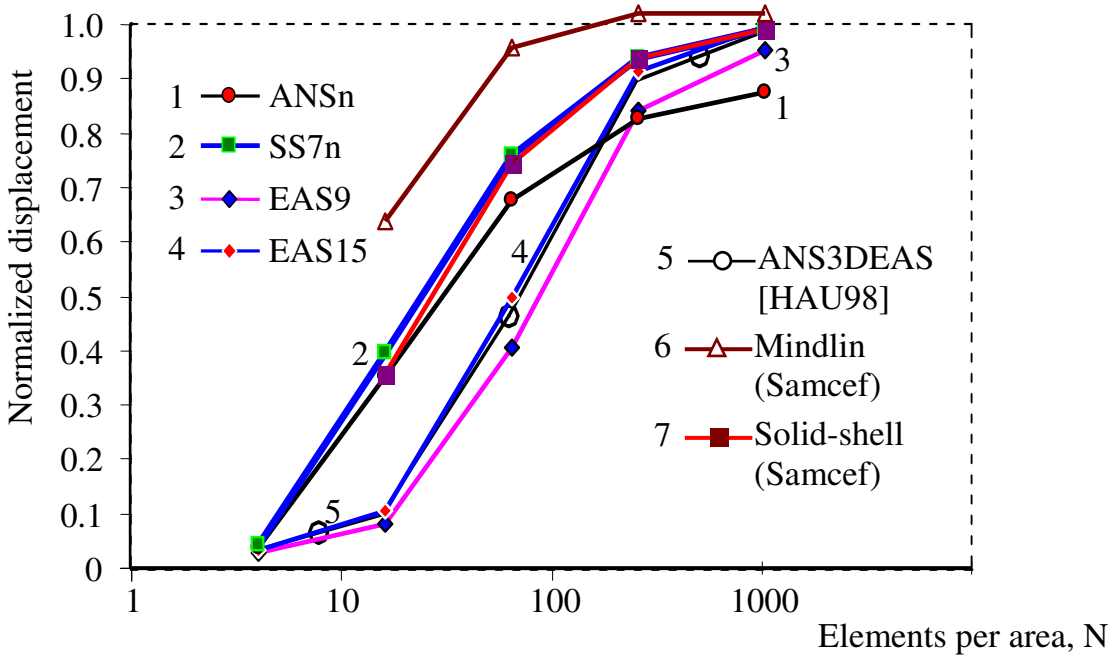

Figure 4.1.8: Convergence investigation for the pinched cylinder

4.1.7 Morley spherical shell

A benchmark test for shell elements of McNeal and Harder [MAC85] is considered. The structure consists of a thin hemispherical shell, Figure 4.1.9. The middle radius of the shell is R = 10, the thickness t = 0.04. Material properties are elastic modulus E = 6.825×10^7 and Poisson's ratio υ = 0.3. Concentrated loads F of opposite signs position at every 90° in the equatorial plane.

Table 4.1.10. Morley spherical shell - Normalized displacements at test point

Mesh	Q1	EAS9	EAS15	ANSn, ANS	SS7n, SS7
2×2	1.064e-4	3.192e-4	4.255e-4	0.985	1.053
4×4	0.001	0.010	0.040	1.022	1.036
8×8	0.003	0.163	0.746	0.997	1.003
16×16	0.010	0.750	0.989	0.991	0.998
32×32	0.038	0.96	0.984	0.979	0.984

The theoretical displacement of test point is u = 0.0940. Because of the symmetry, a one-fourth of the structure needs to be modeled. One element over thickness will be fixed for all computation while different kinds of mesh in other directions will be tried.

Computed results with the EAS elements as well as the solid-shell elements are compared.

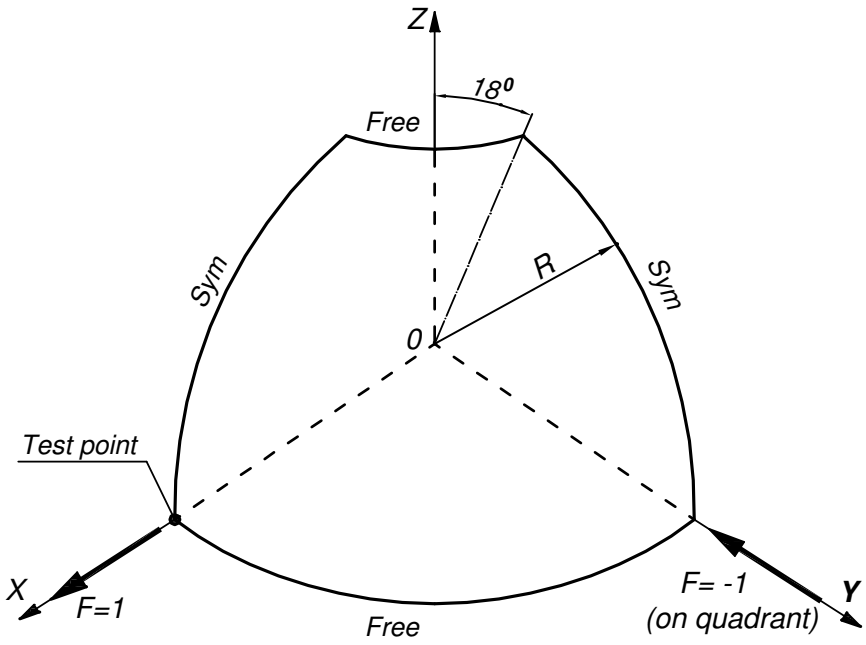

Figure 4.1.9: Morley spherical shell

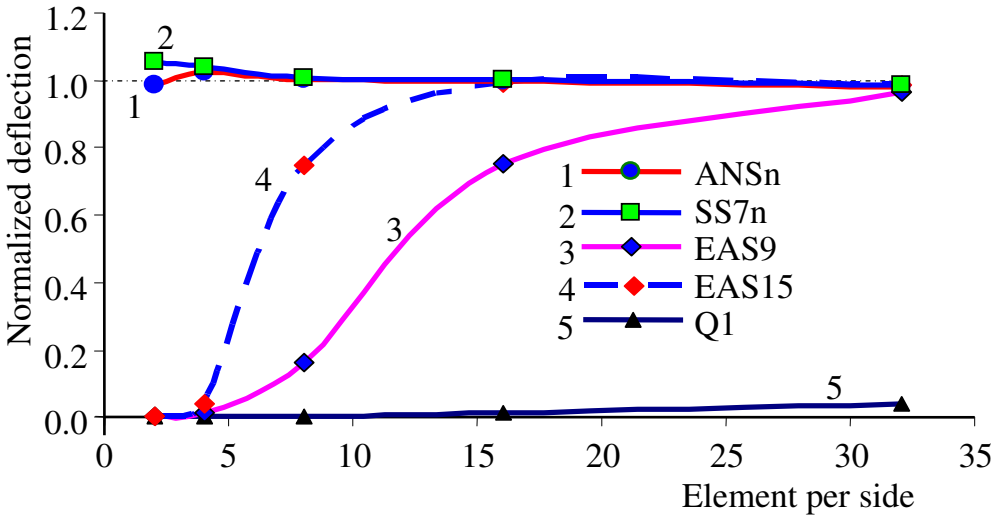

Figure 4.1.10: Convergence of finite element solution

As the spherical shell is very thin, 3D modeling may lead to an ill-conditioned problem, since the distance between two corresponding nodes in the thickness direction is too small in comparison to other directions in the case of a too coarse mesh. Hence, a refinement of mesh will be helpful to handle this problem. Figure 4.1.10 shows results of the solid-shell elements versus the EAS and standard elements with variety of meshes. The EAS9 converges to the exact solution for a very fine mesh (32×32) while the EAS15 converges for a coarser mesh (16×16). However, the solid-shell elements give good

results even at extremely coarse mesh (2×2). The classical ANS elements, ANS and SS7 elements, and the alternative ones, ANSn and SS7n elements, are in this case, totally equivalent.

4.1.8 Thick-walled cylinder

Expansion of a thick cylinder with various Poisson's ratio (ν = 0-0.4999) as described in [MAC85] is considered to investigate the performance of the solid-shell elements in volumetric locking conditions. Elastic modulus is E = 1000. The inner radius of the cylinder is R_i = 3.0, the outer radius is R_o = 9.0 and the thickness is t = 1.0, see Figure 4.1.11. Plane strain conditions are assumed in the thickness direction. The inner surface of the cylinder is loaded by a pressure q = 1/unit area.

A part of the cylinder, as described in Figure 4.1.11, is modeled by a 5×1 mesh. The analytical solution of the problem is given by

$$u = \frac{(1+\nu)pR_i^2}{E(R_o^2 - R_i^2)}[R_o^2/r + (1-2\nu)r] \tag{4.1.6}$$

Numerical solutions, at the inner radius, of elements are tabulated in Table 4.1.11. The results show that the ANS and ANSn elements deliver identical results. The same remark is also shown by the SS7 and SS7n elements. Obviously, volumetric locking response can be observed for the Q1 element. Since volumetric locking cannot be removed by the ANS techniques, the ANS element's response is nearly as stiff as the Q1 standard element for this problem.

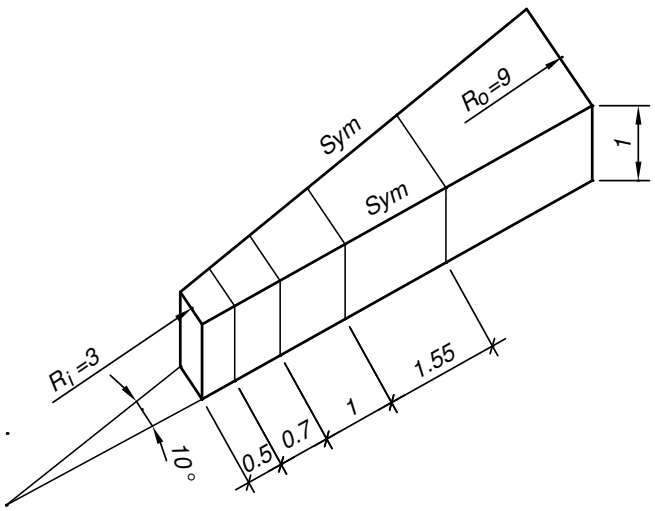

Figure 4.1.11: Thick-walled cylinder

This volumetric locking can be removed with the use of the EAS internal parameters, or more precisely with the introduction of enhanced volumetric modes. Indeed, the ANS technique combined with the EAS technique to result in the solid-shell elements, SS7 and SS7n. The solid-shell elements are free from not only shear locking but also volumetric locking, see Table 4.1.11. Moreover, numerical results show the

EAS9 elements, with 3 volumetric locking modes, and the EAS21, with 9 volumetric locking modes, give almost exact results as the SS7n.

Table 4.1.11. Normalized radial displacement at R_i

ν	Q1	ANSn, ANS	EAS9	EAS21	SS7n, SS7
0.0	0.993	0.996	0.998	0.998	0.998
0.25	0.989	0.992	0.996	0.996	0.996
0.30	0.987	0.990	0.995	0.995	0.995
0.49	0.845	0.848	0.991	0.991	0.991
0.499	0.358	0.360	0.990	0.990	0.990
0.4999	0.053	0.053	0.990	0.990	0.990

4.2 NONLINEAR APPLICATIONS

In this section we investigate performances of the ANSn and SS7n elements in nonlinear problems. All locking effects (shear locking, membrane locking and volumetric locking) are presented in problems.

4.2.1 Cantilever in large displacement

Consider a cantilever under transverse line load, see Figure 4.2.1. Geometry of the cantilever are L×b×h = 10×1×0.1. The elastic modulus is $E = 2.1\times10^5$ and Poisson's ratio is $\upsilon = 0.3$. The cantilever is clamped at one end and suffer a line load $q_0 = 1$ at the other end. Reference solution is numerical results of ANS3DEAS element (see Section 4.1.6) of Hauptmann et al. [HAU01].

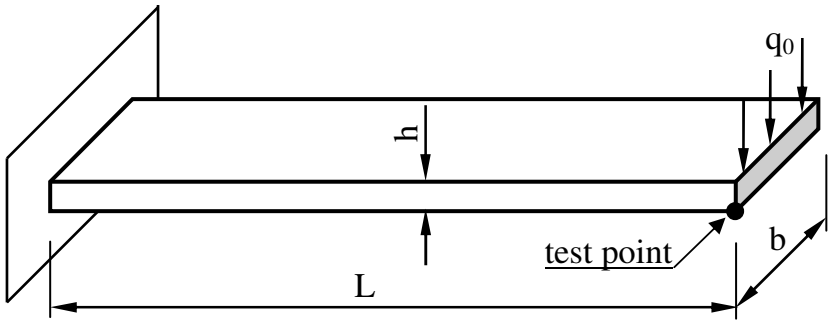

Figure 4.2.1: Cantilever beam

A discretization with a mesh of 10×1×1 elements is used. The load - displacement diagram in Figure 4.2.2 is obtained by using ten equal load steps. It is shown that when the applied load is small or moderate, $q < 0.3q_0$, the EAS15 element performs as well as the SS7n and ANS3DEAS (Hauptmann et al. [HAU98]) elements while the ANSn element is a little stiffer because of Poisson effect. When the applied load continues increasing, the EAS15, due to transverse shear locking, becomes as stiff as the ANSn element due to Poisson thickness locking. Meanwhile the other elements, SS7n and ANS3DEAS, give identically better results than ANSn and EAS15 do.

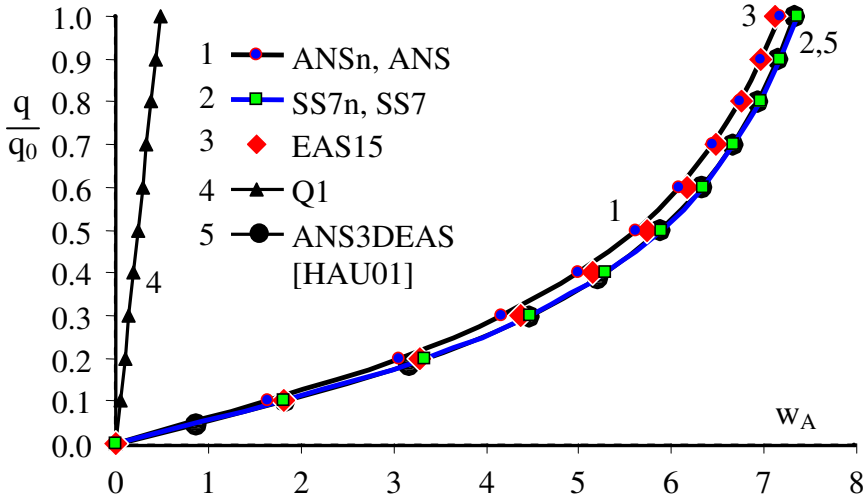

Figure 4.2.2: Displacement of test point

4.2.2 Morley spherical shell – large deformation case

The same data are given as the numerical test in Section 4.1.7 except the thickness is thinner, t = 0.01 and the applied load is larger F=5.0. The mesh is composed of 16×16×1 elements. The total load is applied in 15 equal steps. The problem was considered by Vu-Quoc and Tan [QUO03a] and Klinkel et al. [KLI06] for investigating behavior of their solid-shell elements. This test is considered as one of the most severe bench-mark problems for nonlinear analysis of shell [QUO03a].

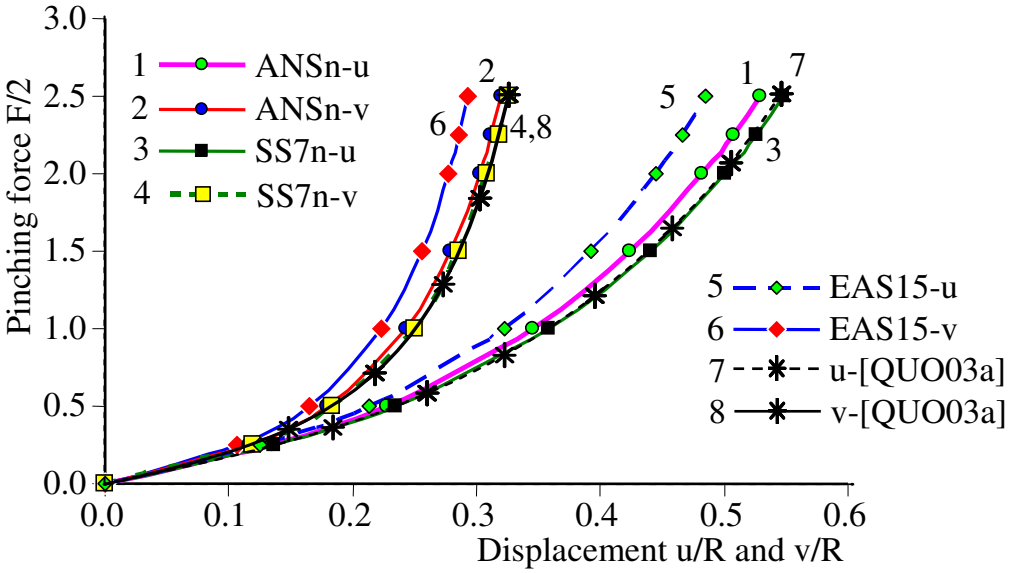

Figure 4.2.3: Load-deflection curves for displacements at points A(u) and B(v)

The inward and outward displacements at the point A and B are plotted versus the pinching load, see Figure 4.2.3. Both membrane and bending strains contribute to the displacements at the load points. The structure is a doubly-curved shell with high aspect

ratio (R/t = 1000), hence, curvature thickness locking, transverse shear locking and membrane locking may simultaneously occur. From Table 4.2.1 the data show that the presented solid-shell element (SS7n) is quite equivalent to the solid-shell element of Vu-Quoc and Tan. Compare with the EAS9 and EAS15, the ANSn element, which is free from shear locking and curvature thickness locking, deliver a very good result. Hence, we can conclude that transverse shear locking and curvature thickness locking are the reason for bad performance of the EAS9 and EAS15 elements in this problem.

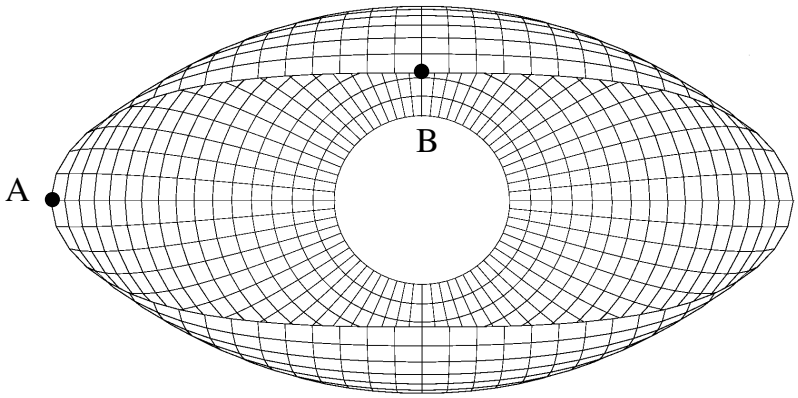

Figure 4.2.4: Deformed hemisphere at F = 5
(without any magnification)

Table 4.2.1: Displacements due to pinched force F = 5

Element	u_A	u_A/u_{ref}	v_B	v_B/v_{ref}
EAS9	2.30850	0.42100	1.69930	0.52117
EAS15	4.85402	0.88523	2.92634	0.89750
ANSn	5.29089	0.96491	3.19503	0.97991
SS7n	5.47885	0.99920	3.26135	1.00024
Reference [QUO03a]	5.48331	1.00000	3.26055	1.00000

4.2.3 Slit annular plate under line force

A circular annular plate has a slit cut (line AB, Figure 4.2.5) along the radial direction. The plate is clamped at one end of the slit and suffers a line force p = 0.8 at the free end. The inner radius is $R_i = 6$, the outer radius is $R_o = 10$, the plate thickness is h = 0.03. Young modulus is $E = 21.0\times10^6$ and Poisson's ratio is $\upsilon = 0.0$. The total load is applied in 10 equal steps. A mesh of 6×30×1 elements is used to model the plate.

Reference solution is numerical result of HS hybrid-stress solid-shell element of Sze et al. [SZE02]. The HS element adopts the ANS method for transverse shear locking and trapezoidal locking removals; and stress components are assumed independently from the ones obtained from the displacement field. Numerical results of the HS element are: vertical displacement at point A: $w_A = 13.618$; vertical displacement at point B: $w_B = 17.257$.

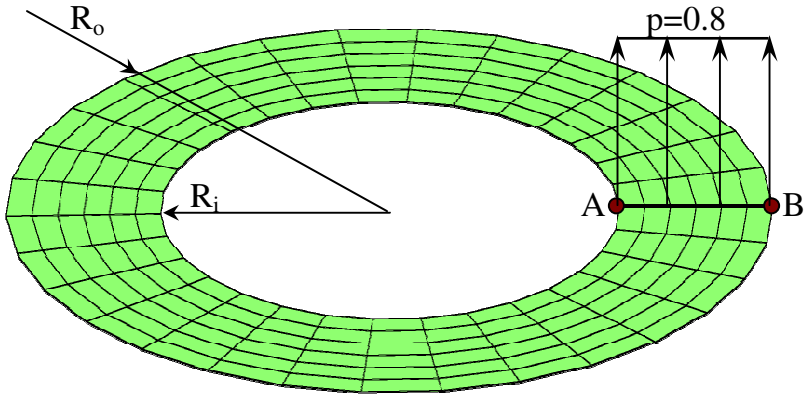

Figure 4.2.5: Slit annular plate - initial configuration

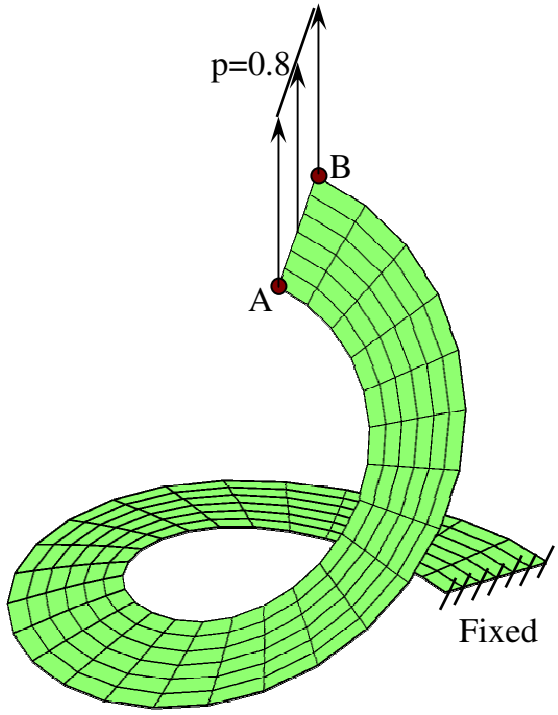

Figure 4.2.6: The deformed configuration at maximum load
(without any magnification)

The annular plate is a thin-walled structure (R/h > 300), hence, transverse shear locking may appear. From numerical results in Figure 4.2.7, we see that the SS7n element performs as well as the HS element of Sze et al. The ANSn element is slightly stiffer than the SS7n and HS elements. Normally, when Poisson's ratio is equal to zero, if only transverse shear locking exists, the ANSn and SS7n should give similar results. In this test, maybe membrane locking occurs, hence, the ANSn is little stiffer than the SS7n. Due to transverse shear locking and high aspect ratio, the EAS9 element behaves too stiff but still too much better than the Q1 standard element.

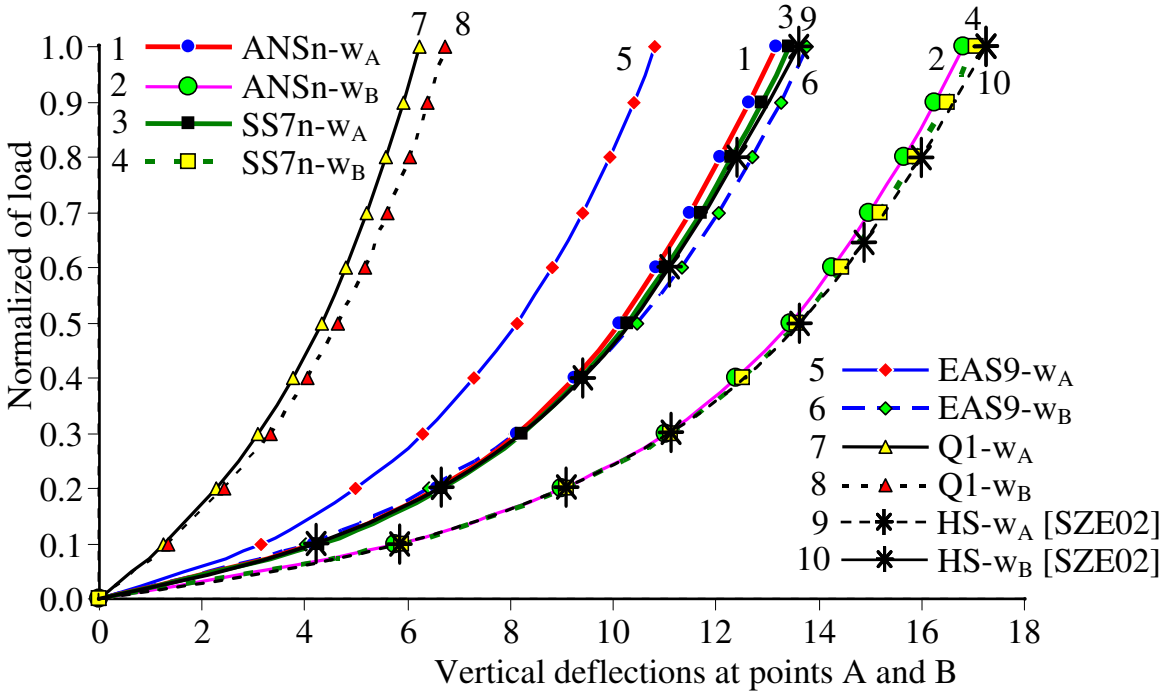

Figure 4.2.7: Load-deflection curves for displacements at points A and B

CONCLUSION

In this chapter, various bench-mark tests (linear and nonlinear problems with various locking effects) have been invoked to demonstrate performance for the SS7n solid-shell element. The SS7n shows good performances for incompressible behavior and for bending behavior of thin and thick-walled structures. However, all of the numerical tests in this chapter are limited to linear material model. In comparison with the classical shell elements, the solid-shell elements allow a straightforward integration of 3D material models since they do not resort to the plane stress assumption. This advantage especially becomes important for implementation of nonlinear material models. This argument is assured in the next chapter, where performances of the SS7n element with nonlinear material models are considered.

Chapter 5. PLASTIC APPLICATIONS

INTRODUCTION

In the last chapter, applications of the SS7n element in linear elasticity and nonlinear elasticity were presented. In order to exploit its performances in plasticity field, the SS7n element has been also implemented in FEAP (Finite Element Analysis Program, [TAY01]). In this chapter we investigate plastic behavior of the ANSn and SS7n elements. First of all, available plastic theory in FEAP is briefly presented. Then, numerical tests are investigated to look for differences in plastic behavior between ANS and ANSn techniques. To carry out that work, stresses in largely plasticity-deformed structures are analysed. Later, apart from the just mentioned tests, a special care is taken for a springback simulation. Springback or elastic recovery relates to the change in shape between the fully loaded and unloaded configurations that the material encounters during a stamping operation. This results in the stamping component being out of tolerance and can create major problems in the assembly or installation. Springback prediction of sheet metal after forming is an important issue in controlling the manufacturing processes. To this end, a benchmark test for high strength steel will be investigated with the ANSn and SS7n elements.

5.1 FINITE STRAIN THEORY

5.1.1 Multiplicative split

Consider a body Ω which contains a line vector $d\boldsymbol{X}$ before deformation (*initial configuration*). After deformed to the *current configuration*, the line vector $d\boldsymbol{X}$ is transformed to $d\boldsymbol{x}$ by a transformation mapping $\boldsymbol{F}$ (Figure 5.1.1). The line vector $d\boldsymbol{X}$ has undergone both elastic and plastic deformation to be transformed to $d\boldsymbol{x}$. The *intermediate configuration* is defined as in which the line vector $d\boldsymbol{x}$ has been unloaded to a stress free state, characterized by line vector $d\boldsymbol{p}$. In other words, the line vector $d\boldsymbol{X}$ in initial configuration has undergone purely plastic deformation to become the line vector $d\boldsymbol{p}$ in the intermediate configuration. That pure plastic transformation can be expressed by:

$$d\boldsymbol{p} = \boldsymbol{F}^{p} d\boldsymbol{X} \tag{5.1.1}$$

And the pure elastic transformation from the intermediate configuration to the current configuration is realized by:

$$d\boldsymbol{x} = \boldsymbol{F}^{e} d\boldsymbol{p} \tag{5.1.2}$$

Then we can write:

$$d\boldsymbol{x} = \boldsymbol{F}^{e} d\boldsymbol{p} = \boldsymbol{F}^{e}\boldsymbol{F}^{p} d\boldsymbol{X} \tag{5.1.3}$$

The finite strain plasticity formulation relies on the local multiplicative decomposition of the deformation gradient $\boldsymbol{F}$ that is derived from (5.1.3) as:

$$\boldsymbol{F} = \boldsymbol{F}^{e}\boldsymbol{F}^{p} \tag{5.1.4}$$

where $\boldsymbol{F}^{e}$ is the deformation caused by the elastic stretching and rotation and $\boldsymbol{F}^{p}$ is the plastic deformation. This is the classical multiplicative decomposition of Lee, see [SIM88a].

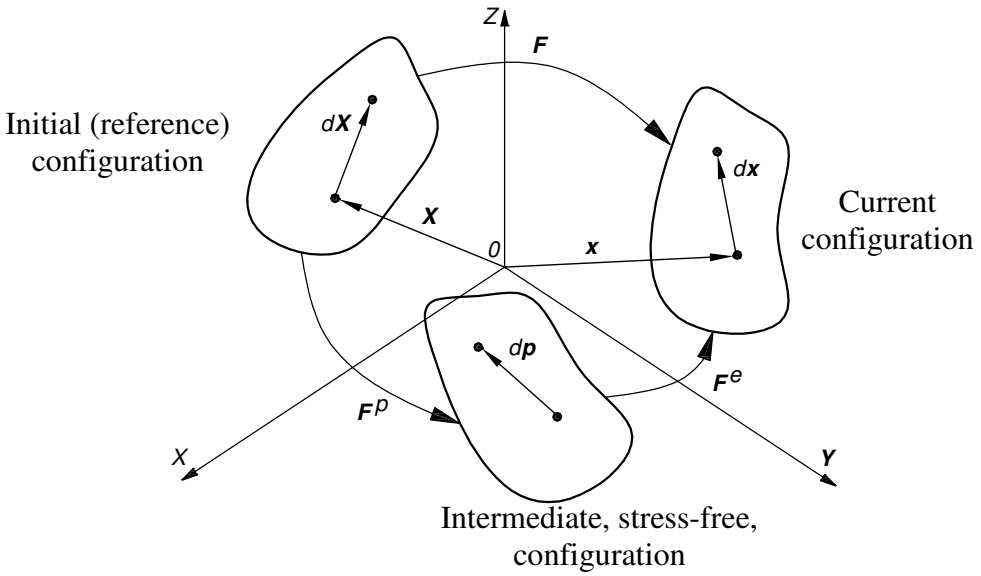

Figure 5.1.1: Schematic diagram of multiplicative decomposition

Due to the total Lagrange formulation of the variational equations for the solid-shell elements, the plasticity model hereafter will be formulated using the right Cauchy strain tensor. As pointed out by Simo [SIM88a], the return-mapping algorithm of infinitesimal plasticity can be carried over to the presented formulation without any modification. With the hyperelastic models, the elastic predictor in the return-mapping algorithm is exactly calculated by using the strain energy function. The Green-Lagrange strain tensor is defined relatively to the reference configuration as:

$$\begin{aligned} \boldsymbol{E} &= \frac{1}{2}(\boldsymbol{F}^{T}\boldsymbol{F} - \boldsymbol{I}) = \frac{1}{2}(\boldsymbol{C} - \boldsymbol{I}) \quad \text{with} \quad \boldsymbol{C} = \boldsymbol{F}^{T}\boldsymbol{F} \\ \boldsymbol{E}^{p} &= \frac{1}{2}(\boldsymbol{F}^{pT}\boldsymbol{F}^{p} - \boldsymbol{I}) = \frac{1}{2}(\boldsymbol{C}^{p} - \boldsymbol{I}) \quad \text{with} \quad \boldsymbol{C}^{p} = \boldsymbol{F}^{pT}\boldsymbol{F}^{p} \end{aligned} \tag{5.1.5}$$

where $\boldsymbol{C}$ is the right Cauchy strain tensor.

Consider a general form of strain energy function:

$$W = W(\boldsymbol{C}, \boldsymbol{C}^{p}) \tag{5.1.6}$$

Assuming hyperelastic response, the second Piola-Kirchhoff stress tensor $\boldsymbol{S}$ is defined as:

$$\boldsymbol{S} = 2\frac{\partial W(\boldsymbol{C}, \boldsymbol{C}^{p})}{\partial \boldsymbol{C}} \tag{5.1.7}$$

5.1.2 Yield condition

Consider a yield surface defined in strain space with a general functional form given by

$$\Phi(\boldsymbol{C},\boldsymbol{C}^p,\boldsymbol{Q}) \le 0 \tag{5.1.8}$$

where $\boldsymbol{Q}$ is a suitable set of internal plastic variable vector.

The evolution of the internal plastic variable vector $\boldsymbol{Q}$ can be determined by a rate equation in the form:

$$\dot{\boldsymbol{Q}} = \dot{\gamma}\,\boldsymbol{H}(\boldsymbol{C},\boldsymbol{C}^p,\boldsymbol{Q}) \tag{5.1.9}$$

where $\boldsymbol{H}(\boldsymbol{C},\boldsymbol{C}^p,\boldsymbol{Q})$ is a prescribed function of the generalized plastic hardening moduli; the initial condition is $\boldsymbol{Q}=\boldsymbol{0}$ at the reference configuration. The term γ is plastic consistency parameter.

5.1.3 Flow rule

As in the infinitesimal theory, in this section, beginning with the principle of maximum plastic dissipation, the evolution of plastic flow is expressed directly in terms of kinematic variables related to the multiplicative decomposition.

Without loss of generality, the elastoplastic behavior is assumed to be characterized by variables $\{\boldsymbol{C},\boldsymbol{C}^p,\boldsymbol{Q}\}$. Furthermore, assume that an elastoplastic potential function can be decoupled into internal-independent contribution $W^C(\boldsymbol{C},\boldsymbol{C}^p)$ and internal-dependent contribution $W^Q(\boldsymbol{Q})$ as:

$$W = W^C(\boldsymbol{C},\boldsymbol{C}^p) + W^Q(\boldsymbol{Q}) \tag{5.1.10}$$

The plastic dissipation at the state defined by $\{\boldsymbol{C},\boldsymbol{C}^p,\boldsymbol{Q}\}$ is:

$$D^p(\boldsymbol{C},\boldsymbol{C}^p,\boldsymbol{Q};\dot{\boldsymbol{C}}^p,\dot{\boldsymbol{Q}}) = -\left(\frac{\partial W}{\partial \boldsymbol{C}^p}:\dot{\boldsymbol{C}}^p + \frac{\partial W}{\partial \boldsymbol{Q}}:\dot{\boldsymbol{Q}}\right) \tag{5.1.11}$$

In local form, the maximum plastic dissipation formulated in strain space may be stated as follows. Give a state $\{\boldsymbol{C},\boldsymbol{C}^p,\boldsymbol{Q}\}$ among all admissible right Cauchy strain tensors satisfying the yield criterion, the actual strain tensor $\boldsymbol{C}$ is the one for which plastic dissipation attains its maximum. Let's consider the maximum plastic dissipation in point of view of optimization theory, the problem may be stated as:

$$\begin{aligned} &\text{Maximize } \{\, D^p(\boldsymbol{C},\boldsymbol{C}^p,\boldsymbol{Q};\dot{\boldsymbol{C}}^p,\dot{\boldsymbol{Q}}) = -\left[\frac{\partial W}{\partial \boldsymbol{C}^p}:\dot{\boldsymbol{C}}^p + \frac{\partial W}{\partial \boldsymbol{Q}^p}:\dot{\boldsymbol{Q}}\right] \} \\ &\text{subject to } K^C = \{\boldsymbol{C} \in R^6 \,\big|\, \Phi(\boldsymbol{C},\boldsymbol{C}^p,\boldsymbol{Q}) \le 0\} \end{aligned} \tag{5.1.12}$$

where K_C is the space of admissible right Cauchy strain tensors at fixed plastic variables $\{\boldsymbol{C}^p,\boldsymbol{Q}\}$; tensor $\boldsymbol{C}$ is symmetric, hence, consists of 6 independent components.

As shown in (5.1.10) and (5.1.11), with a fixed set of $\{\boldsymbol{C}^p,\boldsymbol{Q}\}$ → $\frac{\partial W}{\partial \boldsymbol{Q}}:\dot{\boldsymbol{Q}}$ constant, the maximum of D^p only depends on the term $[-\frac{\partial W^C(\boldsymbol{C},\boldsymbol{C}^p)}{\partial \boldsymbol{C}^p}:\dot{\boldsymbol{C}}^p]$. Hence, the

maximum of D^p is equivalent to the minimum of $[\frac{\partial W^C(\boldsymbol{C},\boldsymbol{C}^p)}{\partial \boldsymbol{C}^p}:\dot{\boldsymbol{C}}^p]$. Thus, the maximum plastic dissipation problem can be changed to:

$$\begin{aligned} &\text{Minimize } \{[\frac{\partial W^C(\boldsymbol{C},\boldsymbol{C}^p)}{\partial \boldsymbol{C}^p}:\dot{\boldsymbol{C}}^p]\} \\ &\text{subject to } K^C=\{\boldsymbol{C}\in R^6 \,\big|\, \Phi(\boldsymbol{C},\boldsymbol{C}^p,\boldsymbol{Q})\le 0\} \end{aligned} \tag{5.1.13}$$

STRAIN-BASED ELASTOPLASTIC CONSTITUTIVE MODEL

1. *Step 1*: Multiplicative decomposition

$$\boldsymbol{F}=\boldsymbol{F}^e\boldsymbol{F}^p$$
$$\boldsymbol{C}=\boldsymbol{F}^T\boldsymbol{F}$$
$$\boldsymbol{C}^p=\boldsymbol{F}^{pT}\boldsymbol{F}^p$$

2. *Step 2*: Hyperelastic stress-strain relations

$$\boldsymbol{S}=2\frac{\partial W^C(\boldsymbol{C},\boldsymbol{C}^p)}{\partial \boldsymbol{C}}$$

3. *Step 3:* constitutive tensors
   - Elastic:
$$^4\boldsymbol{C}=4\frac{\partial^2 W^C}{\partial \boldsymbol{C}\partial \boldsymbol{C}}$$
   - Plastic
$$\boldsymbol{M}=4\frac{\partial^2 W^C}{\partial \boldsymbol{C}\partial \boldsymbol{C}^p}$$

4. *Step 4:* Flow rule

$$\dot{\boldsymbol{S}}^p:=-\frac{1}{2}\boldsymbol{M}(\boldsymbol{C},\boldsymbol{C}^p):\dot{\boldsymbol{C}}^p$$
$$\dot{\boldsymbol{S}}^p=2\dot{\gamma}\frac{\partial \Phi(\boldsymbol{C},\boldsymbol{C}^p,\boldsymbol{Q})}{\partial \boldsymbol{C}}$$

5. *Step 5:* Hardening law

$$\dot{\boldsymbol{Q}}=\dot{\gamma}\boldsymbol{H}(\boldsymbol{C},\boldsymbol{C}^p,\boldsymbol{Q})$$

6. *Step 6:* Loading/unloading conditions

$$\dot{\gamma}\ge 0\ ;\ \ \Phi(\boldsymbol{C},\boldsymbol{C}^p,\boldsymbol{Q})\le 0$$
$$\dot{\gamma}\Phi(\boldsymbol{C},\boldsymbol{C}^p,\boldsymbol{Q})=0$$

Figure 5.1.2: Finite strain theory

We can solve the problem (5.1.13) by the method of Lagrange multipliers to inequality constraints. The Lagrange functional for the problem (5.1.13) is defined:

$$L^p=\frac{\partial W^C(\boldsymbol{C},\boldsymbol{C}^p)}{\partial \boldsymbol{C}^p}:\dot{\boldsymbol{C}}^p+\dot{\gamma}\Phi(\boldsymbol{C},\boldsymbol{C}^p,\boldsymbol{Q}) \tag{5.1.14}$$

where $\dot{\gamma}$ is positive and belongs to the set of square integrable $L^2(\Omega)$ functions, that defined by the positive cone K^p:

$$K^p = \{\dot{\gamma} \in L^2(\Omega) \,\big|\, \dot{\gamma} \geq 0\} \tag{5.1.15}$$

Resulting from (5.1.14) and (5.1.15), the Kuhn-Tucker conditions are:

$$\left.\begin{aligned} &\frac{\partial L^p}{\partial \boldsymbol{C}} = 0 \Leftrightarrow \dot{\boldsymbol{S}}^p = -\frac{1}{2}\boldsymbol{M}(\boldsymbol{C},\boldsymbol{C}^p) : \dot{\boldsymbol{C}}^p = 2\dot{\gamma}\,\frac{\partial \Phi(\boldsymbol{C},\boldsymbol{C}^p,\boldsymbol{Q})}{\partial \boldsymbol{C}} \\ &\dot{\gamma} \geq 0 \\ &\Phi(\boldsymbol{C},\boldsymbol{C}^p,\boldsymbol{Q}) \leq 0 \\ &\dot{\gamma}\,\Phi(\boldsymbol{C},\boldsymbol{C}^p,\boldsymbol{Q}) = 0 \end{aligned}\right\} \tag{5.1.16}$$

where the constitutive tensor $\boldsymbol{M}(\boldsymbol{C},\boldsymbol{C}^p) = 4\dfrac{\partial^2 W^C(\boldsymbol{C},\boldsymbol{C}^p)}{\partial \boldsymbol{C}\partial \boldsymbol{C}^p}$.

The flow rule (5.1.16a) and loading/unloading conditions (5.1.16b-d) are associative with the multiplicative decomposition (5.1.4). The presented theory is summarized in Figure 5.1.2.

5.1.4 Elastoplastic tangent moduli

The requirement for the load point to remain on the yield surface during plastic deformation is called the consistency condition. It enables to determine the plastic multiplier $\dot{\gamma}$. This condition states that plastic loading ($\dot{\gamma} \geq 0$) requires $\partial \Phi(\boldsymbol{C},\boldsymbol{C}^p,\boldsymbol{Q})/\partial t = 0$ as:

$$\frac{\partial \Phi(\boldsymbol{C},\boldsymbol{C}^p,\boldsymbol{Q})}{\partial t} = \dot{\Phi}(\boldsymbol{C},\boldsymbol{C}^p,\boldsymbol{Q}) = 2\frac{\partial \Phi}{\partial \boldsymbol{C}} : \dot{\boldsymbol{C}} + 2\frac{\partial \Phi}{\partial \boldsymbol{C}^p} : \dot{\boldsymbol{C}}^p + \frac{\partial \Phi}{\partial \boldsymbol{Q}} : \dot{\boldsymbol{Q}} = 0 \tag{5.1.17}$$

or

$$2\frac{\partial \Phi}{\partial \boldsymbol{C}} : \dot{\boldsymbol{C}} = \text{-}[2\frac{\partial \Phi}{\partial \boldsymbol{C}^p} : \dot{\boldsymbol{C}}^p + \frac{\partial \Phi}{\partial \boldsymbol{Q}} : \dot{\boldsymbol{Q}}] \tag{5.1.18}$$

Calculate $\dot{\boldsymbol{C}}^p$ from (5.1.16a) then introduce the result into (5.1.18) we can derive the expression for the plastic consistency parameter:

$$\dot{\gamma} = \frac{2\dfrac{\partial \Phi}{\partial \boldsymbol{C}} : \dot{\boldsymbol{C}}}{8\dfrac{\partial \Phi}{\partial \boldsymbol{C}^p} : \boldsymbol{M}^{-1} : \dfrac{\partial \Phi}{\partial \boldsymbol{C}} - \dfrac{\partial \Phi}{\partial \boldsymbol{Q}} : \boldsymbol{H}} \tag{5.1.19}$$

Time differentiating of the elastic constitutive equation (5.1.7) we have:

$$\dot{\boldsymbol{S}} = 4\frac{\partial^2 W}{\partial \boldsymbol{C}\partial \boldsymbol{C}} : \dot{\boldsymbol{C}} + 4\frac{\partial^2 W}{\partial \boldsymbol{C}\partial \boldsymbol{C}^{\boldsymbol{p}}} : \dot{\boldsymbol{C}}^{\boldsymbol{p}} = \boldsymbol{A} : \dot{\boldsymbol{C}} \text{-} 4\dot{\gamma}\frac{\partial \Phi}{\partial \boldsymbol{C}} \tag{5.1.20}$$

where $\boldsymbol{A} = 4\dfrac{\partial^2 W}{\partial \boldsymbol{C}\partial \boldsymbol{C}}$ and $\dfrac{\partial^2 W}{\partial \boldsymbol{C}\partial \boldsymbol{C}^{\boldsymbol{p}}} : \dot{\boldsymbol{C}}^{\boldsymbol{p}} = \text{-}\dot{\gamma}\dfrac{\partial \Phi}{\partial \boldsymbol{C}}$ from (5.1.16a).

By inserting (5.1.19) into (5.1.20) we have the expression:

$$\dot{\boldsymbol{S}} = \boldsymbol{A}^{ep} : \dot{\boldsymbol{C}} \tag{5.1.21}$$

with the elastoplastic tangent moduli: $\boldsymbol{A}^{ep} = \boldsymbol{A} - \dfrac{8\dfrac{\partial \Phi}{\partial \boldsymbol{C}} \otimes \dfrac{\partial \Phi}{\partial \boldsymbol{C}}}{8\dfrac{\partial \Phi}{\partial \boldsymbol{C}^p} : \boldsymbol{M}^{-1} : \dfrac{\partial \Phi}{\partial \boldsymbol{C}} - \dfrac{\partial \Phi}{\partial \boldsymbol{Q}} : \boldsymbol{H}}$

5.2 J2 MATERIAL MODEL

5.2.1 Multiplicative split and elastic response

The material model described above will be applied for J2 materials. The J2 models are well suited to the materials whose elastic volumetric response is uncoupled with elastoplastic deviatoric response, this behavior is observed in metal in plasticity, for instance.

Denote $J = \det(\boldsymbol{F})$, the volume-preserving part of the deformation gradient part is defined:

$$\overline{\boldsymbol{F}} = J^{-1/3}\boldsymbol{F} \tag{5.2.1}$$

with $\det(\overline{\boldsymbol{F}}) = 1$, it means $\overline{\boldsymbol{F}}$ satisfies the incompressible condition.

The right Cauchy strain tensors which are associated with $\overline{\boldsymbol{F}}$ and $\boldsymbol{F}$ are also defined:

$$\overline{\boldsymbol{C}} = \overline{\boldsymbol{F}}^T\overline{\boldsymbol{F}} = J^{-2/3}\boldsymbol{C} \quad \rightarrow \quad \det(\overline{\boldsymbol{C}}) = 1$$
$$\text{and similarly,} \qquad \overline{\boldsymbol{C}}^p = \overline{\boldsymbol{F}}^{pT}\,\overline{\boldsymbol{F}}^p = J^{-2/3}\boldsymbol{C}^p \tag{5.2.2}$$

Account for uncoupled volumetric/deviatoric response the energy function (5.1.10) is in the form:

$$W(\boldsymbol{C},\boldsymbol{C}^p,\boldsymbol{Q}) = W^{vol}(J) + W^{dev}(\overline{\boldsymbol{C}},\boldsymbol{C}^p) + W^{Q}(\boldsymbol{Q}) \tag{5.2.3}$$

The uncoupled energy function in (5.2.3) results in uncoupled volumetric – deviatoric stress-strain relationships. In metal plasticity the plastic deformation is isochoric, i.e. fully incompressible. While elastic deformation is compressible and small in many applications. As an example, an energy function from [SIM92b] is consisted as:

$$\begin{aligned} W^{vol} &= K(\ln J^e)^2/2 = K[\ln(\lambda_1^e\lambda_2^e\lambda_3^e)]^2/2 \\ W^{dev} &= G[(\varepsilon_1^e)^2 + (\varepsilon_2^e)^2 + (\varepsilon_3^e)^2] \\ W^{Q} &= H_{iso}\bar{\varepsilon}_p^2/2 + (\sigma_{y\infty} - \sigma_{y0})\bar{\varepsilon}_p + \delta^{-1}(\sigma_{y\infty} - \sigma_{y0})\exp(-\delta\bar{\varepsilon}_p) \end{aligned} \tag{5.2.4}$$

where

- G and K are constant. They are shear modulus and bulk modulus, respectively;
- $\delta > 0$ is saturation exponent;
- $\varepsilon_i^e = \ln(\lambda_i^e)$; i = 1,2,3; λ_i^e are principal elastic stretches (from eigenvalues of $\boldsymbol{C}$);
- $J^e = \det(\boldsymbol{F}^e)$;
- σ_{y0} and $\sigma_{y\infty}$ are the first yield stress and the saturation yield stress;
- $\bar{\varepsilon}_p$ is the equivalent plastic strain;
- H_{iso} is the linear hardening modulus.

Following (5.1.7), the second Piola-Kirchhoff, for J2 material, is decomposed into the hydrostatic and deviatoric parts as:

$$\begin{aligned} \boldsymbol{S} &= 2\frac{\partial W^{vol}(J)}{\partial \boldsymbol{C}} + 2\frac{\partial W^{dev}(\bar{\boldsymbol{C}}, \boldsymbol{C}^{p})}{\partial \boldsymbol{C}} \\ &= Jp\boldsymbol{C}^{-1} + J^{-2/3}\mathrm{DEV}[2\frac{\partial W^{dev}(\bar{\boldsymbol{C}}, \boldsymbol{C}^{p})}{\partial \bar{\boldsymbol{C}}}] = \boldsymbol{S}^{vol} + \boldsymbol{S}^{dev} \end{aligned} \tag{5.2.5}$$

where $p = \partial W^{vol}(J)/\partial J$ is the hydrostatic pressure. In (5.2.5) we did use the relation (see [HOL00], page 41):

$$\frac{\partial J}{\partial \boldsymbol{C}} = J\boldsymbol{C}^{-1} \tag{5.2.6}$$

and the derivative (see [HOL00], page 229):

$$\frac{\partial \bar{\boldsymbol{C}}}{\partial \boldsymbol{C}} = J^{-2/3}[\boldsymbol{I} - \frac{1}{3}\boldsymbol{C} \otimes \boldsymbol{C}^{-1}] \tag{5.2.7}$$

and the denotation

$$\mathrm{DEV}[\bullet] = (\bullet) - \frac{1}{3}[\boldsymbol{C} : (\bullet)]\boldsymbol{C}^{-1} \tag{5.2.8}$$

In (5.2.5), the hydrostatic stress is presented by the term $Jp\boldsymbol{C}^{-1}$, and DEV[•] gives the physically correct deviator stresses in the reference configuration.

5.2.2 Flow rule and yield function

The yield function, for J2 material model can be assumed to only depend on the deviatoric part of right Cauchy strain tensor $\bar{\boldsymbol{C}}$ as:

$$\Phi(\bar{\boldsymbol{C}}, \boldsymbol{C}^{p}, \boldsymbol{Q}) \le 0 \tag{5.2.9}$$

According to the arguments in the last section with $\bar{\boldsymbol{C}}$, the Kuhn-Tucker conditions (5.1.16) leads to a flow rule as:

$$\left.\begin{aligned} &\dot{\boldsymbol{S}}^{p} = 2\dot{\gamma}\,\frac{\partial \Phi}{\partial \boldsymbol{C}} = 2\dot{\gamma}\,\frac{\partial \Phi}{\partial \bar{\boldsymbol{C}}}\frac{\partial \bar{\boldsymbol{C}}}{\partial \boldsymbol{C}} = 2\dot{\gamma}\,J^{-2/3}\mathrm{DEV}[\frac{\partial \Phi}{\partial \bar{\boldsymbol{C}}}] \\ &\dot{\gamma} \ge 0 \\ &\Phi(\bar{\boldsymbol{C}}, \boldsymbol{C}^{p}, \boldsymbol{Q}) \le 0 \\ &\dot{\gamma}\,\Phi(\bar{\boldsymbol{C}}, \boldsymbol{C}^{p}, \boldsymbol{Q}) = 0 \end{aligned}\right\} \tag{5.2.10}$$

where, similar to (5.1.16a), $\dot{\boldsymbol{S}}^{p}$ is also set:

$$\dot{\boldsymbol{S}}^{p} = -J^{-2/3}\mathrm{DEV}[2\frac{\partial^{2} W^{dev}}{\partial \bar{\boldsymbol{C}} \partial \boldsymbol{C}^{p}} : \boldsymbol{C}^{p}] \tag{5.2.11}$$

The von Mises yield condition in form of spatial terms in stress space is:

$$\begin{aligned} &\phi(\boldsymbol{\tau}, \boldsymbol{Q}) = \left\|\mathrm{dev}[\boldsymbol{\tau} - \boldsymbol{\alpha}]\right\| + q - \sqrt{\frac{2}{3}}\sigma_{y} \le 0 \\ &q = -H_{iso}\kappa \end{aligned} \tag{5.2.12}$$

where:

- σ_y is the yield stress and

- the Kirchhoff stress tensor $\boldsymbol{\tau}$ is the push-forward of the second Piola-Kirchhoff stress $\boldsymbol{S}$ by:

$$\boldsymbol{\tau} = \boldsymbol{F}\boldsymbol{S}\boldsymbol{F}^T \tag{5.2.13}$$

- the hardening variables are:

$$\boldsymbol{Q} = [q, \boldsymbol{\alpha}] \tag{5.2.14}$$

with $\boldsymbol{\alpha}$ is back stress which defines the location of the center of the yield surface. This back stress is used to account for Bauschinger's effect (kinematic hardening). The isotropic hardening is characterized by the internal variable q with isotropic hardening modulus $H_{iso} > 0$. H_{iso} is a function of isotropic hardening variable κ for nonlinear hardening laws, and for linear isotropic hardening laws H_{iso} is a constant.

The algorithm for the presented formulation is straightforward as follows. Integrate the material (reference) description of the flow rule (5.2.10) by an integration scheme, such as backward Euler difference scheme. Substitute the result into the hyperelastic stress-strain relations (5.2.5). The detailed algorithm is listed in Figure 5.2.1. The implementation of the hyperelastic formulation of J2-flow theory reduces to the classical radial return with the elastic predictor computed by energy function evaluation.

We see that maximum of plastic dissipation (5.1.12) leads to a return mapping algorithm, see Figure 5.2.1. That algorithm will look for the solutions on a path that makes the plastic dissipation stationary. Concretely, within a typical time step a trial elastic is calculated first. Then, the actual stress is defined in the closest-point projection of the trial state onto the elastic domain. For J2 flow theory, the closest-point projection boils down to the classical radial return method.

RETURN-MAPPING ALGORITHM FOR J2-FLOW THEORY

1. *Step 1:* Geometry update

$$\boldsymbol{x}_{n+1} = \boldsymbol{x}_n + \boldsymbol{U}$$

$$\boldsymbol{F}_{n+1} = \boldsymbol{F}_n + \mathrm{GRAD}\boldsymbol{U}\ ; \quad \overline{\boldsymbol{F}}_{n+1} = J^{-1/3}\boldsymbol{F}_{n+1}$$

$$\overline{\boldsymbol{C}}_{n+1} = \overline{\boldsymbol{F}}_{n+1}^{T}\overline{\boldsymbol{F}}_{n+1}$$

2. *Step 2:* Elastic predictor (k=0)

$$\boldsymbol{C}_{n+1}^{p(0)} = \boldsymbol{C}_n^p$$

$$\boldsymbol{S}_{n+1}^{(0)} = J^{-2/3}\,\frac{\partial W^{vol}(J_{n+1})}{\partial \overline{\boldsymbol{C}}} + 2J^{-2/3}\,\frac{\partial W^{dev}(\overline{\boldsymbol{C}}_{n+1}, \boldsymbol{C}_{n+1}^{p(0)})}{\partial \overline{\boldsymbol{C}}}$$

$$\boldsymbol{Q}_{n+1}^{(0)} = \boldsymbol{Q}_n$$

3. *Step 3:* Check for yielding

$$\Phi_{n+1}^{(k)} = \Phi(\overline{\boldsymbol{C}}_{n+1}^{(k)}, \boldsymbol{C}_{n+1}^{p(0)}, \boldsymbol{Q}_{n+1}^{(0)})$$

IF $\Phi_{n+1}^{(k)} < \mathrm{TOL}$ THEN

Set $(\bullet)_{n+1} = (\bullet)_{n+1}^{(k)}$ and EXIT (to the next time step)

ELSE continue Step 4 and Step 5

4. *Step 4:* Compute plastic consistency parameter (see (5.1.19))

$$\Delta\gamma_{n+1}^{(k)} = 2\Phi_{n+1}^{(k)} \Bigg/ \left[8J^{-2/3}\,\frac{\partial \Phi}{\partial \boldsymbol{C}^p} : \boldsymbol{M}^{-1} : \frac{\partial \Phi}{\partial \overline{\boldsymbol{C}}} - \frac{\partial \Phi}{\partial \boldsymbol{Q}} \cdot \boldsymbol{H} \right]_{n+1}^{(k)}$$

5. *Step 5:* Update state variables

$$\boldsymbol{S}_{n+1}^{(k+1)} = \boldsymbol{S}_{n+1}^{(k)} - 2J^{-2/3}\Delta\gamma_{n+1}^{(k+1)}\,\frac{\partial \Phi}{\partial \overline{\boldsymbol{C}}}\bigg|_{n+1}^{(k)}$$

$$\boldsymbol{C}_{n+1}^{p(k+1)} = \boldsymbol{C}_{n+1}^{p(k)} - 2J^{-2/3}\Delta\gamma_{n+1}^{(k+1)}\,\boldsymbol{M}^{-1} : \frac{\partial \Phi}{\partial \overline{\boldsymbol{C}}}\bigg|_{n+1}^{(k)}$$

$$\boldsymbol{Q}_{n+1}^{(k+1)} = \boldsymbol{Q}_{n+1}^{(k)} + \Delta\gamma_{n+1}^{(k+1)}\,\boldsymbol{H}\big|_{n+1}^{(k)}$$

Set k = k+1 and RETURN Step 3

Figure 5.2.1: Material stress update algorithm

5.3 PLASTICITY APPLICATIONS

In the sections following we investigate performances of the SS7n element in field of plasticity.

5.3.1 Cantilever at large elastoplastic deformation

Consider a cantilever beam of dimension L×b×h = 15×1×0.7 clamped at left end and loaded by a distributed force (q_0 = 7) at right end, Figure 5.3.1. This test was presented by Huh and Kim [HUH00]. The elastic modulus is E = 2×10^5 N/mm^2 and Poisson's ratio is ν = 0.3. Material law is elastoplastic with isotropic hardening as $\bar{\sigma} = 340 + 1000\bar{\varepsilon}^p$.

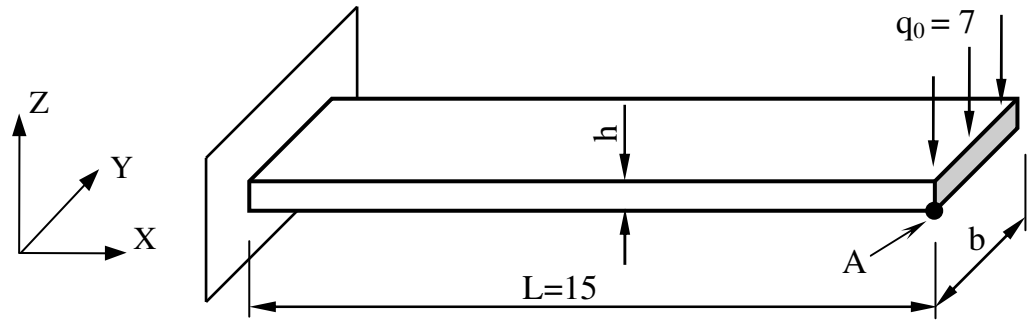

Figure 5.3.1: Cantilever at large elasto-plastic deformation

As proposed in the work of Huh and Kim [HUH00], a very fine mesh of 40×10×1 elements (along L, h and b, respectively) is first employed. By adopting the assumption on a plain strain state, these authors can employ a 2D modeling. Here, with 3D solid elements to simulate 2D modeling, the width of beam (Y direction) will be presented by only one finite element and the plain strain state will be obtained by setting to zero displacement in the width direction. For the comparison between different approaches, the displacement at the tip point A will be considered. The SRI, EAS9, EAS21 (METAFOR software, [MET08]), ANS, ANSn, SS7 and SS7n elements will be involved in the computation.

The SRI element is one of the best elements in removing volumetric locking. However, shear locking in this problem is important. Consequently, in Figure 5.3.2, we see that the SRI element with 10 layers (i.e. 40×10×1 elements) is stiffer than the RI element [HUH00] or the EAS9 with 2, 4 or 10 layers. Results given by the EAS9 with 10 layers are converged to the results given by the EAS21 with 4 or 10 layers, see Figure 5.3.3. If only 1 layer is adopted, both the EAS 9 and EAS21 elements show stiff behaviour, see Figures 5.3.2 and 5.3.3. The EAS21 always gives very good results in both shear and volumetric locking removals, [AND93]. Hence, with a very fine mesh of 40×10×1 elements, result of the EAS21 (METAFOR) element is considered as a reference. We see that this reference is a little softer than the result of the RI element in [HUH00].

Next, the deformation is calculated by the ANS method with various layers of element along the thickness direction. Consider the load-displacement curve, the ANS and ANSn elements give identical results hence only the results of the ANSn are presented here. We see that with 2 layers, the ANSn element is softer than the SRI when $P = q \times b \leq 4.0N$. The reason is due to shear locking. At load level $P > 4.0N$, the cantilever is in larger deformation, effect of volumetric locking become more important, hence, behavior of two-layered ANSn element is stiffer than the SRI element, Figure 5.3.4. With 4 layers, the ANSn element is always softer than the SRI element. When volumetric locking becomes more serious (because of large plasticity deformation), the ANSn element with 4 layers approaches the behavior of the SRI element. Increasing number of layers to 10, ANSn behavior becomes too soft. Compare to the reference result (EAS21), behaviour of the ANSn is too stiff. We see that for this problem, the ANSn element, which is only free from shear locking, should not be used.

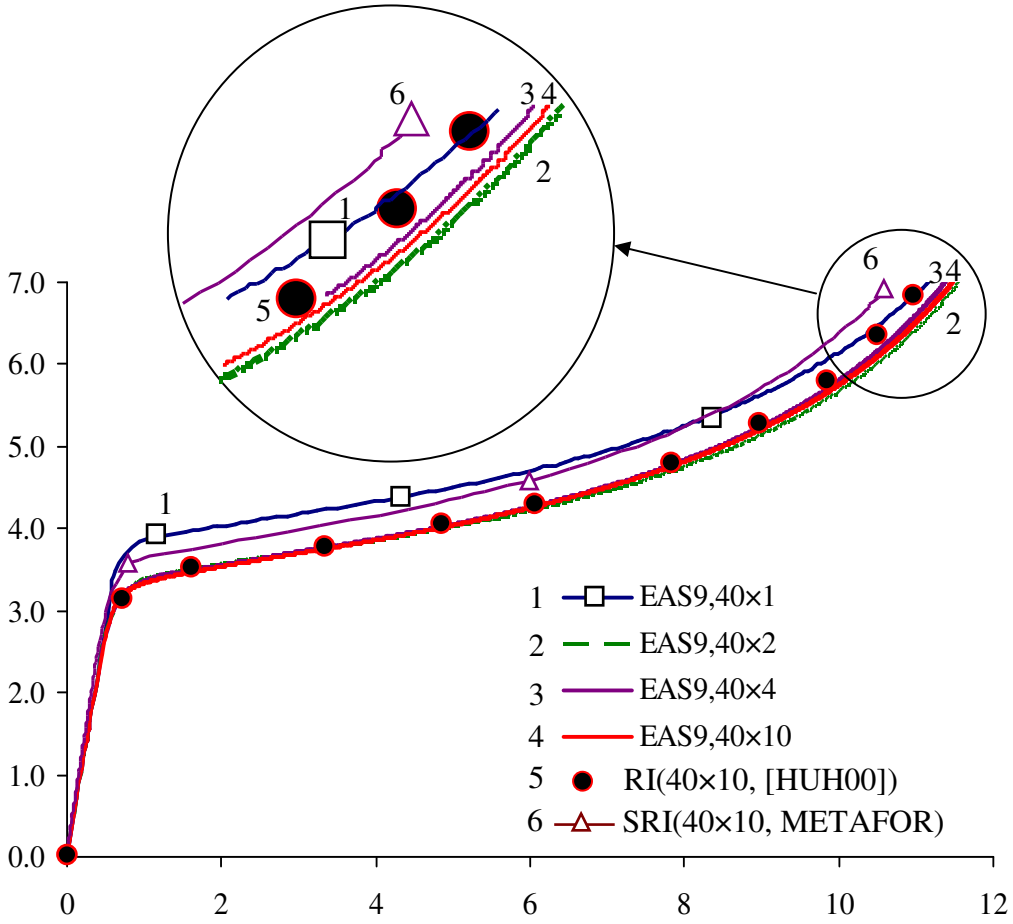

Figure 5.3.2: EAS9 (METAFOR) results with various elements along thickness

Now we investigate the problem with the SS7n element (because the SS7 and SS7n elements give identical results). From Figure 5.3.5 we see that result of the SS7n element, with 2 layers along the thickness, is only close to the result of the EAS21 when shear locking is important (i.e., $P \leq 4.0N$). When $P > 4.0N$, SS7n with 2 layers is a little stiffer than the EAS21 and RI elements. Increasing layers along the thickness to 4 or 10, the SS7n even becomes stiffer. If a very coarse mesh is adopted, i.e. with only 1 layer along the thickness, the SS7n is too stiff. Hence, in this problem, 2 layers of SS7n are the most suitable choice.

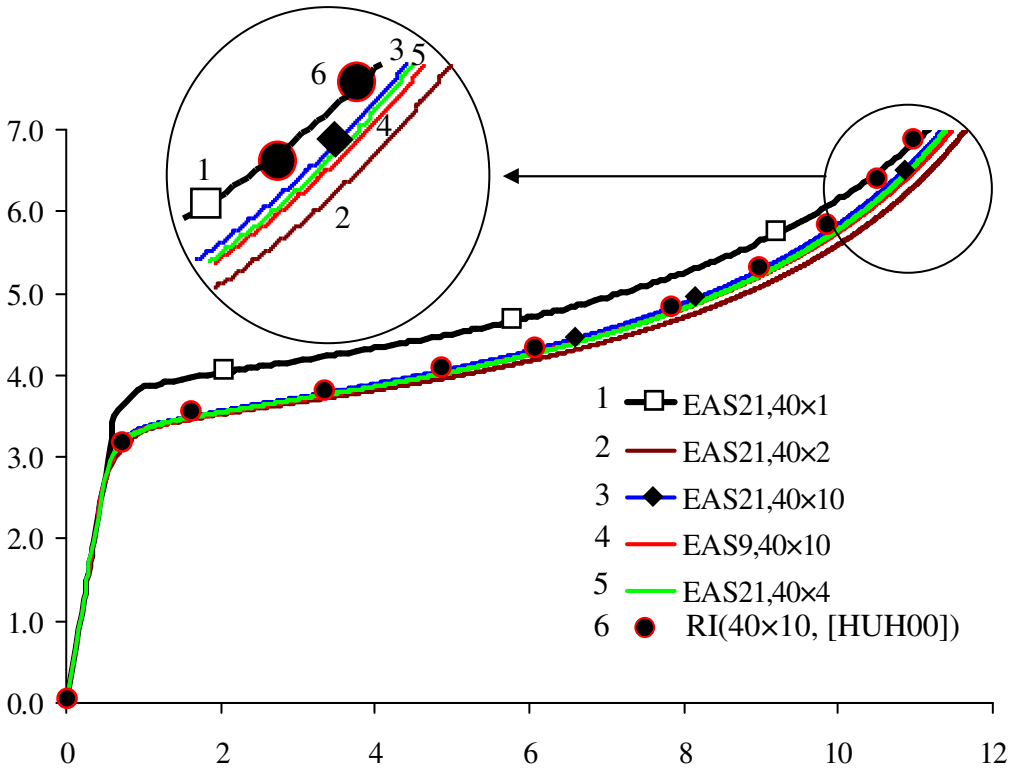

Figure 5.3.3: EAS21 (METAFOR) results with various elements along thickness

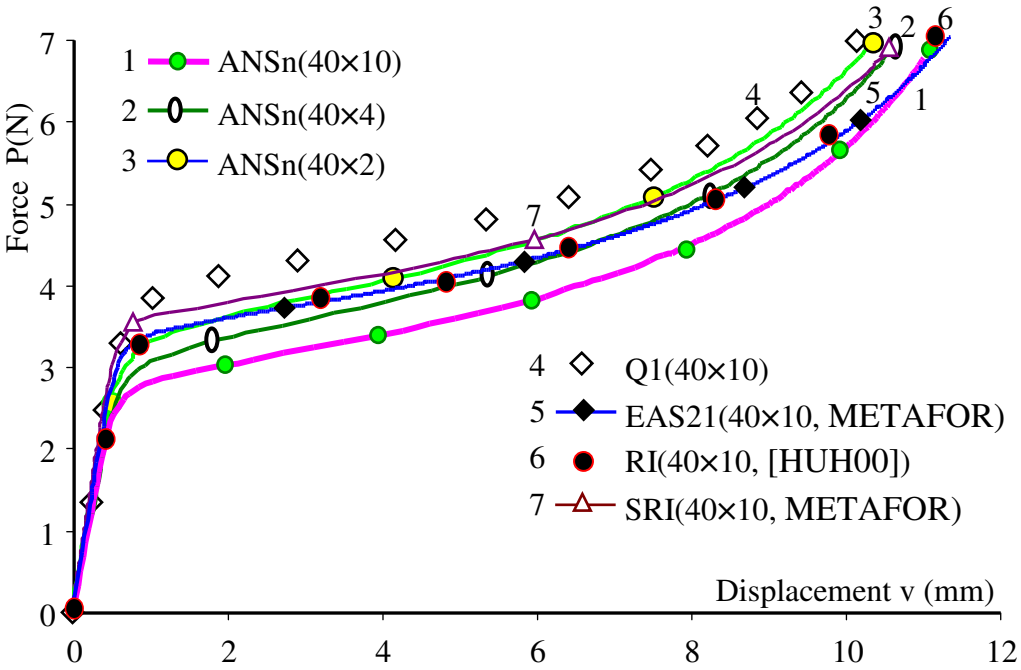

Figure 5.3.4: ANS results with various elements along thickness

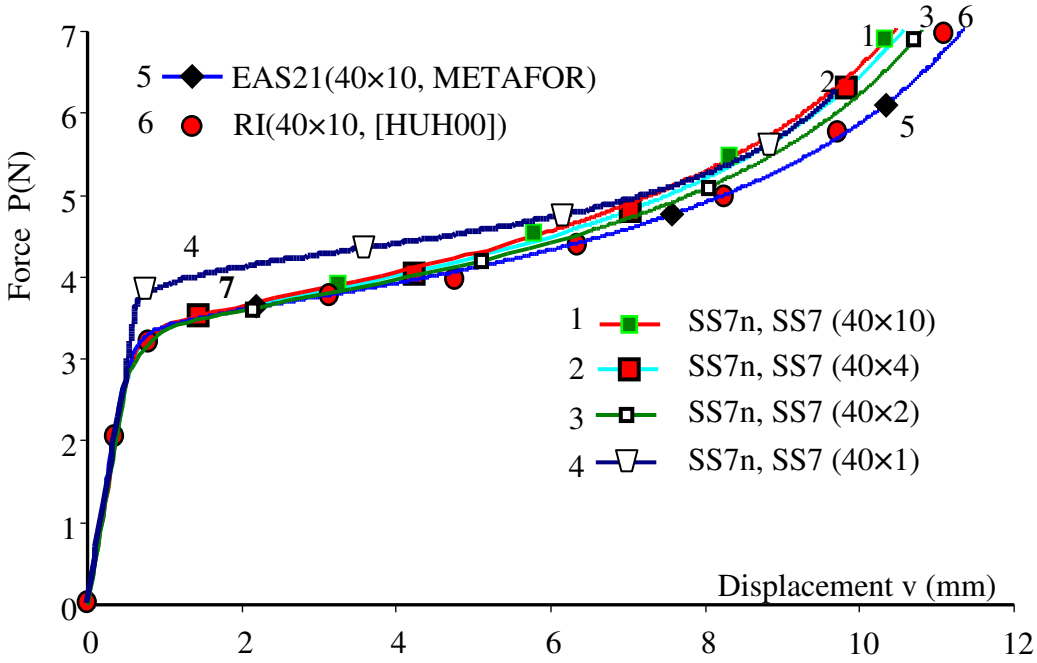

Figure 5.3.5: SS7n results with various elements along thickness

It was presented in Chapter 3 that the ANS and ANSn elements are different in assumed strained components E_{xz} and E_{yz}. These elements will give identical results if transverse shear strains are not important. As in this problem, the ANS and ANSn elements give identical results because the cantilever is not too thin (aspect ratio ≈ 20), hence, transverse shear stresses given by the ANS and ANSn are similar, see Figures 5.3.6-7. Consequently, σ_{xz} stress given by the SS7 and SS7n elements are similar, see Figures 5.3.8-9.

Table 5.3.1. Convergence of σ_{xz} (MPa)

	40×1×1		40×2×1		40×4×1		40×10×1		40×15×1	
	min	max	min	max	min	max	min	max	min	max
EAS9	-400	369	-259	266	-250	245	-247	262	**-246**	**250**
EAS21	-400	369	-262	262	-251	248	-251	258	**-246**	**250**
SS7	-	-	-224	181	-235	226	-242	240	**-246**	**243**
SS7n	-	-	-225	185	-235	225	-241	240	**-245**	**243**

Distribution of σ_{xz} stress in a mesh of 40×10×1 given by the EAS9 element (METAFOR, Figure 5.3.10) and the solid-shell elements (SS7 and SS7n, Figures 5.3.8 and 5.3.9) are similar. However, the ultimate values given by the EAS9 element is larger in comparison with the solid-shell elements (-247MPa vs. -240MPa and 262MPa vs. 240MPa). The convergence value of σ_{xz} is found in Table 5.3.1 with both solid-shell and EAS21 elements (bold letters) with mesh of 40×15×1 elements. Data in Table 5.3.1 shows that the EAS21 and EAS9 elements go to the convergence from higher values. In contrary, the SS7 and SS7n elements go to the convergence from lower values.

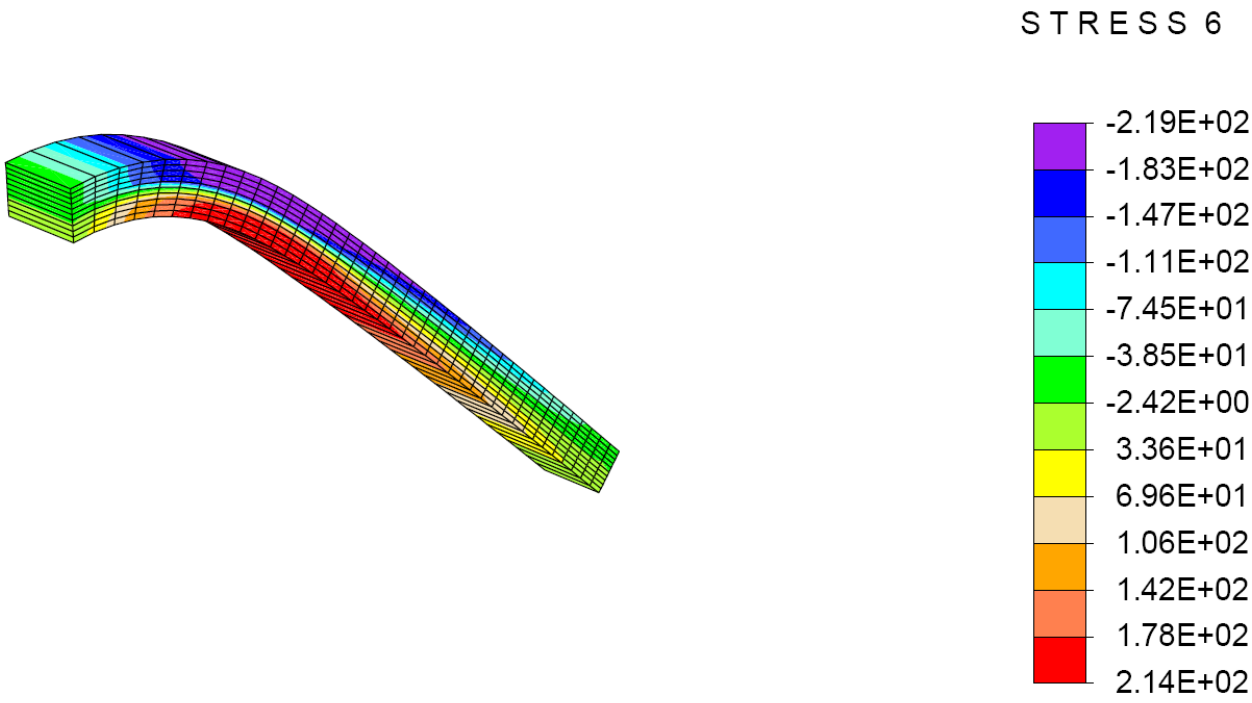

Figure 5.3.6: ANS element - σ_{xz} (mesh 40×10×1)

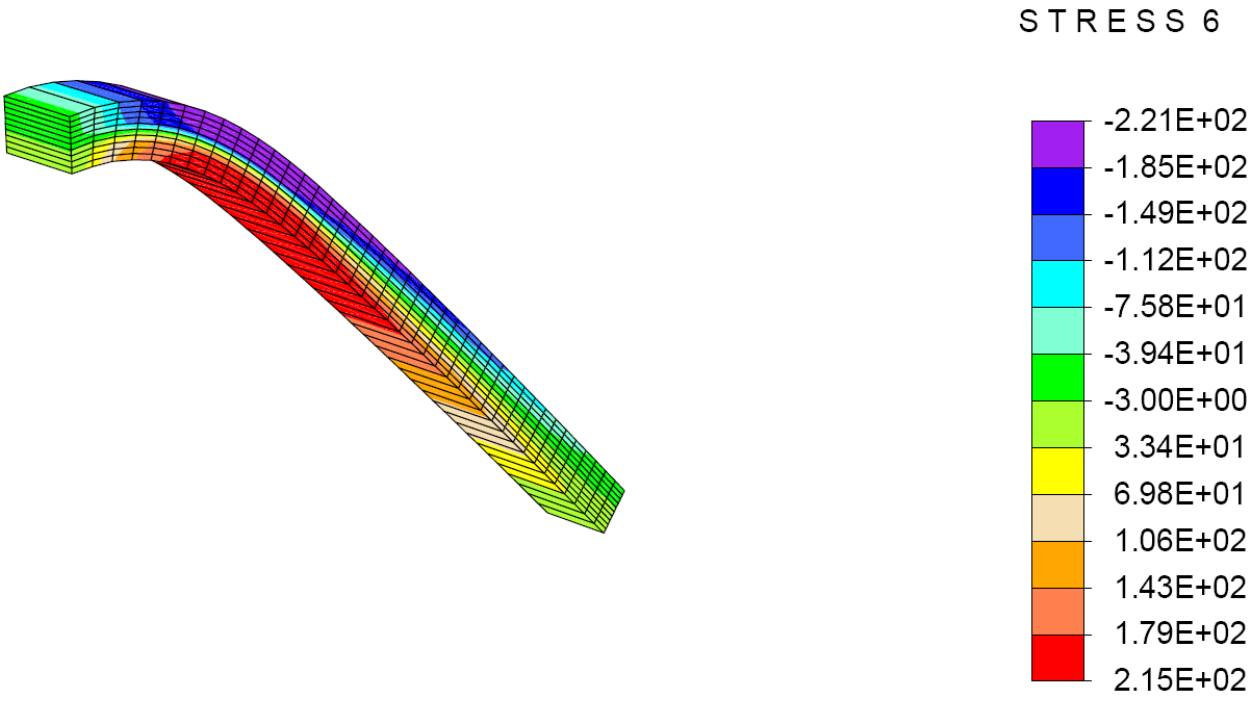

Figure 5.3.7: ANSn element - σ_{xz} (mesh 40×10×1)

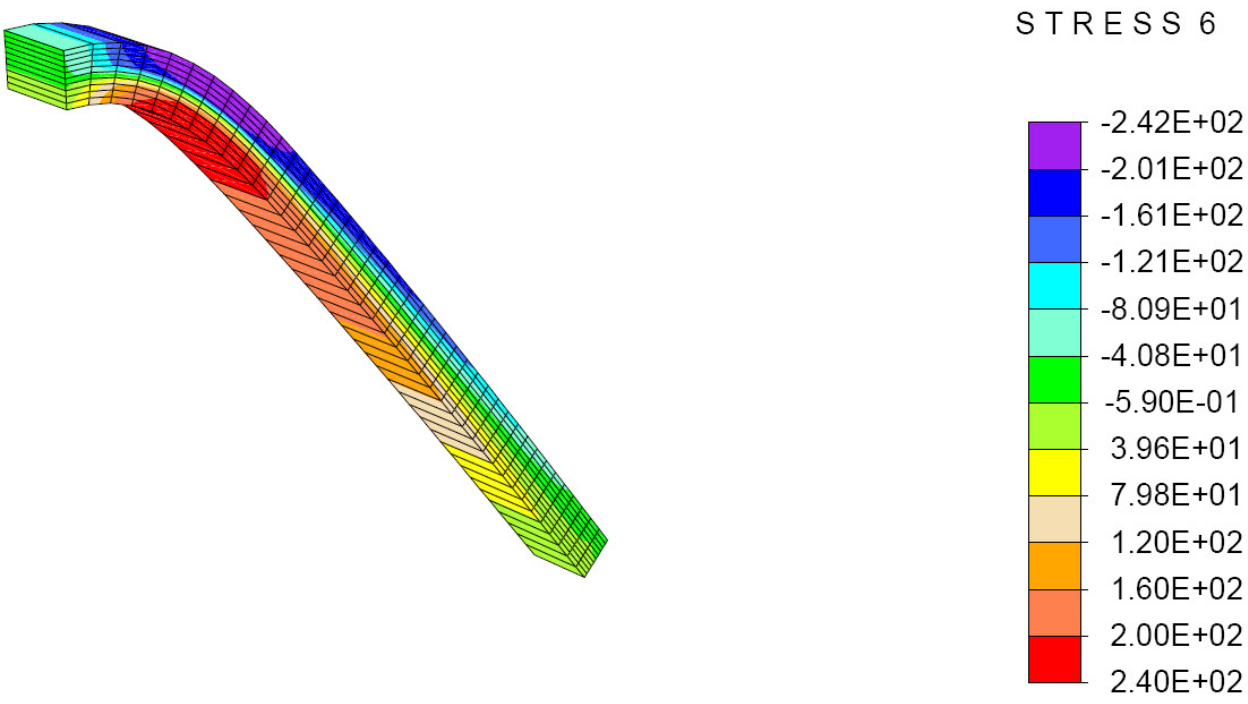

Figure 5.3.8: SS7 element - σ_{xz} stress (mesh 40×10×1)
(the result is shown in the structural coordinate system)

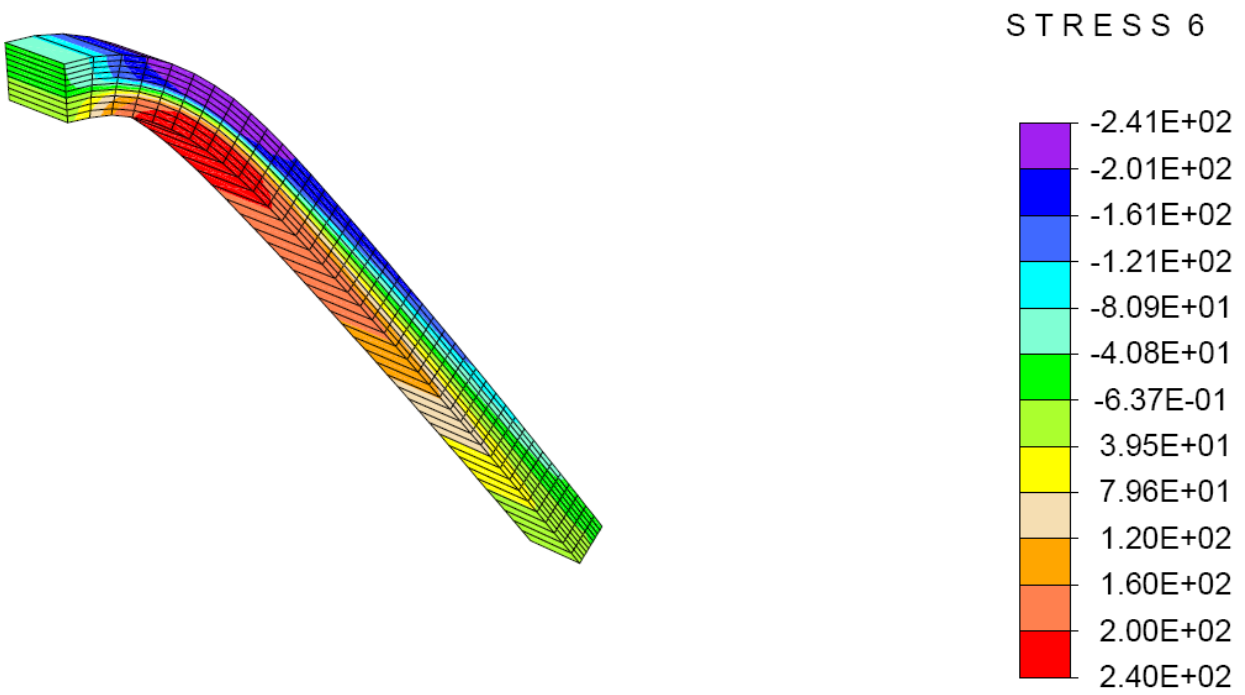

Figure 5.3.9: SS7n element - σ_{xz} stress (mesh 40×10×1)
(the result is shown in the structural coordinate system)

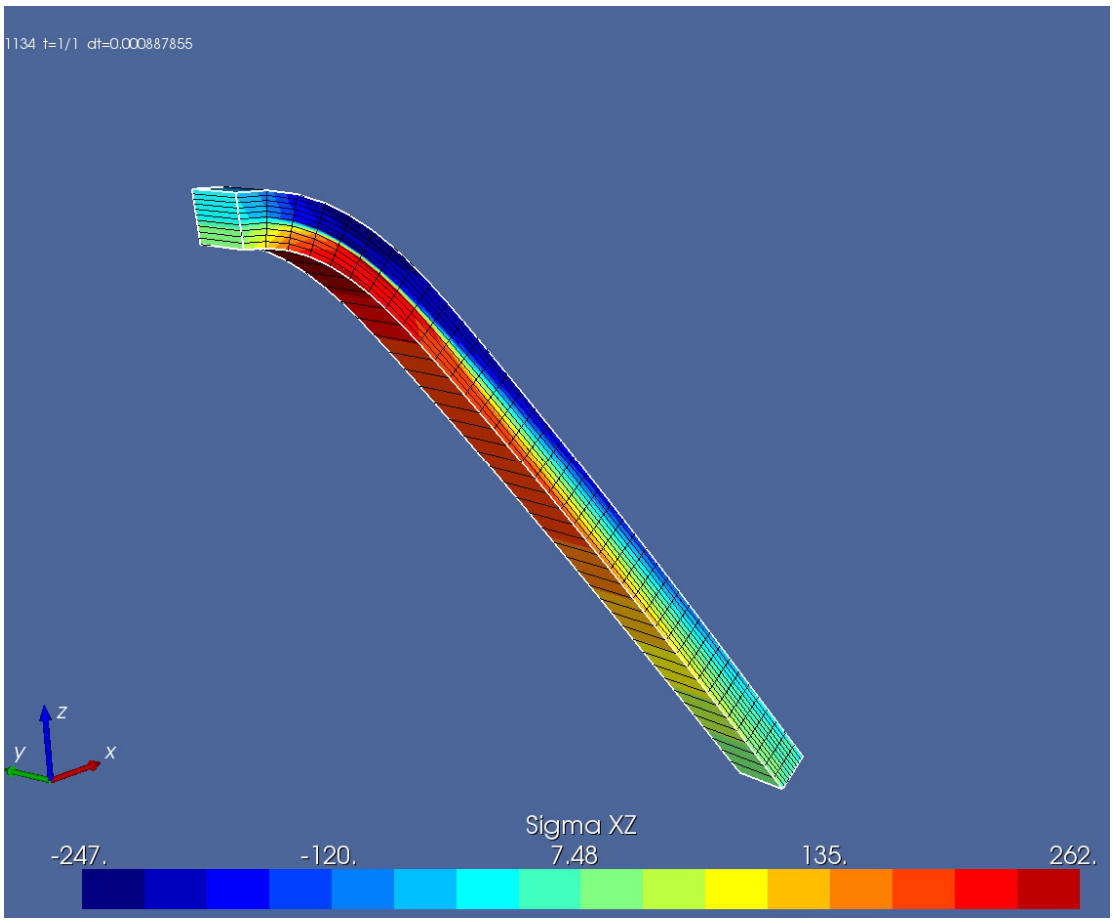

Figure 5.3.10: EAS9 element - σ_{xz} stress (METAFOR, mesh 40×10×1)

5.3.2 Pinched cylinder at large elastoplastic deformations

Consider a cylinder of inner radius r = 300, thickness t = 3 and length L = 600, Figure 5.3.11. Young's modulus is $E = 3\times10^3$ and Poisson's ratio is $\nu = 0.30$. A couple of opposite, concentrated forces F applied at the mid-length of the cylinder. Both ends of the cylinder are pinched, only a free movement in the axial direction Y is possible. Material law is elastoplastic with isotropic hardening as $\bar{\sigma} = 24.3 + 300\bar{\varepsilon}^p$.

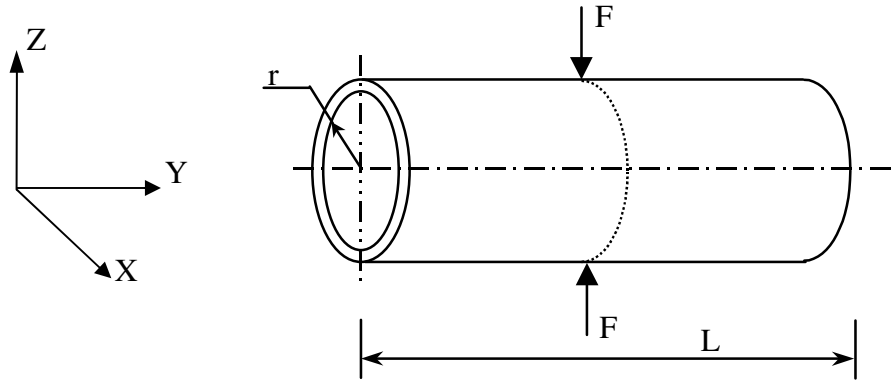

Figure 5.3.11: Pinched cylinder

We investigate deflection coincident with the point load against loads. The deflection response is strongly dominated by inextensional circumferential bending. Due to symmetry, only one eighth of the cylinder is modeled. A result with 3D elements – and mesh of 40×40×1 elements proposed by Wriggers et al. [WRI96b] will be employed as the reference, see Figure 5.3.13. Wriggers did use 3D enhanced element presented by Simo and Armero in [SIM92a]. That element is equivalent to the EAS12 (6v + 6s) element, see Table 2.4.2. It means the reference element is volumetric and shear locking free. Let's investigate convergence of the EAS12 element. We also see that the EAS12 element of METAFOR, Figure 5.3.12, converges with a mesh of 40×40×1 elements. The EAS12 (40×40×1 elements) of METAFOR gives an identical result as the reference [WRI96b], Figure 5.3.13.

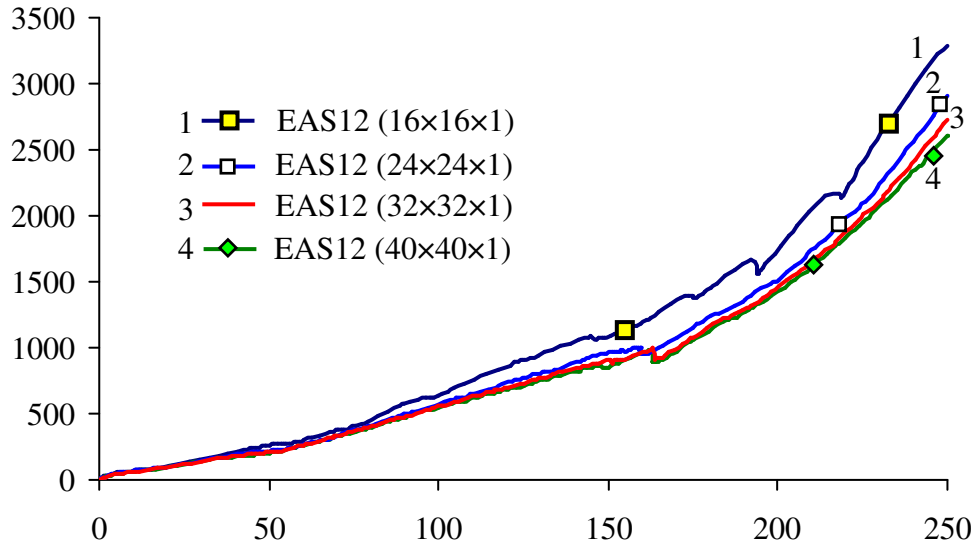

Figure 5.3.12: EAS12 element (METAFOR)

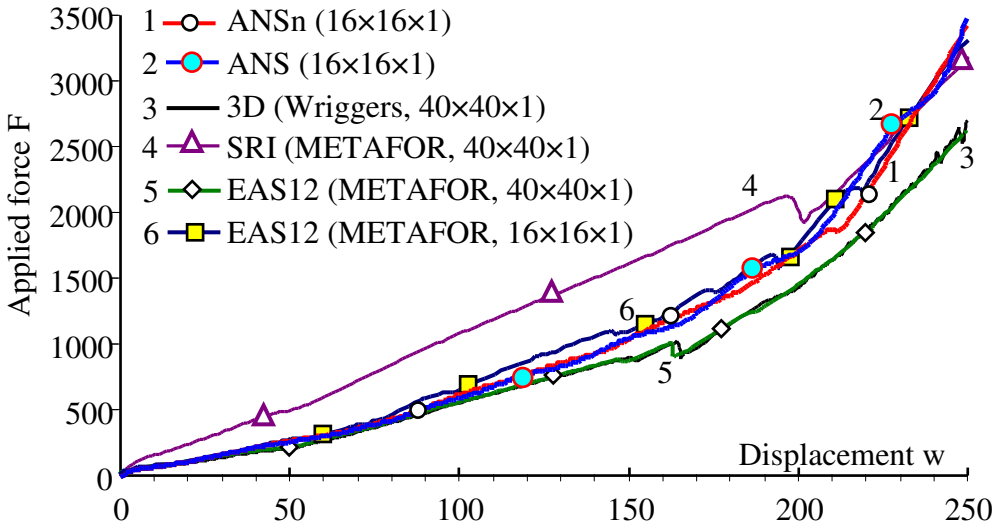

Figure 5.3.13: Pinched cylinder: Force-Displacement

This cylinder is a thin shell structure (R/t = 100 >> 20) and subject to large deformation. Consequently, transverse shear strains are important. In this problem results of the ANS and ANSn elements are not totally coincident, see Figure 5.3.13.

Now we consider the resultant stresses from the ANS and ANSn techniques with a coarse mesh: 16×16×1 elements. Let's concentrate in ultimate transverse shear stresses at the left end of the cylinder and at the area where the load is applied. All results are considered in the structural coordinate system. Data in Figures 5.3.14 - 15 show the σ_{xz} stresses calculated by the SS7 and SS7n elements. Reference result of the σ_{xz} stress is in Figure 5.3.20b. Pay attention that the concentrated load is only applied at the center node. As a consequence, the element containing the center node is singular due to the applied load is unphysical. Hence, in following analyses we will consider stresses at point B instead of stresses at point A, see Figure 5.3.14.

When using the same coarse mesh (16×16×1), the SS7n gives the results, which are closer to the results of the reference - EAS12 (40×40×1) - than the SS7 does, see Table 5.3.2. In Table 5.3.2, transverse shear stresses of the EAS12 (16×16×1) are extracted from Figures 5.3.16 - 17. In that table, transverse shear stresses of the ANS and ANSn elements (16×16×1) are also introduced. We see that transverse shear stresses given by the ANSn are closer to the reference than the result of ANS. Transverse shear stresses predicted by the EAS12 (16×16×1) are worse than the values predicted by the SS7n (except the minimal value of σ_{yz}), Table 5.3.2.

Table 5.3.2. Normalized transverse shear stresses
(*reference values are results of EAS12 - 40×40×1 element*)

		ANS (16×16×1)	ANSn (16×16×1)	SS7 (16×16×1)	SS7n (16×16×1)	EAS12 (16×16×1)	Reference values
σ_{xz}	Max	0.854	0.854	0.695	0.894	0.642	15.1
	Min	0.291	0.648	0.559	0.862	0.836	-31.8
σ_{yz}	Max	0.569	0.643	0.816	0.863	0.580	25.5
	Min	0.557	0.708	0.587	0.925	1.042	-49.6

Data from Figures 5.3.18 -19 show σ_{yz} stress calculated by the SS7 and SS7n elements. Reference result of σ_{yz} stress is in Figure 5.3.21b. When a coarse mesh is

adopted, compare with the reference stresses in areas I and II (Figures 5.3.18, 19 and 21b) we can see that the SS7n element give less worse results than the SS7 element. In detail, stress in area I given by the reference is 10.4 while values given by the SS7 and SS7n are 7.16 and 9.63, respectively. Stress in area II given by the reference is -5.0 while values given by the SS7 and SS7n are -1.9 and -2.7 respectively. The maximal and minimal values of σ_{yz} are listed in Table 5.3.2.

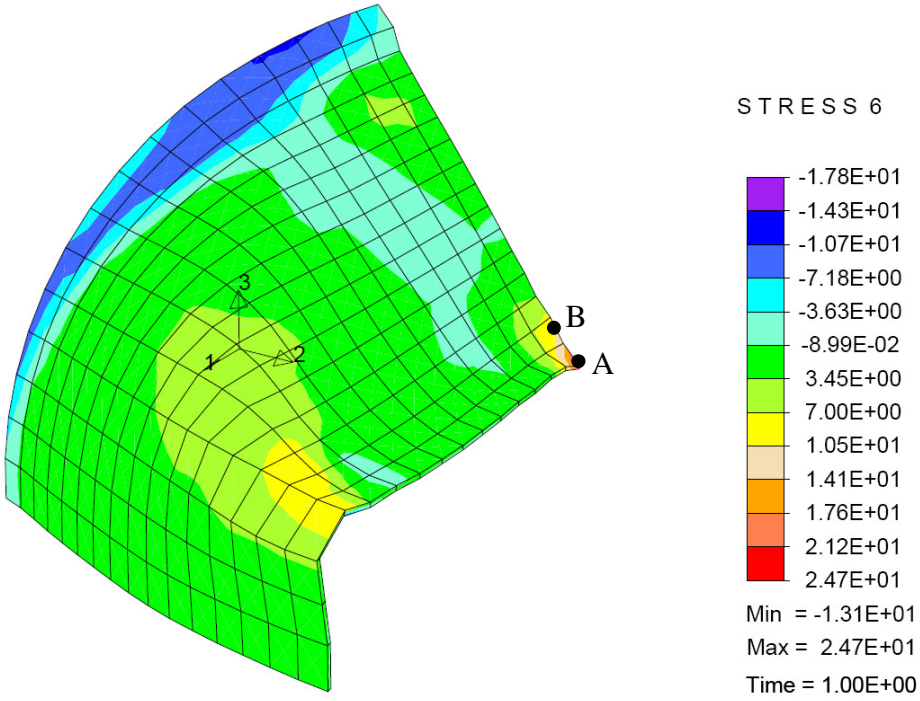

Figure 5.3.14: SS7 element - σ_{xz} (mesh 16×16×1)

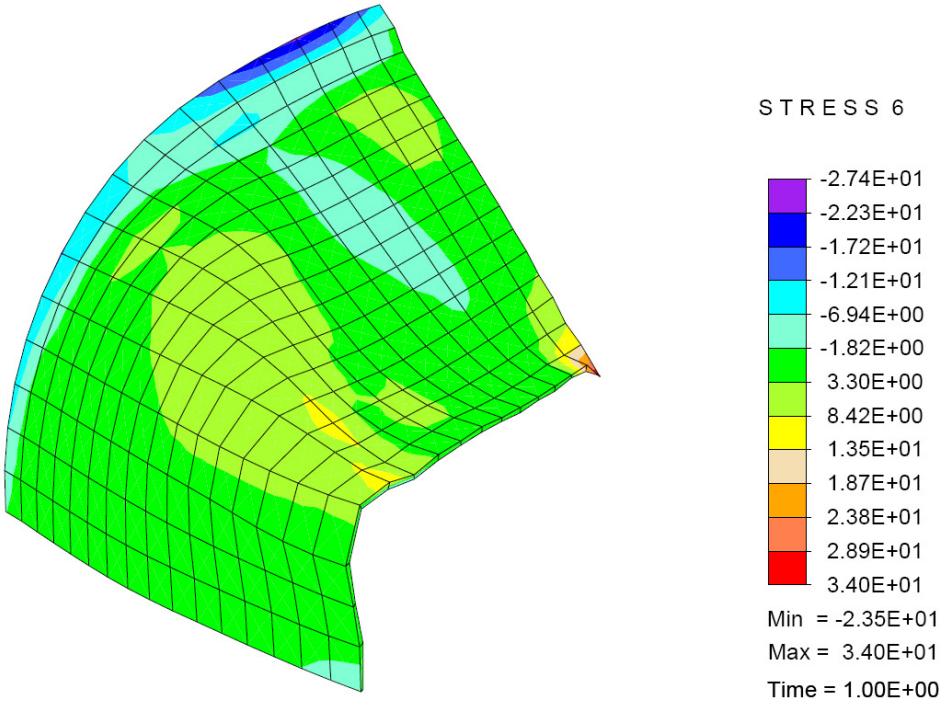

Figure 5.3.15: SS7n element - σ_{xz} (mesh 16×16×1)

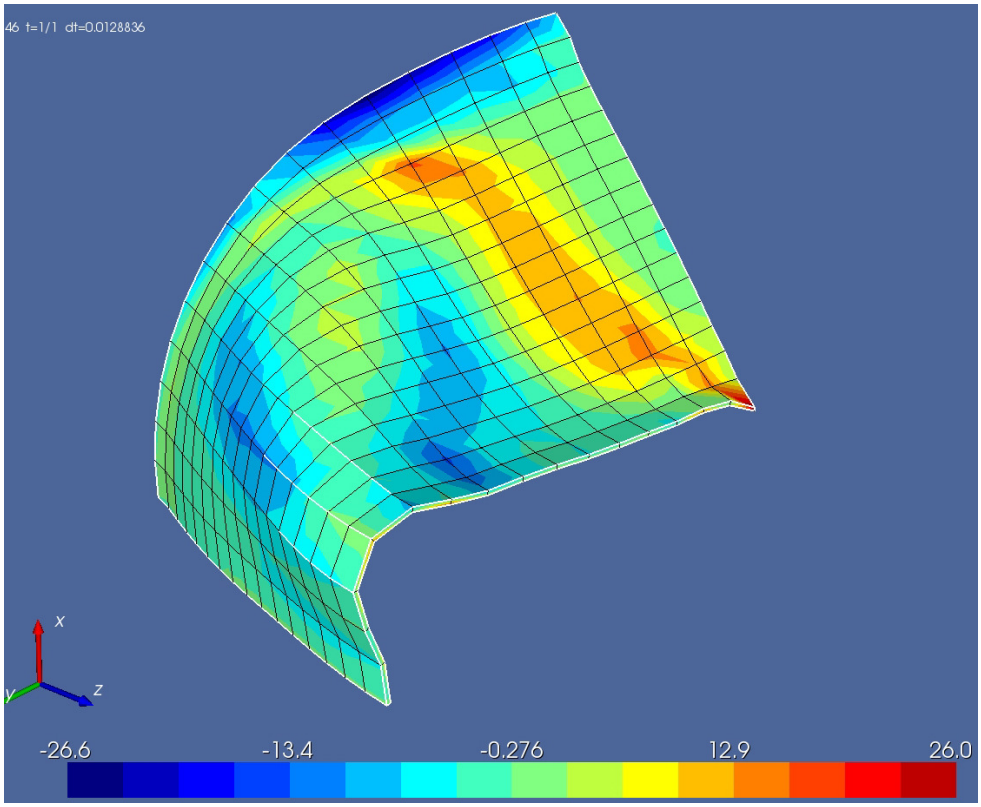

Figure 5.3.16: EAS12 element - σ_{xz} (EAS12,METAFOR, 16×16×1)
(*due to singularity at load point, max. value has been imposed to 26.0*)

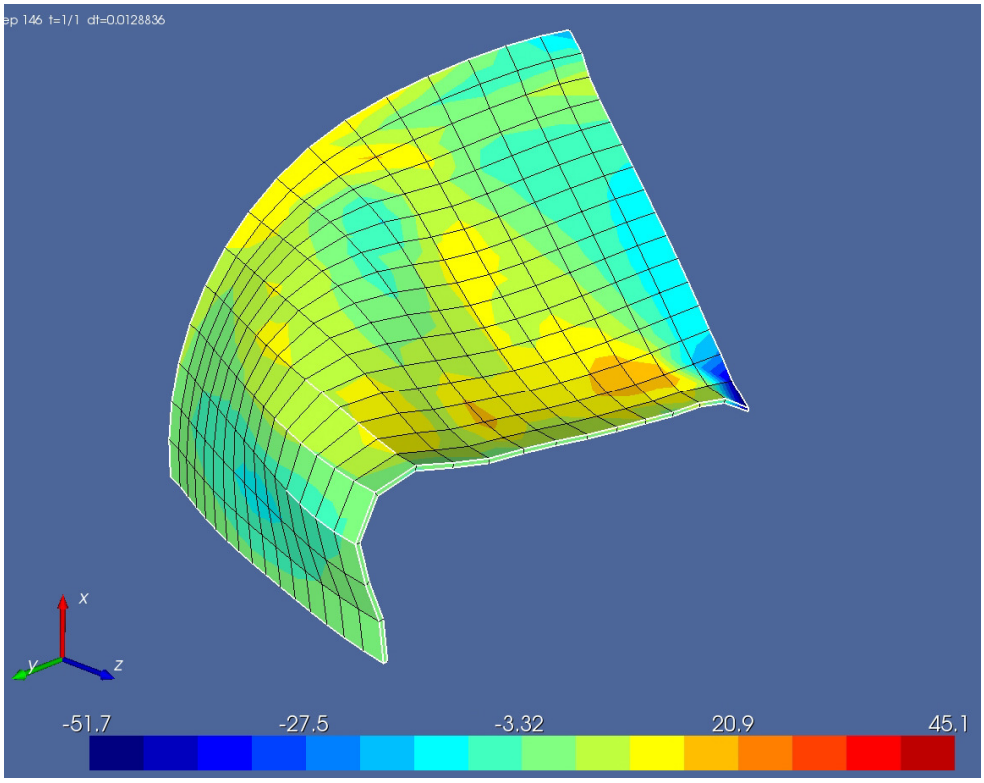

Figure 5.3.17: EAS12 element - σ_{yz} (EAS12,METAFOR, 16×16×1)
(*due to singularity at load point, min. value has been imposed to -51.7*)

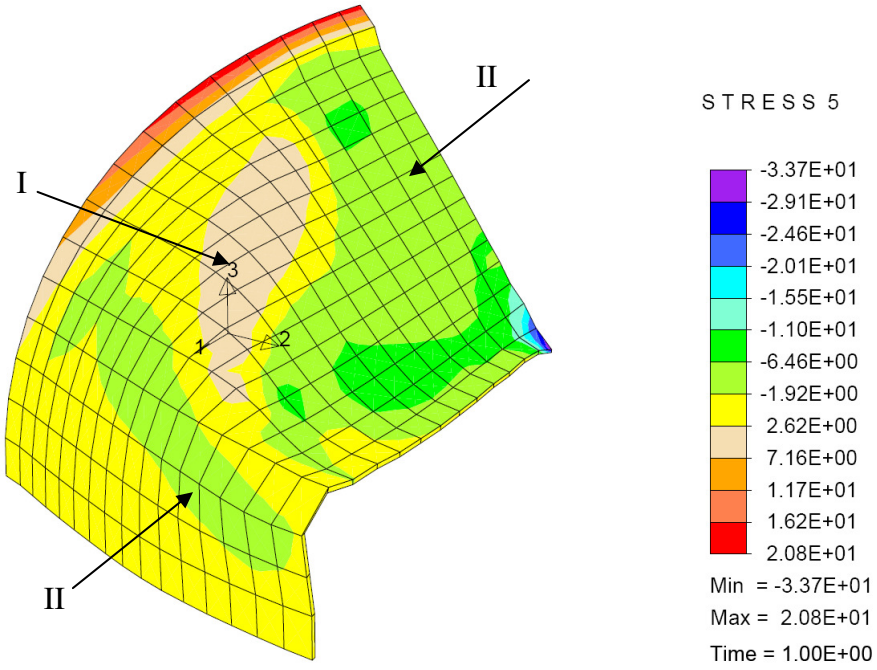

Figure 5.3.18: SS7 element - σ_{yz} (mesh 16×16×1)

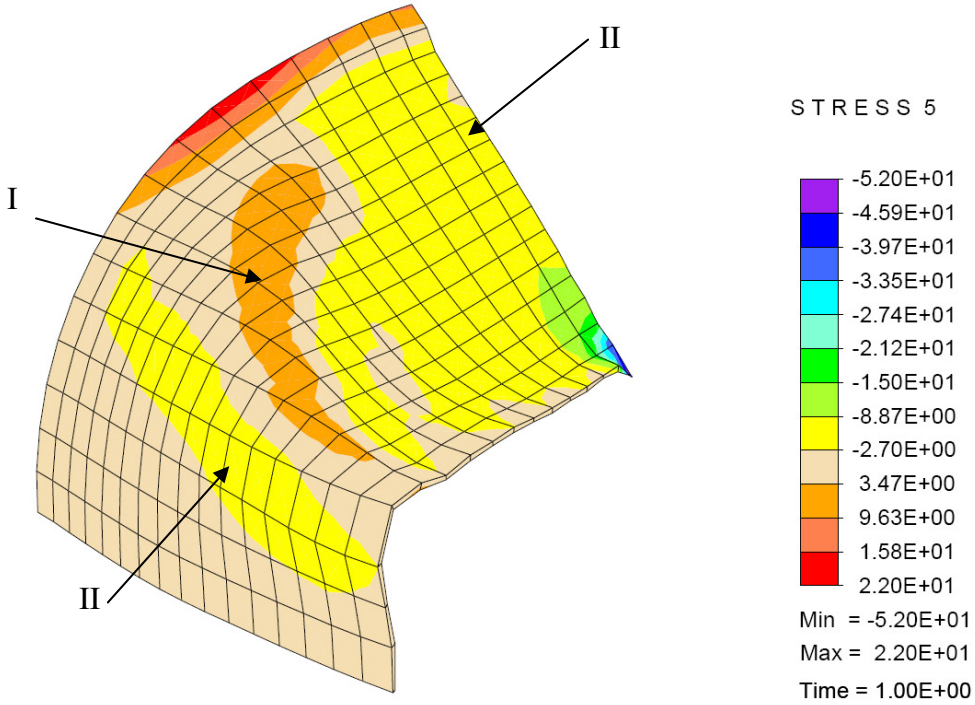

Figure 5.3.19: SS7n element - σ_{yz} (mesh 16×16×1)

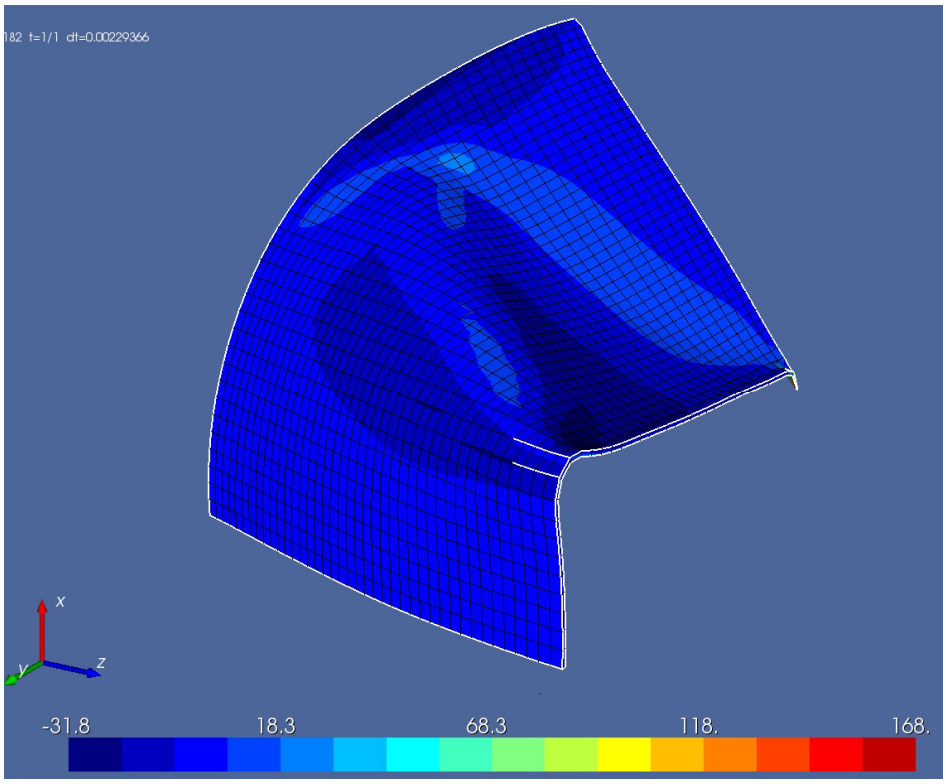

Figure 5.3.20a: Reference - σ_{xz} (EAS12,METAFOR, 40×40×1)

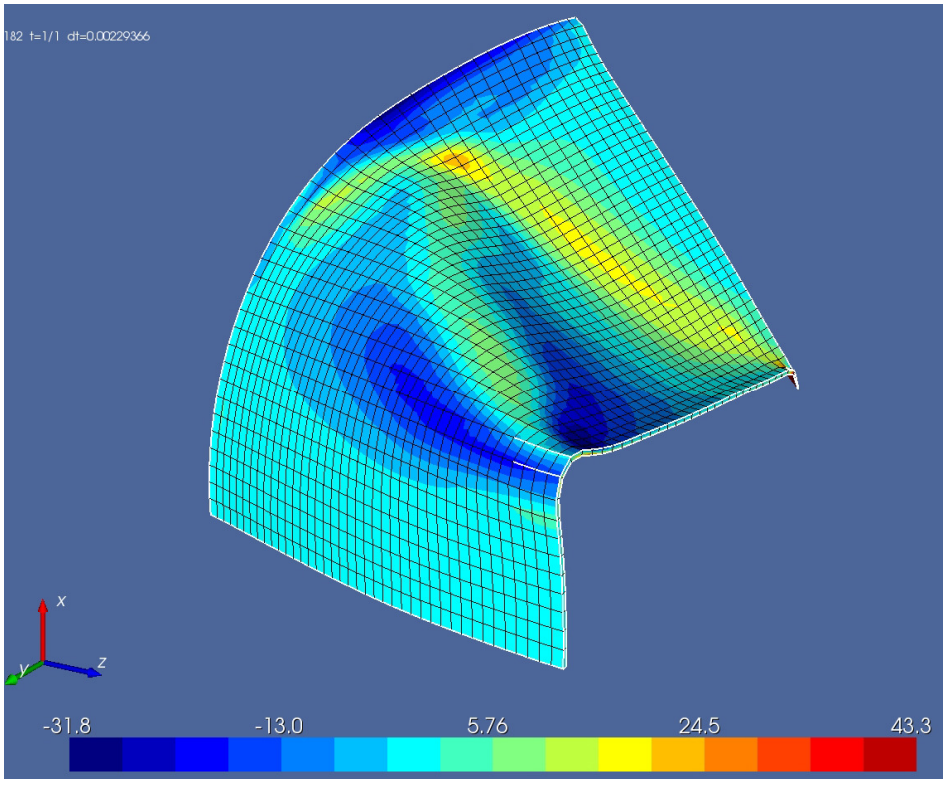

Figure 5.3.20b: Reference - σ_{xz} (EAS12,METAFOR, 40×40×1)
(*due to singularity at load point, max. value for drawing has been imposed to 43.3*)

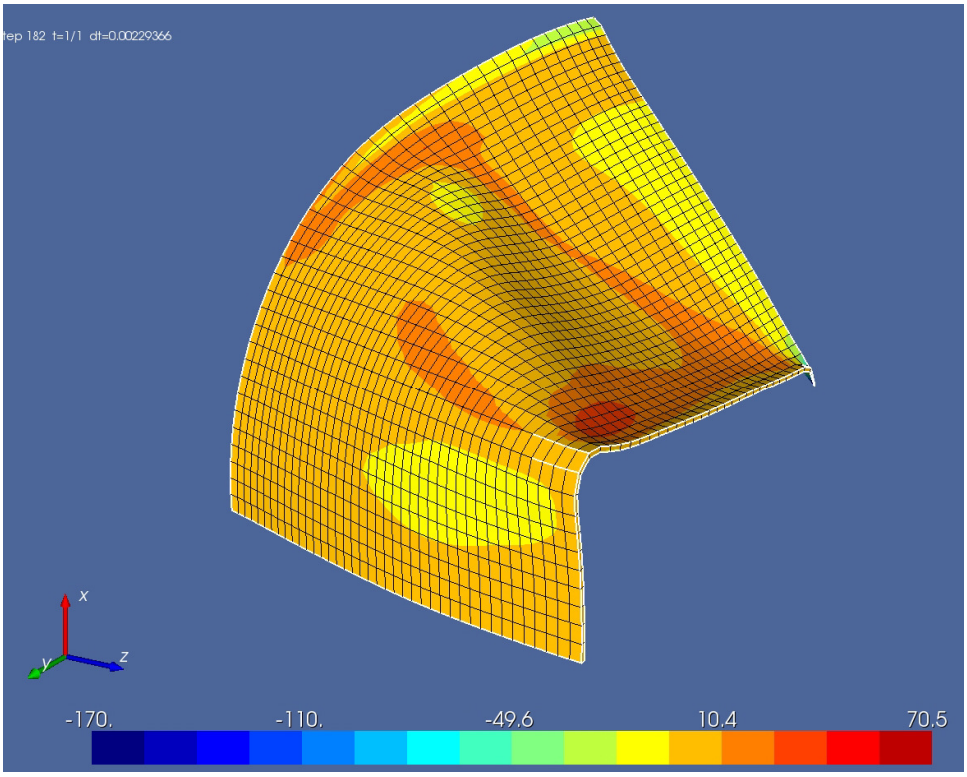

Figure 5.3.21a: Reference - σ_{yz} (EAS12,METAFOR, 40×40×1)

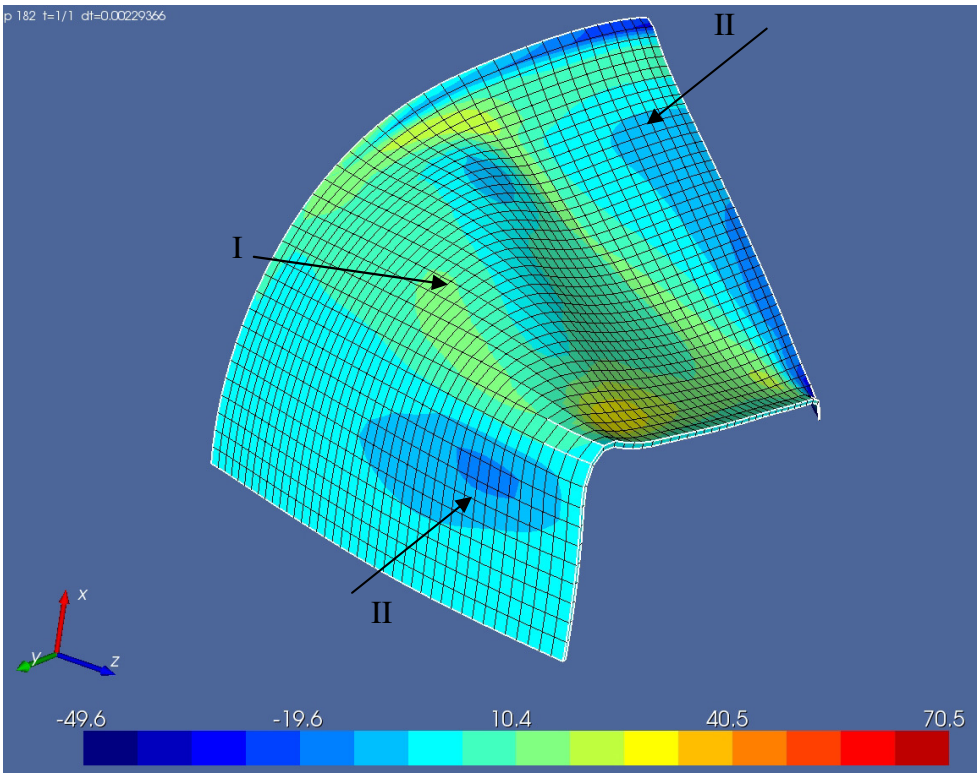

Figure 5.3.21b: Reference - σ_{yz} (EAS12,METAFOR, 40×40×1)
(*due to singularity at load point, min. value for drawing has been imposed to -49.6*)

As analysing above, the differences in transverse shear stresses calculated by the classical ANS technique and the alternative ANS technique lead to difference in von-Mises stress and Load-Displacement curve calculated by the SS7 and SS7n elements, see Figures 5.3.22-24.

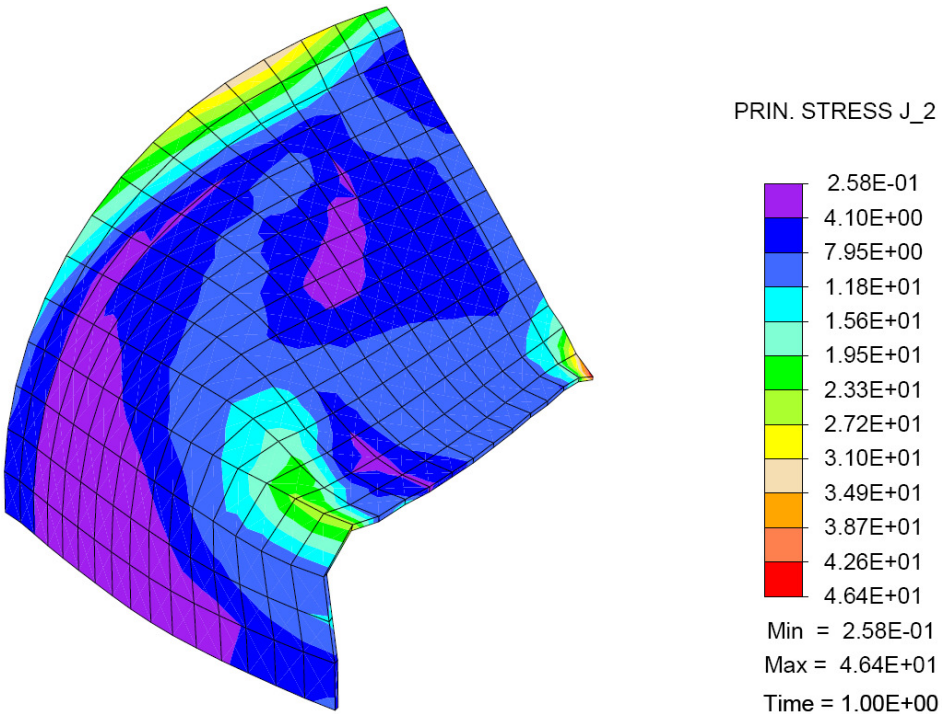

Figure 5.3.22: SS7 element - von Mises stress (mesh 16×16×1)

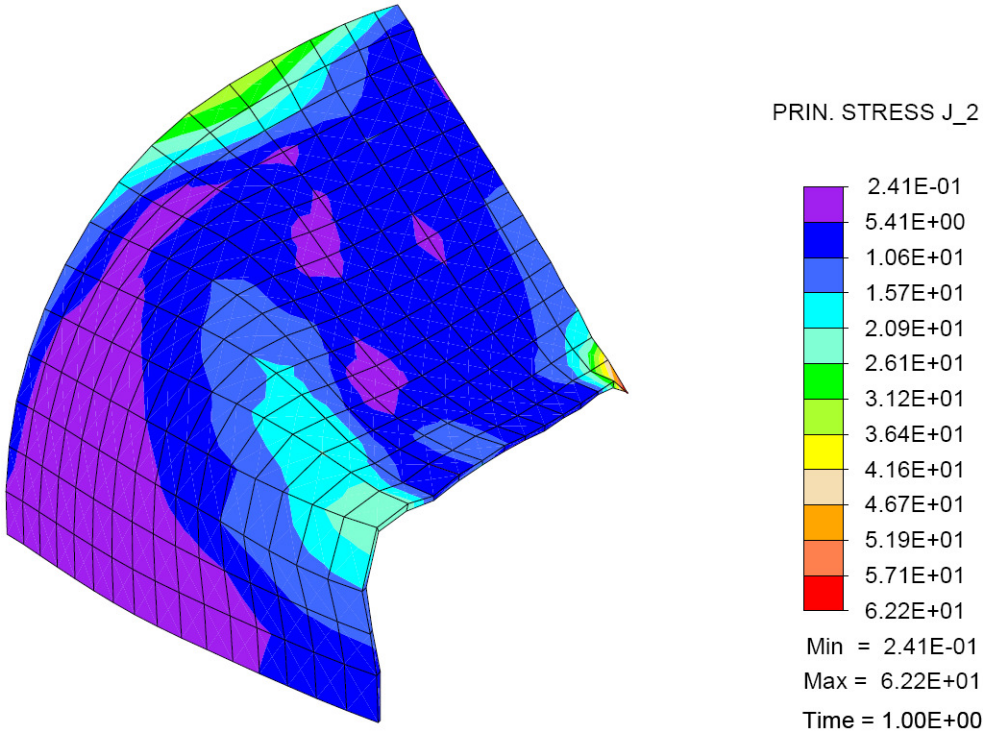

Figure 5.3.23: SS7n element - von Mises stress (mesh 16×16×1)

Next, we compare results of the SS7 and SS7n elements with results of solid element (EAS12) and shell element presented in [WRI96b]. The shell element in [WRI96b] is based on a quasi-Kirchhoff-theory, which means that the assumption of the classical Kirchhoff-Love kinematics is respected via a penalty constraint. A reduced integration for the penalty term was applied in order to obtain locking-free behavior in bending dominated problems.

In Figure 5.3.24 the load-displacements curves for different elements are plotted. In general, the results of the SS7 and SS7n (16×16×1) elements are a little stiffer than the results of 3D calculation (EAS12, 40×40×1 elements). However, with the same coarse mesh (16×16×1) the solid-shell elements, SS7 and SS7n, are comparable to the conventional shell element (RI shell elements, [WRI96b]) and better than results of the EAS12, Figure 5.3.24.

The SS7n element shows a load decrease (at w ≈ 200) as RI shell element does (at w ≈ 210). This consequence arises as a result of the relatively coarse mesh. Hence, it makes the plastic zone cannot developed continuously. This consequence can be canceled by using a finer mesh as appear for the EAS12 results (16×16 vs. 40×40). In Figure 5.3.24 the curve of the SS7 element is smoother than the SS7n.

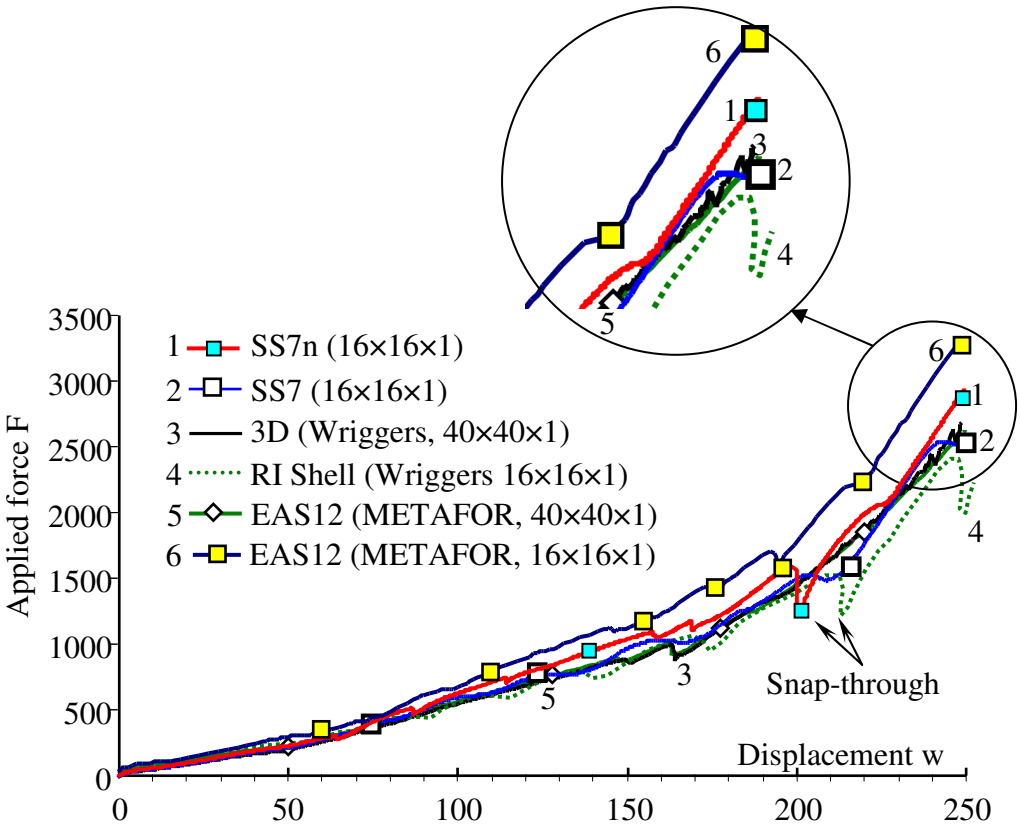

Figure 5.3.24: Pinched cylinder – solid-shell elements

For this problem, behavior of the EAS12 and EAS21 (with both coarse mesh and fine mesh) are similar, see Figures 5.3.24 - 25. Hence, it is reasonable to use 12 internal parameters for the EAS as Wriggers et al. [WRI96b].

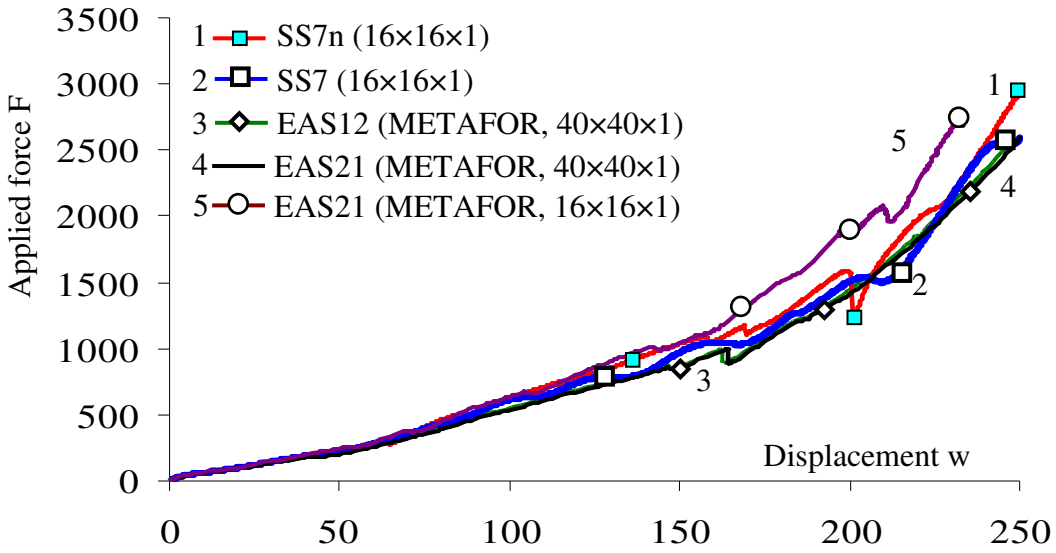

Figure 5.3.24: Pinched cylinder – solid-shell elements

By this numerical test we see that the SS7n element predicts transverse shear stresses better than the SS7 element, Table 5.3.2. For analyzing a thin-walled structure with a coarse mesh, both solid-shell elements, SS7 and SS7n, can work as well as the conventional shell elements, e.g. the shell element in [WRI96b]. The other solid-shell elements, such as the solid-shell element of Samcef (20×20×1 elements) [JET08] provides a result which approximates the result of 3D element of Wriggers (40×40×1 elements). Hence, using the solid-shell elements to simulate thin-walled structures will provide a real 3D model with a cheap computational cost.

5.3.3 Springback of unconstrained cylindrical bending

The following benchmark initially proposed at the NUMISHEET'02 conference [NUM02] has been chosen as a reference case for comparing finite element formulations with various time integration schemes. This benchmark is recommended to investigate springback analysis and complex contact treatment. It consists of an initially flat blank bent into a cylindrical shape and then unloaded. Because there is no blankholder, the problem is called unconstrained bending. The initial geometry and the loading process are described in Figure 5.3.26 (left side). The loading process is stopped when punch and die are concentric (right side of Figure 5.3.26).

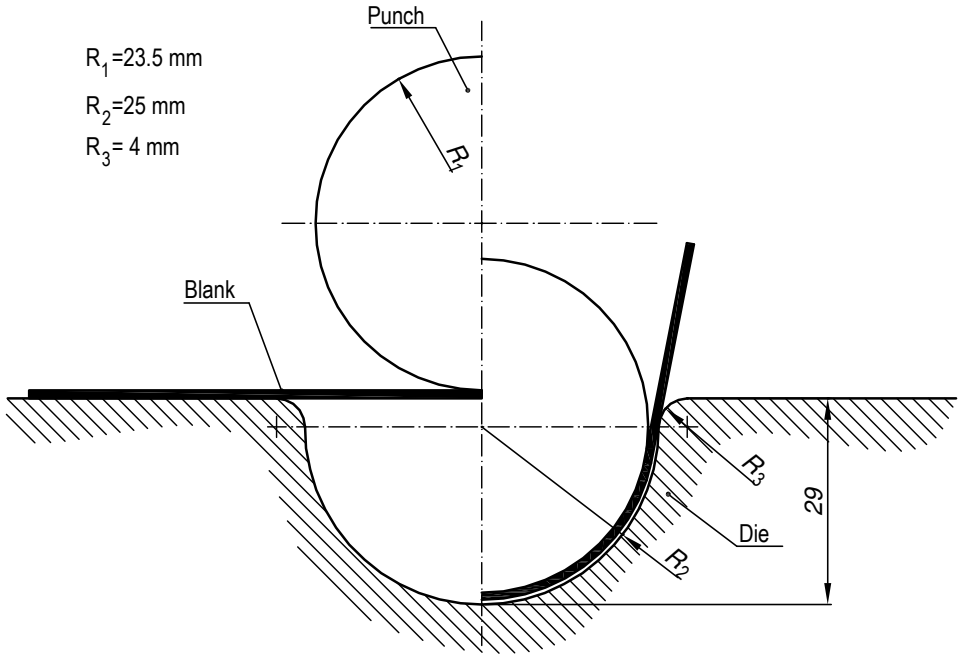

Figure 5.3.26: Initial position (left) and final position (right) for stamping

After the loading phase, the unloading phase takes place and some springback occurs. The amount of springback is quantified in the following way, see Figure 5.3.27.

- Angle between line AB and line CD (Figure 5.3.27a) before and after springback at the final stroke of 28.5 mm.

Other specifications of the problem are:
- The tools are assumed rigid.
- Blank dimension are: length: 120.0mm; thickness: 1mm; width: 30mm.
- Plane strain is assumed during all simulations.
- Friction coefficient: $\mu = 0.1482$.
- The punch speed is kept constant between: (1-50) mm/sec.
- Total punch stroke: 28.5 mm.
- Blank material: isotropic steel with mechanical properties:
  - $\bar{\sigma} = 645.24(\bar{\varepsilon} + 0.0102)^{0.25177}$ MPa;
  - E = 217.500 GPa ; $\nu = 0.3$.

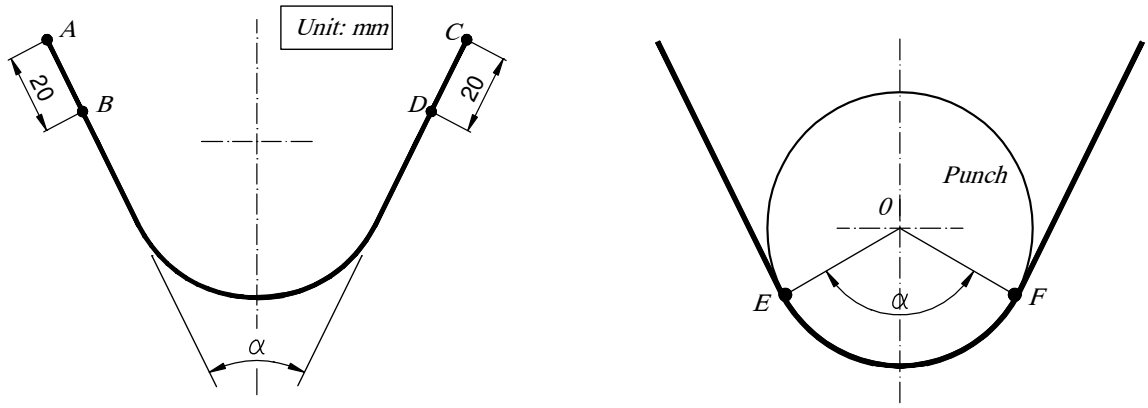

a) between line AB and line CD

b) between 2 contacted points

Figure 5.3.27: Definition of angles
(*point E and point F are the farthest contact points from the centerline*)

First of all a parameter study are undertaken with all elements (EAS, SRI, ANS and solid-shell) in order to determine the sensitivity of the numerical solution with respect to some numerical parameters. Indeed we considered the influence on the results of the discretization, the penalty parameters for contact treatment and the time integration scheme with their associated numerical parameters.

All computations with the EAS and SRI elements were carried out by using METAFOR software [MET08]. All computations with the ANS and solid-shell elements were carried out by using FEAP program [TAY01]. This is a plane strain problem, hence, instead of using the SS7n element its 2D version - 2D.SS4n element will be adopted. The 2D.SS4n is resulted from the 2D.ANSn in (3.3.27) and the EAS4 element, Table 2.4.3.

Simulation with 2D.EAS7 elements

Table 5.3.3 is a survey of some representative results. First of all the blank is divided into three zones (see Figure 5.3.28) whose lengths are respectively given by 21, 18 and 21 mm, respectively. Inside any of the three zones any element has the same length. Then each of the zones has been discretized by imposing n_2 elements through the thickness and respectively n_1 equal elements in the first zone and n_3 and n_4 in the two remaining zones.

The different numerical parameters are then systematically explored. First, mesh size was changed to find out a good mesh quality (Table 5.3.3/Cases 1-4). After having set the mesh, the penalty parameters are varied (Table 5.3.3/Cases 5-6). Then, integration scheme is changed from quasi-static to implicit Chung-Hulbert (Table 5.3.3/Cases 6-8) with parameters are $\alpha_M = -0.97$ and $\alpha_F = 0.01$. This choice for α_M and α_F satisfies the unconditional stability and second order accuracy of Chung-Hulbert scheme [PON99]. Number of elements through the thickness direction was also considered (Table 5.3.3/Cases 6-9). Each input parameter was changed to get a better and better result. The Table 5.3.3/Case 10 with very fine mesh is introduced to get a reference solution.

The areas which are sensible to mesh size are deformed areas (meshed by n_1, n_2, n_3 elements). We only survey the changes of n_1, n_2 and n_3 because the area with n_4 elements is neither deformed nor contacted by the punch or die (see Figure 5.3.28).

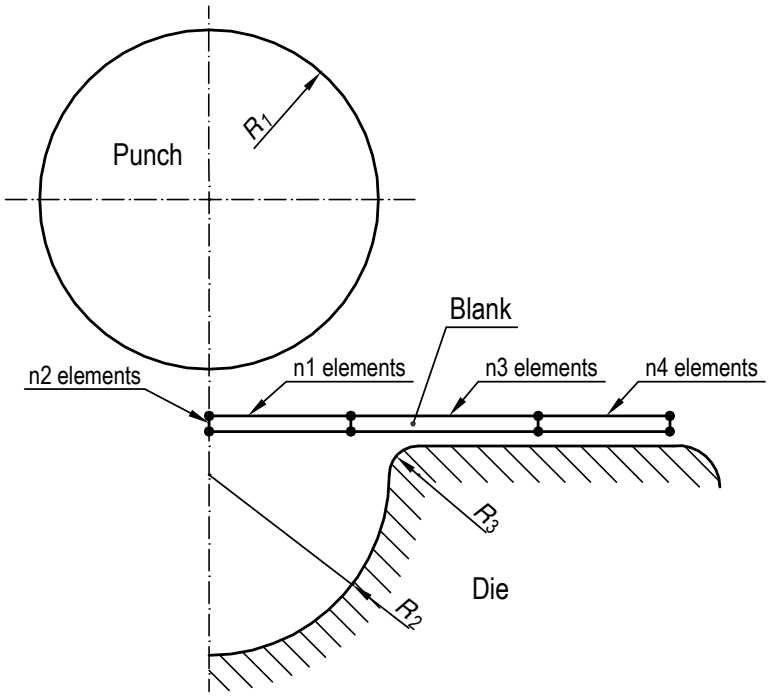

Figure 5.3.28: Discretization of the model: definition of the 3 zones

Then, when a fine enough discretization has been attained for the mesh, the penalty parameters is varied. For reasonable variations, it can be seen in Figure 5.3.30 that there is almost no difference in the force curves. The conclusion is the same when the implicit Chung-Hulbert scheme has been used instead of the quasi-static algorithm. As far as one avoids using only one element through the thickness (Case 9 in Figure 5.3.29) one can also see that the results are quite stable. All the punch force - displacement curves, except the case of using 1 element through the thickness, nearly coincide with the reference curve - Case 10 (Table 5.3.3). So we can conclude that with $\geq$2 elements through the thickness the mesh is refined enough.

Table 5.3.3. Calculation with 2D.EAS7 element

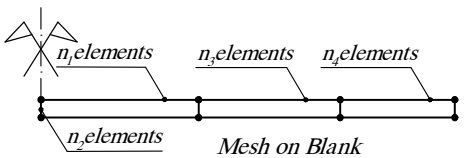

Case	Integration scheme	Penalty	Mesh Size n_1; n_2; n_3; n_4	Note
1	QS	1.0×10^3	30; 2; 40; 20	
2	QS	1.0×10^3	**60**; 2; 40; 20	
3	QS	1.0×10^3	30; 2; **80**; 20	
4	QS	1.0×10^3	30; 2; **100**; 20	
5	QS	$\mathbf{5.0\times10^2}$	30; 2; 100; 20	
6	**C-H**	5.0×10^2	30; 2; 100; 20	Convergence of 2D.EAS7
7	C-H	5.0×10^2	30; **3**; 100; 20	
8	C-H	$\mathbf{3.0\times10^2}$	30; 3; 100; 20	
9	**QS**	$\mathbf{1.0\times10^3}$	30; **1**; 100; 20	
10	QS	1.0×10^3	**150**; **7**; **150**; **30**	Reference

** Bold numbers or letters indicate what has changed from one case to another*
C-H: Chung - Hulbert scheme
QS: Quasi - static

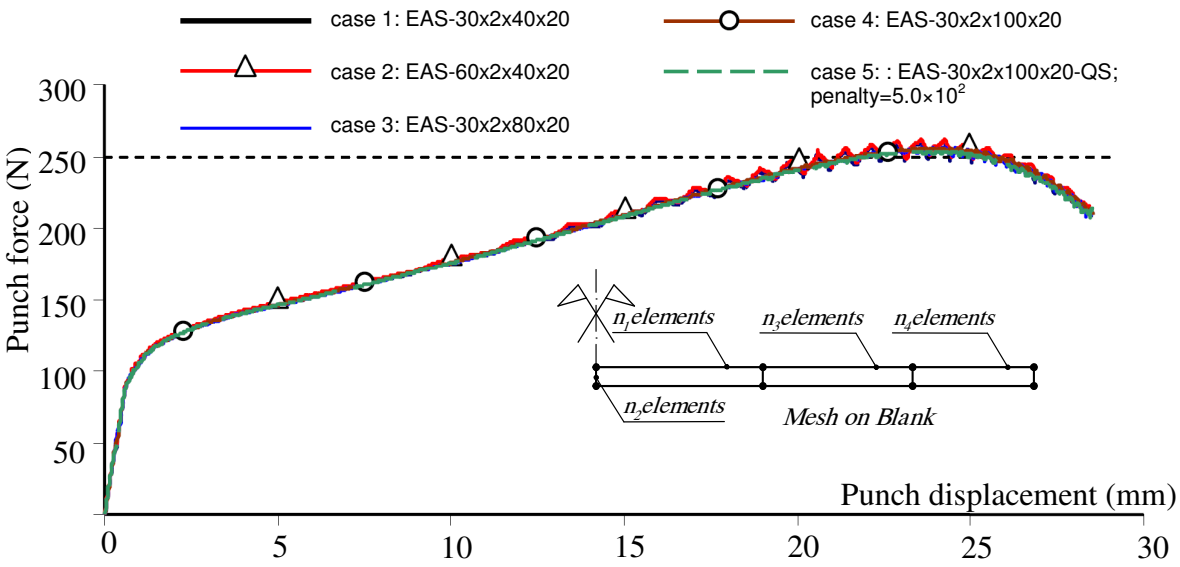

Figure 5.3.29: Punch force vs. punch displacement – EAS element
(*quasi-static; Table 5.3.3/cases 1 to 5; penalty* $=1.0\times10^3$)

For mesh discretization parameter n_3 is the most sensitive. Indeed, a rough discretization in this zone leads to oscillations in the punch force versus punch displacement curve as can be seen in Figure 5.3.29 (Case 2). This can be easily explained since it is the lower side of elements located in this zone that do have a sliding contact with the shoulder of the die (radius R_3 - see Figure 5.3.28). As far as the contact with punch is considered the radius R_1 is much larger than R_3 so it is much less sensitive to discretization. Actually, if n_3 is too small the number of nodes in contact with the die can be reduced to one. As a consequence, this leads to oscillations in the curve. As can be seen in Figure 5.3.29, $n_3 = 100$ lead to almost no oscillation.

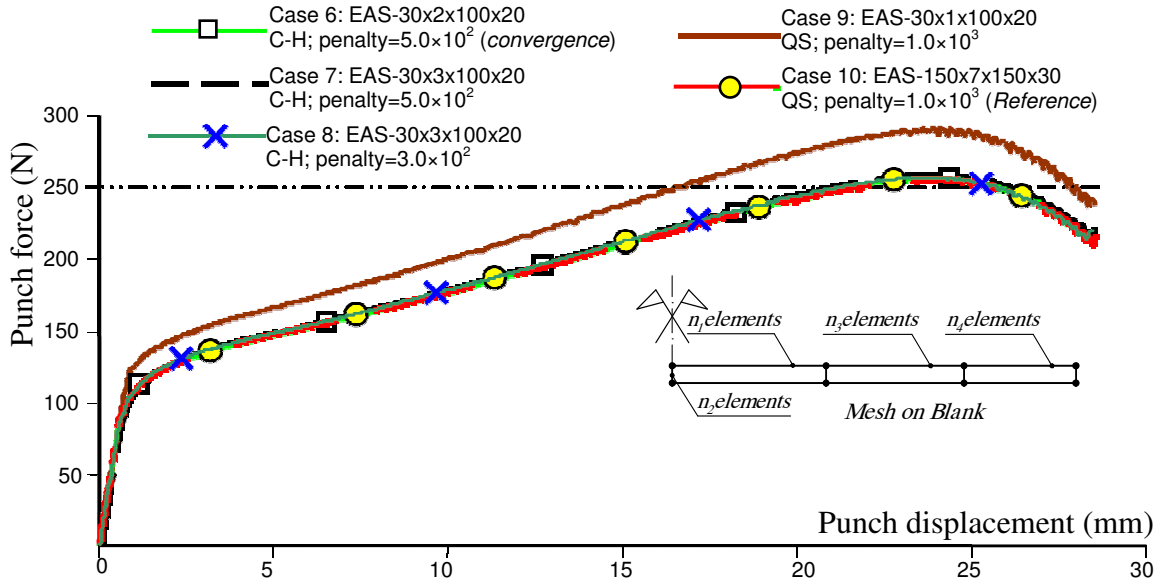

Figure 5.3.30: Punch force vs. punch displacement – EAS element
(*Table 5.3.3/cases 6 to 10*)

In Figure 5.3.30, we see that the results got by using different penalty parameters, which are 2 times of difference (5.0×10^2 and 1×10^3), are generally similar. For this problem, solutions got by quasi-static scheme and dynamic scheme are almost similar. Solutions with 2 or 3 elements on the thickness are similar, except the case of using 1 element on the thickness - Case 9 makes the behavior stiffer.

Simulation with 2D.SRI elements

In this section, a similar study was carried out but this time using 2D.SRI elements. Different results are tabulated in Table 5.3.4.

First of all, we started the 2D.SRI computations with a reasonable mesh for the 2D.EAS7 simulation (reasonable means that the force curve is quite close to the reference one in this case), e.g. $n_1 = 30$; $n_2 = 2$; $n_3 = 100$; $n_4 = 20$ (see Table 5.3.3/Case 6). As can be seen in Figure 5.3.32, the resulting curve exhibits a lack of smoothness. Changing the numerical parameters while keeping $n_1 = 30$ does not affect too much the results (see again Figure 5.3.32), while increasing n_1 will lead to the reference solution - see Figure 5.3.33 - for n_1 equal to or larger than 100.

As a first conclusion, we can state that even if 2D.SRI element are much cheaper than 2D.EAS7 and converge to the reference solution as the mesh is refined, they should be used with some care as they do not exhibit a coarse mesh accuracy as the 2D.EAS7 does. The 2D.SRI element converges with a mesh of 100×2×100×20 element (Table 5.3.4/Case 6). Meshes of cases 7 and 8 are very fine, so they are the best solutions of 2D.SRI elements.

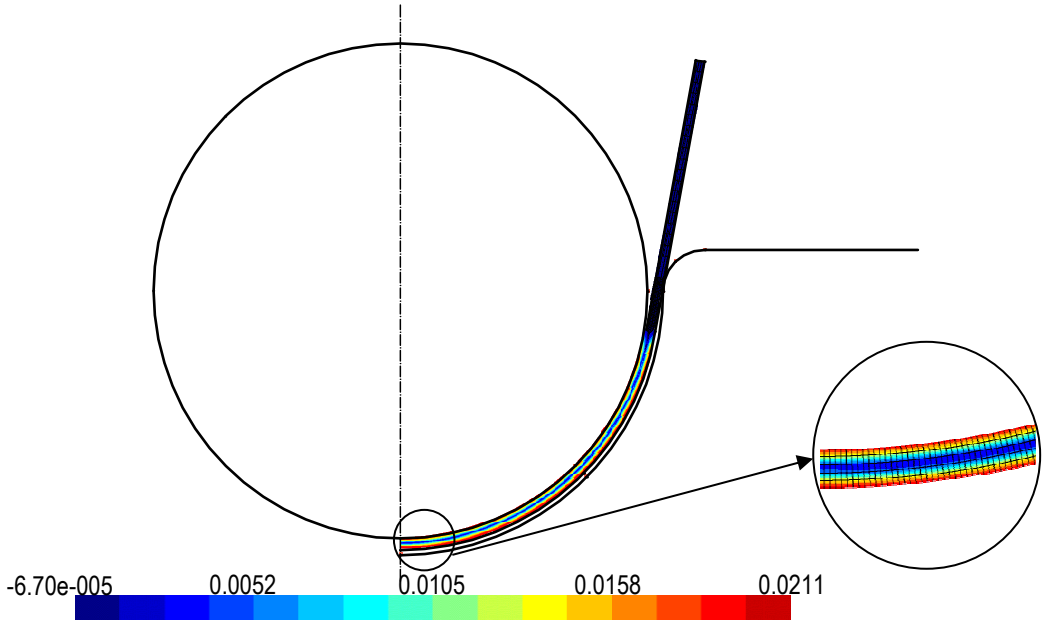

Figure 5.3.31: Reference solution of SRI element
(*Table 5.3.4 /case 7– equivalent plastic strain, simulation with METAFOR*)

Table 5.3.4. Calculation with 2D.SRI element

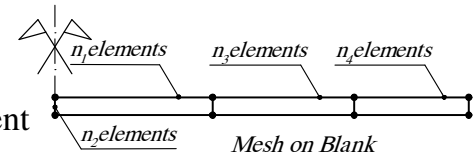

Case	Integration scheme	Penalty	Mesh n_1; n_2; n_3; n_4	Note
1	QS	5.0×10^3	30; 2; 100; 20	
2	QS	**5.0×10^2**	30; 2; 100; 20	
3	**C-H**	**1.0×10^3**	30; 2; 100; 20	
4	C-H	1.0×10^3	30; **3**; 100; 20	
5	**QS**	1.0×10^3	30; **1**; 100; 20	
6	C-H	1.0×10^3	**100**; **2**; 100; 20	Convergence of 2D.SRI
7	**QS**	1.0×10^3	**150**; **5**; **150**; 20	
8	**C-H**	1.0×10^3	**185**; **7**; **185**; **30**	

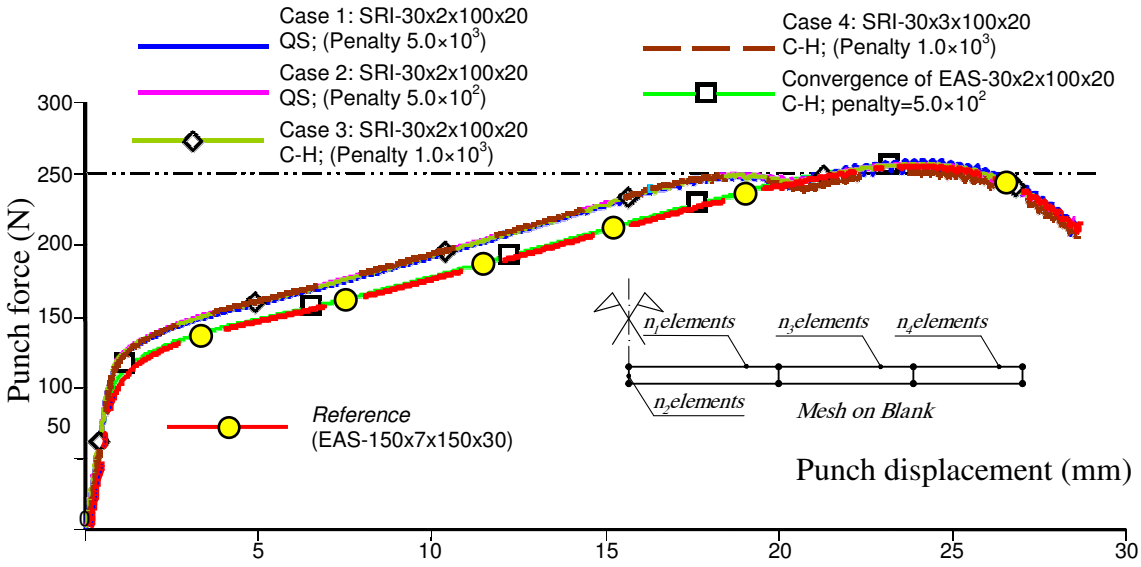

Figure 5.3.32: Punch force vs. punch displacement – SRI element
(*Penalty*=1.0×10^3*; Table5.3.4/cases 1 to 4*)

Simulation with 2D.ANS elements

Before investigate springback with the solid-shell elements, let's consider springback behavior of 2D.ANSn elements. For this springback test, behavior of the ANS and ANSn is similar so only results of the 2D.ANSn are presented in Table 5.3.5. We investigate the ANS computations with a mesh with which the EAS element converged, i.e. $n_1 = 30$; $n_2 = 2$; $n_3 = 100$; $n_4 = 20$ (see Table 5.3.3/Case 6). Due to volumetric locking happens with the 2D.ANSn element, we should start with a higher number of element along the thickness to reduce locking, e.g., $n_2 = 3$. However, as seeing in Figure 5.3.35, the resulting curve still exhibits locking.

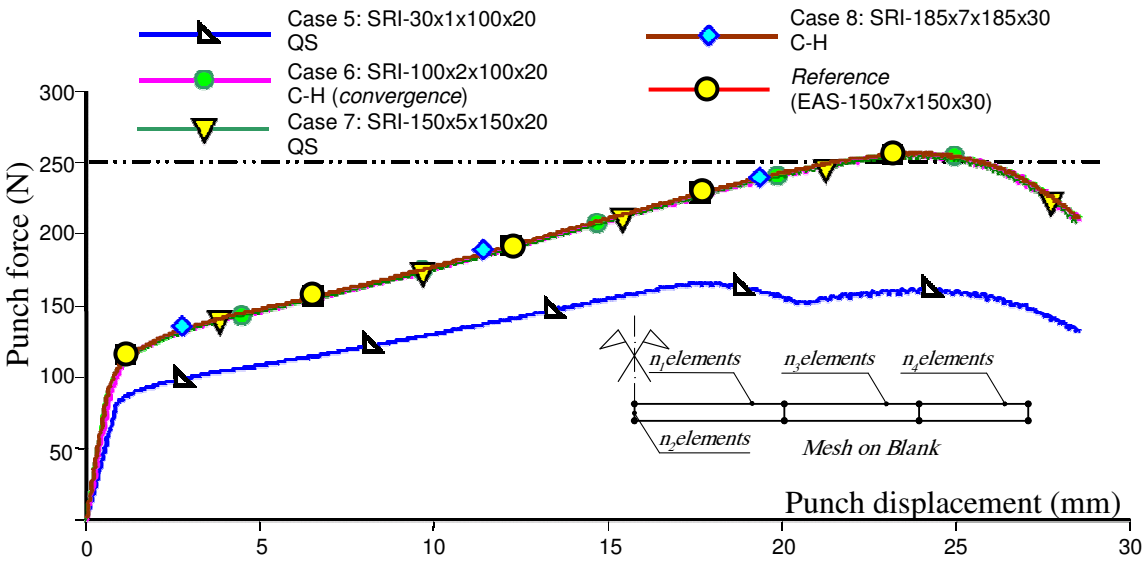

Figure 5.3.33: Punch force vs. punch displacement – SRI element
(*Penalty*=1.0×10^3*; Table5.3.4/cases 5 to 8*)

The punch force - displacement curve with the 2D.ANSn element is stiffer than the reference curve, see Figure 5.3.35. Increasing number of element along the thickness $n_2 = 4$ (Table 5.3.5/Case 2), the resulting curve is closer to the reference one. To get more stringent result, let's trying increasing element number in contact area with punch, $n_1 = 100$ (Table 5.3.5/Case 3). Data in Figure 5.3.34 shows that increasing n_1 has only effect of reducing oscillation of contact force. Meanwhile, increasing number of element along the thickness, $n_2 = 5$ (Table 5.3.5/Case 4), we get better result. The converged result of the ANSn element is obtained with penalty parameter equal to 1.0e+2, Table 5.3.5/Case 4. If we use a higher penalty value (5.0e+2) the computational cost increasing while result is not improved, Figure 5.3.34-36. The consequence is the same when integration scheme is changed from quasi-static to Newmark (because the Chung-Hulbert scheme is not available in FEAP).

Table 5.3.5. Calculation with 2D.ANSn element

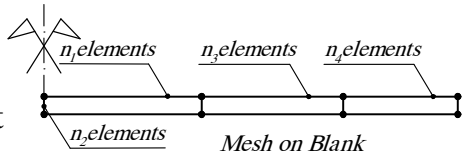

Case	Integration scheme	Penalty	Mesh n_1; n_2; n_3; n_4	Note
1	QS	1.0×10^2	30; **3**; 100; 20	
2	QS	1.0×10^2	30; **4**; 100; 20	
3	QS	1.0×10^2	**100**; 4; 100; 20	
4	QS	1.0×10^2	**30**; **5**; 100; 20	Chosen result of 2D.ANSn
5	QS	1.0×10^2	**100**; 5; 100; 20	
6	QS	**5.0×10^2**	30; 5; 100; 20	
7	**Newmark**	1.0×10^2	30; 5; 100; 20	

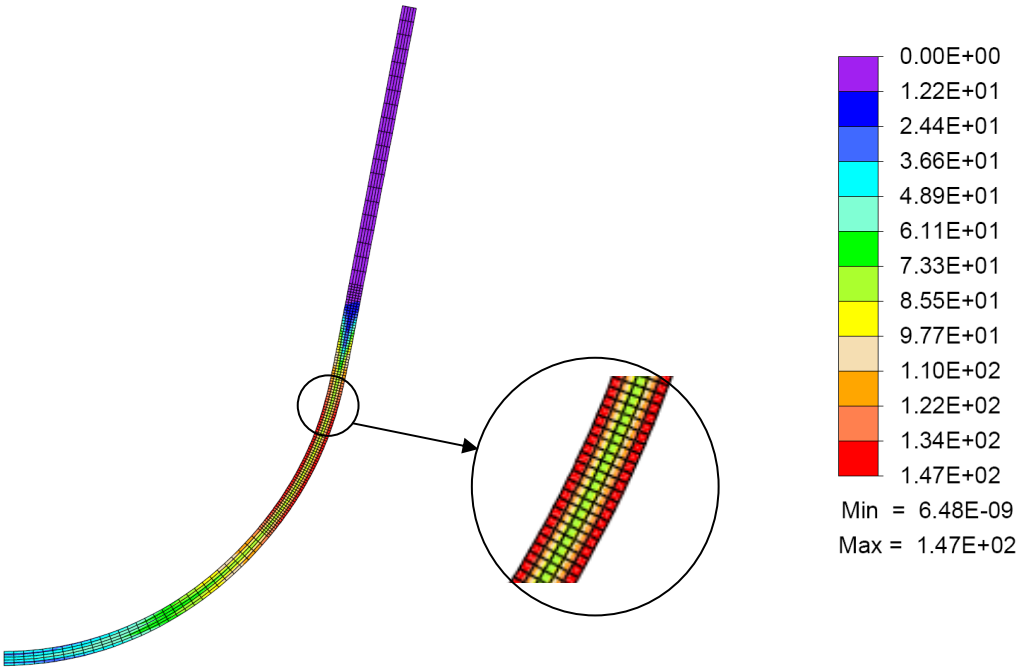

Figure 5.3.34: Chosen solution of 2D.ANSn element
(*Table 5.3.5 /case 6 – von Mises stress, simulation with FEAP*)

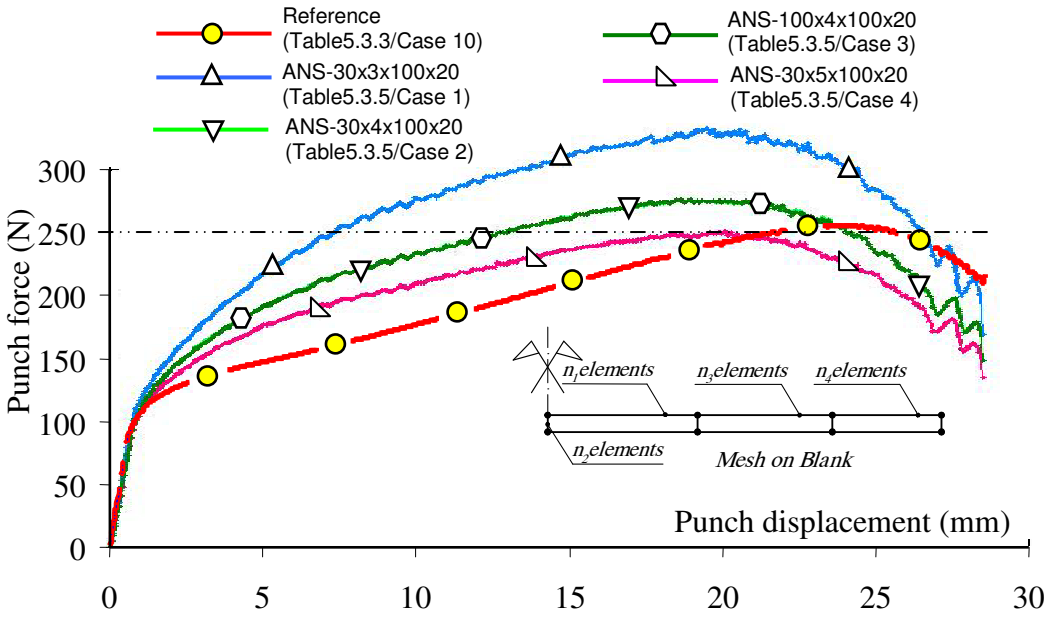

Figure 5.3.35: Punch force vs. punch displacement – ANSn element
(*Table5.3.5/cases 1 to 4*)

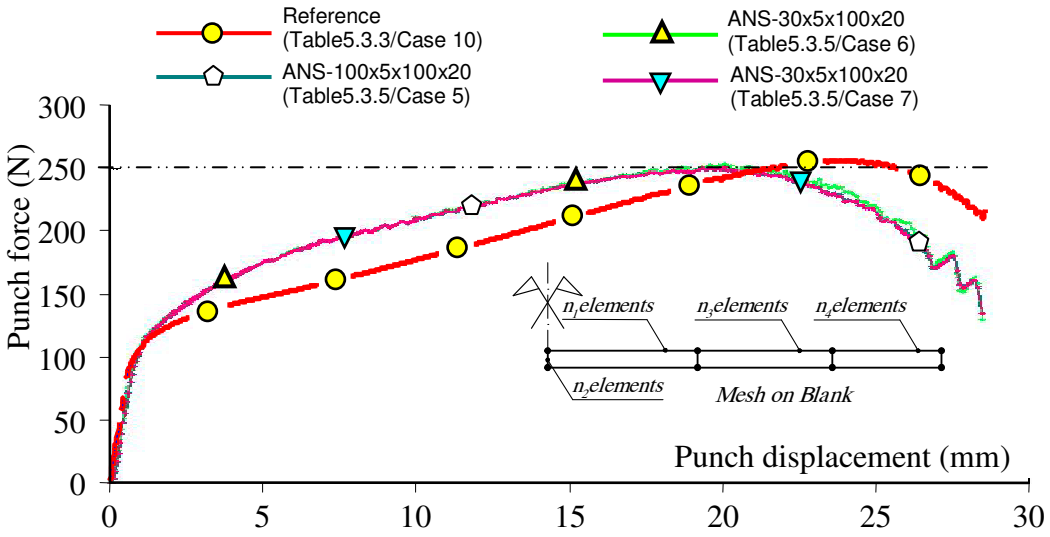

Figure 5.3.36: Punch force vs. punch displacement – ANSn element
(*Table5.3.5/cases 5 to 7*)

We see that ANS computation with 5 layers of element along the thickness gives the same maximal punch force as the one of the EAS element (30×2×100×20), see Figures 5.3.35-36. However, behaviors of the ANS and EAS elements are different. The ANS element is stiffer when punch displacement is smaller than 20mm. When punch displacement is larger than 20mm, ANS behavior is softer. This consequence is reasonable because the ANS element is only shear-locking free.

Simulation with solid-shell element

Finally, springback prediction for this unconstrained bending problem is investigated with the solid-shell element: 2D.SS4n. With this test, behavior of the solid-shell elements using the classical technique and the alternative ANS technique is similar. Hence, only results of the later are presented in Table 5.3.6. We begin the computation with a coarse mesh for EAS simulation, i.e. $n_1 = 30$; $n_2 = 2$; $n_3 = 40$; $n_4 = 20$ (Table 5.3.3/Case 1). Then, the mesh is made finer to get better result. Data from Figure 5.3.38 shows that the solid-shell element converged with rather coarse mesh, $n_1 \times n_2 \times n_3 \times n_4 = 60 \times 2 \times 70 \times 20$.

Table 5.3.6. Calculation with solid-shell element

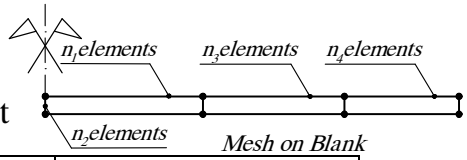

Case	Integration scheme	Penalty	Mesh $n_1; n_2; n_3; n_4$	Note
1	QS	1.0×10^2	30; **2**; 40; 20	
2	QS	1.0×10^2	50; **2**; 60; 20	
3	QS	1.0×10^2	**60**; 2; **70**; 20	Convergence of solid-shell
4	QS	5.0×10^2	60; **3**; 70; 20	
5	**Newmark**	$\mathbf{1.0\times10^2}$	60; **2**; 70; 20	

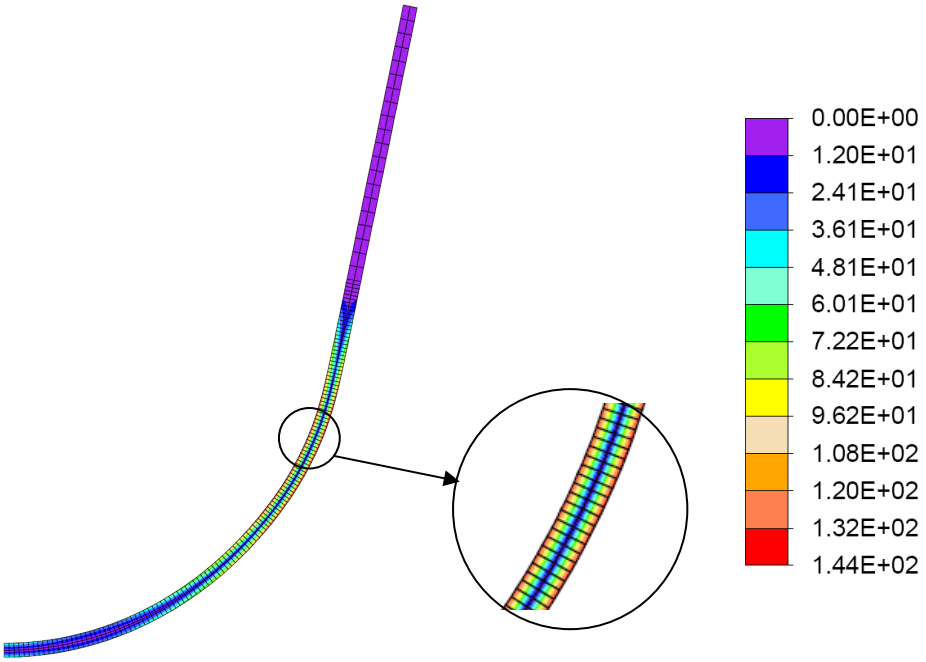

Figure 5.3.37: Reference solution of 2D.SS4n element
(*Table 5.3.6 /case 3 – von Mises stress, simulation with FEAP*)

After having set the mesh, the penalty parameters are varied (Table 5.3.6/Cases 4). Then, integration scheme is changed from quasi-static to Newmark (Table 5.3.6/Cases 5). It can be seen in Figures 5.3.38 - 39 that there is almost no difference in the force curves. The conclusion is the same when the Newmark scheme has been used instead of the quasi-static algorithm. We see that when the punch force is larger than 200N the solid-shell element is a little softer than the reference result.

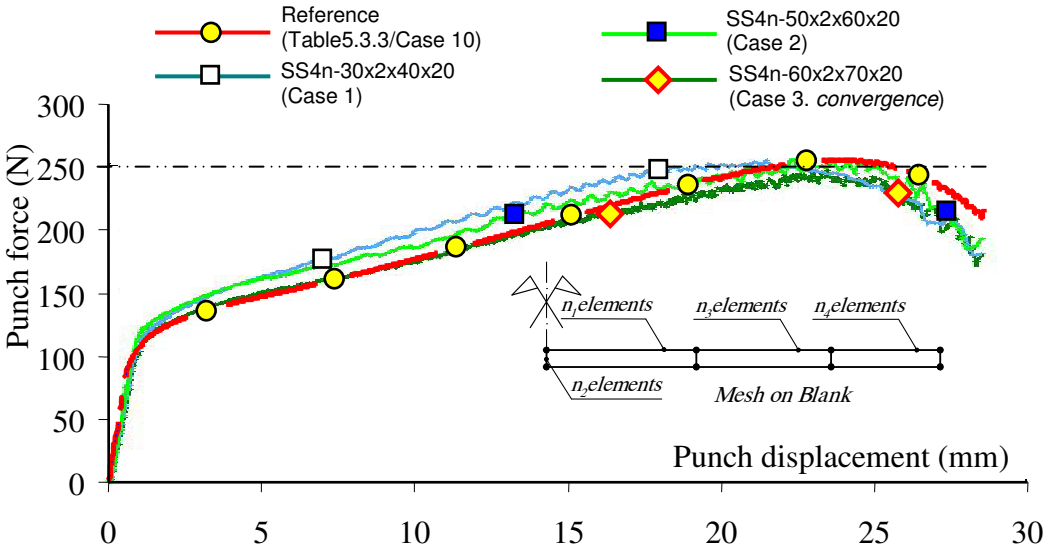

Figure 5.3.38: Punch force vs. punch displacement – 2D.SS4n element
(*Table5.3.6/cases 1 to 3*)

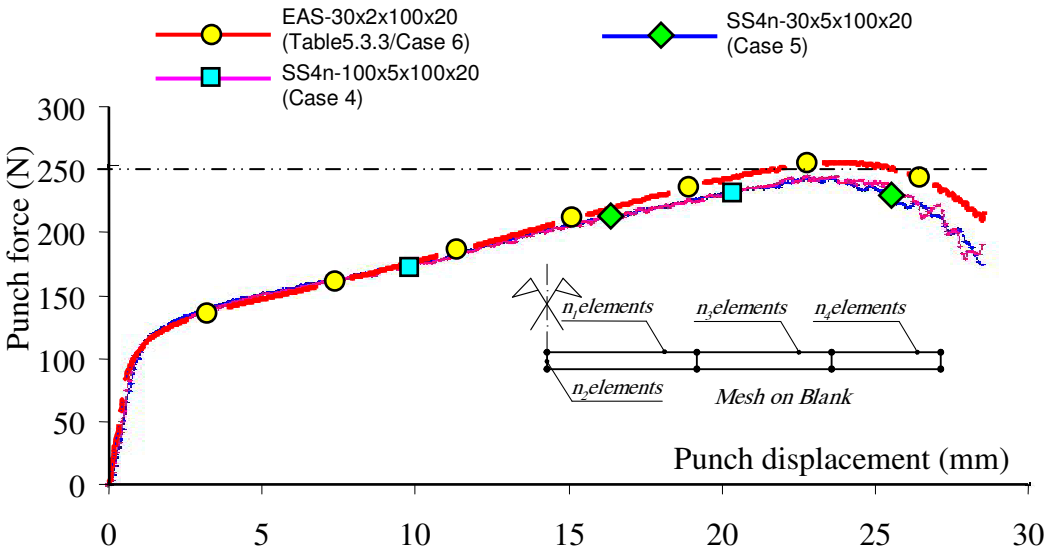

Figure 5.3.39: Punch force vs. punch displacement – 2D.SS4n element
(*Table5.3.6/cases 4 and 5*)

Validation of simulation results

In order to validate results of the solid-shell element, the force curve obtained has been compared to both experimental (BE - Figure 5.3.40) and numerical (BS - Figure 5.3.41) results published in the NUMISHEET'02 proceeding [NUM02]. As can be seen from those figures, numerical results from the 2D.SS4n match quite well the experimental reference results (curve BE-01). It should be noted that numerical results exhibit a quite large dispersion which can be attributed to the variety of finite element codes, as well as the variety of elements (shell, continuum quads, triangles) and time integration algorithm (implicit, quasi-static).

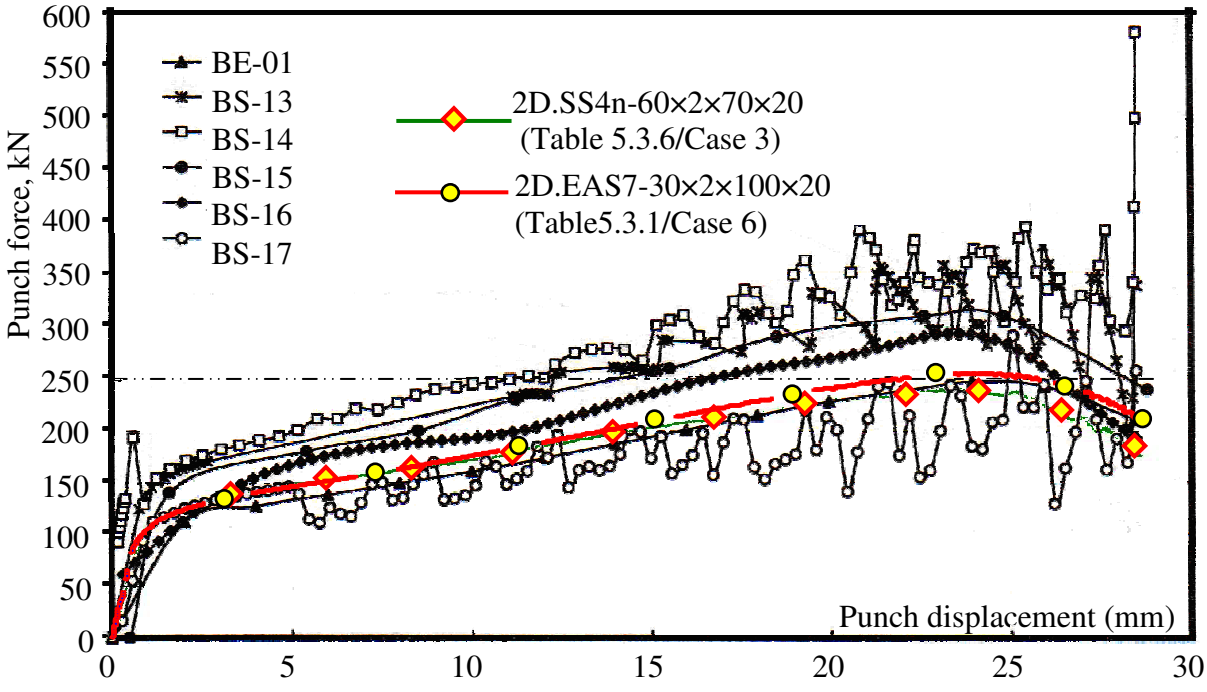

Figure 5.3.40: Punch force vs. punch displacement [NUM02]
(*BS = Benchmark simulation result*)

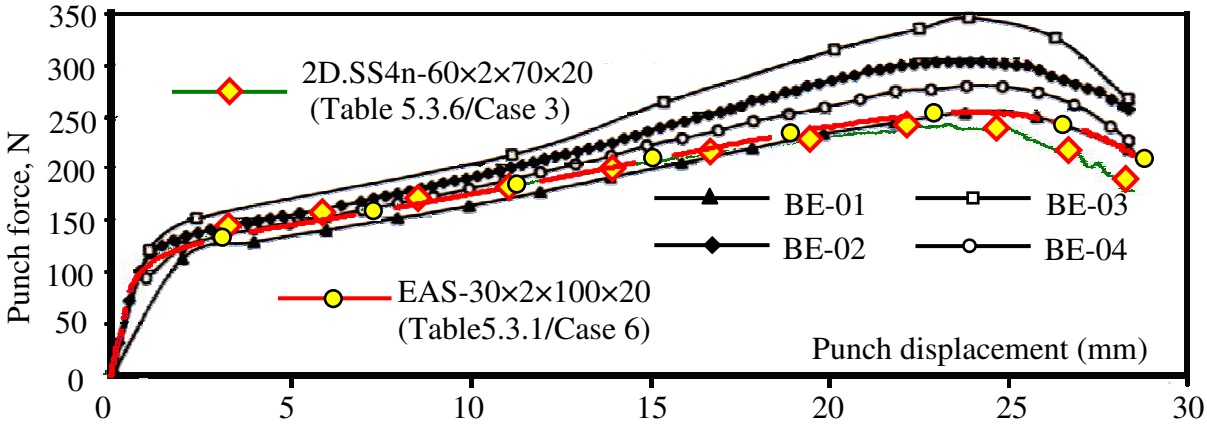

Figure 5.3.41: Punch force vs. punch displacement [NUM02]
(*BE = Benchmark Experiment result*)

When punch force is smaller than 200N results of the 2D.EAS7 and 2D.SS4n are coincident but they are a little different from the experiment results, BE-01. When punch force is larger than 200N, only the 2D.EAS7 gives the identical results with results of the BE-01. Meanwhile, the 2D.SS4n is a little softer than the 2D.EAS7.

As a more local result of the benchmark, it was also asked to evaluate the angle α - see Figure 5.3.27 and Figure 5.3.42 for definition and illustration for different punch stroke, i.e. 7, 14, 21 and 28.5 mm. Results delivered by the 2D.SS4n are very closed to the experimental values (BE-01), see Figure 5.3.43. The convergence results of the other element are also presented in Figure 5.3.43. See Table 5.3.7 - 10 for angle α at different punch strokes in all cases of simulation with the 2D.EAS7, 2D.SRI, 2D.ANSn, 2D.SS4n elements.

Table 5.3.7. Springback angles - calculation with 2D.EAS7 element

Case	Angle (°) between line AB and line CD		Angle (°) between 2 farthest points (from centerline) at stroke			
	before SB	after SB	7mm	14mm	21mm	28.5mm
1	21.864	33.440	16.536	60.298	111.108	158.726
2	21.184	33.436	18.688	62.120	111.228	158.494
3	21.376	33.338	16.964	60.054	112.298	158.406
4	21.378	33.082	16.786	60.182	112.514	158.804
5	21.882	33.850	20.154	63.634	113.386	158.970
6	*21.974*	*33.788*	*20.102*	*63.652*	*113.468*	*158.904*
7	21.630	33.404	20.158	63.550	113.480	158.872
8	21.056	33.968	20.326	63.666	114.338	159.800
9	21.438	35.510	20.322	63.458	113.466	158.702
10	21.344	33.358	18.880	62.260	112.432	158.278

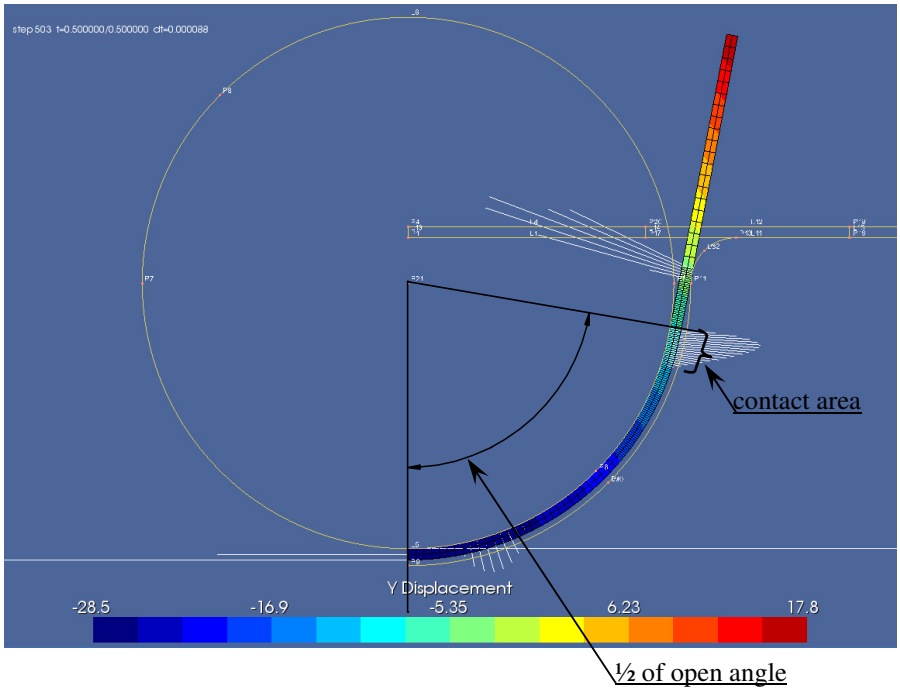

Figure 5.3.42: Definition of the angle between 2 contact points which are the farthest from the centerline

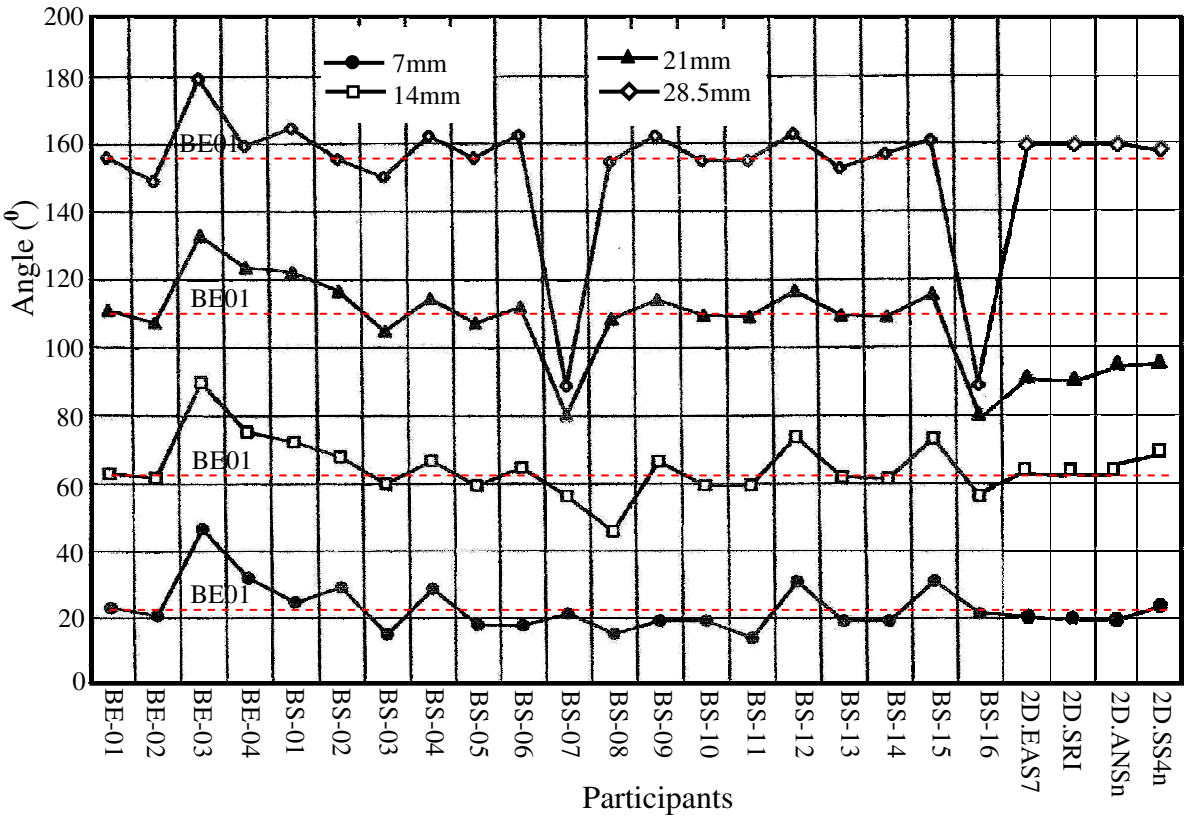

Figure 5.3.43: Angle between 2 contact points which are the farthest from the centerline [NUM02]

Table 5.3.8.: Springback angles - calculation with 2D.SRI element

Case	Angle (°) between line AB and line CD		Angle (°) between 2 farthest points (from centerline) at stroke			
	before SB	after SB	7mm	14mm	21mm	28.5mm
1	21.246	34.086	16.988	60.106	111.550	157.048
2	21.704	34.654	20.258	63.340	113.228	159.652
3	21.652	34.348	20.112	63.606	112.612	158.816
4	21.514	33.400	16.786	60.028	112.446	158.598
5	21.144	35.726	20.238	63.560	113.476	158.806
6	*21.466*	*34.884*	*19.246*	*63.052*	*112.640*	*159.002*
7	21.288	33.430	18.806	62.132	112.388	158.790
8	21.344	33.812	18.550	62.206	112.464	158.462

Table 5.3.9. Springback angles - calculation with 2D.ANSn element

Case	Angle (°) between line AB and line CD		Angle (°) between 2 farthest points (from centerline) at stroke			
	before SB	after SB	7mm	14mm	21mm	28.5mm
1	22.000	49.800	16.000	62.000	116.000	158.000
2	23.000	40.600	18.000	64.000	116.000	159.000
3	23.000	40.600	19.000	64.000	116.000	158.000
4	*23.000*	*37.000*	*19.000*	*63.000*	*116.000*	*159.000*
5	23.000	37.000	19.200	61.500	114.000	159.000
6	21.500	36.000	18.000	63.000	114.000	159.000
7	21.600	36.500	18.000	63.000	114.000	159.000

Table 5.3.10. Springback angles - calculation with 2D.SS4n element

Case	Angle (°) between line AB and line CD		Angle (°) between 2 farthest points (from centerline) at stroke			
	before SB	after SB	7mm	14mm	21mm	28.5mm
1	23.000	34.500	25.000	66.000	117.000	160.000
2	23.000	33.500	24.000	67.500	117.000	161.000
3	*23.000*	*33.500*	*23.000*	*66.000*	*117.000*	*157.500*
4	22.500	32.500	24.000	66.000	114.500	159.000
5	22.500	32.500	22.000	66.000	115.500	159.000

Springback simulation

In order to evaluate the springback, the tools are progressively removed and the resulting opening angle, as defined in Figure 5.3.27a is measured as shown in Figures 5.3.44 and 5.3.45.

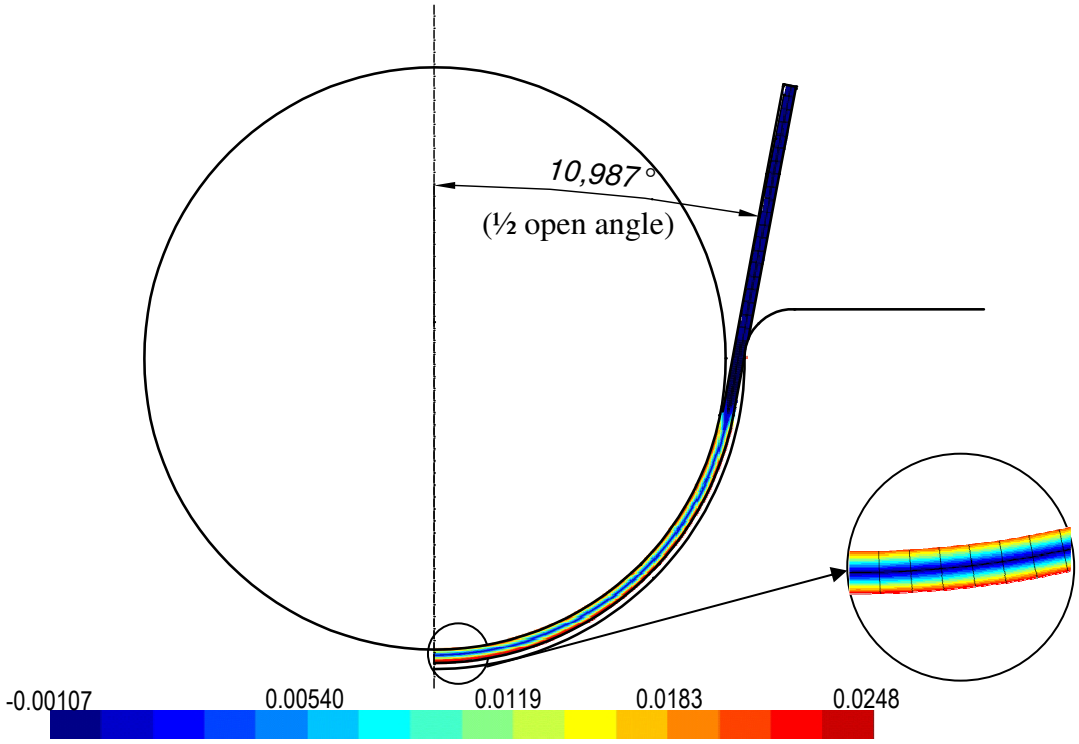

Figure 5.3.44: Open angle between the lines AB and CD before spring back
(*Table 5.3.3/Case 6 - equivalent plastic strain - METAFOR*)

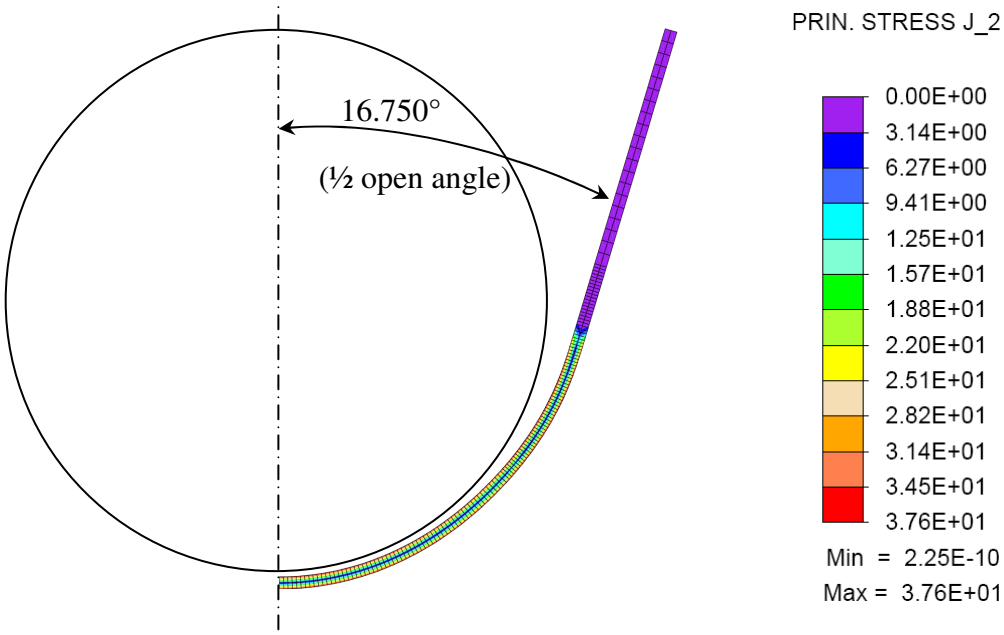

Figure 5.3.45: Open angle between the lines AB and CD after spring back
(*Table 5.3.6/Case 3 - equivalent stress - FEAP*)

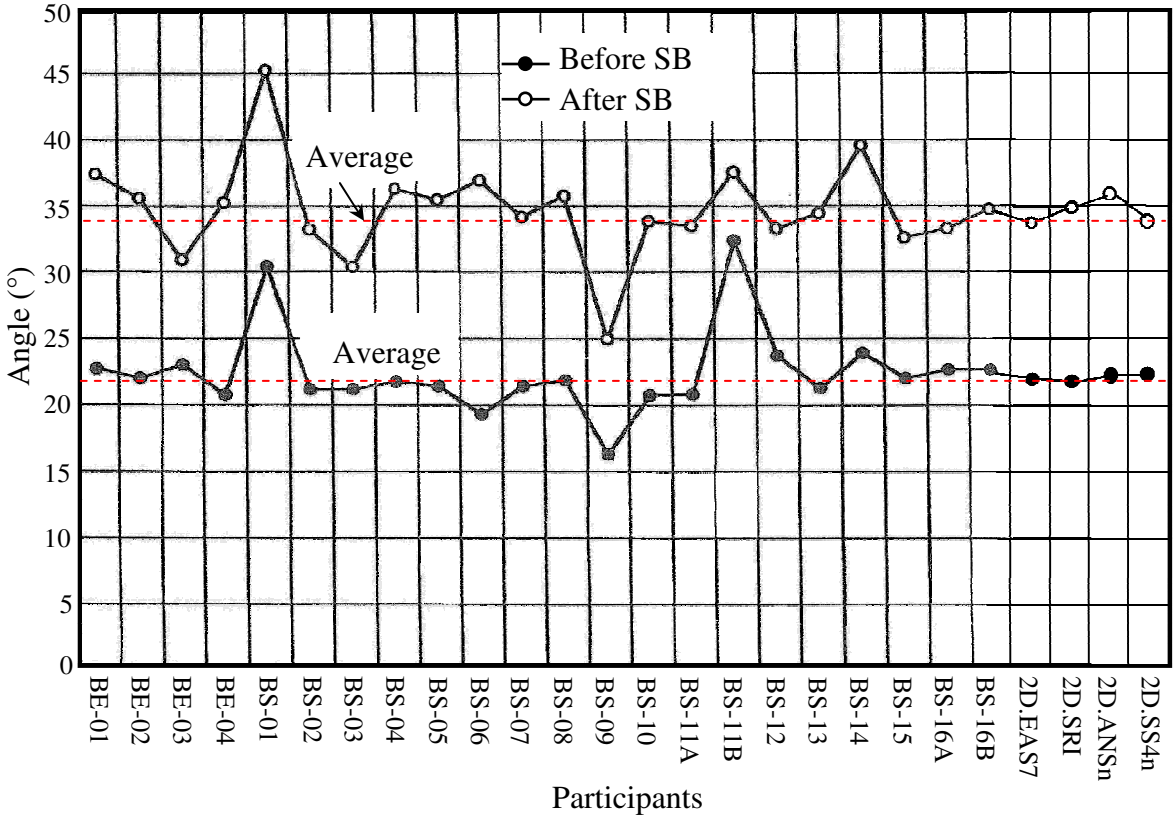

Figure 5.3.46: Angle before and after springback at the final punch stroke of 28.5 mm

Data in Tables 5.3.7 - 5.3.10 are used to compare results of the 2D.EAS7, 2D.SRI, 2D.ANSn and 2D.SS4n with the other sources in [NUM02]. Figure 5.3.46 presents curves for angles before and after springback. Concretely:

- Figure 5.3.46 shows that almost open angles before and after springback concentrate around the mean values, 22° with respect to open angles before springback and 34° with respect to open angles after springback.
- Simulated results of the 2D.EAS7 and 2D.SS4n almost conform to major softwares, concretely, 21.974° (2D.EAS7) and 23.000° (2D.SS4n) with respect to open angles before springback and 33.788° (2D.EAS7) and 33.500° (2D.SS4n) with respect to open angles after springback. For data of all cases see Tables 5.3.7 -5.3.10.

CONCLUSION

In this chapter some plasticity problems were invoked to investigate performances of the solid-shell elements. Only free from shear locking, the ANS element is not suitable to the plasticity tasks. The SS7n element, in general, gives similar results as the SS7, except the cases where large aspect ratio and large deformation occur simultaneously (Section 5.3.2). Being easy for contact handling, the solid-shell elements are well applicable to metal forming problem, such as springback prediction. As we have seen in Section 5.3.3, the simulation accuracy can be improved effectively if a good performance elements is used with a suitable methodology for choosing numerical parameters. In the last section, the 2D.EAS7, 2D.SRI, 2D.ANSn and 2D.SS4n elements are used to predict springback due to elastic recovery of the material under elastoplastic deformation. Comparing between models, the best one costs minimum computational calculation while gives a correct solution. Correlation between the numerical solution of the solid-shell element and the EAS element, a good conformability was found with the experimental solution (BE-01). However, with a limited number of enhanced modes, the solid-shell element proposes a lower computational cost than the EAS elements. Hence, the metal forming simulation with the solid-shell element promises a confident and economical tool for springback prediction in industrial manufacturing.

In conclusion, through all numerical tests, it is possible to state that the solid-shell elements are useful for simulating shell structures with a wide range of thickness (from thin ($1000 > R/t > 20$) to moderately thick ($R/t < 20$)). Advantages of the elements are:

- Connecting of the solid-shell with other continuum elements is simple;
- Easy handling of variable thicknesses;
- Accuracy over a wide range of thickness;
- No more need for mid-surface extraction;
- Easier contact handling.

Chapter 6. GENERAL CONCLUSIONS AND FUTURE WORKS

CONCLUSIONS

In the thesis, locking phenomena which happen with low-order solid elements have been analysed. The free shear locking ANS element and its performance have been introduced. As showed in Chapter 2, the EAS element can circumvent all locking effects but with high computational cost. Hence, an element which can circumvent all locking effects but with lower computational cost than the EAS element is preferred. In chapter 3, the solid-shell element (designated as SS7) has been presented as a combination of the classical ANS element [DVO84] and the EAS element [SIM90]. In comparison with the classical shell elements, the solid-shell elements allow a straightforward integration of 3D material models since they do not resort to the plane stress assumption. Moreover, their solid topology offers an effective doubly sided contact handling possibility. In comparison with the EAS solid elements, the solid-shell elements require only a limited number of EAS parameters, i.e. 7 modes, and the computational effort is thus reduced. Those features, which are truly a combination of the strong points of both the ANS and EAS methods, render the solid-shell elements very attractive.

The thesis concentrates in developing the solid-shell element. As a result, an alternative ANS technique has been presented in Chapter 3. This alternative ANS technique can incorporate with the EAS method to result in a new solid-shell element, named SS7n. This alternative ANS technique assumes that the transverse shear strains are linear in the thickness direction and in an in-plane direction. Meanwhile, following the classical ANS technique, the assumed transverse shear strains are only linear in one in-plane direction. The classical and the alternative ANS techniques were systematically compared together. Both of them can assist the solid-shell elements, SS7 and SS7n, pass the membrane and bending patch tests. Performances of the SS7 and SS7n elements have been investigated for both bulk problems and shell-like structures, ranging from thin to moderately thick structures. Theory in Chapter 3 and the plasticity test with pinched cylinder in Chapter 5 proved that the new solid-shell element, SS7n, leads to a better approximation of strains and stresses in the thickness direction than the SS7 element (with the classical ANS technique). Also, the SS7n element is less sensitive to distorted mesh than the SS7 element, see numerical test 3.6.2.

Numerical results in the thesis show that the SS7n solid-shell element is well adapted to most engineering problems. In particular, for pure bending problems and under nearly incompressible condition the SS7n element exhibits comparable or superior performances with respect to their original ANS and EAS counterparts.

FUTURE WORKS

The solid-shell SS7 and SS7n elements have been implemented in a MATLAB code. This MATLAB code is helpful to investigate linear and nonlinear elastic tests. The solid-shell SS7 and SS7n elements have been also implemented in FEAP [TAY01] to exploit the available plasticity material models and contact algorithm in FEAP. These facilities are necessary for plasticity and springback tests in Chapter 5. However, plasticity behavior and springback prediction are enormous subjects. In the thesis, only some basic aspects of these subjects have been investigated. The following works should be pursued:

- Investigating capabilities of the classical ANS technique and the alternative ANS technique in approximating transverse stresses and strains. The alternative ANS technique allows a better approximation of the stress field in the thickness direction, hence would lead to a more accurate evaluation of stress-based criteria such as delamination criteria in composite materials.
- Exploitation of the SS7 and SS7n in metal forming and springback prediction; These engineering problems are usually too complex (deformation rate, contact condition, material hardening, distorted mesh, etc.) and include a large number of DOF's. Hence, an effective (less computational cost and more accuracy) element is truly demanded.
- Apart from the springback prediction, there are also several interesting topics in metal forming field, such as tearing, wrinkling, limit forming curve, etc. Performances of the solid-shell elements with these topics may be perspective.
- In Chapter 4 we did see that the SS7n element is well applicable to structural problems. For some specific applications, such as collapse of shells, structural stability, etc. peformances of the SS7n would be useful.

The solid-shell theory in this thesis will be useful for researchers who want to apply 3D solid elements to simulate thin-walled structures. In order to facilitate research works in various topics, the solid-shell elements should be implemented in a software which had various material models, integration schemes and contact algorithms.

REFERENCE

[A]

[ADA05] L. Adam, JP. Ponthot, "*Thermomechanical modeling of metals at finite strains: first and mixed order finite elements*", International Journal of Solids and Structures 2005; **42**/21-22: 5615-5655.

[AHM70] S. Ahmad, B.M. Irons, and O.C. Zienkiewicz, "*Analysis of thick and thin shell structures by curved elements*", Int. J. Numer. Meth. Engng. 1970; **2**: 419-451.

[AND93] U. Andelfinger, E. Ramm, "*EAS-elements for two-dimensional, three-dimensional, plate and shell structures and their equivalence to HR-elements*", Int. J. Numer. Meth. Engng. 1993; **36**: 1311-1337.

[B]

[BAR91] F. Barlat, D.J. Lege, J.C. Brem, "*A six component yield function for anisotropic materials*", Int. J. of Plasticity, **7**: 693-712, 1991.

[BAT96] K.J. Bathe, "*Finite Element Procedures*", Prentice Hall, 1996.

[BAT00] K.J. Bathe, A. Iosilevich and D. Chapelle, "*An evaluation of the MITC shell elements*", Computers & Structures, **75** (1): 1-30, 2000.

[BAT03] K.J. Bathe, P.S. Lee and J.F. Hiller, "*Towards Improving the MITC9 Shell Element*", Computers & Structures, **81**: 477-489, 2003.

[BEL93] T. Belytschko, LP. Bindeman, "*Assumed strain stabilization of the eight node hexahedral element*", Computer Methods in Applied Mechanics and Engineering 1993; **105**: 225-260.

[BET95] P. Betsch, E. Stein, "*An assumed strain approach avoiding artificial thickness straining for a non-linear 4-node shell element*", Communications in Numerical Methods in Engineering 1995; **11**: 899-909.

[BET96] P. Betsch, E. Gruttmann, E. Stein, "*A 4-node finite shell element for the implementation of general hyperelastic 3D-elasticity at finite strains*", Comput. Methods Appl. Mech. Engrg. **130** (1996) 57-79.

[BIS97] M. Bischoff, E. Ramm, "*Shear deformable shell elements for large strains and rotations*", Int. J. Numer. Meth. Engng. **40**, 4427–4449 (1997).

[BIS99] M. Bischoff, E. Ramm, D. Braess, "*A class of equivalent enhanced assumed strain and hybrid stress finite elements*", Computational Mechanics, Vol. **22**, pp. 443-449, 1999.

[BIS03] M. Bischoff, F. Koschnick, K.U. Bletzinger, "*Stabilized DSG elements – A new paradigm in finite element technology*", 4th European LS-DYNA users conference, Germany 2003.

[BIS05a] M. Bischoff, K.U. Bletzinger, "*Interaction of locking and element stability at large strains*", VIII International Conference on Computational Plasticity - COMPLAS VIII, E. Onate and D.R.J. Owen (Eds), Barcelona, 2005.

[BIS05b] M. Bischoff, K.U. Bletzinger, "*Advanced Finite Element Methods*", Master Program on Computational Mechanics - Technical University of Munich, Summer Term 2005.

[BLE00] K.U. Bletzinger, "*Theory of Plates: Part II: Plates in bending*", Lecture Notes - Winter Semester, Technische Universität München, 2000

[BRA98] D. Braess, "*Enhanced assumed strain elements and locking in membrane problems*", Comput. Methods Appl. Mech. Engrg. **165** (1998) 155-174.

[BUC93] M.L. Bucalem and K.J. Bathe, "*Higher-Order MITC General Shell Elements*", Int. J. Numer. Meth. Engng. 1993; **36**: 3729-3754.

[BUI02] Q.V. BUI, "*Validation of enhanced assumed strains (EAS) 8-node brick elements in METAFOR*" - Université de Liège, LTAS-Milieux Continus & Thermomécanique, 2002.

[BUI04] Q.V. Bui, L. Papeleux, J.P. Ponthot, "*Numerical simulation of Springback using enhanced assumed strain elements*", Journal of Materials Processing Technology 2004; **153-15**:314-318.

[C]

[CAO02] Y.P. Cao, N. Hu, J. Lu, H. Fukunaga and Z.H. Yao, "*A 3D brick element based on Hu–Washizu variational principle for mesh distortion*", Int. J. Numer. Meth. Engng. 2002; **53**: 2529–2548.

[CAR07] RPR. Cardoso, JW. Yoon, M. Mahardika, S. Choudhry, RJ. Alves de Sousa, RA. Fontes Valente. "*Enhanced assumed strain (EAS) and assumed natural strain (ANS) methods for one-point quadrature solid-shell elements*". International Journal for Numerical Methods in Engineering 2007; **69**:627-663.

[CHA89] S. Chandra and G. Prathap, "*A field-consistent formulation for the eight-noded solid finite element*", Computers and Structures **33** (1989) 345-355.

[CHO01] C.K. Choi, K.Y. Chung, T.Y. Lee, "*A direct modification method for strains due to non-conforming modes*", Structural Engineering and Mechanics 2001; Vol. **11**: 325–340.

[CHU92] K. Chung, Shah K. "*Finite element simulation of sheet metal forming for planar anisotropic metals*". International Journal of Plasticity 1992; **8**: 453 - 476.

[D]

[DJO05] J.K. Djoko, B.P. Lamichhane, B.D. Reddy and B. I. Wohlmuth, "*Conditions for equivalence between the Hu-Washizu and related formulations, and computational behavior in the incompressible limit*", Institut fur Angewandte Analysis und Numerische Simulation (IANS), 2005.

[DOL00] S. Doll, K. Schweizerhof, R. Hauptmann, C. Freischläger, "*On volumetric locking of low-order solid and solid-shell elements for finite elasto-viscoplastic deformation and selective reduced integration*", Engineering Computations, vol. **17**, pp 874-902, 2000.

[DUR58] A.J. Durelli, E.A. Phillips and C.H. Tsao, "*Introduction to the theoretical and experimental analysis of stress and strain"* - New York : McGraw-Hill, 1958.

[DVO84] E.N. Dvorkin, K.J. Bathe, "*A continuum mechanics based four-node shell element for general non-linear analysis*", Engrg. Comput. **1** (1984) 77–88.

[DVO95] E.N. Dvorkin, D. Pantuso and E.A. Repetto, "*A formulation of the MITC4 shell element for finite strain elasto-plastic analysis*", Comput. Meth. Appl. Mechs. Engrg., **125**, 17-40, 1995.

[F]

[FEL02] C.A. Felippa and K.C. Park, "*Fitting Strains and Displacements by Minimizing Dislocation Energy*", 6th International Conference on Computational Structures Technology, Prague - Czech Republic, September 2002.

[FEL03] C.A. Felippa, "*Advanced Finite Element Methods (ASEN 5367)*" (http://titan.colorado.edu/courses.d/AFEM.d/), Colorado, 2003.

[FEL05a] C.A. Felippa, "*Supernatural Quad4: A template formulation*" Report No. CU-CAS-05-06, Dept. of Aerospace Engineering Sciences and Center for Aerospace Structures, Univ. of Colorado, 2005.

[FEL05b] C.A. Felippa, "*A template tutorial*", Ch. 3 of *Computational Mechanics Theory and Practice*, ed. by K. M. Mathisen, T. Kvamsdal and K. M. Okstad, CIMNE, Barcelona, 2005.

[FLU73] W. Flugge, " *Stresses in shells*", Springer-Verlag - NewYork, 1973.

[FRE07] M. Fredriksson and N. S. Ottosen, "*Accurate eight-node hexahedral element*", Int. J. Numer. Meth. Engng.; **72**: 631-657, 2007.

[FRE96] C. Freischläger, K. Schweizerhof, "*On a systematic development of trilinear three-dimensional solid elements based on Simo's enhanced strain formulation"*, Int. J. Solids Struct.; Vol. **33**, No. 20-22: 2993-3017, 1996.

[H]

[HAC89] W.L. Hacker, H.L. Schreyer, "*Eigenvalue analysis of compatible and incompatible rectangular four-node quadrilateral elements*", Int. J. Numer. Meth. Engng.; **28**: 687–703, 1989.

[HAN98] P. Hansbo, "*A new approach to quadrature for finite elements incorporating hourglass control as a special case*", Comput. Methods Appl. Mech. Engrg. **158**: 301-309, 1998.

[HAR02] M. Harnau, K. Schweizerhof, "*About linear and quadratic ''Solid-Shell'' elements at large deformation*", Computers and Structures **80**: 805–817, 2002.

[HAU98] R. Hauptmann, K. Schweizerhof, "*A systematic development of `solid-shell' element formulations for linear and non-linear analyses employing only displacement degrees of freedom*", Int. J. Numer. Meth. Engng **42**, 49-69, 1998.

[HAU00] R. Hauptmann, K. Schweizerhof, S. Doll, "*Extension of the 'solid-shell' concept for application to large elastic and large elastoplastic deformations*", Int. J. Numer. Meth. Engng; **49**: 1121-1141, 2000.

[HAU01] R. Hauptmann, S. Doll, M. Harnau, K. Schweizerhof, "*'Solid-shell' elements with linear and quadratic shape functions at large deformations with nearly incompressible materials*", Computers and Structures; **79** : 1671-1685, 2001.

[HIL90] R. Hill, "*Constitutive modelling of orthotropic plasticity in sheet metals*", J. Mech. Phys. Solids, **38** (3) 405-417, 1990.

[HIL00] R. Hill, "*Plastic anisotropy and the geometry of yield surface in stress space*", J. Mech. Phys. Solids, **48**: 1093-1106, 2000.

[HOG76] M. Hogge, "*Transfert de chaleur et contraintes thermiques dans les structures par la méthode des éléments finis*". PhD thesis (in French), Université de Liège, Liège, Belgium, 1976.

[HOL96] GA. Holzapfela, R. Eberleinb, P. Wriggers, HW. Weizsäcker. "*Large strain analysis of soft biological membranes: Formulation and finite element analysis*". Comput. Methods Appl. Mech. Engrg, **132** (1-2): 45-61, 1996.

[HOL00] G.A. Holzapfel, "*Nonlinear solid mechanics*", Jonh Wiley & Sons, Ltd., Chichester 2000.

[HUG81] T.J.R. Hughes, T.E. Tezduyar, "*Finite elements based upon Mindlin plate theory with particular reference to the four-node bilinear isoparametric element*", J. Appl. Mech., **48**: 587-596, 1981.

[HUH00] H. Huh, S.H. Kim, "*Stress evaluation with numerical integration schemes in finite element analysis of elasto-plastic bending*", Commun. Numer. Meth. Engng, **16** (11): 755 – 767, 2000.

[J]

[JET08] P. Jetteur, "*Elément "Solid shell" dans Samcef*", Rapport 252, Samtech (2008).

[JIA97] Z.P. Jiao, T.H.H. Pian, S. Yong, "*A new formulation of isoparametric finite elements and the relationship between hybrid stress element and incompatible element*", Int. J. Numer. Meth. Engng **40**, 15-27, 1997.

[K]

[KAS00a] E.P. Kasper, R.L. Taylor, "*A mixed-enhanced strain method Part I: Geometrically linear problems*", Computers and Structures **75** 237-250, 2000.

[KAS00b] E.P. Kasper, R.L. Taylor , "*A mixed-enhanced strain method Part II: Geometrically nonlinear problems*", Computers and Structures **75** 251-260, 2000.

[KLI97] S. Klinkel and W. Wagner, "*A geometrical non-linear brick element based on the EAS-method*", Int. J. Numer. Meth. Engng **40**, 4529-4545, 1997.

[KLI02] S. Klinkel and S. Govindjee, "*Using finite strain 3D-material models in beam and shell elements*", Engineering Computations, Vol. **19** No. 8, pp. 902-921, 2002.

[KLI06] S. Klinkel, F. Gruttmann and W. Wagner, "*A robust non-linear solid shell element based on a mixed variational formulation*", Comput. Methods Appl. Mech. Engrg. **195** 179–201, 2006.

[KUH00] D. Kuhl, E. Ramm, "*Time Integration in the Context of Energy Control and Locking Free Finite Elements*", Comput. Methods in Engrg. Vol. **7,** Issue **3** 299-332, 2000.

[L]

[LAU00] N. Lautersztajn-S and A. Samuelsson, "*Further discussion on four-node isoparametric elements in plane bending*", Int. J. Numer. Meth. Engrg., **47**, 129–140, 2000.

[LEM90] J. Lemaitre and J.L. Chaboche, "*Mechanics of solid materials*", Trans. by B. Shrivastava, Cambridge University Press, Cambridge, UK, 1990.

[LI97] K.P. Li and S. Cescotto, "*An 8-node brick element with mixed formulation for large deformation analyses*", Comp. Methods Appl. Mech. Engrg., **141**, 157-204, 1997

[M]

[MAC85] R.H. McNeal and R.L. Harder, "*A proposed standard set of problems to test finite element accuracy*", Finite Elements in Analysis and Design, Volume **1**, Issue 1, April 1985, Pages 3-20.

[MAC87] R.H. McNeal, "*A theorem regarding the locking of tappered four-noded membrane elements*", Int. J. Numer. Meth. Engng. 1987; **24**: 1793-1799.

[MAC92] R.H. McNeal, "*On the limits of finite element perfectability*", Int. J. Numer. Meth. Engng.; **35**: 1589-1601, 1992.

[MAC94] R.H. McNeal, "*Finite elements : their design and performance (Mechanical engineering series/ 89)*", Marcel Dekker, New York, 1994.

[MAL69] L.E. Malvern, "*Introduction to the mechanics of a continuous medium*", Prentice-Hall, Englewood Cliffs, New Jersay, 1969.

[MET08] METAFOR. "A finite element software for large strain analysis", *http://www.ltas-mnl.ulg.ac.be/dokuwiki/doku.php*, Liège, 2008.

[MIE04] C. Miehe, N. Apel, "*Anisotropic elastic-plastic analysis of shells at large strains. A comparison of multiplicative and additive approaches to enhanced finite element design and constitutive modelling*", Int. J. Numer. Meth. Engng.; **61**: 2067-2113, 2004.

[MIL90a] C. Militello and C.A. Felippa, "*A variational justification of the assumed natural strain formulation of finite elements—I. Variational principles*", Computers and Structures **34**: 431-438, 1990.

[MIL90b] C. Militello and C.A. Felippa, "*A variational justification of the assumed natural strain formulation of finite elements— II. The C^0 four-node plate element*", Computers and Structures **34**: 439-444, 1990.

[N]

[NGU08] N.H. Nguyen, V.N. Pham, M. Hogge and J.P. Ponthot. "*An assumed natural strain technique for 2D solid-shell elements*". ACOMEN 2008, Editors: M. Hogge, R. Van Keer, L. Noels, L. Stainier, J.-P. Ponthot, J.-F. Remacle, E. Dick. University of Liège, Belgium, 26-28 May 2008.

[NUM02] NUMISHEET 2002, in: D.Y. Yang, S.I. Oh, H. Huh, Y.H. Kim (Eds.),. "*Proceedings of the 5th International Conference and Workshop on Numerical Simulation of 3D Sheet Forming Processes - Verification of Simulation with Experiments*". Jeju Island, Korea, 2002.

[O]

[OWE86] D.R.J. Owen and E. Hinton, "*Finite elements in Plasticity: theory and practice*", Pineridge Press Ltd., Swansea, UK. 1986.

[P]

[PAP98] P. Papadopoulos and J. Lu, "*A general framework for the numerical solution of problems in finite elasto-plasticity*", Comput. Methods Appl. Mech. Engrg. 1998, **159**: 1–18.

[PAP01] P. Papadopoulos and J. Lu, "*On the formulation and numerical solution of problems in anisotropic finite plasticity*", Comput. Methods Appl. Mech. Engrg. 2001, **190** (37-38): 4889–4910.

[PAR86] K.C. Park and G.M. Stanley, "*A curved C^0 shell element based on assumed natural coordinate strains*", J. Appl. Mech. 1986, **53**: 278–290.

[PIA86] T.H.H. Pian, "*Relations between incompatible displacement model and hybrid stress model*", Int. J. Numer. Meth. Engng. 1986; **22**: 173-181.

[PIA06] T.H.H. Pian, C.C. Wu, "*Hybrid and incompatible finite element methods*", Boca Raton: Chapman & Hall/CRC, 2006.

[PIL99] R. Piltner and R.L. Taylor, "*A systematic construction of B-bar functions for linear and non-linear mixed-enhanced finite elements for plane elasticity problems*", Int. J. Numer. Meth. Engng. 1999; **44**: 615-639.

[PIL00] R. Piltner, "*An implementation of mixed enhanced finite elements with strains assumed in Cartesian and natural element coordinates using sparse $\overline{B}$ -matrices*", Engng. Comput 2000; Vol. **17** № **8**: 933-949.

[PON94] J-P. Ponthot and M. Hogge, "*On relative merits of implicit / explicit algorithms for transient problems in metal forming simulation*". In International Conference on Numerical Methods for Metal Forming in Industry, Vol **2**, pp 128-148, Baden-Baden, Germany, Sept. 1994.

[PON95] J-P. Ponthot, "*Traîtement unifié de la Mécanique des Milieux Continus solides en grandes transformations par la méthode des éléments finis*". PhD thesis (in French), Université de Liège, Liège, Belgium, 1995.

[PON99] J-P Ponthot and D. Graillet, "*Efficient implicit schemes for the treatment of the contact between deformable bodies: Application to shock-absorber devices*", International Journal of Crashworthiness; **4**: 273-286, 1999.

[PRA85] G. Prathap, "*The poor bending response of the four-node plane stress quadrilateral*", Int. J. Numer. Meth. Engng.; **21**: 825-835, 1985.

[PRA01] G. Prathap, "*Finite element analysis as computation*", On-line book of *http://www.cmmacs.ernet.in/*, Bangalore, 2001.

[PUS00] M.A. Puso, "*A highly efficient enhanced assumed strain physically stabilized hexahedral element*", Int. J. Numer. Meth. Engng.; **49**:1029-1064, 2000.

[Q]

[QUO03a] L. Vu-Quoc and X.G. Tan, "*Optimal solid shells for non-linear analyses of multilayer composites. I. Statics*", Comput. Methods Appl. Mech. Engrg. **192** (2003) 975–1016.

[QUO03b] L. Vu-Quoc and X.G. Tan, "*Optimal solid shells for non-linear analyses of multilayer composites. II. Dynamics*", Comput. Methods Appl. Mech. Engrg. **192** (2003) 1017–1059.

[R]

[RAO01] K.M. Rao and U. Shrinivasa, "*A set of pathological tests to validate new finite elements*", Sadhana Vol. **26**, Part 6, December 2001, pp. 549–590. © Printed in India.

[REE05] S. Reese, "*On a physically stabilized one point finite element formulation for three-dimensional finite elasto-plasticity*", Comput. Methods Appl. Mech. Engrg. **194** (2005) 4685–4715.

[REE07] S. Reese, "*A large deformation solid-shell concept based on reduced integration with hourglass stabilization*". International Journal for Numerical Methods in Engineering 2007; **69**:1671-1716.

[S]

[SCH02] J. Schröder, F. Gruttmann and J. Löblein, "A simple orthotropic finite elasto–plasticity model based on generalized stress–strain measures", Computational Mechanics **30** (2002), 48–64.

[SCI02] F.M. Sciarra, "*Relations between enhanced strain methods and the HR method*", Comput. Methods Appl. Mech. Engrg. **191** (2002), 2661–2677.

[SIM86] J.C. Simo, T.J.R. Hughes, "*On the variational foundations of assumed strain methods*", ASME J. Appl. Mech. 1986; **53**: 51–54.

[SIM88a] J.C. Simo, "*A frame work for finite strain elastoplasticity based on maximum plastic dissipation and the multiplicative decomposition: Part I. Continuum formulation*", Comput. Meth. Appl. Mechs. Engrg., **66**, 199-219, 1988.

[SIM88b] J.C. Simo, "*A frame work for finite strain elastoplasticity based on maximum plastic dissipation and the multiplicative decomposition: Part II. Computational aspect*", Comput. Meth. Appl. Mechs. Engrg., **68**, 1-31, 1988.

[SIM90] J.C. Simo, M.S. Rifai, "*A class of mixed assumed strain methods and the method of incompatible mode*", Int. J. Numer. Meth. Engng. 1990; **29**: 1595–1638.

[SIM92a] J.C. Simo, F. Armero, "*Geometrically nonlinear enhanced-strain mixed methods and the method of incompatible modes*", Int. J. Numer. Meth. Engng. 1992; **33**: 1413-1449.

[SIM92b] J.C. Simo, "*Algorithms for static and dynamic multiplicative plasticity that preserve the classical return mapping schemes of the infinitesimal theory*" Comput. Methods Appl. Mech. Engrg. 1992; **99**(1): 61 - 112.

[SIM93] J.C. Simo, F. Armero, R. L. Taylor, "*Improved versions of assumed enhanced strain tri-linear elements for 3D finite deformation problem*", Comput. Methods Appl. Mech. Engrg. **110** (1993) 359–386.

[SIM98] J.C. Simo, T.J.R. Hughes, "*Computational Inelasticity*" - Interdisciplinar Applied Mathematics Vol. 7, Springer Verlag, New York, 1998.

[SLA94] R. Slavkovic, M. Zivkovic, M. Kojic, "*Enhanced 8-node three-dimensional solid and 4-node shell elements with incompatible generalized displacements*", Commun. Numer. Meth. Engng. **10** (1994) 699–709.

[STE94] P. Steinmann, C. Miehe, E. Stein, "*On the localization analysis of orthotropic Hill-type elastoplastic solids*", J. Mech. Phys. Solids, **42** (1994) 1969-1994.

[STO82] H. Stolarski, T. Belytshcko, "*Membrane locking and reduced integration for curved elements*", Journal of Applied Mechanics. **49** (1982) 172–176.

[STO83] H. Stolarski, T. Belytshcko, "*Shear and membrane locking in curved C^0 elements*", Comput. Methods Appl. Mech. Engrg. **41** (1983) 279-296.

[STO95] H. Stolarski, T. Belytschko, S.H. Lee, "*A review of shell finite elements and corotational theories*", Computational Mechanics Advances. **2** (1995) 125-212.

[SZE00] K. Y. Sze, L. Q. Yao, "*A hybrid stress ANS solid-shell element and its generalization for smart structure modelling. Part I*solid-shell element formulation*", Int. J. Numer. Meth. Engng. 2000; **48**: 545–564.

[T]

[TAN05] X.G. Tan and L. Vu-Quoc, "*Efficient and accurate multilayer solid-shell element: Non-linear materials at finite strain*", Int. J. Numer. Meth. Engng. **63**: 2124–2170 (2005).

[TAY76] R.L. Taylor, P.J. Beresford, E.L. Wilson, "*A non-conforming element for stress analysis*", Int. J. Numer. Meth. Engng. **10**, 1211-1219 (1976).

[TAY00] R.L. Taylor, "*A mixed-enhanced formulation fortetrahedral finite elements*", Int. J. Numer. Meth. Engng. **47**, 205-227 (2000).

[TAY01] R.L. Taylor, "*FEAP - A Finite Element Analysis Program: Theory Manual, University of California, Berkeley, 2001*", http://www.ce.berkeley.edu/~rlt/feap/.

[TIM59] S.P. Timoshenko and S. Woinowsky-Krieger, "*Theory of plates and shells"* - 2th Edition, Engineering Societies Monographs, New York: McGraw-Hill, 1959. US.

[V]

[VLA49] V. Vlasov, "*Some new problems on shells and thin structures*", Washington : National advisory committee for aeronautics, 1949.

[W]

[WIL02] K.J. Willam, "*Constitutive models for engineering materials*", Encyclopedia of Physical Science & Technology – 3rd Edition, Volume **3** pp. 603-633, Academic Press, 2002.

[WIL73] E.L. Wilson, R.L. Taylor, W.P. Doherty, J. Ghaboussi, "*Incompatible displacement modes*", in: S.J. Fenves, N. Perrone, A.R. Robinson, W.C. Sehnobrich (Eds.), Numerical and Computer Models in Structural Mechanics, Academic Press, New York, 1973.

[WRI96a] P. Wriggers, S. Reese, "*A note on enhanced strain methods for large deformations*", Comput. Methods Appl. Mech. Engrg. **135** (1996) 201-209.

[WRI96b] P. Wriggers, R. Eberlein and S. Reese, "*A comparison of three-dimensional continuum and shell elements for finite plasticity*", Int. J. of Solids Structures Vol. **33**, No 20-22, p 3309-3326, 1996.

[Y]

[YAN00] H.T.Y Yang, S. Saigal, A. Masud, R.K. Kapania, "*A survey of recent shell finite elements*", Int. J. Numer. Meth. Engng. **47**, 101-127 (2000).

[YOO99] J.W. Yoon, D.Y. Yang and K. Chung, "*Elasto-plastic finite element method based on incremental deformation theory and continuum based shell elements for planar anisotropic sheet materials*", Computer Methods in Applied Mechanics & Engineering **174**, 23-56 (1999).

[Z]

[ZIE00a] O.C. Zienkiewicz and R.L. Taylor, "*The Finite Element Method ,* Volume 1: *The Basis*" - 5th Edition, Butterworth-Heinemann, 2000. UK.

[ZIE00b] O.C. Zienkiewicz and R.L. Taylor, "*The Finite Element Method ,* Volume 2: *Solid mechanics"* - 5th Edition, Butterworth-Heinemann, 2000. UK.

CONTENTS